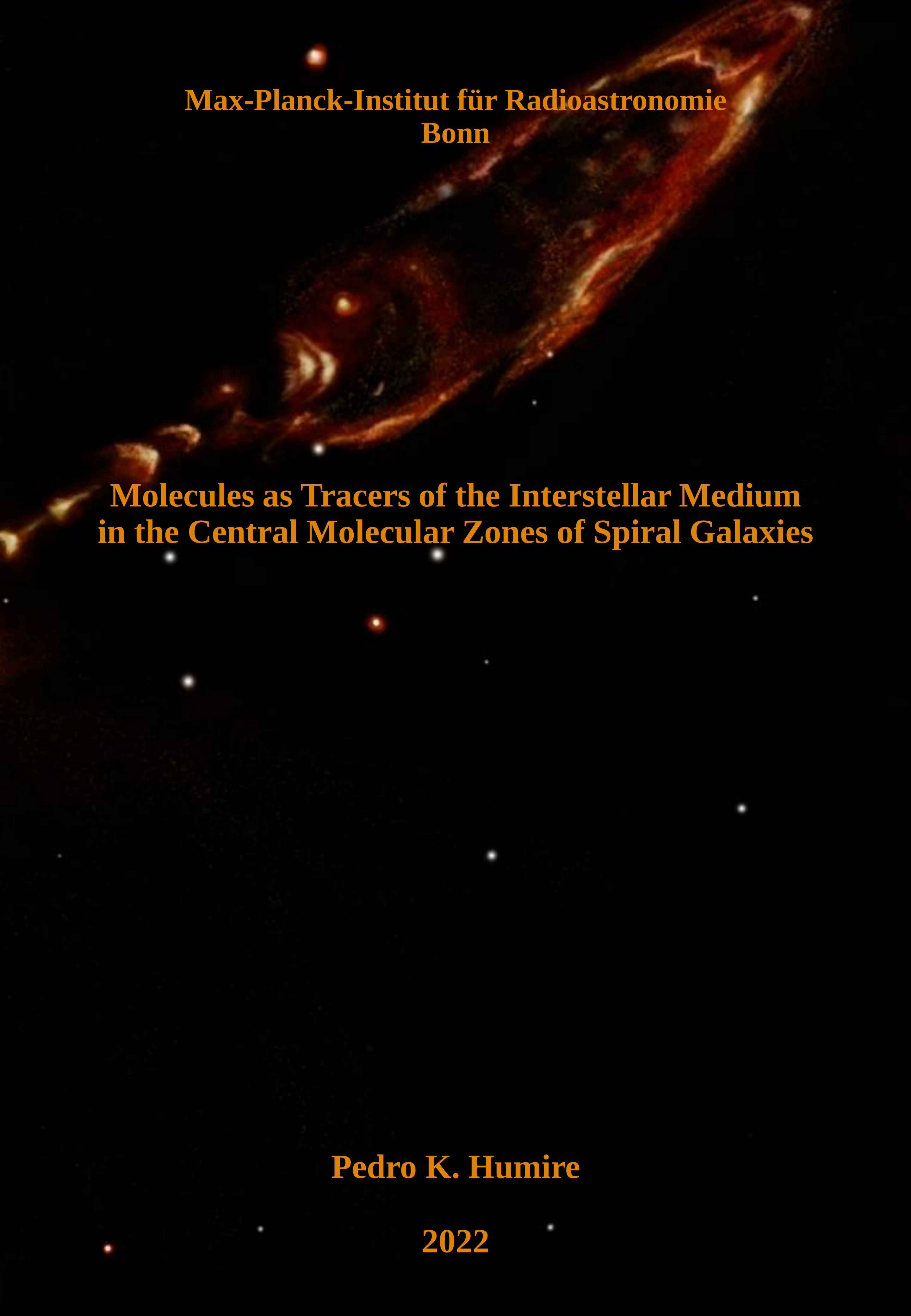

Max-Planck-Institut für Radioastronomie
Bonn

Molecules as Tracers of the Interstellar Medium in the Central Molecular Zones of Spiral Galaxies

Pedro K. Humire

2022

Molecules as Tracers of the Interstellar Medium in the Central Molecular Zones of Spiral Galaxies

Dissertation
zur
Erlangung des Doktorgrades (Dr. rer. nat.)
der
Mathematisch-Naturwissenschaftlichen Fakultät
der
Rheinischen Friedrich-Wilhelms-Universität Bonn

vorgelegt von
Pedro K. Humire
aus
Arica, Chile

Bonn 2022

Angefertigt mit Genehmigung der Mathematisch-Naturwissenschaftlichen Fakultät der Rheinischen Friedrich-Wilhelms-Universität Bonn

1. Gutachter:	Prof. Dr. Anton Zensus
2. Gutachter:	Prof. Dr. Frank Bertoldi

Tag der Promotion: 19.12.2022
Erscheinungsjahr: 2023

Abstract

This thesis is devoted to the investigation of two important astronomical topics related to prevailing conditions in the central molecular zone (CMZ) of spiral galaxies. The first one is based on the analysis of sulfur and carbon rare isotopes, mainly synthesized in massive stars and expelled to the interstellar medium by stellar winds and supernova explosions. Without the contribution of massive stars, our universe would show quite a different kinematics and would be devoid of life, since they are responsible for releasing the most complex elements into the interstellar medium. These elements, heavier than iron, are often recycled by less massive stars that have succeeded them, as is the case of our Sun. The Sun inherited these substances as a second or third generation star, explaining the complex materials present in its surrounding planets. Although hydrogen and helium make up 98% of the baryonic mass in the universe, hydrogen is responsible for only 10% of human being's compositions. In contrast, 73% of the atoms in the human body are related to material released in exploding massive stars.

The study of sulfur and carbon through its most abundant molecule, carbon monosulfide (CS), is a feasible path to probe what happens inside of stars. By using carbon isotopologue ratios it is possible to prove that the nucleus of our Galaxy is "older" compared to their spiral arms, suporting the inside-out growth scenario of the Galactic Disk. The CS observation also gives us information about the metallicity of the environment in which massive stars reside. The latter is relevant for the refinement of star formation models.

The second topic covered by this work is about the microwave amplification by stimulated emission of radiation (maser lines) from interstellar molecules. While the searching for sulfur across the Milky Way works as an archeologist looking for the previous existence of massive stars, masers occur at early stages of star formation. Masers can originate in a variety of environments, from planetary nebulae to active galactic nuclei. Methanol masers are more restricted in origin and can be used to trace the earliest stages of high-mass star formation. The study of extragalactic methanol masers is a promising new field of research and has great potential to be explored in detail in the coming years.

In the course of this thesis more than 110 (12 m array) and 260 (ACA) hours of integration time have been used from the Atacama Large (sub)millimiter array (ALMA), and more than 60 hours with the Effelsberg telescope. Further ALMA observations have been recycled from the Ph.D. Thesis of Vivien Thiel (2019) and combined with newly observed IRAM 30 m and APEX data.

The main findings of this thesis can be summarized as follows. Regarding the first topic, we have found that the decreasing trend of the ^{32}S/^{34}S abundance ratio towards the Galactic nucleus is halted somewhere between 1 kpc and $\sim$130 pc from the galactic center and then reverts to values similar to those encountered in the solar neighborhood. This confirms that the metallicity in the nuclear regions of our Galaxy is similar to the solar one, and indicates a drop in the production of massive stars from the outer limits of our Galaxy until 1 kpc from its nucleus. With respect to the second topic, we have found that methanol masers pumped by shocks are the brightest, and that the conditions required to produce them are weak shocks, generated where entrained material by spiral arms interacts with the nuclear bar. Complementarily, dissociating UV radiation is the most likely explanation for the lack of methanol masers at the very center of spiral galaxies. Quantitatively speaking, we have increased the amount of known galaxies hosting methanol masers beyond the local group: the sample now includes Maffei 2. Furthermore, we have expanded the number of extragalactic methanol maser transitions detected so far from 5 to 11, reporting the first detections at 95, 132, 146, 198, 229, and 278 GHz around the core of NGC 253.

Acknowledgements

Several people enabled me to complete my doctoral studies. From the Max Planck Society, I owe first of all my gratitude to the Max Planck International Research School (IMPRS) for Astronomy & Astrophysics, for the invaluable support throughout these long years, including financial, administrative, logistical, and psychological one. All of these are natural needs that arise when studying in a foreign country. In this regard, the help and infinite patience of Simone Pott, Tuyet-Le Tran, and Barbara Menten was crucial. In the academic field I could not wish for better advisors than Christian Henkel, Rainer Mauersberger, and Sergio Martín, thanks to whom the common problems between students and advisors were just a myth for me. On the contrary, the patience they devoted to me is a luxury few can boast of. Their human quality above all is a lesson that I will keep beyond my studies and the academic field. I also want to thank Sergio Martín for his warm welcome and help during my stay in Santiago de Chile, which was critical to bring my latest work to fruition. Regarding the latter, I owe a debt of gratitude to the European Southern Observatory for making the collaboration possible. Furthermore, I am also indebted to my entire advisory committee, that includes not only the mentioned advisors, but also Anton Zensus and Frank Bertoldi. Without the financial and administrative support they represent, my path to a doctorate would certainly have been impossible.

During all these years the backing of my family, mainly my parents, brother, and my dear Claudia, formed a great support of which I availed myself almost daily. Without them my life would have been very complicated. Periodic travels to Chile gave me the necessary energy to finish my doctorate.

Something I will never forget were my first days in Germany, during which Anne & Jürgen signified a new niche from which to stand, helped me to adjust to my new life. Learning the rules of conduct along with glimpses of the wonderful German language made my experience similar to being born again. Then, the first months resulted in the creation of new friendships, among them I must highlight the affection given by Mrs. Elke, who loves Chile and has treated me like a son. Thanks to you I was able to survive difficult moments of loneliness and mourning during the worst days of the pandemic.

It is impossible not to mention my friends at the Max Planck for Radio Astronomy, especially Antonio and Gisela for their sincere friendship from which I drew a lot and on which I could rely during the pandemic, when they became the only ones I could visit. It is gratifying to know that we are currently involved in several projects together, and I hope that this will continue in the near future.

I would like to express my sincere admiration to all the collaborators that I have accreted during these long years, such as all the co-authors of my publications, both in the master's and doctoral programs. It is important to highlight the great work of my favorite journal, Astronomy & Astrophysics, for bringing my writings to fruition and not charging for their edition, allowing to bring science closer to the community.

When I was finishing my master's studies, one of my dearest loved ones left this world. I dedicated my thesis at that time to him, my paternal grandfather. My grandparents were in charge of teaching me the first steps to live, instilling in me a strong duty and sake of studying. Now, in these days of the middle of the year, I have turned my gaze recurrently to the one who was born on a day like today, my father, Pedro Humire (without a “K”). I still can’t believe that you are no longer here to congratulate me for my achievements, but you have to know that, without you, the fundamental questions would not have such a latent importance in my life. It is for that, and many other things impossible to say in words, that I dedicate this, my last thesis, to you.

List of publications

1. **Humire, P. K.**; Henkel, C.; Hernández-Gómez, A.; Martín, S.; Mangum, J.; Harada, N.; Muller, S.; Sakamoto, K.; Tanaka, K.; Yoshimura, Y.; Nakanishi, K.; Mühle, S.; Herrero-Illana, R.; Meier, D. S.; Caux, E.; Aladro, R.; Mauersberger, R.; Viti, S.; Colzi, L.; Rivilla, V. M.; Gorski, M.; Menten, K. M.; Huang, K. -Y.; Aalto, S.; van der Werf, P. P.; Emig, K. L. (2022). Methanol masers in NGC 253 with ALCHEMI *Astronomy & Astrophysics*, 663A, 33H.

   Author contributions: P.H. was the primary author and main contributor to the article. A.H. gave advice on the radiative transfer models and blending line identification and also gave supervision to the article writing since the earliest stages. S.M., J.M., and N.H. are the PIs of the ALCHEMI collaboration, giving support all along with the article, including the observation proposal, data reduction and distribution, and periodic advice. J.M. provided helpful suggestions for the article structure. S.M. gave further advice during a two-months internship of P.H. at ESO. S. Muller provided important suggestions and comments especially useful for Appendix A and also provided Fig. 11. S. Muller, S.K., K.T., Y.Y., K.N., S. Mühle, and R.H-I. were in charge of the data reduction. D.S.M. and S.K. provided essential advice on the scientific aspects of the text. E.C. checked the radiative transfer models with a special emphasis in Appendix C. The remaining authors gave helpful suggestions throughout the text.

2. **Humire, P. K.**; Thiel, V.; Henkel, C.; Belloche, A.; Loison, J. -C.; Pillai, T.; Riquelme, D.; Wakelam, V.; Langer, N.; Hernández-Gómez, A.; Mauersberger, R.; Menten, K. M. (2020). Sulphur and carbon isotopes towards Galactic centre clouds *Astronomy & Astrophysics*, 642A, 222H.

   Author contributions: P.H. performed the analysis and largely contributed to the article. The second and fourth authors, V.T. & A.B. conducted the data reduction of Sgr B2(N). V.T. analyzed the Sgr B2(N) data, and performed the radiative transfer fitting to the l.o.s. towards Sgr B2(N) (see Fig. 3.) and provided a continuum image (Fig. 1.). J-C.L. built the chemical fractionation model used in Sect. 4.3. T.P. & D.R. observed the +50 $\mathrm{km\,s^{-1}}$ Cloud and provided the FITS files. V.W. ran the chemical fractionation models. N.L. provided useful information and updated references about stellar nucleosynthesis and stellar evolution models. The remaining authors provided suggestions and also gave interpretations of the obtained results.

3. **Humire, P. K.**; Henkel, C.; Gong, Y.; Leurini, S.; Mauersberger, R.; Levshakov, S. A.; Winkel, B.; Tarchi, A.; Castangia, P.; Malawi, A.; Asiri, H.; Ellingsen, S. P.; McCarthy, T. P.; Chen, X.; Tang, X. (2020). 36 GHz methanol lines from nearby galaxies: maser or quasi-thermal emission? *Astronomy & Astrophysics*, 633A, 106H.

   Author contributions: P.H. was the main contributor of the article. P.H. & C.H. performed the observations. The remaining authors provided suggestions and also gave interpretations of the obtained results. C. H. performed the data reduction and wrote the proposal to Effelsberg.

Publications as a member of the ALCHEMI Collaboration

P.H. contributed with suggestions in various sections of the articles. P.H. also contributed with part of the continuum analysis presented in Section 4.1 and Fig. 5 of the second last article (*B*).

E A Haasler, D.; Rivilla, V. M.; Martín, S.; Holdship, J.; Viti, S.; Harada, N.; Mangum, J.; Sakamoto, K.; Muller, S.; Tanaka, K.; Yoshimura, Y.; Nakanishi, K.; Colzi, L.; Hunt, L.; Emig, K. L.; Aladro, R.; **Humire, P.**; Henkel, C.; van der Werf, P. (2022). First extragalactic detection of a phosphorus-bearing molecule with ALCHEMI: Phosphorus nitride (PN). *Astronomy & Astrophysics*, 659A, 158H.

D A Harada, Nanase; Martín, Sergio; Mangum, Jeffrey G.; Sakamoto, Kazushi; Muller, Sebastien; Tanaka, Kunihiko; Nakanishi, Kouichiro; Herrero-Illana, Rubén; Yoshimura, Yuki; Mühle, Stefanie; Aladro, Rebeca; Colzi, Laura; Rivilla, Víctor M.; Aalto, Susanne; Behrens, Erica; Henkel, Christian; Holdship, Jonathan; **Humire, P. K.**; Meier, David S.; Nishimura, Yuri; van der Werf, Paul P.; Viti, Serena. (2021). Starburst Energy Feedback Seen through HCO^+/HOC^+ Emission in NGC 253 from ALCHEMI. *The Astrophysical Journal*, 923, 24H.

C A Barrientos, Alejandro; Holdship, Jonathan; Solar, Mauricio; Martín, Sergio; Rivilla, Víctor M.; Viti, Serena; Mangum, Jeff; Harada, Nanase; Sakamoto, Kazushi; Muller, Sébastien; Tanaka, Kunihiko; Yoshimura, Yuki; Nakanishi, Kouichiro; Herrero-Illana, Rubén; Mühle, Stefanie; Aladro, Rebeca; Aalto, Susanne; Henkel, Christian; **Humire, Pedro**. (2021). Towards the prediction of molecular parameters from astronomical emission lines using Neural Networks. *Experimental Astronomy*, 52, 157B.

B A Martín, S.; Mangum, J. G.; Harada, N.; Costagliola, F.; Sakamoto, K.; Muller, S.; Aladro, R.; Tanaka, K.; Yoshimura, Y.; Nakanishi, K.; Herrero-Illana, R.; Mühle, S.; Aalto, S.; Behrens, E.; Colzi, L.; Emig, K. L.; Fuller, G. A.; García-Burillo, S.; Greve, T. R.; Henkel, C.; Holdship, J.; **Humire, P.**; Hunt, L.; Izumi, T.; Kohno, K.; König, S.; Meier, D. S.; Nakajima, T.; Nishimura, Y.; Padovani, M.; Rivilla, V. M.; Takano, S.; van der Werf, P. P.; Viti, S.; Yan, Y. T. (2021). ALCHEMI, an ALMA Comprehensive High-resolution Extragalactic Molecular Inventory. Survey presentation and first results from the ACA array *Astronomy & Astrophysics*, 656A, 46M.

A A Holdship, J.; Viti, S.; Martín, S.; Harada, N.; Mangum, J.; Sakamoto, K.; Muller, S.; Tanaka, K.; Yoshimura, Y.; Nakanishi, K.; Herrero-Illana, R.; Mühle, S.; Aladro, R.; Colzi, L.; Emig, K. L.; García-Burillo, S.; Henkel, C.; **Humire, P.**; Meier, D. S.; Rivilla, V. M.; van der Werf, P. (2021). The distribution and origin of C2H in NGC 253 from ALCHEMI. *Astronomy & Astrophysics*, 654A, 55H.

Contents

CHAPTER 1

Introduction

1.1 Context

1.1.1 Low to high mass star formation

Intermediate- and low-mass stars

The formation of a Sun-like star is a complex process which includes competing forces such as gravitational collapse, magnetic fields, nuclear processes, thermal pressures, and stellar winds. Although optical wavelengths are obstructed by the dust that swaddles a protostar, we can use infrared radiation to observe these objects, as their longer wavelengths can evade the dust grains and so escape from the cloud's inner layers.

A Sun-like star formation consists in a series of stages that span more than 50 million years. Such formation begins inside dark molecular clouds containing high-density regions that collapse gravitationally in fragments of $\sim$10 pc size and temperatures of 10–20 K (Shu et al., 1987; Lada & Shu, 1990). During this initial stage, the parent molecular cloud is detected almost exclusively by (sub)millimiter wavelengths of dust and molecules. Inside these fragments, there is a collapsing core that forms a protostar, consisting of a sphere in hydrostatic equilibrium referred as "first hydrostatic core" (Larson, 1969) and a circumstellar disk fed by dust and gas from the surrounding envelope. Some percentage of the inner parts of the accreting disk feed the central object while the remaining fraction is ejected by bipolar outflows produced by magnetic forces coiled around the accretion disk. These outflows liberate the excess of angular momentum of the infalling material and push away the remaining dust and gas envelope (André et al., 1993). The involved accretion and mass-loss processes can be indirectly studied through the observation of Herbig-Haro flows and associated weak 22 GHz water masers (Reipurth & Bally, 2001). The protostar period lasts 10^{4-5} years and is divided in different classes ranging from Class 0 to Class III protostars, distinguished by means of their spectral energy distribution (SED; André et al., 1993; Greene et al., 1994). Consecutive formation stages, such as pre-main-sequence (PMS) stars, can be also distinguished through SED observations, as depicted in Fig. 1.1.

As the dusty envelope dissipates, the object becomes visible in optical wavelengths for the first time. After a few million years, the dusty disk concentrates in the equator, revealing a pre-main-sequence star at its center. The star continues its gravitational collapse until its core temperature becomes hot enough for nuclear fusion, with temperatures of $\sim 10^6$ K, giving way to a main-sequence star.

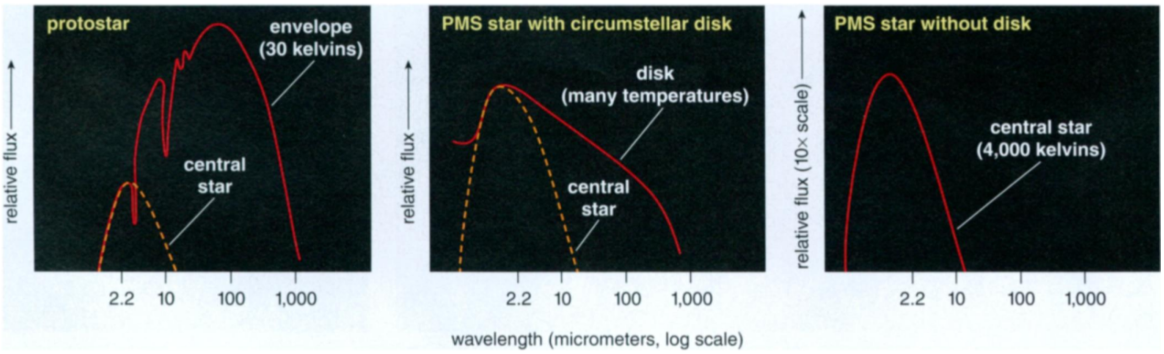

Figure 1.1: Spectral energy distributions (SED) at infrared wavelengths indicating different classes of young stellar objects as labeled in the panels. From left to right they correspond to: protostars, pre-main-sequence (PMS) stars with and without a disk. Since longer wavelengths correspond to lower temperatures, the cold envelope of a protostars dominates its SED at 100 micrometers (μm; left panel). For the case of a PMS star, the circumstellar disk increases its emission and temperature when approaching the central engine, spanning a broad range of wavelengths (middle panel). Finally, a bare PMS star emits at around 2 μm, indicating a temperature of ~4,000 K (right panel). Figure taken from Greene (2001).

Since the comprehensive models of Shu et al. (1987) successfully explaining the formation of single low-mass stars, important theoretical and observational progress has been made (Chabrier & Baraffe, 2000). Although some authors include Sun-like stars in the category of low-mass stars, others make the distinction and define low-mass stars as those in the mass range of 0.2–0.075 $M_\odot$ (e.g., Luhman, 2012). Below 0.075 $M_\odot$, the object is called brown dwarf, whose lower-mass limit is given by the hydrogen burning mass threshold of 0.012 $M_\odot$ (Burrows et al., 1997; Spiegel et al., 2011).

High-mass stars

Massive stars are usually defined as stars with a mass above 8 $M_\odot$, spectral types of B3 or earlier, and luminosities larger than $10^3 L_\odot$ (e.g., Zinnecker & Yorke, 2007; Motte et al., 2018). They constitute the principal source of heavy elements and UV radiation in the Universe, being responsible for significant changes in their host galaxy, including physical, chemical, and morphological effects. For example, the radiation they emit ionizes their interstellar surroundings and may suppress the subsequent formation of stars (Aharonian et al., 2019; Semenov et al., 2021). Other ways of feedback from massive stars include winds, supernovae, and radiation pressure. Through these mechanisms, massive stars can blow out their surrounding molecular gas creating an expanding shell (Grudić et al., 2018) where new stars may be born.

Environments where massive stars form vary from a single/runaway OB star (Lamb et al., 2010) to associations of hundreds of O-stars (Figer et al., 2002; Sabín-Sanjulián et al., 2017). These stars form in the densest regions of molecular clouds and remain embedded in them by 2–7 Myr. During this time-lapse, equivalent to 17-47 percent of the parent cloud lifetime in the embedded phase of star formation (Kim et al., 2021), they are invisible at optical wavelengths.

Due to their brief life span (4–20 Myr; Leitherer et al. 2014; Chevance et al. 2022), statistically significant studies of massive stars describing their evolution and behavior in detail were difficult to achieve until a couple of decades ago (see, e.g., Hunter et al., 2008). They were restricted to theoretical approaches (Ekström, 2021). Fortunately, their trail can be followed through the heavy chemical elements they leave behind such as rare sulfur isotopologues[1] (particularly ^{36}S compared to ^{32}S abundances, Mauersberger et al. 1996, 2004), indicating, for example, where and in what proportion massive stars have existed throughout the history of our Galaxy. Complementarily, the usage of complex organic molecules (COMs)[2] has been probed to be an efficient way to measure density, temperature, and evolutionary stage[3] of molecular clumps, not only preceding the formation of massive stars (e.g., Lin et al., 2022; Bouscasse et al., 2022), but also in the vicinity of massive young stellar objects (MYSOs; see left panel of Fig. 1.3) and in cold molecular gas. In this way, the study of sulfur isotopologues can serve, for instance, to analyze the massive stellar evolution played in quiescent galaxies. The latter is important considering that the fraction of quiescent galaxies has doubled from z=3 to the present day (Domínguez Sánchez et al., 2011). The analysis of COMs is relevant for regions with an active star formation, such as the vicinity of compact H II regions in the Galactic disk or the inner few hundred parsecs of our Galaxy and local starburst systems.

In the Galactic disk, massive stars form in small (0.01–0.1 pc), dense ($n_{\mathrm{H}_2} \geq 10^5$–$10^7$ cm^{-3}), and cold ($T_{\mathrm{kin}} \sim 15$ K; in the absence of previous star formation) molecular clouds and also in giant massive filaments (Zhang et al. (2015); see also André et al. (2014) for a universal scenario) (Kennicutt & Evans, 2012; Motte et al., 2018). These clouds are defined as self-gravitating, magnetized, turbulent, and compressible fluids (Williams et al., 2000). Molecular clouds form in a set of discrete clumps, which in turn contain dense hot cores[4] where the star formation occurs. By evaporation and sublimation of ice grain mantles, hot molecular cores are the most chemically rich sources in the Galaxy, including COMs (Belloche et al., 2013) and prebiotic precursors/intermediates (Rivilla et al., 2022).

In the Galactic CMZ, the ISM is more turbulent and energetic compared to the Galactic disk. Although there is a debate regarding the evolutionary stage at which we are witnessing stellar formation in the CMZ (Ginsburg et al., 2016; Williams et al., 2022), star production is embedded in ambient conditions with kinetic temperatures and velocity dispersion much higher than in the Galactic disk: 60 K vs 15 K and 5–20 km s^{-1} vs 1 km s^{-1} (e.g., Williams et al., 2022, and references therein).

In Fig. 1.2 we present a general picture of massive star formation in protocluster environments, where a collapsing core inside a clumpy molecular cloud increases its density and temperature, sublimating the ice and thus creating chemical shells rich in molecules such as methanol (CH_3OH) and formylium (HCO^+). Methanol masers emerge mainly during the hot molecular core stage, but are also observed in previous and subsequent stages of high-mass star formation.

Two main competing models are aiming at describing the formation of massive stars. On the one hand, we have the **monolithic collapse**, also known as turbulent core accretion model, where stellar masses depend on the mass distribution of the cloud condensations, similar to the case of low-mass stars (Shu, 1977). In this framework, the star grows in mass and size through the accretion of material from a surrounding disk (McKee & Tan, 2002). The material transport efficiency from the accretion disk to the central star is, however, under debate (Yorke & Bodenheimer, 1999). This framework is supported by some observations and simulations indicating a subvirial condition in massive cores, which can prevent fragmentation, and requires a weak magnetic field (Rosen et al., 2019; Fontani et al., 2018; Rosen & Krumholz, 2020). The second scenario is **competitive accretion** (Bonnell et al., 2001; Wang et al., 2013) in a protocluster environment, where the massive star feeds material from

---

[1] the term isotopologue refers to an isotope from a molecular species.

[2] those with more than five atoms (Herbst & van Dishoeck, 2009).

[3] see, e.g., Allen et al. (2018)

[4] the term hot corinos, on the other hand, is used to indicate the environment where low-mass stars form (Ceccarelli, 2004).

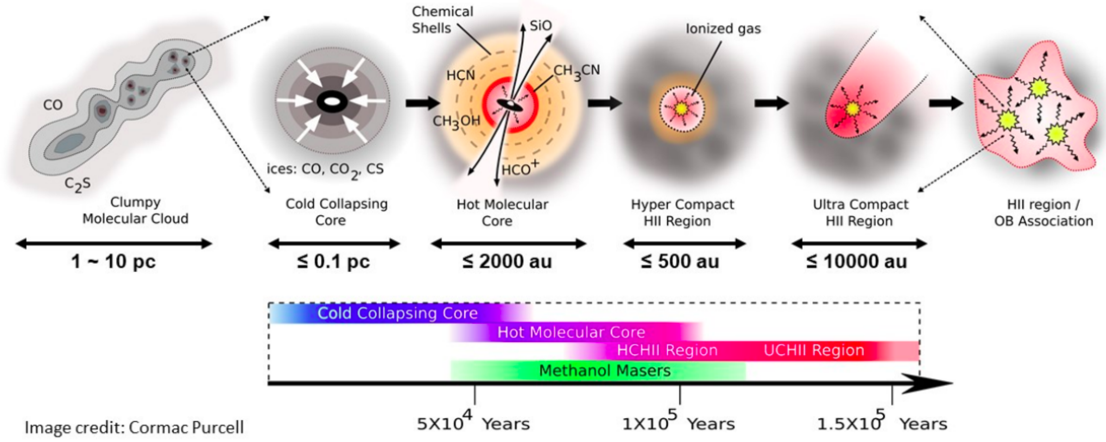

Image credit: Cormac Purcell

Figure 1.2: Different stages of high-mass star formation. With time going from left to right, the stages are: (1) Massive filaments and spherical clumps, called ridges and hubs, host massive dense cores which (2) collapse due to gravity and increase in density and temperature accreting material from the parent cloud and forming a hot molecular core (3) whose temperatures, above 100-150 K (van Dishoeck & Blake, 1998), sublimate the ice and associated molecules creating chemically rich shells. Then, high-mass protostars become IR-bright for stellar embryos with masses larger than 8 $M_\odot$ (4). Subsequently, the accretion phase terminates when stellar UV field ionizes the protostellar envelope (5) developing an H II region and OB-star associations (6) (Motte et al., 2018). Figure credits: Dr. Cormac Purcell (personal website: `https://crpurcell.github.io/index.html`), Macquarie University.

different parts of the parent cloud (Zinnecker & Yorke, 2007). Both models can achieve the accretion rates necessary to produce massive stars. Their differences are mainly addressing the question in how far pre-stellar cores fragment and how the accretion of massive stars evolves (Rosen et al., 2019).

Methanol masers constitute an excellent tool to characterize conditions where massive stars form, capable of being detected in highly dusty embedded sources (Paulson & Pandian, 2020). Unlike OH and H_2O masers[5], Class II 6.7-GHz methanol masers are exclusively correlated with high-mass star-forming regions (Walsh et al., 1997; Breen et al., 2013). Additionally, during the initial forming stages, high-mass stars undergo outflows or winds, which can be traced by Class I methanol masers such as the $4_{-1} \rightarrow 3_0 - E$ transition at 36 GHz (see right panel of Fig. 1.3), a difficult task to achieve at higher frequencies (IR, optical) where the ambient gas is opaque (e.g., Leurini et al., 2016).

At the end of their lives, massive stars explode as supernovae (SNe). There are two main types of them: gravitational and thermonuclear. Gravitational SNe, also known as core-collapse SNe, can be of Type II, Ib, and Ic: Type II if they display hydrogen, Type Ib if they show helium, and Type Ic if neither hydrogen nor helium are present. A thermonuclear explosion occurs in binary systems in which a white dwarf has been accreting matter from the outer layers of its companion until it reaches thermonuclear ignition, giving way to a Type Ia supernova. The core of a star forms elements up to iron. Then, heavier elements are synthesized and expelled into the interstellar medium (ISM) during a supernova explosion (e.g., Sukhbold et al., 2016). These elements become as complex as silicon or

---

[5] water masers are also related to accretion disks or jets (e.g., Henkel et al., 2004), as well as to oxygen-rich red (super) giant stars atmospheres and envelopes (e.g., Menten et al., 2008). OH masers can be found in circumstellar envelopes, one example being late M-type long-period Mira variables (Wilson & Barrett, 1972; Dos Santos & Lepine, 1979).

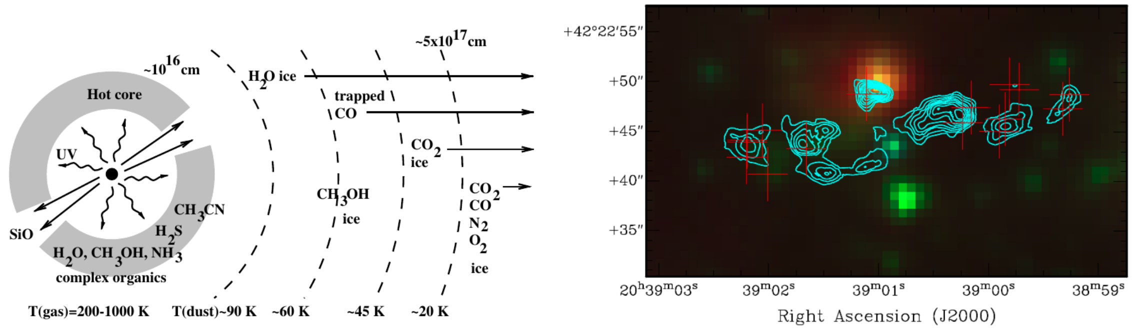

Figure 1.3: Molecules in the vicinities of massive stars. Left panel: Schematic illustration of the chemical environment of massive YSOs. The variation in the chemical structure of the ice mantle in the envelope due to thermal desorption is shown. From van Dishoeck & Blake (1998) and references therein. Right panel: $4_{-1} \rightarrow 3_0 - E$ methanol maser transition at 36 GHz (red crosses) tracing the stellar outflow of the massive star-forming core DR21(OH). Cyan: methanol $4_2 \rightarrow 3_1 - E$ thermal emission. Background: IRAC image (3.6 μm blue, 4.5 μm green, 8.0 μm red) of DR21(OH). From Leurini et al. (2016).

uranium in the case of SNe produced by massive stars (Kobayashi et al., 2020), which have the most significant influence on the enrichment of the ISM. It is interesting to also note that 73% of the mass in the human body are related to material released in exploding massive stars[6].

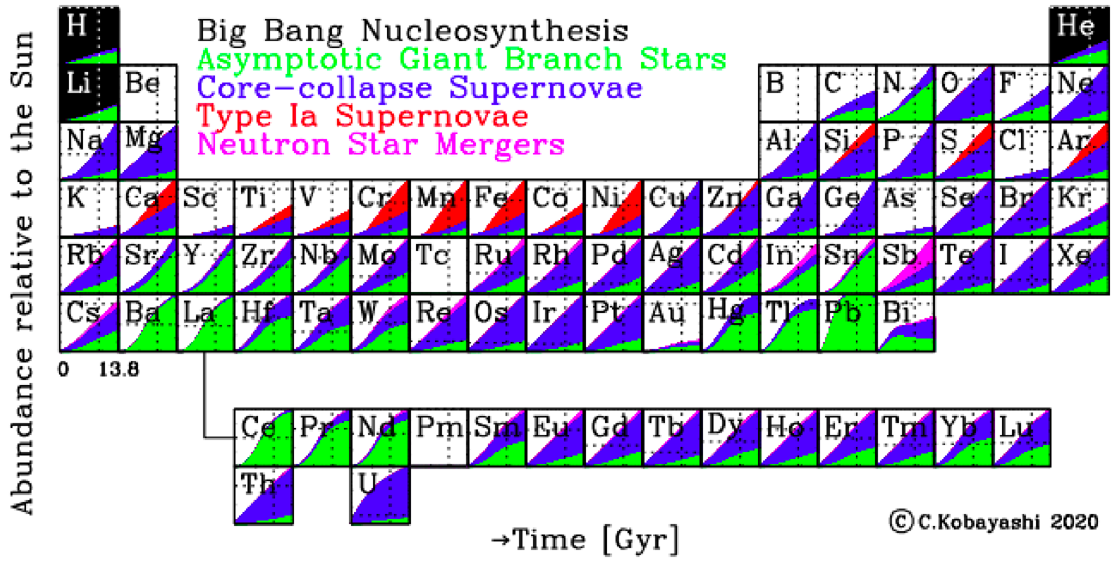

Figure 1.4: Periodic table showing the origin of elements in the Solar System, taken from Kobayashi et al. (2020). Dotted lines indicate the observed solar values. The x-axis of each box represents time from the Big Bang to present, while the y-axis shows linear abundance relative to the Sun.

---

[6] `https://chandra.harvard.edu/photo/2017/casa_life/`

Table 1.1: Stable sulfur isotopes and their solar abundances (data taken from Clayton (2007)).

Mass number	Solar %	Solar abundance per 10^6 Si atoms
32	95.0	489,000
33	0.75	3,860
34	4.21	21,700
36	0.02	103

1.1.2 Sulfur as a massive star tracer

Nucleosynthesis of massive Stars

Rare isotopes usually involve a considerable degree of contamination or blending in the optical regime, being difficult to disentangle from main isotopic spectra. This complicates the study of stellar nucleosynthesis (e.g., Hawkins & Jura, 1987; Levshakov et al., 2006; Hunter et al., 2008; Ritchey et al., 2011). However, at radio wavelengths, transitions from rare isotopic substitutions of a given molecular species, the so-called isotopologues, are well separated in frequency from their main species, typically by a few percent of their rest frequency.

While C, N, and O isotopes are useful to provide information about carbon, nitrogen, and oxygen (CNO cycle) and helium burning, sulfur isotopes allow us to study *late* evolutionary stages of massive stars and supernovae (SNe) of Type Ib/c and II (oxygen-burning, neon-burning, and s-process nucleosynthesis; Wilson & Rood, 1994; Chin et al., 1996; Mauersberger et al., 1996). In this way, sulfur isotopes fill an important gap in our understanding of stellar nucleosynthesis and the chemical evolution of the universe (e.g., Wang et al., 2013).

Sulfur is the tenth most abundant element in the universe, its main molecular species in CS, usually observed in very dense regions and recently detected in maser emission around a High-mass YSO by Ginsburg & Goddi (2019). Sulfur is mostly formed during oxygen burning, after which a part of it is destroyed due to the synthesis of iron-group elements, during the silicon burning. Sulfur possesses four stable isotopes with masses corresponding to 32, 33, 34, and 36 atomic mass units. The main isotope, ^{32}S, constitute 95% of the available sulfur in the solar system (see Table 1.1).

Carbon Monosulfide Chemistry

In the ISM, atomic sulfur is thought to freeze out on dust grain mantles and to be later released from the grains due to shocks, leading to the formation of several molecular species in the gas phase such as OCS, SO_2, H_2S, and H_2CS (Millar & Herbst, 1990). Those species serve as both shock and high-mass star formation tracers in starburst galaxies (Bayet et al., 2009).

To date, 32 sulfur-bearing molecules have been detected in the ISM, one of them with even 9 atoms (see Table 1.2). Among the sulfur-bearing compounds, CS is the most commonly molecular species. Rotational CS lines are ubiquitous in the dense ISM and tend to be strong at sites of massive star formation in the spiral arms of the Galaxy, in the Galactic center (GC) region, and external galaxies (e.g., Linke & Goldsmith, 1980; Mauersberger et al., 1989; Bayet et al., 2009; Aladro et al., 2011; Kelly et al., 2015; Martín et al., 2021).

In diffuse clouds, CS was suggested to be formed mainly by exothermic ion-molecule reactions of S^+ with CH and C_2 (Drdla et al., 1989; van Dishoeck & Blake, 1998). However, those species require to

Table 1.2: Sulfur-bearing molecules detected in the ISM as of November 2021 (Data sorted following the number of atoms, taken from The Cologne Database for Molecular Spectroscopy, CDMS `https://cdms.astro.uni-koeln.de/classic/molecules`).

Number of atoms							
2	3	4	5	6	7	8	9
NS	C_2S	C_3S	HC_3S^+	CH_3SH			CH_3CH_2SH
SO	HCS^+	HNCS	H_2C_2S	C_5S			
SO^+	H_2S	H_2CS	C_4S	H_2C_3S			
SiS	OCS	HSCN	HC(O)SH	HCCCHS			
CS	SO_2	HCCS	HC(S)CN				
SH^+	HS_2						
SH	HCS						
NS^+	HSC						
	NCS						

be one order of magnitude more abundant than currently observed to reproduce the observed quantities of CS (Lucas & Liszt, 2002). Presently, CS formation is believed to be dominated by the exothermic route (1.1) (Drdla et al., 1989; Lucas & Liszt, 2002; Montaigne et al., 2005; Laas & Caselli, 2019):

$$HCS^+ + e^- \rightarrow CS + H. \tag{1.1}$$

Subsequently, the dominant destruction route of CS is photodissociation, with destruction by He^+ being only significant in denser clouds (Drdla et al., 1989).

At higher densities, while route (1.1) still contributes to CS formation, dark cloud conditions make the substitution reaction (1.2) the predominant one to form CS (Nilsson et al., 2000; Lucas & Liszt, 2002; Destree et al., 2009; Forrey et al., 2018):

$$SO + C \rightarrow CS + O. \tag{1.2}$$

Later, CS is destroyed by atomic oxygen (route (1.3); Lucas & Liszt 2002):

$$CS + O \rightarrow CO + S. \tag{1.3}$$

Recent studies agree with these findings, but indicate that the dominant mechanism depends on the cosmic ray ionization rates (CRIR). At high CRIR, reactions (1.2) and (1.3) dominate CS formation and destruction but, at lower CRIR, the abundance of CS decreases while that of H_3O^+ increases (Bayet et al., 2011, their Fig. 4). Then, the following reaction (route (1.4)) becomes dominant for the destruction of CS (Kelly et al., 2015; Viti, 2016):

$$H_3O^+ + CS \rightarrow HCS^+ + H_2O. \tag{1.4}$$

The rising of H_3O^+ at lower CRIR may be counterintuitive as ions seem to form mostly at higher rates of cosmic rays. However, the production of H_3O^+ strongly depends on H_2 through the formation routes: $H_2 + H_2O^+$ or $H_3^+ + H_2O$, where H_3^+ comes from H_2 (Serena Viti, priv. comm.). As can be seen in Fig. 3 of Bayet et al. (2011), at a CRIR higher than $10^{14}s^{-1}$, H_2 starts to dissociate preventing the formation of H_3O^+.

Very deep into the cloud, where the electron fraction is small, the following reactive scattering process can become the primary formation mechanism (Esplugues et al., 2014):

$$S + C_2 \rightarrow CS + C. \tag{1.5}$$

In hot cores and corinos, recent models suggest some changes in sulfur chemistry (Vidal et al., 2018). Specifically for CS, the main paths for its formation and destruction continue being routes (1.2) and (1.3), respectively. CS is initially destroyed by atomic oxygen (1.3) both at 100 and 300 K, during 10^4 and 10^3 yr, respectively. Nevertheless, CS is then also produced by:

$$S + CH_2 \rightarrow HCS \xrightarrow{S} CS_2 \xrightarrow{H} CS, \tag{1.6}$$

after $\sim 10^4$ yr, at $T_{\mathrm{kin}} \sim 100$ K. At 300 K, the CS abundance is increased by

$$C_4H_2 + S^+ \rightarrow HC_4S^+ \xrightarrow{e^-} C_3S \xrightarrow{O} CCS \xrightarrow{S,N} CS, \tag{1.7}$$

during 10^3 yr and then decreased via (Vidal et al., 2018):

$$CS + HCNH^+ \rightarrow HCN + HCS^+. \tag{1.8}$$

CS is also, to a lesser degree, formed by electronic recombination of $HOCS^+$, and also via $OCS + CH \rightarrow H + CO + CS$ (Vidal et al., 2018). During hot core evolution its formation has been claimed to be dominated by (Esplugues et al., 2014):

$$CH_2 + S \rightarrow CS + H_2. \tag{1.9}$$

Sulfur fractionation

When obtaining element abundances from isotope ratios of molecular species, it is important to take into account the level of enhancement or depletion of these isotopologues with respect to the local ISM isotopic ratio (see, e.g., Sect. 6. of Jørgensen et al., 2020). This difference in abundance is normally referred as isotopic fractionation, an effect of endothermic or exothermic molecular reactions. For the case of sulfur, Loison et al. (2019) found some fractionation induced at low temperature by the $^{34}S^+ + CS \rightarrow S^+ + C^{34}S$ reaction. This implies that not all the carbon and sulfur in its main isotopic forms (^{12}C and ^{32}S) are represented by CS, but that also some percentage of them is being transferred to $C^{34}S$. Therefore, the $^{32}S/^{34}S$ ratio is not equivalent to the $^{12}C^{32}S/^{12}C^{34}S$ ratio. We therefore need a certain fractionation estimation to convert from the observed $^{12}C^{32}S/^{12}C^{34}S$ to the desired $^{32}S/^{34}S$ ratio.

Sulfur fractionation for CS isotopic ratios is considered to be not significant (Chin et al., 1996), and is $\leq$20% in the case of SO/S^{34}O isotopic ratios (Loison et al., 2019, their Fig. 3 (middle)). The bulk of the CS emission, which allows us to measure rare isotopes, arises from the densest parts of the molecular clouds only, where massive stars heat the gas to kinetic temperatures that inhibit significant fractionation (Chin et al., 1996). In Appendix A, we have also reviewed the effect of fractionation using the same formalism as in Loison et al. (2019) but this time looking at the case of CS/C^{34}S isotopologue ratios for environments ranging from high-mass star-forming sites (Sgr B2(N) and the +50 km s^{-1} Cloud) to diffuse/translucent clouds (see also Thiel et al., 2019, for the latter). In CS forming environments, no more than 10–15% of fractionation is expected from the models; this percentage is strongly temperature-dependent only at low kinetic temperature (∼15–20 K; see Humire et al. 2020b). Therefore, CS emission can be used directly to determine sulfur isotope ratios from warm sources. Currently, too few studies in the Milky Way, as well as for other galaxies, are available about sulfur isotopes. Some of the first attempts to establish a database were made by Chin et al. (1996) and Mauersberger et al. (1996).

Sulfur isotope ratios and metallicity

Among the four stable sulfur isotopes (^{32}S, ^{33}S, ^{34}S, and ^{36}S), ^{32}S is a primary isotope, that is to say, with stellar yields mostly independent of its parent stellar metallicity ([Fe/H][7]). ^{32}S is mostly formed during stages of hydrostatic and explosive oxygen-burning (Wilson & Matteucci, 1992) either preceding a Type II supernova event or in a Type Ia event, where two ^{16}O nuclei collide to form ^{28}Si and ^{4}He, with these products subsequently fusing to yield ^{32}S (e.g., Arnett, 1974):

$$^{16}\mathrm{O} + {}^{16}\mathrm{O} \rightarrow {}^{28}\mathrm{Si} + {}^{4}\mathrm{He}, {}^{28}\mathrm{Si} + {}^{4}\mathrm{He} \rightarrow {}^{32}\mathrm{S}. \tag{1.10}$$

Type II supernovae synthesize around ten times more ^{32}S than a Type I event, and occur roughly 5 times more often (Clayton, 2007). ^{33}S is partly a secondary isotope because it can be formed by neutron capture from newly made ^{32}S if the star not only has hydrogen and helium, but also carbon and oxygen in its initial composition (Clayton, 2007). It is synthesized in hydrostatic and explosive oxygen- and neon-burning, also produced in massive stars. ^{34}S is partly a secondary product because it can be formed from newly made ^{32}S and ^{33}S by neutron capture, but also during oxygen burning in supernovae like the primary isotope, ^{32}S (Hughes et al., 2008, and references therein). While the comprehensive calculations of Woosley & Weaver (1995) also identify ^{32}S as a primary isotope, the same study also found that ^{34}S is not a clean primary isotope; its yields decrease with decreasing metallicity. However, they identify ^{33}S as a primary isotope, in contradiction with later findings (Clayton, 2007). ^{36}S is probably the only purely secondary sulfur isotope, being produced by s-process nucleosynthesis in massive stars (Thielemann & Arnett, 1985; Mauersberger et al., 1996) and also by explosive C and He burning and via direct neutron capture from ^{34}S, according to models (Pignatari et al., 2016). ^{36}S could be the only S isotope not only produced from massive stars but also, to a lesser extent, from asymptotic giant branch (AGB) stars (Pignatari et al., 2016). Unfortunately, due to the very low abundance of ^{36}S, lines from C^{36}S are too weak to be detected in this thesis. Massive stars, as well as Type Ib/c and II supernovae, appear to slightly overproduce ^{34}S and underproduce ^{33}S compared to ^{32}S, relative to the solar vicinity (Timmes et al., 1995).

The comprehensive study by Kobayashi et al. (2011) relates sulfur abundances with metallicity ([Fe/H]) for different regions of the Galaxy: solar neighborhood, halo, bulge, and thick disk. In Fig. 1.5 we can see an example of different isotope ratios with respect to their main species. For the case of sulfur, all possible isotopologue ratios are shown.

The mass fraction of isotopes at the mentioned Galactic regions is shown in Table 3 of Kobayashi et al. (2011). The case of sulfur is reproduced in Table 1.3.

We can further relate metallicities to the distance from the Galactic center (D_{GC}) by using the relation found by Genovali et al. (2014) who determined a metallicity gradient in a D_{GC} range of 5 to 19 kpc that can be extrapolated, following Inno et al. (2019), down to a D_{GC} distance of 2.53 kpc. This gradient is expressed in Eq. 1.11:

---

[7] where [Fe/H] = log10([N_{Fe}/N_{H}])$_{star}$ - log10([N_{Fe}/N_{H}])$_{sun}$.

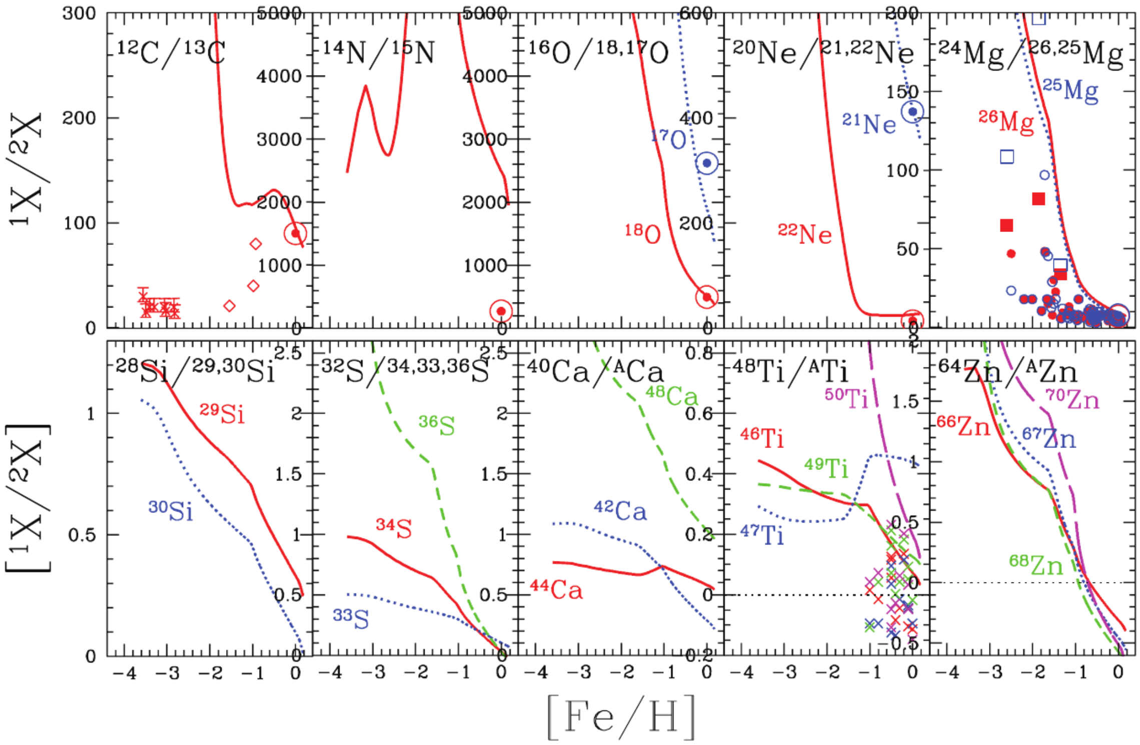

Figure 1.5: Isotope ratios against metallicity [Fe/H]. For the case of sulfur, presented in the second bottom panel, ratios are with respect to ^{32}S: ^{32}S/^{33}S (in blue), ^{32}S/^{34}S (in red), and ^{32}S/^{36}S (in green). Figure from Kobayashi et al. (2011), where those diagrams not referring to sulfur are fully explained.

Table 1.3: Modeled sulfur abundances in the Galaxy (or mass fractions, i.e., fraction with respect to the total mass; from Kobayashi et al. (2011)). With [Fe/H] we refer to metallicity, taking the solar value as a reference point.

Model	Solar	Solar -1.1	Solar	Solar	Halo	Bulge	Thick
[Fe/H]	-2.6	-1.1	-0.5	0	-0.5	-0.5	-0.5
32S	2.93E-06	8.61E-05	2.16E-04	4.43E-04	1.88E-04	2.95E-04	2.45E-04
33S	8.42E-09	3.37E-07	1.10E-06	2.79E-06	8.70E-07	1.69E-06	1.27E-06
34S	2.06E-08	1.43E-06	6.53E-06	1.91E-05	4.49E-06	1.14E-05	7.80E-06
36S	6.34E-12	2.70E-09	2.70E-08	9.63E-08	1.48E-08	5.82E-08	3.43E-08

$$[\mathrm{Fe/H}] = (-0.06 \pm 0.002) \times D_{\mathrm{GC}}/\mathrm{kpc} + 0.57 \pm 0.02, \tag{1.11}$$

with [Fe/H] mostly in the range between -0.5 and 0.5 (Genovali et al., 2014). From Table 1.3 we obtain ^{32}S/^{34}S ratios of about 33.1 and 23.2, for solar metallicities of -0.5 and 0, respectively. From these two points we obtain a relation between ^{32}S/^{34}S and [Fe/H] given in Eq. 1.12:

$$\frac{^{32}\mathrm{S}}{^{34}\mathrm{S}} = -19.8 \times [\mathrm{Fe/H}] + 23.2. \tag{1.12}$$

Finally, from Equations 1.11 and 1.12 we obtain Eq. 1.13,

$$\frac{^{32}\mathrm{S}}{^{34}\mathrm{S}} = (1.2 \mp 0.4) \times D_{\mathrm{GC}}/\mathrm{kpc} + 11.9 \mp 0.4, \tag{1.13}$$

which is plotted in the upper right panel of Fig. 1.6. Eq. 1.13 is also plotted in magenta in Fig 5. of Appendix A, along with observational measurements that we will explain in the following.

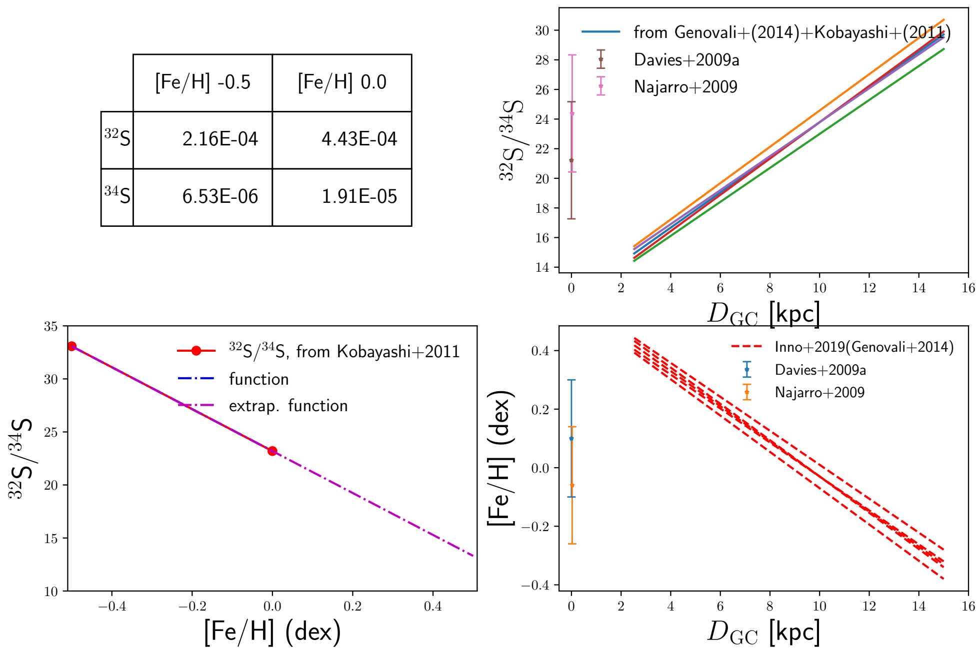

	[Fe/H] -0.5	[Fe/H] 0.0
^{32}S	2.16E-04	4.43E-04
^{34}S	6.53E-06	1.91E-05

Figure 1.6: Combination of relations required to obtain the ^{32}S/^{34}S ratios along D_{GC}. Upper left panel: sulfur abundances from models performed by Kobayashi et al. (2011). Lower left panel: sulfur abundances for metallicities of interest, extrapolated from [Fe/H] in the range between –0.5 and 0.0, toward [Fe/H] up to 0.5. Lower right panel: metallicity gradient obtained by Genovali et al. (2014) plus a couple of data points from Davies et al. (2009) and Najarro et al. (2009) observed very close to the Galactic center. Upper right panel: Combination of the two relations presented in the bottom panels as given in Eq. 1.13.

The ^{32}S/^{34}S gradient

As first noted by Chin et al. (1996), there is a gradient in the sulfur ^{32}S/^{34}S isotopologue ratios across the Galaxy disk at distances between 2.9 and 9.0 kpc from the galactic center (D_{GC}). This has been confirmed by Yu et al. (2020). However, there remains a strong deficit of Galactic center data, while it is important to know whether the gradient in the disk continues right until the very center of our Galaxy. For this aim, in Appendix A (for a summary, see Chapter 2) we observed the +50 km s^{-1} Cloud and Sgr B2(N), located at a D_{GC} of 3±3 pc and 130^{+60}_{-30} pc, respectively (Ferrière, 2012; Reid et al., 2009). We also observed line-of-sight clouds towards Sgr B2(N), located within 1 kpc from the Galactic center. An overview of the Galactic center showing the location of the mentioned objects in the plane of the sky is presented in Fig. 1.7.

It is interesting to note how the metallicity across the Galaxy can explain the observed ^{32}S/^{34}S gradient, as can be inferred from Figure 1.8, taken from Kovtyukh et al. (2019). Since the ^{34}S abundance is proportional to metallicity, while ^{32}S species can be considered being expelled to the ISM in similar proportion at any place of the Galaxy, the ^{32}S/^{34}S gradient is inversely proportional to the metallicity (see also Eq. 1.12). The plateau and further increment in [Fe/H] toward the Galaxy center is explained in terms of chemo-dynamical evolutionary models at 0–4 kpc from the Galaxy center and an observed chemistry similar to the Solar system in the central part of our Galaxy (Kovtyukh et al., 2019, and references therein). The suggested plateau at $D_{\rm GC}$ <4kpc (see Fig. 1.8) is, however, not supported by current (Yu et al., 2020) and forthcoming (Yang, Y. T., submitted) studies in CS isotopologue ratios. The proposed scenario rather favors a slope followed by a high dispersion in the Galaxy center (Y. T. Yan & C. Henkel; priv. comm.).

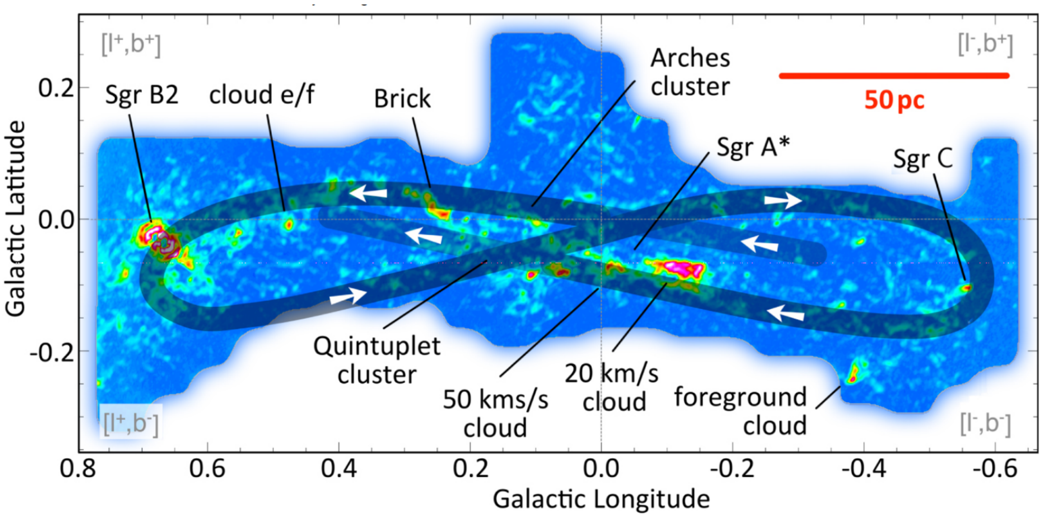

Figure 1.7: The inner region of our Galaxy highlighting the ∞-shaped flows discovered by Molinari et al. (2011) later parametrised as a sequence of stream segments, as indicated by arrows, by Kruijssen et al. (2015). Two objects of interest for this thesis are labeled: the hot molecular core Sgr B2 and the 50 km s^{-1}Cloud (see Section 1.3.1 for more details). The background is NH$_3$ peak intensity. Figure from Krieger et al. (2017).

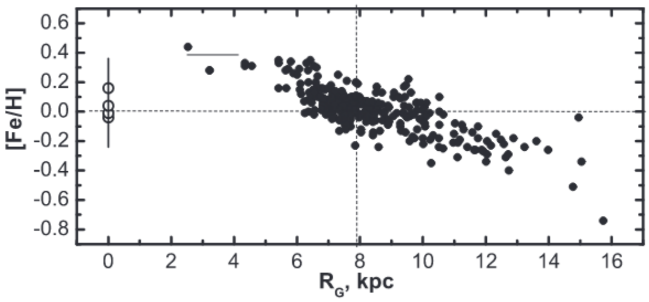

Figure 1.8: Metallicity [Fe/H] gradient along different radial distances from the Galaxy center ($R_{\rm G}$). Filled and open circles correspond to Galactic Cepheids taken at different epochs. Plot taken from Kovtyukh et al. (2019).

The mentioned high dispersion in ^{32}S/^{34}S ratios at the Galaxy center may be reconciled with episodic events of star formation recently supported by both theoretical and observational studies (Krumholz

& Kruijssen, 2015; Sormani et al., 2020; Orr et al., 2021; Hatchfield et al., 2021,?; Henshaw et al., 2022), which in turn favor the “Pearls on a string” scenario (see Subsect. 1.1.4). This irregular stellar production could be explained by periodic fuel of material through dust lanes in the inner portions of the Galactic bar and CMZ edges (x_1/x_2 interactions), as observed in some spiral galaxies (Allard et al., 2006; Sarzi et al., 2007). Furthermore, the episodic events of star formation also observed in lenticular (S0) galaxies (Johnston et al., 2014) might provide some hints in favor of a more evolved stage of the Milky Way as compared to the bulk/average of spiral galaxies, being a half way between a spiral and lenticular configuration at least in its nuclear regions. All of these questions can be complementarily addressed by the study of sulfur isotopologue ratios, providing an independent tool ready to be exploited both for our local ISM and at extragalactic scales.

1.1.3 Methanol as a shock tracer

Methanol characteristics

Methanol (CH_3OH), first detected in space toward the Sagittarius complex by Ball et al. (1970) and in an extragalactic object (NGC 253) by Henkel et al. (1987), consists of a methyl group (CH_3) attached to a hydroxyl group (OH). Methanol is one of the simplest COMs. This molecule is also referred as “weed” in observational spectroscopy due to the large number of spectral features in the millimeter and sub-millimeter windows. Hundreds of methanol transitions are detectable in the sub-millimeter regime. For instance, a total of ~780 transitions, including CH_3OD, isotopomers, and their torsionally excited states, are detectable in Orion KL in the 605−725 GHz and 795−903 GHz windows (Schilke et al., 2001; Comito et al., 2005).

Methanol is a slightly asymmetric top molecule (κ=0.98, with κ deviating either from +1 or −1 being a measure of asymmetry [see, e.g., Mangum & Shirley (2015), their Eq. (45)]). The methyl group alone is a symmetric top molecule and isomorphous to the C_{3v} group, that is, it does not change its geometry after a rotation of 120° around its center, the carbon atom, if the hydrogen atoms remain on the same plane (Herzberg, 1945). However, the hydrogen atom of the OH (hydroxyl) tail of the molecule is off the main molecular axis. Usually, the torsion-rotation energy levels of methanol are approximated by the C_{3v} group (A_1, A_2, and E), where the E levels do not need to be further separated (Lees, 1973).

There are two methanol species depending on the spin arrangement in the hydrogen atoms belonging to the methyl group (CH_3). Parallel spins conform the A-CH_3OH. In contrast, E-CH_3OH has one of its hydrogen atoms with an antiparallel spin.

In quantum mechanics, three constants (a, b, and c) describe the CH_3OH total rotation and are associated with the moments of inertia I_a, I_b, and I_c, along the three principal axes of this molecule. J gives the total angular momentum, and K quantifies the projection onto the three axes mentioned above.

Apart from its overall rotation, methanol also presents a hindered rotation between CH_3 and OH, producing a torsional oscillation with respect to one another (e.g., Koehler & Dennison, 1940). In Figure 1.9 we provide an example of the potential barrier of this rotation. This methanol internal rotation, together with the molecule’s lightness (among species with internal rotation), allows observers to measure the proton-to-electron mass ratio with the highest precision and over vast distances (e.g., Bagdonaite et al., 2013; Jansen et al., 2014) and also across the Milky Way (Levshakov et al., 2022). The torsional angle between CH_3 and OH is denoted by γ. Considering the reduced moment of inertia

I_{red} (= $\frac{I_{a1} I_{a2}}{I_a}$), the moment of inertia of the methyl group I_{a2}, and that of the hydroxyl group I_a, as well as its difference I_{a1} = I_a - I_{a2}, the lowest-order Hamiltonian of methanol can be written as (Jansen et al., 2014):

$$H = \frac{1}{2}\frac{P_a^2}{I_a} + \frac{1}{2}\frac{P_b^2}{I_b} + \frac{1}{2}\frac{P_c^2}{I_c} + \frac{1}{2}\frac{1}{I_{red}}p_\gamma^2 + \frac{1}{2}V_3(1 - cos3\gamma), \tag{1.14}$$

where the first three terms refer to the overall rotation around the three axes of symmetry (a, b, and c; see Fig. 1.9). More specifically, P_a, P_b, P_c are constants that can be expressed in terms of angles relating the methyl group and the hydroxyl group to the fixed axes (a, b, and c) of the molecule (Duan & McCoy, 2001). The fourth term describes the internal rotation along the a axis, and the fifth term comes from the hindered rotation between the OH bar and the methyl group (Koehler & Dennison, 1940). The potential term V_3 (see, e.g., Duan et al., 2002) is depicted in the left panel of Fig. 1.9. Updated values for P_a, P_b, P_c, p_γ^2, and V_3 can be found in Table 1 of Duan & McCoy (2001).

More detailed approaches to the Hamiltonian of methanol can be found in Herbst et al. (1984) and Nakagawa et al. (1987).

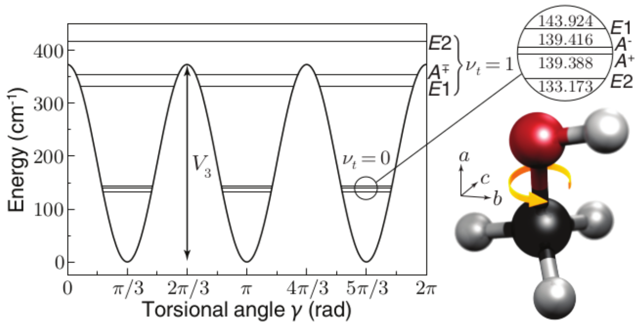

Figure 1.9: Potential energy barrier of methanol per torsional angle γ and its sketched geometry along its three main axes. The J=1, $|K|$=1 energies of the lowest torsion-vibrational levels, v_t =0, are shown. Plot taken from Jansen et al. (2014).

As an example of the dense/bulky methanol spectrum in the sub-mm, in Fig. 1.10 we present a synthetic spectrum of methanol following our best fitting results to region 4 in NGC 253 (see Tables 1 and 3 of Appendix C for the locations of the regions and model parameters, respectively).

From the astrophysical perspective, methanol has been detected in a variety of environments, ranging from cold, dark clouds to hot molecular cores (Friberg et al., 1988; Pei et al., 2000; Ikeda et al., 2001), as well as dense molecular clouds (Leurini et al., 2004) and comets (Mumma et al., 2001). Due to its abundance and morphological asymmetry, it can also serve as a thermometer and densitometer when torsionally and vibrationally excited transitions, v_t = 1, are available (Leurini et al., 2007).

Astrophysical maser lines

The term maser stands for Microwave Amplification by Stimulated Emission of Radiation. As its name indicates, maser phenomena can not occur without stimulation or excitation. This can be of radiative origin (star formation sites, AGN, etc) or collisional origin (e.g., stellar outflows, x_1/x_2 interactions (Regan & Teuben, 2003)). Thanks to this stimulation, a population of molecules are excited or "pumped" from state E_1 to a higher energetic level, named E_3. Then, the population undergoes a fast spontaneous decay to the state E_2, emitting an $E_3 - E_2$ photon. If the E_2 state is metaestable, the system may reside far a longer time in E_2, yielding an overpopulation of E_2 relative

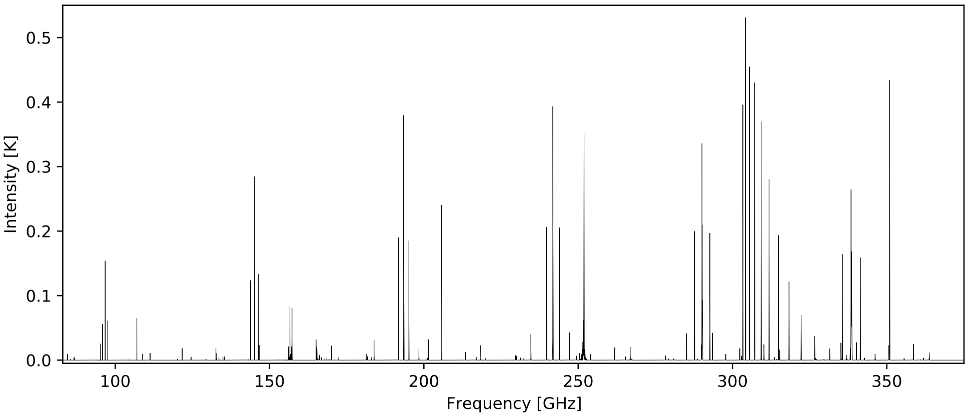

Figure 1.10: Methanol synthetic spectrum in the sub-mm range between 84 and 373 GHz according to the LTE model performed for region 4 of NGC 253 (see Tables 1 and 3 of Appendix C).

to E_1. We refer to the latter as population inversion since more atoms have electrons at higher energy levels (E_2) than at lowest ones (E_1). Once an important bunch of electrons is retained at an excited, metaestable level E_2, something possible due to the extremely low densities typically encountered in the ISM, an incident photon can suddenly depopulate them. The incident photon passing through the inverted populated region will produce another one of the same frequency, so the radiation will be amplified which each photon having an energy equal to the difference of energetic levels: $E_2 - E_1$. The incident photon is said to trigger stimulated emission at the $E_2 - E_1$ frequency. A scheme of this stimulation process, with the photons already in the metaestable level E_2, is shown in Fig. 1.11:

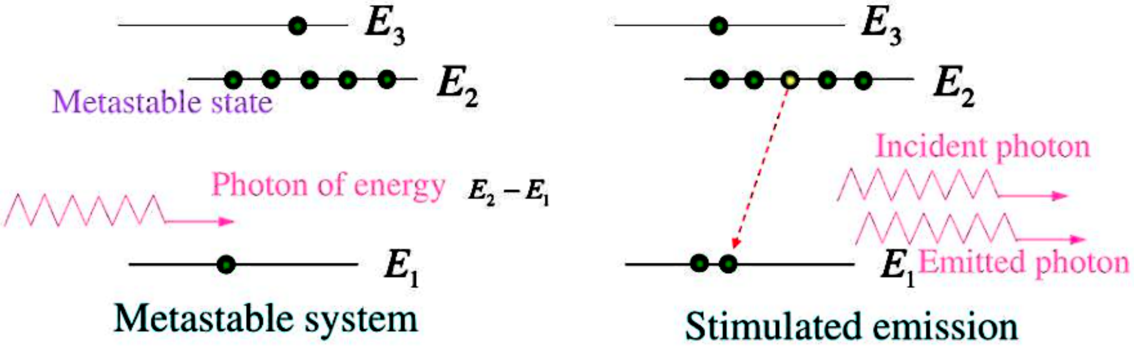

Figure 1.11: Schematic point of view of population inversion. An incident photon of energy $h\nu$, equal to the difference in the photon jump ($E_2 - E_1$) passes through a populated inverted environment. After transferring its energy, a second photon is released, producing an amplification of the incident photon by a factor of two. The second photon will have the same energy, phase, and direction, providing overall a monochromatic and coherent emission. Figure taken from Gamada Seghen's presentation. (`https://www.slideserve.com/gamada/lasers-light-amplification-by-stimulated-emission-of-radiation`)

Astronomical masers can be identified by at least one of the following properties [8]:
1.- Variability with time.
2.- Very narrow linewidths.
3.- Abnormal line ratios, indicating departure from thermal and radiative equilibrium.

Interstellar maser emission has been detected in many molecular and atomic transitions: in Hnα recombination lines, as well as in OH, CS, CH, SiO, SiS, H_2O, HCN, HNCO, NH_3, H_2CO, HC_3N, and CH_3OH (Martín-Pintado et al., 1989; Draine, 2011; Ginsburg & Goddi, 2019; Zeng et al., 2020; Chen et al., 2020a). Most of them are found in sites of recent formation of young stellar objects (YSOs), although they can also trace evolved stars, low-mass stars, and late-type stars (e.g., Engels, 1979; Reid & Moran, 1981; Kalenskii et al., 2010, 2017; Messineo et al., 2002). Among the different masing molecules, methanol masers seem to be the only ones exclusively correlated with star-forming regions (Walsh et al., 2001).

It has been proposed that masers from different species can serve as astrophysical clocks for star formation (Ellingsen, 2006; Reid, 2007; Ellingsen et al., 2007, 2012), as presented in Fig.1.12. Later findings are, however, debating the existence of such an evolutionary scheme (Voronkov et al., 2014, their Sect. 4.5).

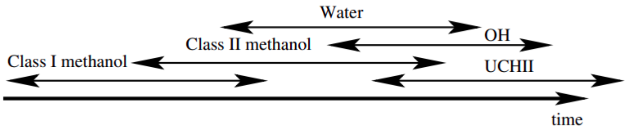

Figure 1.12: Proposed chronology for the emergence of masers associated with regions of massive star formation. Figure from Ellingsen et al. (2007).

Methanol masers

Methanol masers can be entirely classified into two varieties, named I and II (Batrla et al., 1987; Menten, 1991b), although subcategories have also been introduced (Sobolev, 1993). Class I methanol masers result from collisional excitation followed by spontaneous radiative decay (Cragg et al., 1992), they are associated with a number of phenomena (see below). Class II methanol masers are pumped by far IR radiation and arise from hot molecular shells heated around embedded high-mass YSOs (MYSOs). They are so far exclusively associated with the earliest evolutionary phases of MYSOs (Walsh et al., 1998), where the radiation density is much higher than required for Class I methanol masers (Sobolev et al., 2007). This difference in pumping mechanism between the two methanol maser classes leads to different distances where they show up with respect to high-mass protostars which are functioning as engines of both far-IR radiation and stellar outflows. In fact, while Class II methanol masers are typically found within few tens of milli-parsecs from the exciting MYSOs (Caswell et al., 2010), Class I methanol masers lie at distances from of 0.1 to 1 parsecs from them (Kurtz et al., 2004; Cyganowski et al., 2009; Voronkov et al., 2014).

Conditions for Class II maser emission include temperatures of ~150 K, methanol column densities of $>10^{15}\,\mathrm{cm}^{-2}$, and volume densities of $>10^{8}\,\mathrm{cm}^{-3}$ (Sobolev et al., 1997). Radiative pumping leads to absorption when there is Class I emission and vice-versa, this is known as anti-inversion. Best-known absorption lines are the $5_1 \longrightarrow 6_0 - A^+$ and $2_0 \longrightarrow 3_{-1} - E$ transitions at 6.7 and 12.2 GHz, respectively (see dashed-blue lines in Fig. 1.13).

---

[8] `https://ned.ipac.caltech.edu/level5/ESSAYS/Elitzur/elitzur.html`

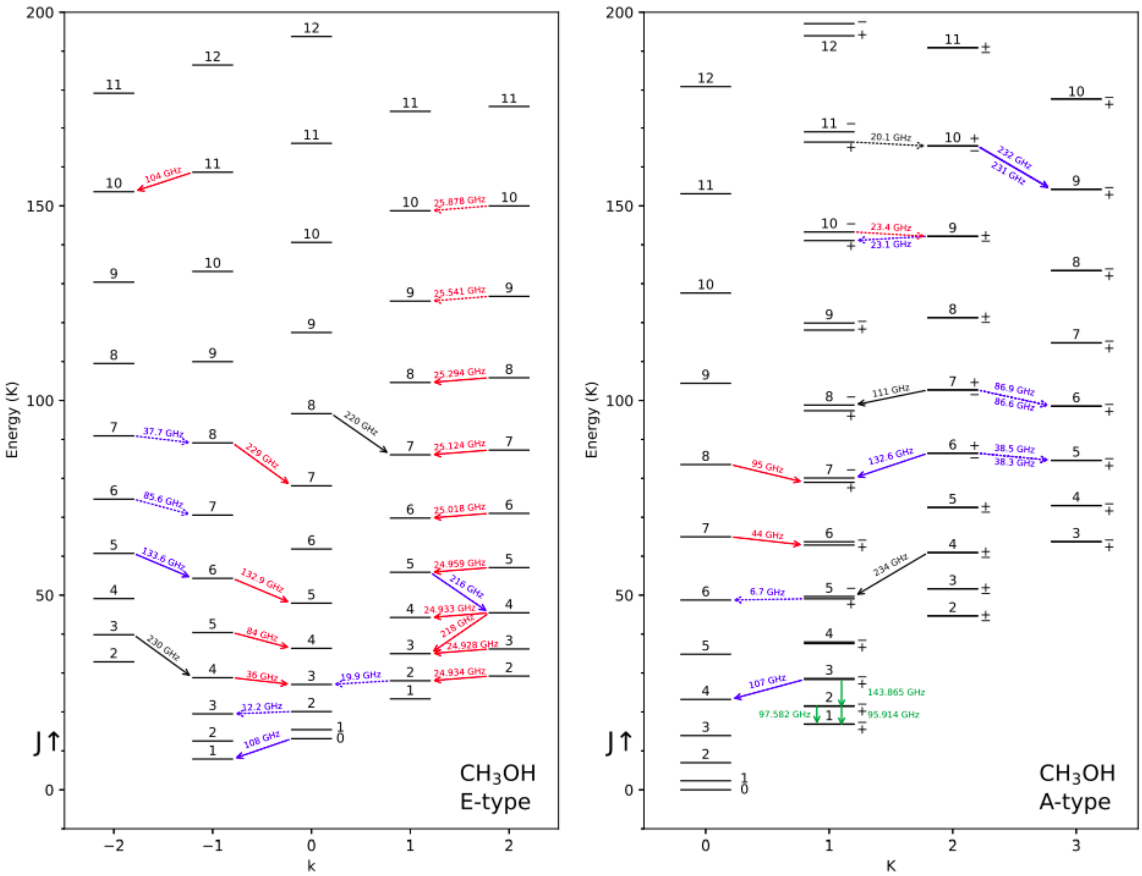

Figure 1.13: Energy level diagram for methanol E (left panel) and A (right panel) species. Class I and II masers are marked in red and blue, respectively. Dotted-blue lines connect anti-inverted transitions. Thermal emission in the $(J+1)_1 \rightarrow J_1 - A$ series detected in W3(OH) is indicated in green, while black arrows indicate transitions without maser emission detected so far. Figure from Yang et al. (2022).

Class I methanol masers

As shown by Lees (1973), among E-type methanol transitions, Class I population inversion is favored in the $K = -1$ relative to the $K = 0$ or $K = -2$ ladders. This leads to the prominence of the $J_{-1} \rightarrow (J-1)_0 - E$ series. For A-type methanol, population inversion in the $K = 0$ relative to the $K = 1$ ladder is favored, playing out in the $J_0 \rightarrow (J-1)_1 - A^+$ series. Class I methanol masers may be associated with a variety of phenomena, such as supernova remnants (Plambeck & Menten, 1990; Pihlström et al., 2014), shocking material produced at the interface between molecular outflows and the parent cloud (Plambeck & Menten, 1990; Johnston et al., 1992), massive protostellar induced outflows (Cyganowski et al., 2018), and interactions of expanding H II regions with surrounding molecular gas (Voronkov et al., 2010, 2014), namely regions where shocks compress and heat the gas. In the CMZ of our Galaxy, cosmic ray interactions with molecular clouds have been claimed to be an additional source of methanol production (Yusef-Zadeh et al., 2013). While a high methanol abundance alone is certainly not sufficient to trigger maser emission, there seems to be indeed a clear enhancement of Class I masers in this region (Yusef-Zadeh et al., 2013; Cotton & Yusef-Zadeh, 2016; Ladeyschikov et al., 2019). In particular, extended strong emission showing characteristics of maser action had been found by Haschick & Baan (1993) and Salii et al. (2002) in the G1.6−0.025 region at the periphery of the CMZ and by Szczepanski et al. (1989) and Liechti & Wilson (1996) in a region in which the supernova remnant Sgr A East interacts with a giant molecular cloud (GMC). Noteworthy, CMZ conditions in the Milky Way should provide some guidance to the central regions of starburst galaxies (Belloche et al., 2013; Schwörer et al., 2019). Extragalactic Class I methanol masers conform the topic of our Chapters B and C, and a summary is provided below (Subsect. 1.1.3).

Among the different types of shock scenarios prone to produce Class I methanol maser emission, the most related to our work at extragalactic objects seems to be cloud-cloud collisions (Ellingsen et al., 2017). Radiative transfer modeling for sources located at the Galactic CMZ edges, such as the above-mentioned G1.6−0.025 region, provide strong support in favor of cloud-cloud collisions as a primary engine for maser Class I emission. With the aid of updated collisional rate coefficients it is possible to properly model methanol lines and unveil conditions for population inversion. In this manner, using models developed by Leurini et al. (2004), Menten et al. (2009) obtained a large range of conditions for maser action in G1.6−0.025. Earlier models already explained methanol population inversion and anti-inversion due to cloud collisions in G1.6−0.025 (Sobolev, 1992). State-of-the-art methanol maser modeling suggests a number of parameters to be taken into account, including CRIR level, shock velocity, molecular density, and distance from the shock front (Nesterenok, 2022).

One of the common conclusions from those models is that, to tightly constrain the ISM conditions where methanol masers emerge, a large number of transitions, including different line series, are required. For example, with a handle of methanol lines belonging to the $J_{-1} \rightarrow (J-1)_0 - E$ and $J_2 \rightarrow J_1 - E$ line series, Zeng et al. (2020) were unable to tightly constrain the kinetic temperatures presented toward G+0.0693−0.03, although they effectively constrained the molecular density ($n_{\mathrm{H_2}}$), found to lie in the 10^{4-5} cm^{-3} range, in agreement with the commonly established picture (Menten, 2012). Examples of model results for collisionally pumped methanol masers are presented in our Fig. 1.14.

Galactic methanol masers

The first detection of methanol masers dates back to the early 1970s by observations in the Orion-KL nebula (Barrett et al., 1971). They detected methanol maser emission in the $J_2 \rightarrow J_1 - E$ series, with J =2–7, at ~25 GHz (Class II). This discovery was followed by Turner et al. (1972) with the detection of the $4_1 \rightarrow 3_0 - E$ transition (at 36 GHz, Class I). The number of methanol Class I masing transitions increased to five in the late 1990s and 13 by the end of 2019 (Ladeyschikov et al., 2019). Currently, more than 40 methanol transitions have been found to show maser emission, including detections in torsionally excited methanol and isotopic methanol (^{13}CH$_3$OH) (Cragg et al., 2005; Breen et al., 2019; Brogan et al., 2019; MacLeod et al., 2019; Chen et al., 2020b). Figure 1.13 summarizes the most common methanol masers detected to date.

The CMZ harbors the highest number of known methanol maser spots in the Galaxy. For example, the survey performed by Cotton & Yusef-Zadeh (2016) reported 2240 methanol maser spots at 36 GHz (Class I) in that zone. The same happens for maser spots at 6.7 GHz (Class I), where the highest concentrations lie in the CMZ, followed by the 3-kpc expanding arm (Caswell et al., 2010). It is important to note that the sources detected by Cotton & Yusef-Zadeh (2016) only represent the tip of the iceberg of a spatially continuous emission, since most of it is lost due to the missing flux problem

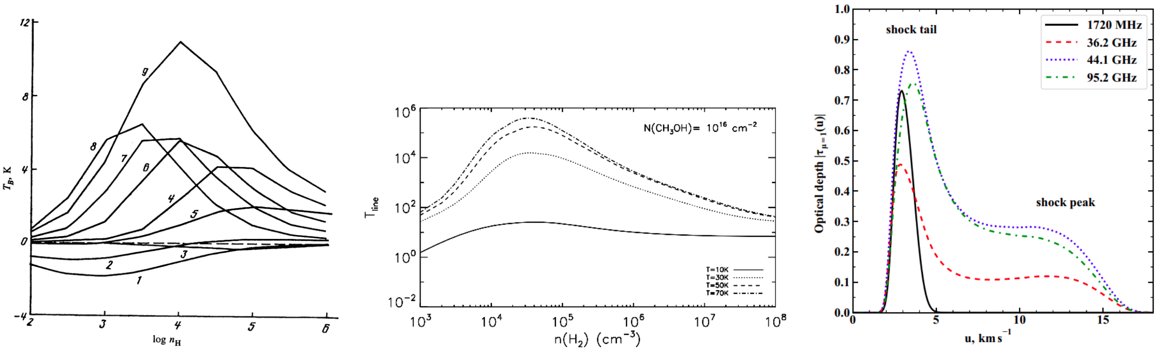

Figure 1.14: Radiative transfer models exemplifying conditions required for collisionally pumped methanol population inversion (and also anti-inversion; left panel). Left panel: Brightness temperature ($T_B\,[K]$) as a function of atomic hydrogen density (n_{H}) under a T_{K} of 150 K. Each numbered curve represents a different methanol E-type transition; those are: 1) $2_0 \rightarrow 3_{-1}$ (12.1 GHz), 2) $1_0 \rightarrow 2_{-1}$ (60.5 GHz), 3) $7_{-2} \rightarrow 8_{-1}$ (12.1 GHz), 4) $8_{-1} \rightarrow 7_0$ (229.7 GHz), 5) $4_0 \rightarrow 4_{-1}$ (157.2 GHz), 6) $6_{-1} \rightarrow 5_0$ (132.8 GHz), 7) $5_{-1} \rightarrow 4_0$ (84.5 GHz), 8) $4_{-1} \rightarrow 3_0$ (36.1 GHz), and 9) $5_{-1} \rightarrow 4_{-1}$ (240.9 GHz) (taken from Sobolev, 1992). Middle panel: Line intensities for the $5_{-1} \rightarrow 4_0 - E$ (at 84.5 GHz) methanol maser transition as a function of molecular hydrogen abundance (n_{H_2}), with a methanol column density of $10^{16}\,\mathrm{cm}^{-2}$ and a T_{K} of 10 K (solid line), 30 K (points), 50 K (dashed line), and 70 K (dot-dashed lines) (taken from Menten et al., 2009). Right panel: Optical depth magnitude as a function of frequency shifts, in km s^{-1}, for different methanol Class I maser transitions and also hydroxyl (at 1720 MHz) as labeled in the upper right corner (taken from Nesterenok, 2022).

present in interferometric measurements. Moreover, in their compilation of Class I methanol masers, Ladeyschikov et al. (2019) found an important difference between Class I and Class II methanol maser distributions. Class I masers are more concentrated in the Galactic disk, with 90% of them located in the inner 1.5 degrees concerning the Galactic plane ($|b| < 1.5°$). In contrast, Class II methanol masers are more widespread both with respect to the Galactic plane and the CMZ. The authors infer that this may be provoked by the collision and radiative excitation mechanism of methanol Class I masers, as the CMZ is the most active and dynamic zone in the Milky Way. Indeed, the inner few hundred parsecs around the Galactic center display a much more turbulent environment than the rest of the Galaxy, including a higher velocity dispersion, temperature, cosmic-ray flux, pressure, and turbulent Mach number (Yusef-Zadeh et al., 2013; Ginsburg et al., 2016).

As a result of the analysis of the largest sample of dust-associated class II methanol masers, those at 6.7 GHz, Billington et al. (2019) concluded that class II masers are a reliable way to trace high-mass star formation at its very early stages. Previous studies already reported these 6.7 GHz maser spots to be highly correlated (99%) with cold dust emission, detected at 870μm, from dense clumps across the Galactic plane (Urquhart et al., 2015).

Extragalactic methanol masers

More than 100 galaxies exhibiting OH or H_2O megamasers[9] have been detected (e.g., Rosenthal & Zaw, 2020). However, their match with extragalactic class II methanol masers at 6.7 GHz has not been fruitful (Ellingsen et al., 1994a; Phillips et al., 1998; Darling et al., 2003) with the possible exception of a recent tentative detection (Chen et al., 2022). On the other hand, the search for Class I methanol

---

[9] those 10^6 times brighter than Galactic counterparts (see, e.g., Lo, 2005)

masers has been successful. The first extragalactic detection, in the $4_1 \rightarrow 3_0 - E$ methanol transition, by Ellingsen et al. (2014), was soon confirmed by follow up observations (Ellingsen et al., 2017; Gorski et al., 2019; McCarthy et al., 2020) and augmented by detections at 44 and 84 GHz (Ellingsen et al., 2017; McCarthy et al., 2018a). These findings motivated the search for Class I maser emission over Class II, and resulted in detections in other nearby targets such as NGC 4945, IC 342, NGC 6946, and Maffei 2 (McCarthy et al., 2017; Gorski et al., 2018; Humire et al., 2020a), all of them barred spirals and some of them experiencing a nuclear starburst event.

Most of the previously referred discoveries were made thanks to the Karl G. Jansky Very Large Array (JVLA) and the Australia Telescope Compact Array (ATCA) facilities, which can, however, not be tuned to frequencies higher than 50 and 105 GHz, respectively. This limitation is the starting point to exploit the potential of the Atacama Large Millimeter/submillimeter Array (ALMA) in the search for methanol masers in the mm and sub-mm regime, as foreseen by Voronkov[10] and Henkel et al. (2018). As a result, we have recently published the detection of a number of Class I methanol maser transitions above the frequency range previously reported for the first time in an extragalactic object (NGC 253; see Appendix C and Humire et al. 2022). The new methanol maser transitions detected belong to the same line series found by the above mentioned works: The $J_{-1} \rightarrow (J-1)_0 - E$ line series (at 36, 84, 132, 229, and 278 GHz) and the $J_0 \rightarrow (J-1)_1 - A$ series (at 44, 95, 146, and 198 GHz).

In the Galaxy, methanol Class I masers have been detected in a variety of phenomena, mostly related to shocked environments such as cloud-cloud collisions, interactions of supernova remnants (SNR), H II regions, or stellar outflows with the surrounding material (e.g., Ladeyschikov et al., 2019, and references therein).

Cosmic rays can also pump Class I methanol masers, potentially also explaining their presence in the CMZ (Cotton & Yusef-Zadeh, 2016). However, this is a matter of debate when considering, for instance, the CMZ of NGC 253, where mechanical heating may predominate (Rosenberg et al., 2014). Interactions between a molecular bar (x_1 orbits) and the CMZ (x_2 orbits) seem to be the most plausible cause of maser emission in nearby galaxies, also leading to megamaser emission (Chen et al., 2022).

1.1.4 The central molecular zone

Differences between Galactic and extragalactic nuclei and the large-scale disk

The term central molecular zone (CMZ) was coined by Morris & Serabyn (1996) to name a bright region in both radio and infrared continuum located in the inner ~200 pc of our Galaxy. Already in the eighties, astronomers identified a clear difference between the large-scale Galactic disk and the CMZ based on its molecular content (5% of the Galaxy; Dahmen et al. 1998), high density ($\sim 10^{3-4}$ cm^{-3}; Güsten & Henkel 1983), high volume filling factor ($f \geq 0.1$) leading to a gas content of the order of $10^{7-8}\, M_\odot$ (Armstrong & Barrett, 1985; Tsuboi et al., 1989). Depending on the molecular thermometer used, the kinetic temperature ($T_{\rm kin}$) varies between 50 K and 600 K (Mills & Morris, 2013; Ginsburg et al., 2016). The velocity dispersion measured in this zone is also very high, with a median of $\sim$10 km s^{-1} but reaching values as high as 53 km s^{-1} (Henshaw et al., 2016). The elevated temperatures and linewidths may be linked through conversion of turbulent energy into gas heating (Wilson et al., 1982).

---

[10] `https://www.atnf.csiro.au/research/workshops/2012/ALMA/Voronkov_ALMAWorkshop2012.pdf`

Such an extreme environment observed in the CMZ represents a considerable challenge when reconciling its star formation (SF) conditions in comparison to the large-scale disk. In the large-scale disk, observations favor a rather modest SF environment, with cold (∼15 K) molecular gas allowing gravitational compression to overcome internal radiative pressure until a star is born (e.g., Kennicutt & Evans, 2012; Motte et al., 2018). Counterintuitively, in spite of the high turbulence, the CMZ harbors one of the sites with the highest star formation rates (SFRs) in the Galaxy, Sagittarius B2 (Sgr B2; see, e.g., Schwörer et al., 2019). The same difficulty to explain SF holds for nuclear starburst systems, whose CMZ is triggering stars at rates several times higher than in the Milky Way (e.g., Leroy et al., 2018). In some well-known targets, temperatures as elevated as 300 K or beyond (Mauersberger et al., 2003; Mangum et al., 2019) complicate the SF scenario, which forces us to rethink the physics that takes place there. In this regard, cloud-cloud collisions and other sources affected by shocks such as supernova remnants and stellar winds have been proposed as alternative mechanisms for star formation in the Galactic CMZ.

The Galactic CMZ harbors three massive clusters: the Arches, the Quintuplet and the central cluster, spanning ages between ∼2 Myr (Arches) to 6 Myr (central cluster) and sampling the upper part of the Hertzsprung-Russell diagram (e.g., Martins et al., 2008). In Figure 1.15 we present multi-wavelength observations of the CMZ, ranging from 20 cm (1.28 GHz) MeerKAT observations (Heywood et al., 2022) to 8μm emission from Spitzer (Churchwell et al., 2009) (see Henshaw et al. (2022) for details). Labels inset in the Figure highlight several structures observed in the CMZ; among them, Sgr B2 and the +50 km s^{-1} Cloud are relevant for this thesis. We therefore provide a detailed description of these two sources in Sect. 1.3.1 and in Appendix A.

Kinematics of the Galactic CMZ and similarities with extragalactic CMZs

The CMZ has a total gas mass of approximately $5{\times}10^7 M_\odot$ (Dahmen et al., 1998), which amounts to roughly 5% of all the molecular gas in the Galaxy. Around 3/4 of this gas, as seen through ^{13}CO and CS, resides above the Galactic plane (Bally et al., 1988). Simulations show that fluctuations produced in large-scale turbulent flows can explain this distribution (Sormani et al., 2018).

Two main kinematic components have been identified in the Galactic nucleus, a high-velocity component of 130-200 km s^{-1} with a radius of about 180 pc and expanding at ∼150 km s^{-1} within the CMZ (Oka & Geballe, 2020), commonly referred to as the "180 pc expanding ring" (Scoville, 1972; Oka & Geballe, 2020). Inside that ring we can find a population of dense and massive molecular clouds with typical velocities of ≤100 km s^{-1}, commonly referred as "disk population" (Morris & Serabyn, 1996).

The structure observed in HI is more spiral-like, while in H2, the morphology is more ring-like (Tress et al., 2020). This tracer-dependent gas distribution is typical also for other galaxies (e.g., Izumi et al., 2013), implying that the CMZ of our Galaxy is a good reference to the ones in more distant targets. Dynamical models of Tress et al. (2020) explain this morphological discrepancy in terms of a regular time-averaged distribution superimposed on a transient and complex instantaneous morphology. In the same study, Tress et al. explain the ∞-shaped flows[11] discovered by Molinari et al. (2011) due to tilts produced by gas accretion through dust lanes.

The accretion of material through dust lanes would feed the CMZ. Its interaction with the 100-pc ring (e.g., Langer et al., 2017) will trigger the formation of new stars through cloud-cloud collisions.

---

[11] see also our Figure 1.7

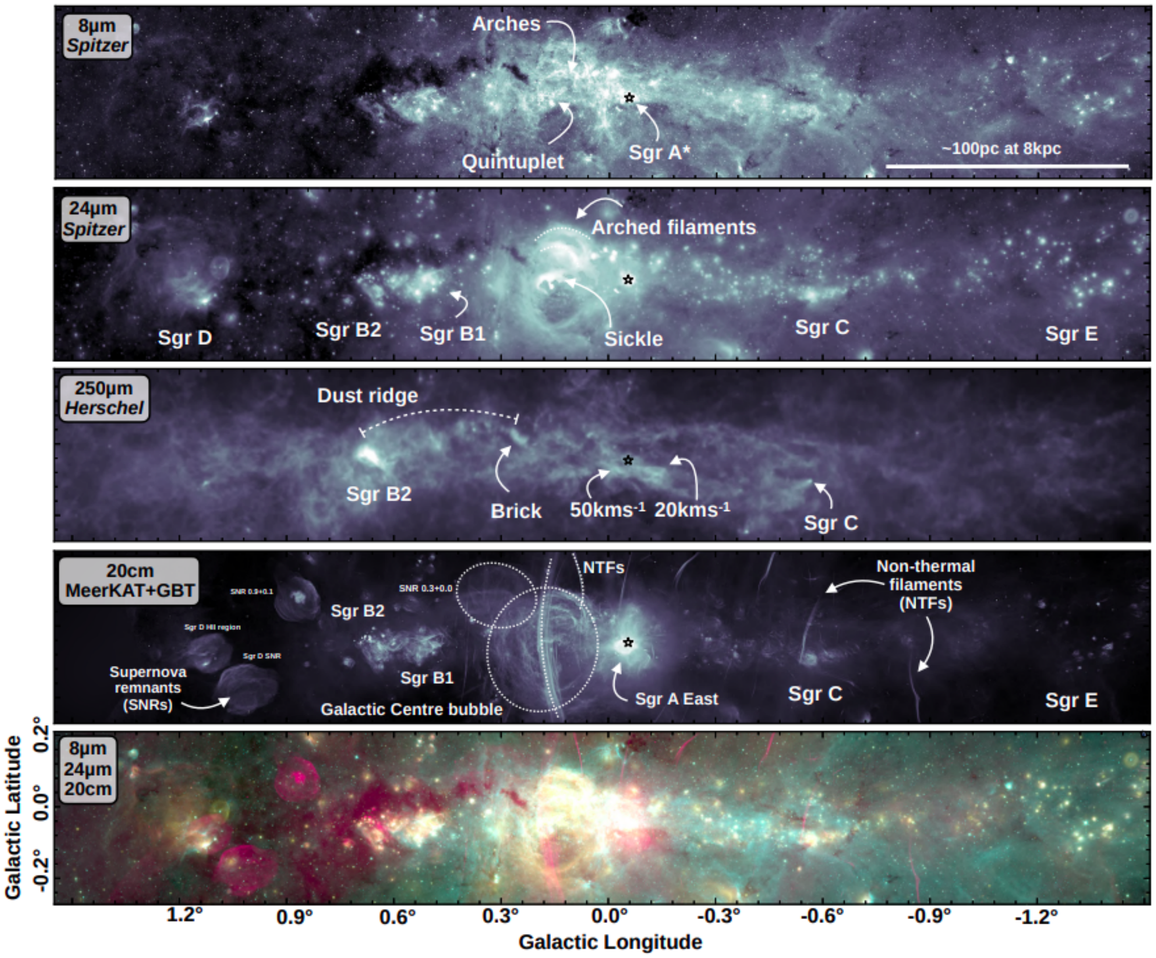

Figure 1.15: The Galactic CMZ observed at different wavelengths. From top to bottom: 8 (Churchwell et al., 2009) and 24μm (Carey et al., 2009) emission from Spitzer, 250μm observations by Herschel (Molinari et al., 2010), 20 cm emission detected with MeerKAT (Heywood et al., 2022) and the Green Bank Telescope (GBT; Law et al., 2008). The bottom panel contains the above-mentioned observations as a three-composite color image. Figures and labels taken from Henshaw et al. (2022).

This scenario is known as "Pearls on a string." It implies an evolutionary sequence starting with newborn stars from interactions between x_1 and x_2 orbits, toward more apocenter-distant regions in the nuclear disk, as depicted in the left panel of Fig. 1.16.

Therefore, by studying the Milky Way's CMZ, we can better understand the evolution of the nuclei of other galaxies. At the same time, even with the implied lower resolution, the research of nearby galaxies offers us both the possibility to probe CMZ's conditions from a panoramic perspective and to study it at different times of its evolution, from periods of inactive star formation to starburst events.

As a primary target for studying nuclear conditions in extragalactic targets, we focus on the case of NGC 253's CMZ, a nearby spiral galaxy known for its chemical prominence in the sub-mm regime, displaying many molecular species (e.g., Martín et al., 2006, 2021).

The SF in the CMZ of the nuclear starburst NGC 253 does not seem to be explicitly fueled by x_1/x_2

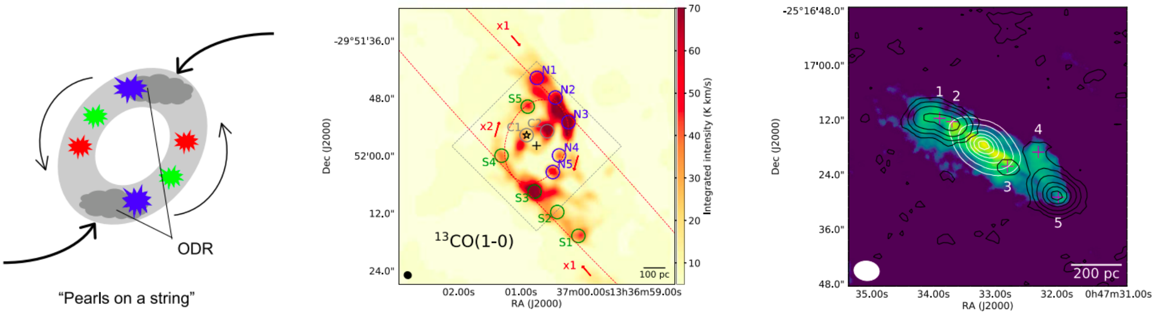

Figure 1.16: x_1/x_2 interactions in the CMZ of galaxies. Left: Sketch of the “Pearls on a string” scenario, in which star formation is cultivated near to the apocenters of the inner (x_2) orbit (thin arrows), where it intersects with entrained gas from the dust lanes (x_1 orbit, bold arrows). These interactions give way to over-density regions (ODRs) that will create newer stars (in blue) compared to more evolved stars (in green) and the oldest ones (in red). Sketch taken from Böker et al. (2008). Middle: ^{13}CO J =1–0 emission of the nuclear ring of M 83 highlighting positions studied in Harada et al. (2019), labeled in blue (N1-5), green (S1-5), and gray (C1-2) circles. x_1 and x_2 orbits are shown with red dashed ellipses. Figure taken from Harada et al. (2019). Right: The CMZ of NGC 253. Black contours represent integrated $4_{-1} \rightarrow 3_0 - E$ methanol emission (at 36.2 GHz), white contours indicate 7–mm continuum emission. CO J =2–1 emission (from Sakamoto et al., 2011) is shown in the background. Magenta plus signs indicate locations of methanol maser emission. Figure from McCarthy et al. (2020).

interactions through recombination lines, as the most intense SFR occurs in the very nuclear regions (Bendo et al., 2015). We can infer whether x_1/x_2 interactions are at play through shock tracers. In this regard, HNCO appears as an ideal tracer (see Appendix C).

It can be that weak shocks produced by cloud-cloud collisions are the main dynamic feature at the end of the nuclear bar while stronger shocks, traced by SiO, act deeper in the nucleus. HNCO is also a tracer of dense gas, indicating the presence of over densities produced in the interface between the spiral arms and the nuclear bar in NGC 253. The distribution of HNCO has been claimed to be co-spatial with methanol Class I masers by Ellingsen et al. (2014). In Appendix C we confirm this scenario regarding the $J_{-1} \rightarrow (J-1)_0 - E$ methanol line series (at 36, 84, 132, 229, and 278 GHz), all of Class I maser type, pumped by shocks (see Sect. 1.1.3). They are effectively masing at the outskirts of the CMZ of NGC 253.

It can be that cloud-cloud collisions emerge as the first and main pumping mechanism for the above-mentioned methanol maser transitions. The over-densities produced following the “Pearls on a string” framework increase the gas column densities at the boundaries of the inner bar allowing us to detect its signal in the sub-mm window. The lack of recombination lines at these boundaries discard triggered star-formation as the mechanism to produce methanol masers.

1.2 Scientific Aims

The general idea of this thesis can be summarized as a search for differences between prevailing conditions in the CMZ and the large-scale disk, both in our Galaxy and in nearby galaxies such as the closest nuclear starburst system, NGC 253. In Sections 1.3.1 and 1.3.5 we describe studied targets and facilities used along this thesis.

In Appendix A we mainly measured ^{32}S/^{34}S ratios toward the CMZ of our Galaxy, a region largely unexplored in this aspect (Chin et al., 1996). To this end, we utilized APEX, IRAM, and ALMA observations of the +50 km s^{-1} Cloud, Sgr B2(N), its envelope, and line-of-sight (l.o.s.) clouds toward it. We are interested in:

- Estimating the ^{32}S/^{34}S ratios in the Galactic CMZ, comparing it with the one measured along the large-scale disk.
- Improving existing radiative transfer modeling of sulfur-bearing species in the CMZ.
- Providing up-to-date constrains to nucleosynthesis models of the elusive, short lived, massive stars in the Galactic CMZ, starting with what is already known in the Galactic disk.
- Comparing ^{32}S/^{34}S gradients with metallicity gradients across the Galaxy radius, as metallicity is directly related to ^{34}S abundances, while it does not affect the production of the main species (Woosley & Weaver, 1995).
- Providing and independent test for the widely accepted inside-out growth scenario for the formation of galaxies (Patel et al., 2013), since metallicity (Fe/H) increases with time (Wheeler et al., 1989) and it is inversely proportional to ^{32}S/^{34}S ratios. We expect a decrease in these ratios as we approach the Galactic center.

Methanol maser emission has been extensively studied in the Milky Way but scarcely detected and characterized in extragalactic objects. To this aim, in Appendix B we performed observations of the nearby galaxies M 82, NGC 4388, Arp 220, Maffei 2, IC 342, and NGC 5728; with special emphasis on Arp 220 and IC 342 (Gorski et al., 2018; Sakamoto et al., 2021). The observations were performed with the Effelsberg telescope at 23" angular resolution, covering a region comparable to the central molecular zone (CMZ) on each of these two mentioned objects. Our main interests include to:

- Expand the number of galaxies beyond the local group known to host methanol Class I masers. Previous to this thesis, methanol masers were reported in only five sources: NGC 253, NGC 4945, NGC 6946, IC 342, and Arp 220 plus one non-confirmed detection in NGC 1068 (Wang et al., 2014). We therefore search for this kind of masers in six sources: Maffei 2, IC 342, M 82, NGC 4388, NGC 5728, and Arp 220.
- Confirm the previously reported detection of methanol masers in Arp 220 and IC 342 (Chen et al., 2015; Gorski et al., 2018).
- Test the dependence between methanol Class I maser emission and IR radiation in extragalactic objects.
- Compare the methanol $4_{-1} \rightarrow 3_0 - E$ transition at 36 GHz with the methanol $7_0 \rightarrow 6_1 - A^+$ transition at 44 GHz. Strong Galactic methanol maser emission has been largely reported in these transitions, with the line at 44 GHz being the strongest Galactic Class I methanol maser. Previous related work found an inverted picture in external galaxies, with the transition line at 36 GHz being stronger than the one at 44 GHz in NGC 253. We therefore want to check if this is true for other galaxies.

In order to study methanol maser emission with a higher degree of detail, in Appendix C we make use of the ALMA Comprehensive High-Resolution Extragalactic Molecular Inventory (ALCHEMI) large program. This inventory allows us to explore the appearance of methanol maser emission at an unprecedented synergy of frequency coverage (84−373 GHz), sensitivity (30−50 mK), angular (1.6"∼27 pc), and spectral (8−9km s^{-1}) resolution (Martín et al., 2021). ALCHEMI focuses on one of the closest nuclear starburst galaxies: NGC 253 (Leroy et al., 2018), known to harbor methanol maser emission at 36, 44, and 84 GHz (Ellingsen et al., 2014, 2017; McCarthy et al., 2018b). The main reasons to perform Appendix C can be summarized as follows:

- Expand the number of methanol maser transitions known in galaxies beyond the Local Group with the help of the ALMA telescope.
- Study the CMZ of NGC 253, one of the closest starburst systems. Its proximity gives us a panoramic view of extreme conditions in the ISM.
- Probe the pumping mechanism of Class I methanol masers in external objects with the aim to identify what differentiates it from Galactic conditions, where Class II methanol masers are the strongest.
- Characterize the ISM, in terms of column density and temperature, where methanol masers are emerging. For this purpose we employ radiative transfer modeling and rotation diagrams across 10 selected regions located at the core of giant molecular clouds previously identified in the CMZ of NGC 253.

1.3 Methods

1.3.1 Studied objects

In this section, we describe our research targets, first our Galactic sources and then the extragalactic environments. We start, in Appendix A, by studying the +50 km s^{-1} Cloud and Sgr B2(N), two massive star-forming molecular clouds located within the central ∼130 pc of our Galaxy. We further analyzed unpublished data from Thiel (2019), devoted to the study of translucent and diffuse clouds along the l.o.s. toward Sgr B2(N). Those clouds are located across the inner 1 kpc of our Galaxy.

In Appendix B, we study five nearby galaxies with special focus on the CMZ of Maffei 2 and IC 342, prone to produce methanol masers in the $4_{-1} \rightarrow 3_0 - E$ and $7_0 \rightarrow 6_1 - A^+$ transtions at 36 and 44 GHz, respectively (see Table 1 of Appendix B). Finally, in Appendix C, we search for methanol masers spanning frequencies between 84 and 374 GHz in the central regions of the nuclear starburst galaxy NGC 253.

The +50 km s^{-1} Cloud

The +50 km s^{-1} Cloud (a.k.a. M–0.02–0.07; Ferrière 2012) is a GMC located at few parsecs from the Galactic center, 3±3 pc in projection toward us, 7±3 pc and 4.5±3 pc to the east and south, along the Galactic plane, respectively (Ferrière, 2012, considering CS emission). Its total mass is ∼5×$10^5 M_\odot$, with a characteristic density of 10^{4-5} cm^{-3}, gas temperatures ranging from 80-100 K (e.g., in NH_3;

Güsten et al. 1985), through ~190 K (from H_2CO, Ao et al., 2013), until 410 K (from NH_3; Mills & Morris 2013), and dust temperatures ranging between 20 and 30 K (Sandqvist et al., 2008).

The energetics of at least a part of the +50 km s^{-1} Cloud are influenced by the supernova (SN) remnant Sgr A East (Tsuboi et al., 2009; Ferrière, 2012; Uehara et al., 2019). More recent studies found a half-shell-like feature (see Fig. 1.17) in this object hosting several compact H II regions (e.g., Mills et al., 2011). Strong SiO emission indicates quite a disturbed environment likely triggered by cloud-cloud collisions, proposed as an agent to induce star formation (Tsuboi et al., 2015). CS J =1–0 emission indicates two kinematic components associated with (1) an interacting region with the Sgr A east shell presenting the highest velocity dispersion (60 km s^{-1}) and (2) a molecular shell of 100" diameter expanding at 28 km s^{-1}.

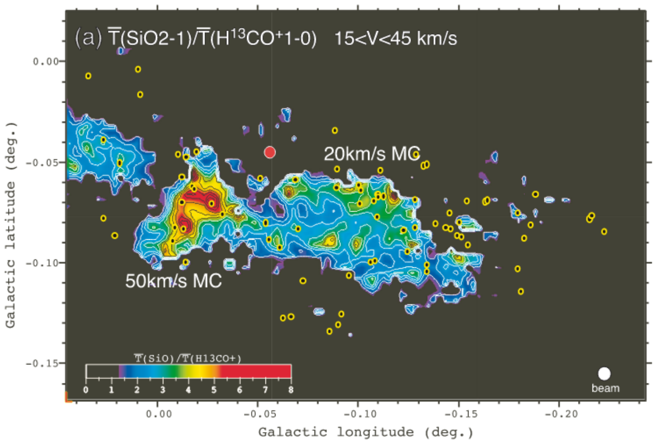

Figure 1.17: The 20 and 50 km s^{-1} clouds in an integrated intensity ratio of SiO J =2–1 over $H^{13}CO^+$ J =1–0 within a velocity range of V_{LSR} =15–45 km s^{-1}. The red circle indicates the position of the Galactic center, Sgr A*. Yellow circles mark CH_3OH Class I maser spots or peaks of quasi-thermal emission in the $4_{-1} \rightarrow 3_0 - E$ transition, at 36 GHz. Figure taken from Tsuboi et al. (2015).

Sgr B2(N)

The GC region harbours one of the most intense, densest, and luminous sites of massive star formation in the Galaxy, Sgr B2 (~$10^7 M_\odot$) (Molinari et al., 2014; Ginsburg et al., 2018). It provides an extreme environment in terms of pressure, turbulent Mach number, and gas temperature (Ginsburg et al., 2016) over a much more extended region than encountered in star-forming regions throughout the Galactic disk (Morris & Serabyn, 1996; Ginsburg et al., 2016; Schwörer et al., 2019; Dale et al., 2019). These conditions are comparable to those in starburst galaxies (Belloche et al., 2013; Schwörer et al., 2019).

Sgr B2(N)orth is located inside Sgr B2 and is at a galactocentric distance of 130^{+60}_{-30} pc from Sgr A* (from Reid et al., 2009, considering the projected distance of 100 pc as lower limit) or ~8 kpc from us. Its diameter is ~0.8 pc (Lis & Goldsmith, 1990; Schmiedeke et al., 2016).

This massive star-forming region harbours five hot cores, namely Sgr B2(N1–N5), with kinetic temperatures ranging from ~130 to 150 K for N3–N5, between 150 and 200 K for N2, and between 160 and 200 K for N1, assuming LTE conditions in all these cases (Belloche et al., 2016; Bonfand et al., 2017; Belloche et al., 2019). In addition, there are 20 1.3 mm continuum sources associated with dense clouds in Sgr B2(N) that exhibit a rich chemistry (Sánchez-Monge et al., 2017; Schwörer et al., 2019). Ginsburg et al. (2018) detected 271 compact continuum sources at ~3 mm in the extended Sgr B2 cloud, thought to be high-mass protostellar cores, representing the largest cluster of high-mass young stellar objects reported to date in the Galaxy.

Maffei 2

Maffei 2 is an Sbc Starburst/AGN galaxy located in the Maffei group. This group contains at least nine galaxies and is located at a distance of ~5.73±0.4 Mpc ($V_{\rm LSR}$ =-128±33 km s^{-1}) (Anand et al., 2019). Maffei 2 has an inclination angle of 67° and a position angle of 35° (Hurt et al., 1996; Jarrett et al., 2003). Due to a high extinction (5.7 A_V; Fingerhut et al. 2007) given its location behind the Galactic plane, previous studies greatly underestimated its distance, leading to a rather small estimation of its CMZ: 300 pc (Meier & Turner, 2012), while its actual dimension is of the order of 800–900 pc. Similar to other Sb galaxies, a massive star formation is observed at the boundaries of the CMZ, at the interface between the nuclear bar and the spiral arms. The observed asymmetry in HI profiles as well as in the tidal arms suggests an ongoing minor merger in this source (Hurt et al., 1996). This minor merger, altogether with cloud-cloud collisions, feeding material by the prominent bar, and an enhancement of cosmic rays, have been proposed to explain the high gas temperatures measured through ammonia ($T_{\rm rot}$ =~115 K, $T_{\rm kin}$ =~200 K) at the nucleus of this starburst system (Henkel et al., 2000). The disturbed kinematics in Maffei 2 mentioned above is possibly facilitating the suitable conditions (i.e., a shocked environment; see, e.g., Sobolev 1992; Zeng et al. 2020) for the pumping of Class I methanol masers reported recently by Chen et al. (2022). On the other hand, the high nuclear radiation field is a likely explanation for the tentative detection of the methanol maser line at 6.7 GHz, which emits at velocities between −150 and +100 km s^{-1}, namely, around the kinematic center of this nearby galaxy. The above-mentioned conditions taking place in the nuclear regions of Maffei 2 are sketched in the middle and rightmost panels of Figure1.18, while the leftmost panel of this Figure provides us with a perspective of the CMZ (inset in the cyan square) with respect to the entire galaxy.

Position-velocity (PV) diagrams performed by Kuno et al. (2008) reported no CO J =2–1 emission at the center of Maffei 2. In addition, kinematic studies on CMZ scales revealed molecular gas orbiting within the potential of a nuclear bar (Meier et al., 2008) that is 7° clockwise misaligned with the large-scale bar (PA=~40°) and is decoupled from it with a pattern speed four times faster (Meier et al., 2008).

IC 342

IC 342 (a.k.a. Cadwell 5) is a late-type spiral galaxy of type SAB(rs)cd (de Vaucouleurs et al., 1976) located at a distance of ~3.93 Mpc (Tikhonov & Galazutdinova, 2018), which makes it one of the closest spiral galaxies to Earth. A circular velocity of 31±3 km s^{-1} and an inclination of 25° (nearly face-on) were calculated by Newton (1980) using neutral hydrogen. Maps of CO J =1–0 show a ring-like structure with signs of very slow circular motions (8 km s^{-1}) in the galactic nucleus and two prominant narrow ridges separated by ~9" running north-south (Ishizuki et al., 1990; Schinnerer et al., 2008). Strong emission from warm dust grains is the main contributor to the strong mid- and far-infrared luminosity concentrated in the inner 700 pc region ($4\times10^9 L_\odot$; Becklin et al. 1980), while its overall infrared luminosity is $9\times10^9 L_\odot$ (Young et al., 1996). The above indicates that IC 342 is similar to our Galaxy in terms of star formation (Mao et al., 2010).

Its proximity and low inclination allowed astronomers to characterize for the first time the magnetic field coiled around the spiral arms of a galaxy (Beck, 2015), revealing polarized radio emission along the inner side (and possibly also in the outer side) of some arms, as shown in Fig. 1.19. The magnetic pattern is supposed to be more stable than the observed dynamics of gas and dust, having a velocity pattern that should remain approximately the same over a few galactic rotation periods.

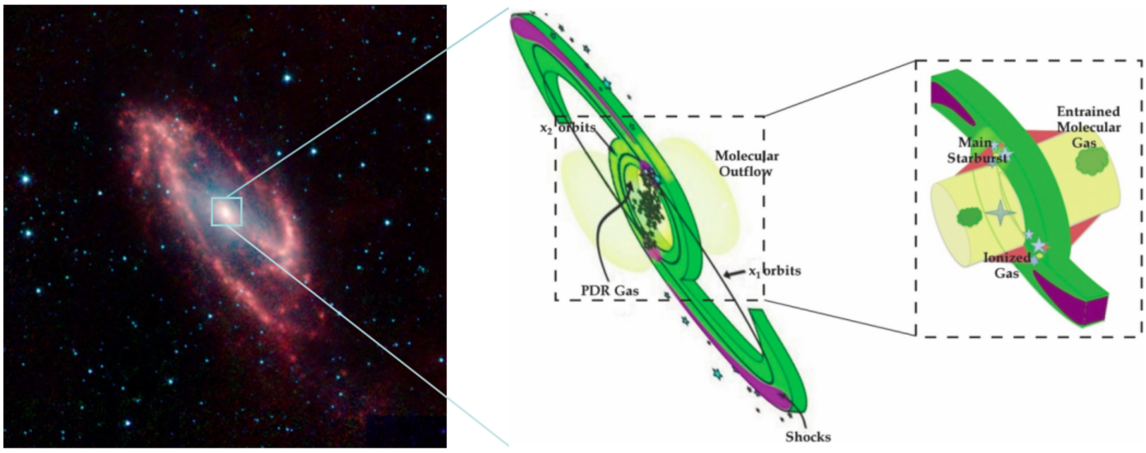

Figure 1.18: Different perspectives of Maffei 2. Left: Infrared image from the Spitzer Space Telescope covering the entire galaxy (`https://www.spitzer.caltech.edu/image/sig10-025-maffei-2-the-hidden-galaxy`). Middle and Right: CMZ's sketch taken from Meier & Turner (2012), indicating the kinematics (x_1 and x_2 orbits (see e.g. Regan & Teuben, 2003; Harada et al., 2019), entrained material, and shocks) and chemistry (photodissociated regions, ionized gas) that can be found in the nuclear starburst of Maffei 2.

Contrary to the global dynamics, greatly influenced by a large-scale bar, the inner 50 pc gas flow is affected by mechanical feedback from the nuclear star formation. This star formation is likely responsible for the formation of Hα shells, which are co-spatial with CO J =1–0 emission, that can generate an energy of at least ~1.2×10^{52} erg and disturb the inner gas morphology (Schinnerer et al., 2008).

NGC 253

NGC 253 is a nearby (D ~3.5 Mpc, Rekola et al., 2005) highly inclined ($i \sim 70^\circ$–79°, Pence 1980; Iodice et al. 2014) SAB(s)c galaxy (de Vaucouleurs et al., 1991) with a systemic heliocentric velocity ($v_{\rm sys}$) of ~258.8 km s^{-1} (Meyer et al., 2004). Assuming a distance of 3.5 Mpc (Rekola et al., 2005), 1" corresponds to ~17 pc. The total star formation rate (SFR) of this starburst galaxy is 5 $M_\odot$ yr^{-1}, of which ~2 $M_\odot$ yr^{-1} belong to the central few hundred parsecs (Leroy et al., 2015; Bendo et al., 2015). The position angle (PA) of the large-scale bar is 51° (Pence, 1980). This bar's PA continues inwards till the central ~170 parsecs. Further into the core, the isovelocity contours of the gas change their orientation by about 90° possibly due to the existence of a nuclear bar (Cohen et al., 2020). As in the case of our Galaxy, NGC 253 is characterized by a particularly strong and diverse molecular emission in its central 500 pc (Sakamoto et al., 2006), which we therefore identify as its CMZ.

Due to their vigorous star formation compared to the Milky Way, starburst galaxies such as NGC 253 represent a great test-bed to study stellar feedback mechanisms such as the ISM heating and ionization from UV photons, mechanical energy injection, and cosmic rays produced by massive stars (Harada et al., 2021). The stellar production in the nucleus of NGC 253 is comparable to more distant starburst galaxies, allowing us to have a closer view into the processes taking place in these kinds of systems (Leroy et al., 2015). In Fig. 1.20 we present a schematic view of the CMZ of NGC 253, widely studied

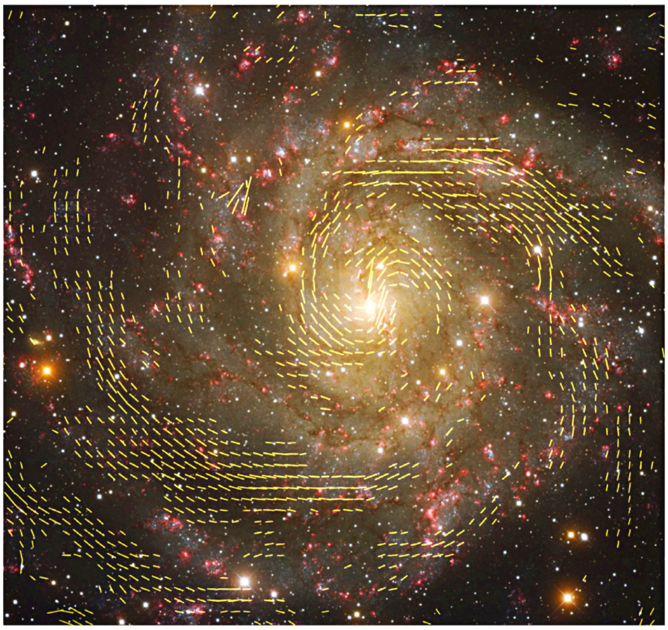

Figure 1.19: Composited image of IC 342. Background image from the Kitt Peak Observatory. Magnetic fields at λ6.2 cm at 25" resolution from VLA and Effelsberg are marked by yellow lines. Image taken from Beck (2015) and references therein.

for decades.

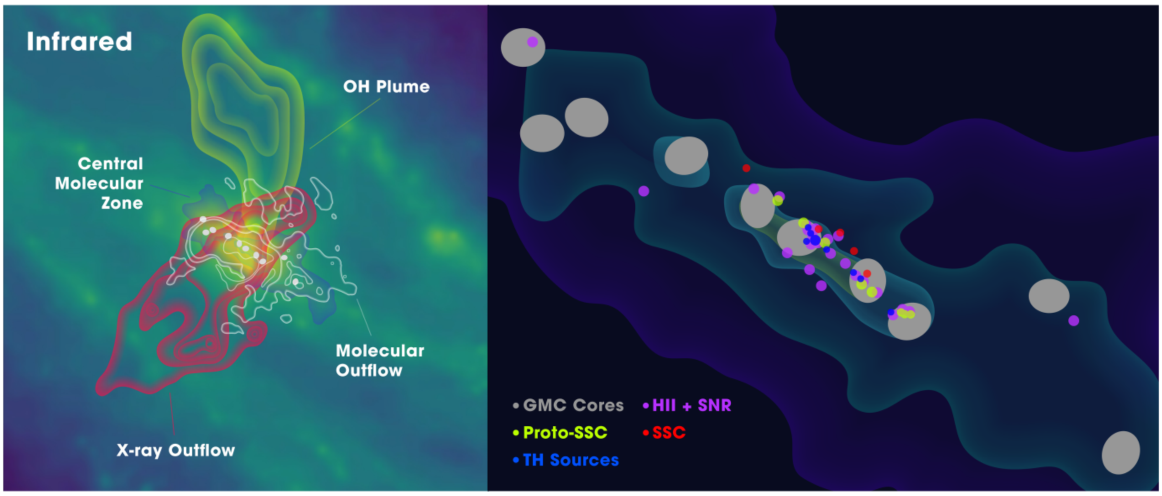

Figure 1.20: Schematic view of the CMZ of NGC 253 from multi-wavelength observations. Location of ten GMCs from Leroy et al. (2018) are indicated with grey circles. Left: 8 µm Spitzer observations as background from Dale et al. (2009); outflow traced by Chandra (Strickland et al., 2000); 18 cm OH plume (Turner, 1985), and CO outflow observed by Bolatto et al. (2013). Right: 2 cm continuum emission (Turner & Ho, 1985)

Similarities of the NGC 253's CMZ with G+0.693–0.027

G+0.693–0.027 is a quiescent giant molecular cloud located within the Sgr B2 star-forming complex. Its chemical complexity is attributed to low-velocity shocks (less than 40 km s^{-1}; Requena-Torres et al., 2008). Its excitation temperature (T_{ex}) derived from N-bearing molecules such as HNCO and CH_3CN ranges between 9 and 30 K, being significantly lower than the gas temperature $T_{\rm kin}$ of 73–140 K, implying sub-thermal excitation (Zeng et al., 2018).

The conditions prevailing at the circumnuclear ring of NGC 253, where the gas/dust lanes of the bar interact with the CMZ, resemble the ones observed in G+0.693–0.027: weak continuum emission and multi kinematic components in shock tracer molecules such as SiO and HNCO (Zeng et al., 2020). HNCO, proposed to be a tracer of warm gas and/or weak shocks (Kelly et al., 2015; Huang et al., 2022) shows stronger emission at the outskirts of the CMZ of NGC 253 while a complex emission profile (up to four components) is detected in the nuclear regions (see Fig 1.21).

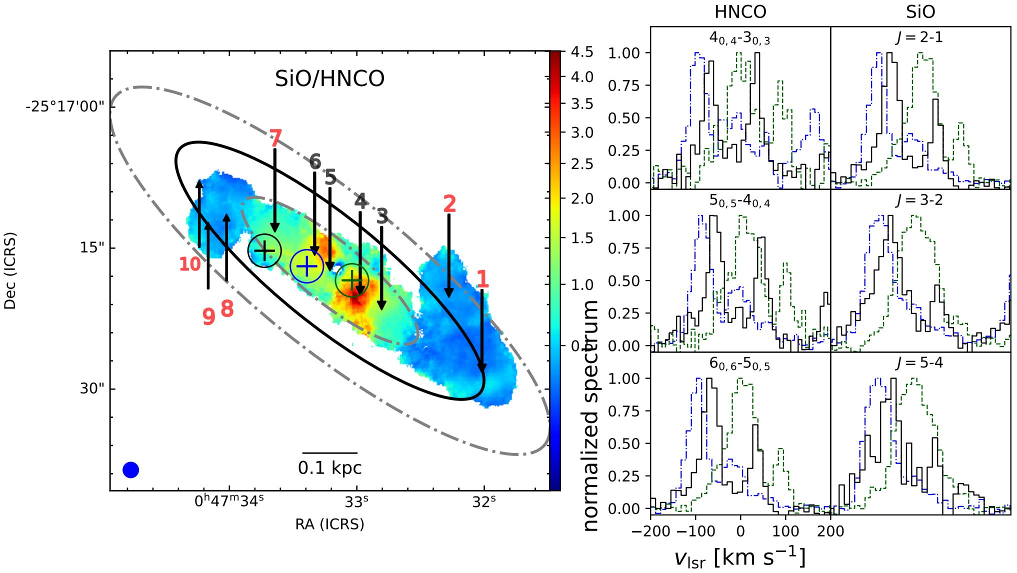

Figure 1.21: SiO and HNCO molecular emission in the CMZ of NGC 253. Left: integrated intensity ratios between the SiO J =2–1 and HNCO ($4_{0,4}$–$3_{0,3}$) transitions. High values trace regions were strong shocks predominate. A 3σ clipping was applied. Data are shown in square root stretch. Labels, symbols and colors are the same as for Figure 4 of Appendix C, central panel. Encircled crosses show the spaxel position where spectra of the right were extracted, using the same color scheme. Right: Spectra of HNCO and SiO in the selected transitions used as inputs for XCLASS (see Table D.2). From east to west they are: solid black, dashed-dot blue, and dashed green lines, respectively.

1.3.2 Rotation diagrams

In Appendix C, we employ rotation diagrams as a first method to discriminate between methanol lines in local thermodynamic equilibrium (LTE) and those out of LTE within the CMZ of NGC 253. This method also allowed us to derive methanol's total column densities and excitation temperatures ($T_{\rm ex}$). Here, we will highlight some of the essential concepts of this method while we refer the reader to Goldsmith & Langer (1999) for a comprehensive review.

In a rotation diagram, the natural logarithm of column density of the upper of the two levels ($N_{\rm u}$) per statistical weight ($g_{\rm u}$) of a certain number of molecular transitions are arranged as a function of their energy ($E_{\rm u}$) above the ground level in terms of excitation temperature divided by the Boltzmann constant k. Considering the Boltzmann distribution and assuming LTE conditions, we have:

$$N_\mathrm{u} = \frac{N}{Z} g_\mathrm{u} exp(-E_\mathrm{u}/kT_\mathrm{ex}), \tag{1.15}$$

where N is the total column density. A thorough derivation of the total column density is given in Mangum & Shirley (2015). Z is the partition function,

$$Z = \sum_{all\, levels} N_i, \tag{1.16}$$

which relates to the micro-state probabilities of a system relative to the entire system.

We may reorganize Eq. 1.15 to obtain:

$$ln\left(\frac{N_\mathrm{u}}{g_\mathrm{u}}\right) = ln(N) - ln(Z) - \frac{E_u}{kT_{ex}} \tag{1.17}$$

Under LTE conditions and having a beam filling factor of 1 as well as an optical depth small compared to unity, Eq. 1.17 gives a straight line with a slope proportional to the negative reciprocal of the temperature (-1/T_ex). Once having the temperature, we can derive the total column density N just by isolating it from Eq. 1.15. The partition function depends on the temperature and can be found in various archives, for instance in the Cologne Database for Molecular Spectroscopy (CDMS) or inside the sqlPartitionMole directory of the CASSIS software (Centre d'Analyse Scientifique de Spectres Instrumentaux et Synthétiques).

Another important parameter is the critical density. The critical density is, by definition, the density above which collisional de-excitation balances the radiative excitation. In other words, the density above which populations start to be dominated by collisional processes. Its equation in its simpler form is Eq. 1.18:

$$n_{crit} = \frac{A_{ij}}{C_{ij}}, \tag{1.18}$$

where A_{ij} and C_{ij} are the Einstein coefficient for spontaneous emission and the collisional rate, respectively. The collisional rate is given by[12]:

$$C_{ij} = n \cdot \langle \sigma_{ij} \cdot v \rangle, \tag{1.19}$$

where n is the number density of the particles responsible for the collisions, σ is their cross section, and v is their velocity. When the particles are virialized, that is, in equilibrium and without a preferred direction, then we talk about velocity dispersion. This dispersion is defined either by collisions or radiation, being normally a mixture of both. The velocity dispersion is given by $\sqrt{kT_\mathrm{kin}/M}$, where k is the Boltzmann constant, M is the mass, and T_kin is the gas temperature (e.g., Draine, 2011). Now connecting the critical density with the particles' velocity ($\propto \sqrt{T_\mathrm{kin}}$), from Equations 1.18 and 1.19, it is clear that the critical density depends on the temperature and the specific transition (ij) for a certain molecule. An example of n_crit variations for the same molecule at different transition levels can be seen in Gómez-Ruiz et al. (2015).

---

[12] see, e.g., `https://astro.uni-bonn.de/~uklein/teaching/ISM/InterstellarMedium.pdf`

In Appendix C we use the collisional rates from Lique et al. (2006) and the Einstein A coefficients from the Jet Propulsion Laboratory (JPL) catalog[13]. To disentangle between methanol A and E types, we used the VASTEL catalog, based on JPL.

The C_{ij} are usually computed for discrete temperatures, although for certain cases it is possible to approximate them by a function (Mangum et al., 2019). For the analysis performed to produce Fig. 3 in Appendix C, we used the collision rate coefficients inside CASSIS and obtained from the work of Rabli & Flower (2010) in steps of 10 K from 10 to 200 K. As an example, we present in Fig. 1.22 the interpolation for A–CH_3OH transitions selected in region 6 (see Table A.1 in Appendix C).

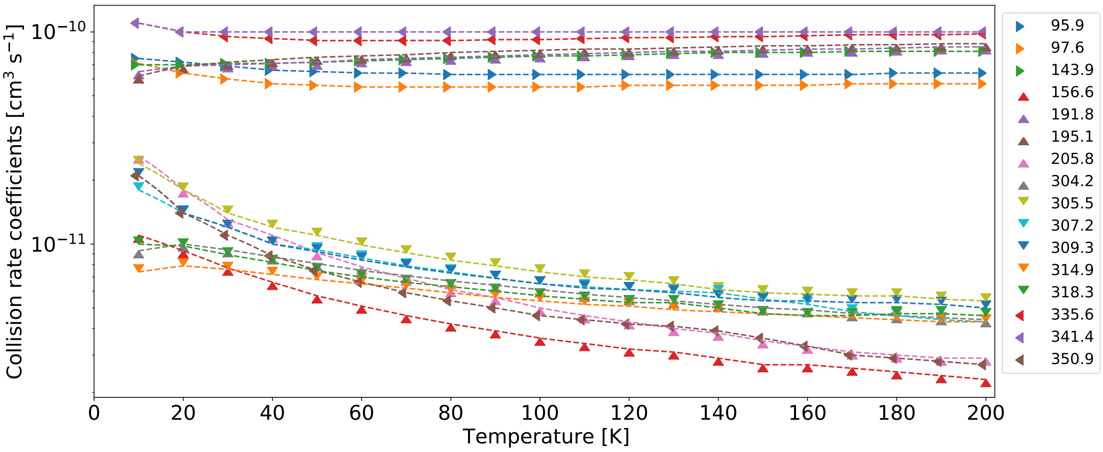

Figure 1.22: Collision rates obtained from Rabli & Flower (2010) for A–CH_3OH. Points indicate discrete values while dashed lines denote the interpolation. The x–axis shows the kinetic temperature while the y–axis presents the collision rate coefficients on a logarithmic scale. The legend box to the right contains the frequencies (in GHz) of the selected (non-blended) transitions of A–CH_3OH with the corresponding color and symbol (see Table A.1. of Appendix C).

Figure 1.22 shows that temperatures below 10 K are unreliable for non-LTE synthetic models (which require collision rates). Although CASSIS can continue extrapolating the points denoted in this figure at lower temperatures when needed, the delivered values may be wrongly interpreted.

As a final remark, the critical density is not always a proper estimation of the density at which a certain molecular transition is excited. Although limited by the kinetic temperature and molecular complexity, the "effective excitation density" has been proposed as a more accurate tool. Unlike the critical density, the effective excitation density accounts for radiative trapping, which is very important for tracers of dense gas such as N_2H^+, CN, or $H^{13}CN$ (e.g., Kirk et al., 2007; Vasyunina et al., 2011; Loinard et al., 2012). Radiative trapping occurs when a photon emitted at a given transition species is reabsorbed soon after by the same species, decreasing the number of emerging photons and increasing the number of species in an excited state (Draine, 2011, its Chapter 14). The effective excitation density, $n_{\rm eff}$, is defined as (Evans, 1999):

$$n_{\rm eff} = n_{\rm crit} \ni \int T_{\rm R} {\rm d}v = 1\,{\rm K\,km}^{-1}, \tag{1.20}$$

---

[13] `https://spec.jpl.nasa.gov/ftp/pub/catalog/catdir.html`

where T_R is the radiation temperature (see below). Equation 1.20 indicates that n_eff is the density at which a particular species emits $1\,\mathrm{K\,km^{-1}}$ of integrated intensity. That brings a workaround to the problem of molecules showing strong emission lines at densities below their n_crit, something that should not occur. Also, n_eff nicely differentiates between species with similar Einstein A coefficients and collision rates, such as $\mathrm{H^{13}CN}$, HCN, but where the isotopologue is much less abundant and emerges from denser environments since it is optically thinner. For the mentioned case of HCN and its isotopologue, Shirley (2015) finds n_eff 41 times higher for $\mathrm{H^{13}CN}$ than for HCN, closer to observation results of ∼50, and much better than n_crit ratios of about unity.

1.3.3 Radiative transfer

In the following, we summarize the radiative transfer formalism, as it is used in both Appendices B and C. The description of radiative processes is critical to characterizing many astrophysical phenomena and environments, even in their local thermodynamic equilibrium (LTE) approximation.

Considering that only emission and absorption effects are taking place along the line of sight toward an emitting source, in other words, without scattering effects, the source intensity at specific frequency ν can be described in the following manner:

$$\frac{dI_\nu}{ds} = -\alpha_\nu I_\nu + j_\nu, \tag{1.21}$$

where s is the thickness of the material the emission is passing through, and therefore the lefthand term represents the change of the source intensity I_ν as its light passes through the material. To the right of the equation, α_ν and j_ν are the absorption and emission coefficients, respectively. The absorption coefficient has dimensions of length^{-1} while the emission coefficient j_ν has dimensions of power per unit volume per unit frequency per unit solid angle. The median covered distance by a photon of frequency ν before being absorbed is the inverse of α_ν, known as the mean free path. When the photon crosses a free space without interactions, the absorption and emission coefficients are equal to zero.

Other important parameters to define are the opacity of a line τ and the source function S_ν:

$$d\tau = \alpha_\nu ds, \tag{1.22}$$

$$S_\nu = \frac{j_\nu}{\alpha_\nu}. \tag{1.23}$$

Incorporating them in Eq. 1.21, we obtain:

$$\frac{dI_\nu}{d\tau_\nu} = -I_\nu + S_\nu. \tag{1.24}$$

The integral form of this last expression, Eq. 1.24, can be derived through the following formulation:

$$dI_\nu = -I_\nu d\tau_\nu + S_\nu d\tau_\nu. \tag{1.25}$$

Adding $I_\nu d\tau_\nu$ on both sides of the equation, we obtain:

$$dI_\nu + I_\nu d\tau_\nu = S_\nu d\tau_\nu. \tag{1.26}$$

Applying an exponential term, e^{τ_ν}, on both sides of the equation, this formulation results in:

$$d(e^{\tau_\nu} I_\nu) = e^{\tau_\nu} S_\nu d\tau_\nu. \tag{1.27}$$

Integrating both sides of the last expression ($\int_0^{\tau_\nu}$), we have:

$$\int_0^{\tau_\nu} d(e^{\tau_\nu} I_\nu) = \int_0^{\tau_\nu} e^{\tau'_\nu} S_\nu d\tau'_\nu. \tag{1.28}$$

Solving the left-hand integral, we obtain:

$$e^{\tau_\nu} I_\nu(\tau_\nu) - I_\nu(0) = \int_0^{\tau_\nu} e^{\tau'_\nu} S_\nu d\tau'_\nu. \tag{1.29}$$

Multiplying with an exponential, $e^{-\tau_\nu}$, on both sides of the formulation, we have:

$$I_\nu(\tau_\nu) - I_\nu(0)e^{-\tau_\nu} = \int_0^{\tau_\nu} S_\nu e^{-(\tau_\nu - \tau'_\nu)} d\tau'_\nu, \tag{1.30}$$

which is equivalent to:

$$I_\nu(\tau_\nu) = I_\nu(0)e^{-\tau_\nu} + \int_0^{\tau_\nu} S_\nu e^{-(\tau_\nu - \tau'_\nu)} d\tau'_\nu, \tag{1.31}$$

Eq. 1.31 can be understood as follows: the measured intensity $I_\nu(\tau_\nu)$ corresponds to the sum of the background intensity $I_\nu(0)$ attenuated by the factor of $e^{-\tau_\nu}$, plus the superposition of all the layers of the region along the line of sight, each one with intensity $S_\nu(\tau'_\nu)$ attenuated by a factor $e^{-(-\tau_\nu - \tau'_\nu)}$. This last factor $e^{-(-\tau_\nu - \tau'_\nu)}$ considers the effective absorption between the layer where the source is located (there the opacity is τ'_ν) and the closest region toward the observer, τ_ν. Fig. 1.23 presents a sketch of this.

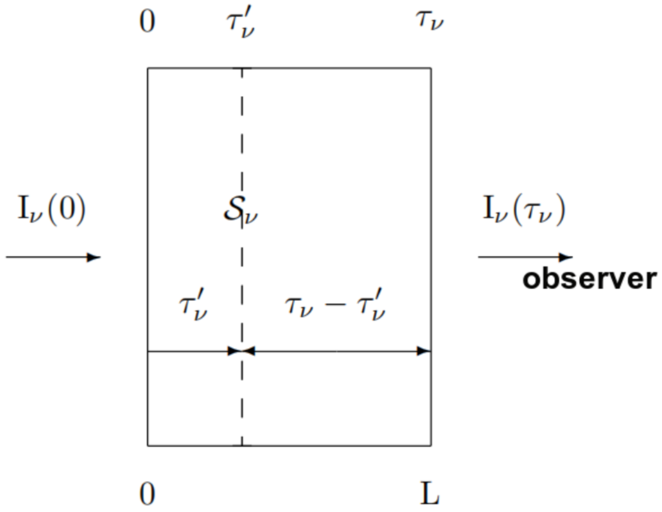

Figure 1.23: Radiative transfer framework. L is the length of the region between the background intensity $I_\nu(0)$ and the front part of the region. The background intensity is attenuated by a factor $e^{-\tau_\nu}$ while the layers inside the region, each with an intensity of $S_\nu(\tau'_\nu)$ are attenuated by a factor $e^{-(\tau_\nu - \tau'_\nu)}$. Taken from Estalella & Anglada's book "Introducción a la física del medio interestelar" (`http://www.publicacions.ub.es/refs/indices/06905.pdf`).

For a uniform medium in LTE acting as a blackbody, a beam of radiance passing through it will undergo absorption while emission from the matter takes place. Therefore, the source function can also be expressed in terms of the Planck function considering the following:

$$I_\nu(l, \nu, T) = B_\nu(\nu, T(l)), \tag{1.32}$$

where l denotes the position along the path the beam takes through the medium. Considering a constant source function and after integrating the second term, Eq. 1.31 can be expressed as:

$$I_\nu(\tau_\nu) = I_\nu(0)e^{-\tau_\nu} + S_\nu(1 - e^{-\tau_\nu}). \tag{1.33}$$

From this latter equation, two limiting cases can be derived, describing optically thin (τ_ν « 1) and optically thick ($\tau_\nu \gtrsim 1$) emission. For the optically thin case, the term $e^{-\tau_\nu}$ becomes $1-\tau$ and the term $1-e^{-\tau_\nu}$ is approximately τ_ν. Then Eq. 1.33 becomes:

$$I_\nu \approx I_\nu(0) + S_\nu\tau_\nu = I_\nu(0) + \int_0^{\mathrm{L}} j_\nu dl. \tag{1.34}$$

L encompasses the entire path from the background emission to the observer. Therefore, for the optically thin case the background emission is observed practically without attenuation, and the radiation observed corresponds to the total radiation emitted by the whole region considering the sum along all layers.

In the optically thick case, when the region is opaque, the attenuation $e^{-\tau_\nu}$ tends to absorb the entire I_ν emission ,and we only observe the source function, namely, $I_\nu \sim S_\nu$. This means that we mostly observe the surface of the emitting region S_ν, which is equal to the emissivity of a star or other radiating material divided by its opacity (Eq. 1.23). The larger the opacity, the less emission we receive from the background object, as the observed emission arises from a thinner region at and underneath the surface.

We can finally add that the transfer equation (Eq. 1.31) is sometimes expressed as:

$$I_\nu(\tau_\nu) = B_\nu(T_{\mathrm{bg}})e^{-\tau_\nu} + B_\nu(T_{\mathrm{ex}})(1 - e^{-\tau_\nu}). \tag{1.35}$$

where the background intensity $I_\nu(0)$ has been approximated to the Planck function of the background temperature ($B_\nu(T_{\mathrm{bg}})$), where T_{bg} =2.73 K at redshift zero (see, e.g., Muller et al. (2013) and Riechers et al. (2022) for high-redshift T_{bg} determinations). Similarly, the source function, S_ν, after integration, can be approximated by the Planck function of the excitation temperature, $B_\nu(T_{\mathrm{ex}})$.

Excitation temperature

Assuming thermal equilibrium, the Planck function allows us to relate the spectral radiance of a body, $B(\nu, T)$, with its temperature:

$$B(\nu, T) = \frac{2h\nu^3}{c^2}\frac{1}{e^{\frac{h\nu}{k_B T_{ex}}} - 1}. \tag{1.36}$$

Here k_B is the Boltzmann constant (equal to 1,380649 $\times 10^{-23}$ J/K[14]), ν is the frequency at which the object is being observed, c is the speed of light (299,792.358 km s^{-1}), and h is the Plack constant (6,62607015$\times 10^{-34}$ J Hz^{-1}). T_{ex} is known as the excitation temperature, which determines the relative

---

[14] where J stands for *joule*, equal to kg·m^{2}s^{-2}

level populations. $T_{\rm ex}$ is the temperature for which the source function is equal to the Planck function at a given frequency:

$$S_\nu = B_\nu(T_{\rm ex}). \tag{1.37}$$

In Radio and sub-mm astronomy, the Planck function can be replaced by the Rayleight-Jeans approximation if $h\nu \ll k_B T_{ex}$. This leads to:

$$S_\nu = \frac{2h\nu^2 k_B T_{\rm ex}}{c^2}, \tag{1.38}$$

since $\mathrm{e}^{\frac{h\nu}{k_{\rm B}T_{\rm ex}}} \sim 1 + \frac{h\nu}{k_B T_{\rm ex}}$. When Eq. 1.38 is not valid, it is necessary to replace $T_{\rm ex}$ by the $J_\nu(T_{\rm ex})$ function, which is the intensity in terms of temperature:

$$J_\nu(T_{\rm ex}) = \frac{h\nu/k}{e^{h\nu/kT_{\rm ex}} - 1}. \tag{1.39}$$

Taking advantage of Eq. 1.39, we can redefine the background and observed intensities ($I_\nu(0)$ and $I_\nu(\tau_\nu)$) in terms of temperatures, $T_{\rm B}$ and $T_{\rm bg}$, respectively; where $T_{\rm B}$ corresponds to the observed brightness temperature and $T_{\rm bg}$ is the brightness temperature of the background. In its general form and considering the above, Eq. 1.33 becomes:

$$T_{\rm R} \equiv J_\nu(T_{\rm B}) = J_\nu(T_{\rm bg})e^{-\tau_\nu} + J_\nu(T_{\rm ex})(1 - e^{-\tau_\nu}), \tag{1.40}$$

where $T_{\rm R}$ is the radiation temperature. $T_{\rm ex}$, and the optical depth τ_ν completely describe the emission and absorption of the radiation, and their knowledge is therefore equivalent to the known absorption κ_ν and emission j_ν coefficients. The limiting cases of expression 1.40 are (1) optically thin emission, $T_{\rm B} \sim T_{\rm bg} + T_{\rm ex}\tau_\nu$, and (2) optically thick emission $T_{\rm B} \sim T_{\rm ex}$. From (1) it can be noted that the reason why spectral lines often show a Gaussian-like distribution is due to the opacity and not to their temperature.

In the optically thick limiting case (2), the line shape becomes flat and constant at a given temperature equal to $T_{\rm ex}$, allowing us to easily measure the excitation temperature. When that happens, the line is said to be saturated. An example of this can be seen in Fig. 4 of Martín et al. (2019), reproduced in Fig. 1.24. In this figure synthetic spectra of HC_3N for three transitions are shown. Upper energy levels and transitions are specified above each panel, while colors represent column densities at 10^{14} cm^{-2} (green), 10^{15} cm^{-2} (red), 10^{16} cm^{-2} (magenta), and 10^{17} cm^{-2} (blue). As the opacity increases, the lines become wider and saturated. We note, however, that such lineshapes are rarely seen in the ISM with its typically spatially unresolved fine structure, providing peak line variations in excess of what is being obtained from the noise of the used spectrometer.

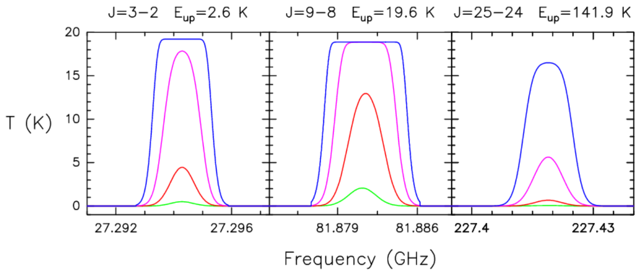

Figure 1.24: Synthetic spectra of three transitions of HC_3N at column densities varying between 10^{14} and 10^{16} cm^{-2} showing saturation effects. Transitions and upper energy levels are indicated above each panel. Figure reproduced from Martín et al. (2019).

1.3.4 Interferometry

When observing with a radio telescope, the detected portion of the sky is limited by the primary beam, equal to the first minimum of sensitivity. This minimum represents our resolution level, given by $1.22\lambda/D$, where λ is the wavelength we observe, and D is the diameter of the radio telescope. To observe a portion of the sky with a high level of detail, we require a higher angular resolution. Following the equation mentioned above, there are two ways to increase this resolution (1) either going to higher frequencies, decreasing the wavelength, or (2) increasing the telescope's diameter. Our atmosphere constrains the range of frequencies available at the Earth's surface; this represents a limit for point (1) in the case of ground-based facilities. It is also essential to consider that some objects emit at specific frequencies only, so we can not freely choose the range of frequencies to observe them. Regarding point (2), the diameter of a telescope has physical limitations. The telescope cannot move freely beyond a few hundred meters in size, and gravity represents a big problem in keeping the surface accuracy of the approximately parabolic mirror.

An elegant workaround is to virtually create a giant antenna by arranging smaller antennas as if they were replacing a section of the parabolic dish of this giant antenna. The arrangement can be of different configurations, varying the antennas' separations and displacements. In Fig. 1.25 we present various configurations along with the imaging results. Following the figure from left to right, we can infer that close antennas make an image brighter. More antennas improve the sensitivity. The addition of antennas at larger distances improves the angular resolution, while antennas positioned further obtain finer details but lose diffuse extended structures.

This technique is called interferometry. Martin Ryle and his group in the 60s considerably improved this technique thanks to computing developments. He and collaborators conceived what is known today as aperture synthesis, which mixes signals, in terms of amplitude and phase, from a collection of telescopes to create an image through the inverse Fourier transform (Ryle & Hewish, 1960).

While a complete derivation of main principles of synthesis imaging is given in the 1998 collection of the Synthesis Imaging in Radio Astronomy (Taylor et al., 1999)[15], we summarize important aspects below.

Here we consider an object without polarization, located very far away so that what we observe is just the emission radiated by its surface. Let us also assume a spherical configuration of the source, with radius **R** and following the Huygens' principle, the radiation E_ν this object is sending to us can be expressed as:

$$E_\nu(\mathbf{r}) = \int \mathcal{E}_\nu(\mathbf{R}) \frac{e^{2\pi i\nu|\mathbf{R}-\mathbf{r}|/c}}{|\mathbf{R}-\mathbf{r}|} dS, \tag{1.41}$$

---

[15] The book can be found here: `https://leo.phys.unm.edu/~gbtaylor/astr423/s98book.pdf`

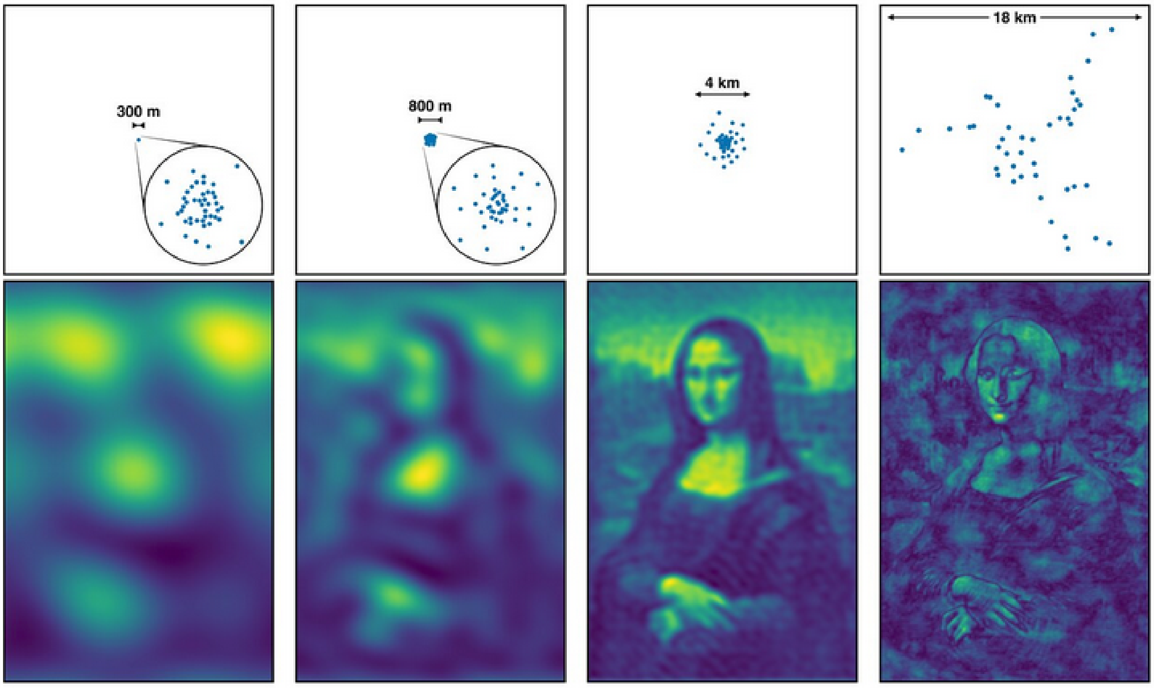

Figure 1.25: Different configurations of the antennas in an interferometer. The results for each arrangement is shown at the bottom. Image credit: ESO/J. C. Muñoz-Mateos (`https://www.eso.org/public/teles-instr/technology/interferometry/`).

where **r** is the position of the observer with respect to the target, dS is a differential element of the surface area of the object, c is the speed of light, and $\mathcal{E}_\nu$ is the distribution of the electric field on the surface of the observed object.

One of the properties of the observed electric field E_ν is its correlation at two different points, which from now on we will call $\mathbf{r_1}$ and $\mathbf{r_2}$.

A way to quantify this correlation between the signal observed by two radio telescopes is called complex visibility, V_ν, defined as the radiation received by a pair of antennas, expressed as the product of E_ν with its complex conjugate, denoted with the term *: $V_\nu(r_1, r_2) = \langle \mathbf{E}_\nu(\mathbf{r_1})\mathbf{E}^*_\nu(\mathbf{r_2})\rangle$.

With respect to $\mathcal{E}_\nu$, the radiation emitted by different points at the surface of the target is not coherent. This implies that different regions on the surface do not emit exactly the same signal and the same phase. Therefore, we have $\langle \mathcal{E}_\nu(\mathrm{R}_1)\mathcal{E}^*_\nu(\mathrm{R}_2)\rangle = 0$, for $\mathrm{R}_1 \neq \mathrm{R}_2$. With all these assumptions, from Equation 1.41, we can obtain the following:

$$V_\nu(r_1, r_2) = \int \langle|\mathcal{E}_\nu(\mathbf{R})|^2\rangle|\mathbf{R}|^2 \frac{\mathrm{e}^{2\pi i\nu|\mathbf{R}-\mathbf{r_1}|/c}}{|\mathbf{R}-\mathbf{r_1}|}\frac{\mathrm{e}^{-2\pi i\nu|\mathbf{R}-\mathbf{r_2}|/c}}{|\mathbf{R}-\mathbf{r_2}|}dS. \tag{1.42}$$

We can redefine the unit vector $\mathbf{R}/|\mathbf{R}|$ by $\mathbf{s}$, and express the observed intensity $\mathbf{R}^2$ $\langle|\mathcal{E}_\nu(\mathbf{s})|^2\rangle$ as $\boldsymbol{I}_\nu(\mathbf{s})$. Given the high distance to the observed targets, we can neglect the term $|\mathbf{r}/\mathbf{R}|$. From Equation 1.42, we can obtain the following:

$$V_\nu(r_1, r_2) = \int I_\nu(s) e^{-2\pi i \nu \mathbf{s}\cdot(\mathbf{r}_1-\mathbf{r}_2)/c} d\Omega, \tag{1.43}$$

where ν is the frequency at which we are observing, and dS was replaced by a differential unit of solid angle, $|\mathbf{R}|^2 d\Omega$. It can be noted that Eq. 1.43 depends only on the distance between telescopes. The complex visibility, $V_\nu(r_1, r_2)$, is also known as the spatial coherence function or spatial autocorrelation function of the field $E_\nu(\mathbf{r})$, and this is what an interferometer measures.

By doing a change of variables such that $\mathbf{r_1}-\mathbf{r_2} = \lambda(u, v, 0)$, where $\lambda = c/\nu$, we obtain the common expression for the visibility and also its inverse Fourier transform, namely:

$$\begin{aligned} V_\nu(u, v) &= \int\int I_\nu(x, y) e^{-2\pi i(ux+vy)} dxdy, \\ I_\nu(x, y) &= \int\int V_\nu(u, v) e^{2\pi i(ux+vy)} dudv, \end{aligned} \tag{1.44}$$

respectively. The first term in Eq. 1.44 indicates that a measurement done by two antennas at a given time is related to a single point in the so-called (u, v) plane. The scope of an interferometer is to cover this plane as much as possible. If all points inside an (u, v) plane would be filled, then the recovered image would be exactly the same as the one performed by a radio telescope of diameter equal to the largest baseline. To fill the gaps in the $uv-$plane, more than two telescopes will help as well as making use of the rotation of the Earth, which changes actual baselines as a function of time. Thus, detailed maps can be obtained covering the beam size of the individual antennas.

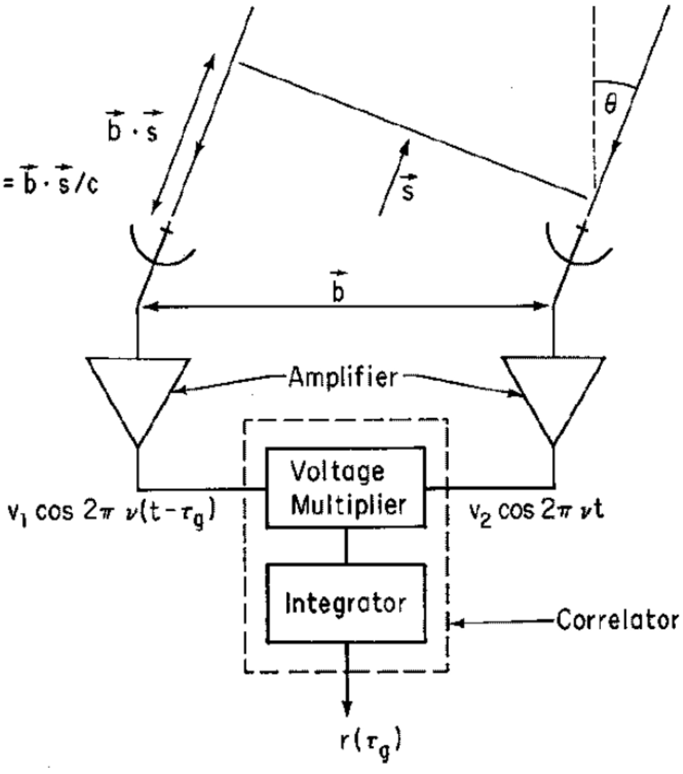

Figure 1.26: Schematic view of an interferometer with two antennas. Taken from Taylor et al. (1999).

Taking into account the (geometric) delay at which the signal arrives to different antennas, $\tau_g = \mathbf{b}\cdot\mathbf{s}/c$, we can also represent this complex visibility as:

$$V \equiv Ae^{-i\phi} = \int_S \mathcal{A}(\sigma)I(\sigma)e^{-2\pi i\nu\mathbf{b}\cdot\mathbf{s}/c}d\Omega, \tag{1.45}$$

where $\mathcal{A}$ is the normalized antenna reception pattern and **b** is the interferometer baseline. The second term in the above expression includes the amplitude and phase of the signal, and can be also related to the outputs R_c and R_s of a correlator as[16]:

$$\begin{aligned} A &= \sqrt{R_c^2 + R_s^2}, \\ \phi &= tan^{-1}\left(\frac{R_s}{R_c}\right) \end{aligned} \tag{1.46}$$

where the cosine correlator, R_c, is equal to $(V^2/2)\cos(\nu\tau_g)$ and $R_s = (V^2/2)\sin(\nu\tau_g)$, being ν the observed frequency (see Fig. 1.26).[17]

Thanks to very long baseline interferometry it is possible to reach resolution accuracies of the order of microarcseconds (μas). This technique correlates observations from two or more telescopes distributed worldwide or in the space, like the RadioAstron telescope. The latter was capable of reaching baselines distances of up to ~20 Earth diameters, which translates to a synthesized beam of 11 μas (e.g., Gómez et al., 2022; Zhao et al., 2022; Baan et al., 2022).

1.3.5 Facilities

The data obtained for the completion of this thesis come from a variety of facilities. In this Section we will highlight important aspects of them.

Effelsberg 100-m telescope

In Appendix B, we present observations performed with the Effelsberg telescope between January and March of 2019. The Effelsberg telescope recently (2021) celebrated its 50th anniversary. It is located in Bad Münstereifel, in the southern part of the federal state of North Rhine-Westphalia (Germany). Placed at an altitude of 319 m above the sea level, it was during 29 years the largest fully steerable telescope (100 m diameter). This telescope is operated by the Max-Planck-Institut für Radioastronomie (MPIfR) and observes at wavelengths between 3.6 mm and 90 cm (333 MHz–83.3 GHz) for both stand-alone observations as well as part of Very Long Baseline Interferometry (VLBI) experiments.

In order to observe methanol maser lines centered at 36 and 44 GHz, we used the Q-Band receiver, which operates at frequencies between 33 and 55 GHz, and provides both polarizations, see Fig. 1.27, right panel.

---

[16] see, e.g., `https://www.mpifr-bonn.mpg.de/3244039/IMPRS_BB_HRK4.pdf`

[17] see, e.g., `http://tube.utu.fi/courses/lib/exe/fetch.php?media=lecture5.pdf`

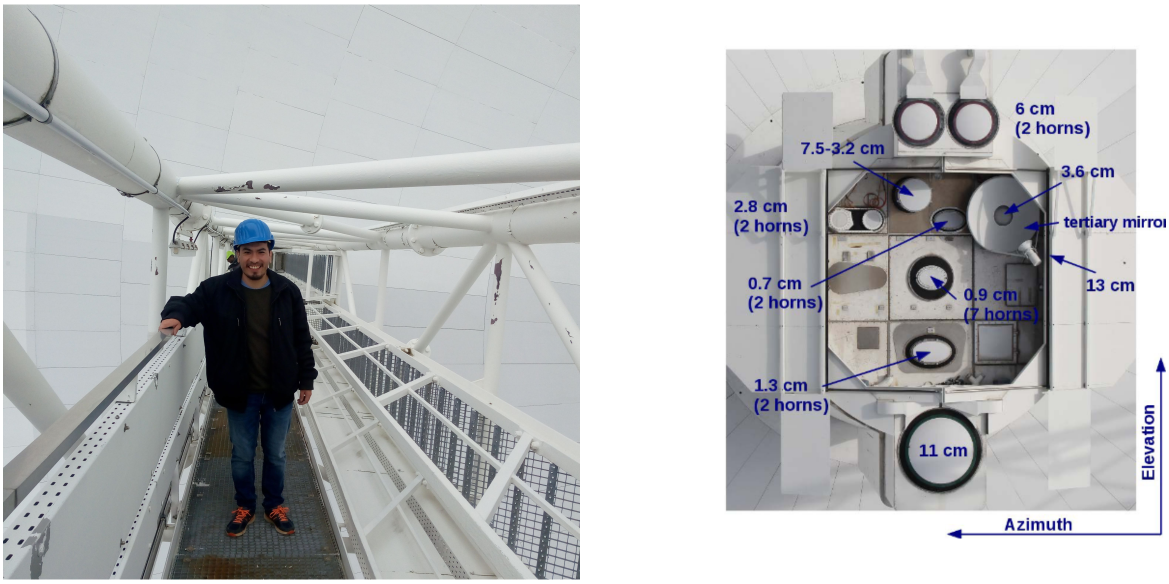

Figure 1.27: The Effelsberg telescope. Left: Me at the Effelsberg telescope's dish inclined at nearly 90° during maintenance duties. Right: Secondary focus cabin equipped with 9 receivers. The Q-band receiver is labeled as 0.7 cm and is located close to the tertiary mirror. Image taken from `https://www.mpifr-bonn.mpg.de/4334693/Eff-news-sep2018.pdf`.

In Appendix A we utilized three facilities: IRAM 30 m, APEX, and ALMA, with angular resolutions of ~16–27", ~21–22", and ~1.3–2.9", respectively. A summary of them is presented below.

Institut de radioastronomie millimétrique (IRAM) Telescope

The IRAM telescope is located on the Pico Veleta near Granada, Spain, and is placed at an altitude of 2850 m. The IRAM telescope has a diameter of 30 m and works at frequencies between 83 and 360 GHz (Carter et al., 2012) with a surface precision of 55 micrometers, comparable to a human hair width. At the time we observed, between the years 2015 and 2016, IRAM had Eight MIxer Receivers (EMIR) working at the following frequencies: 83–117 GHz (EMIR90), 124–184 GHz (EMIR150), 202–274 GHz (EMIR230), and 277–350 GHz (EMIR330). All EMIR bands are equipped with dual sideband mixers resulting in 8 GHz of instantaneous bandwidth per sideband and per polarization. IRAM also has a dual-band millimeter camera: the Neel-IRAM-KID-Array 2 (NIKA2) and a bolometer: the Goddard IRAM Superconducting Millimeter Observer (GISMO2).

The Atacama PathFinder EXperiment (APEX) telescope

At an altitude of 5107 m above the sea level, the APEX telescope is located in the Chajnantor plateau in the Chilean High Andes (Güsten et al., 2006). It has a diameter of 12 m and works mainly in the submillimeter regime: from 0.2 to 1.5 mm. APEX is a joint project among the MPIfR (55%), the Onsala Space Observatory (OSO, 13%), and the European Southern Observatory (ESO, 32%).

The FLASH 345 (Klein et al., 2014) receiver, utilized in Appendix A, was decommissioned after 15 years of continuous operations, in December 2019, and substituted by the nFLASH receivers. FLASH 345 was a dual-frequency MPIfR principal investigator (PI) receiver, operating simultaneously in the 345 GHz and the 460 GHz atmospheric windows. Considering both atmospheric windows, FLASH had a 16 GHz bandwidth.

The Atacama Large Millimeter/submillimeter Array (ALMA)

ALMA is an aperture synthesis telescope located at the Chajnantor plateau in Chile at an altitude between 4576 and 5044 m over the sea level (most of it is located above 5000 m) and at a latitude of -23°. ALMA has a total of 66 antennas. The main array contains 50 moveable antennas of 12 m, resulting in a total of 1225 baselines. The ALMA Compact Array (ACA, also known as Morita array) is a smaller array inside the ALMA system which mostly stays in a fixed configuration. It contains four 12 m–antennas ("Total Power") and twelve 7 m–antennas ("7–m array"). Because interferometers filter out extended emission, the compact array is critical to retrieve the missing flux. The third and fourth panels of Fig. 1.25 give an idea of what ALMA would observe with and without the ACA array, respectively. The maximum baseline of ALMA is 16 km, and it is designed to work in a range of frequencies between 35 and 950 GHz (see Table 1.4).

The current ALMA wavelength coverage[18] complements the spectral window available at other facilities like the Jansky Very Large Array (JVLA) or the James Webb Space Telescope. This facility observes cold regions in the universe, invisible or opaque at other wavelengths. ALMA probes a variety of phenomena such as protoplanetary disks (Pérez et al., 2016), molecular outflows (Cicone et al., 2014), high-redshift submillimeter galaxies (Simpson et al., 2014), and lensing clusters (Laporte et al., 2021), to mention a few. ALMA also extends the knowledge gained initially through optical or IR astronomy. Thanks to it, we have a deeper look into the chromospheric layers of our Sun (Alissandrakis et al., 2022). We can also better constrain the different SED components in nearby galaxies, observing where the Rayleigh-Jeans tail of the dust continuum meets the free-free emission from ionized gas (e.g., Martín et al., 2021).

Our observations with ALMA were obtained in cycles 0 and 1 (PI: A. Belloche, see also Appendix A), and cycles 5 and 6 (PIs: Costagliola and Martín, respectively; see also Appendix C). Those cycles started both on October 1st in the years 2017 and 2018, respectively. During cycle 6, the longest baseline separation ranged between 0.16 and 16.2 km, corresponding to angular resolutions of about 0.1 to 12 arcseconds. [19]

1.3.6 The ALCHEMI inventory

Scientific motivation

The Appendix C of this thesis is completely based on observations performed by the ALCHEMI collaboration [20] achieved with the maximum capability of the ALMA arrays. Details about data reduction and data analysis were recently published by Martín et al. (2021), which focused on the low

---

[18] from 84 to 950 GHz or 3.6 to 0.3 mm, respectively.

[19] where the angular resolution, in units of arcseconds, is ~0.574λ divided by the 80th percentile of the longest uv distance. Assuming that the baselines are uniformly distributed and taking as reference a frequency of 228 GHz, the mean frequency of ALCHEMI observations (see Sect. 1.3.6).

[20] ALMA Comprehensive High-resolution Extragalactic Molecular Inventory, consisting on ALMA Cycles 5 and 6 observations: ALMA Large Program 2017.1.00161.L, PIs: Costagliola, Mangum, and Harada; and 2018.1.00162.S, PI: Sergio Martín, respectively.

Table 1.4: ALMA Receiver Bands. Bands used by the ALCHEMI collaboration are bathed in grey (adapted from `https://www.eso.org/public/teles-instr/alma/receiver-bands/`).

ALMA Band	Coverage [mm/GHz]	Noise Temperature [K]	Receiver Technology	Produced by	First light
1	6–8.5/35–50	26	TBD	HEMT	TBD
2	3.3–4.5/65–90	47	TBD	HEMT	TBD
3	2.6–3.6/84–116	60	HIA	SIS	2009
4	1.8–2.4/125–163	82	NAOJ	SIS	2013
5	1.4–1.8/163–211	105	OSO/NOVA	SIS	2016
6	1.1–1.4/211–275	136	NRAO	SIS	2009
7	0.8–1.1/275–373	219	IRAM	SIS	2009
8	0.6–0.8/385–500	292	NAOJ	SIS	2013
9	0.4–0.5/602–720	261	NOVA	SIS	2011
10	0.3–0.4/787–950	344	NAOJ	SIS	2012

resolution ($15''$ ~255 pc) 7 m array data. We will summarize the main topics of this publication in order to facilitate the comprehension of Appendix C.

ALCHEMI aims to unveil the physical and chemical conditions in the central region of NGC 253. This nearby galaxy (see Sect. 1.3.1) is an ideal testbed to probe the vigorous star formation ocurring at higher redshifts because the nucleus of NGC 253 harbors conditions similar to the ones taking place in starburst galaxies much farther away (Leroy et al., 2018). When studying the chemistry of a molecule, it is crucial to measure as many transitions as possible, to limit the degrees of freedom of the radiative transfer equation. For example, with a couple of transitions, there are more than three different results available in the case of our observations of CS (see Appendix D.2.1). On the contrary, by detecting many transitions widely separated in frequency and therefore encompassing many energy levels, very restricted radiative transfer solutions with their respective constrained excitation conditions are accomplished (Aladro et al., 2011; Pérez-Beaupuits et al., 2018). From the above, the main advantage that ALCHEMI offers to the community is to observe a very ample portion of the sub-mm window with unprecedented sensitivity and high levels of angular and spectral resolution. The ALMA bands covered by this large program are indicated in Table 1.4.

With radiative transfer models yielding constrained solutions, we can improve our knowledge on conditions of already reported species and assure the detection of new ones. These new species may be undetected at specific transitions due to blending with brighter molecules, lack of bandwidth coverage, telluric lines, confusion limits, or opaque environments. For example, the extensive frequency coverage of ALCHEMI has recently revealed the first extragalactic detection of a P-bearing molecule: phosphorus nitride (PN; Haasler et al. 2022). This molecule was undetected in many transitions: J =4–3 up to J =7–6, but it is detected in its J =2–1 (at 93.98 GHz) and J =3–2 (at 140.97 GHz) transitions. A more limited spectral survey restricted to frequencies above 125 GHz (above ALMA Band 4) would be unable to confirm this first extragalactic detection of PN.

For the case of methanol (CH_3OH), one of the simplest complex organic molecules (COMs), showing quite a crowded spectrum, it is crucial to select transitions free of line blending. Apart from that, there are some line series known to undergo maser emission under specific conditions, like the $J_{-1} \rightarrow (J-1)_0 - E$ line series (at 36, 84, 132, 229, and 278 GHz) or the $J_0 \rightarrow (J-1)_1 - A$ series (at 44, 95, 146, and 198 GHz). However, most lines are not masers but are quasi-thermally excited. In Appendix C, we find that the $J_K \rightarrow (J-1)_K$ line series, which fall, within the ALCHEMI frequency coverage, at ~96.7 GHz (J = 2), ~145.1 GHz (J =3), ~193.5 GHz (J =4), ~241.8 GHz (J =5), and ~290.1 GHz (J =6), reveal quasi-thermal lines (see Appendix C). Among the science goals of the ALCHEMI collaboration it is the search for methanol masers in the CMZ of NGC 253. This project was led by the author of this thesis and resulted in Appendix C.

ALCHEMI Observations

ALCHEMI observations have an almost unbiased frequency coverage between 84.2 and 373.2 GHz, except for spectral regions where the atmosphere is opaque. Therefore, this includes a broad frequency range of 298 GHz, an angular resolution of 1.6" (27 pc at the distance to NGC 253), and a sensitivity of 30–50 mK (see below). The observations cover a uniform sensitivity area of 20"×50" (see Fig. 1.28) or ~340×850 pc with a PA of 65°. The nominal phase center of the observations is $\alpha = 00^h47^m33^s.26$, $\delta = -25^\circ17'17''.7$ (ICRS[21]). This region required a single pointing in Band 3 and Nyquist-sampled mosaic patterns of 5 to 19 pointings for the remaining bands. The average integration time per mosaic pointing to achieve the desired sensitivity varied from ~2.6 hours in Band 3 (50 mK), ~12 min in Band 4 (50 mK), ~9 min in Band 5 (40 mK), ~4 min in Band 6 (30 mK), and ~2.5 min in Band 7 (30 mK).

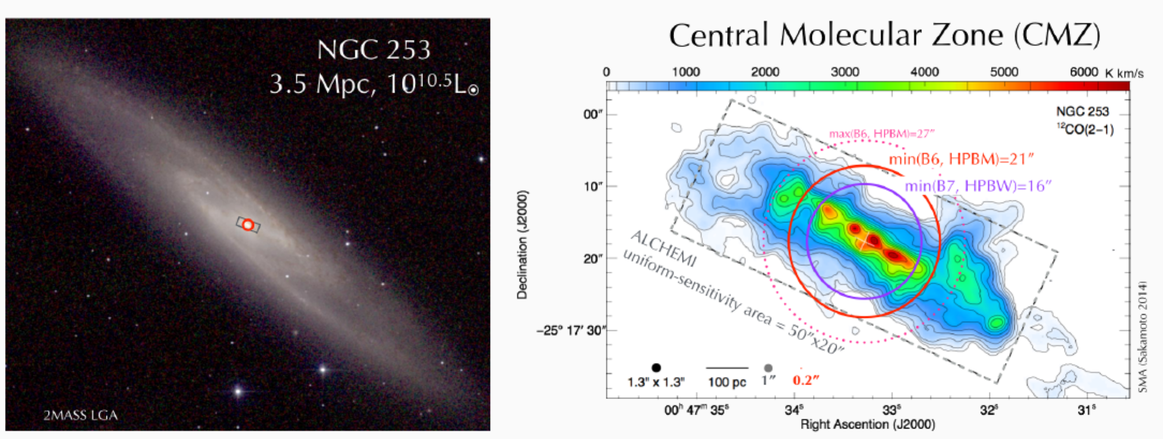

Figure 1.28: The nuclear starburst NGC 253, the target of investigation of the ALCHEMI collaboration. Left: panoramic view of the whole galaxy with its central colecular zone inside the blue rectangle (2MASS JHK composite image; see e.g., Bolatto et al. 2013, their Figure 1). Right: zoom into the mentioned rectangle showing ^{12}CO J =2–1 emission and indicating the common maximum recoverable scale (MRS) per channel estimated for 12-m and 7-m array configurations. Both HPBM and HPBW stand for the full half-power beam width, that is, the full angle in which the relative power is more than 50% of the peak power of the beam. Left image from near-infrared 2MASS observations. Right panel CO map from Sakamoto (2014).

Additional single pointing observations with the total power and the 7 m array were performed to achieve a common maximum recoverable scale (MRS) of 15″ (~254 pc) across the whole ALCHEMI frequency range. This was motivated by the extent of the CO J =1–0 emission measured by Meier et al. (2015), the outflow extension observed by Bolatto et al. (2013), and the need to capture all the emission from the NGC 253's CMZ. We can expect a small contribution from extended emission ($\geq$15") regarding strong lines such as CO and HCN in the ALMA low-frequency bands ($\lesssim$200 GHz), as can be seen in the departure above the horizontal blue line in Fig. 1.29. The recommended workaround for the latter issue consists in selecting visibilities under a given uv radius during the data reduction of ALCHEMI data (Martín et al., 2021).

---

[21] International Celestial Reference System, equivalent to J2000 within a few milli–arcseconds.

The relative flux calibration accuracy across the spectral window for each tuning is expected to be of the order of 1%, while the absolute flux calibration accuracy is of the order of 10%, 5%, 20%, 10%, and 11% for Bands 3 (84 to 116 GHz), 4 (125 to 163 GHz), 5 (163 to 211 GHz), 6 (211 to 275 GHz), and 7 (275 to 373 GHz), respectively.

The frequency gaps between 84.2 and 373.2 GHz are: 9 GHz between bands 3 and 4 (116–125 GHz) due to the telluric oxygen line at 118.75 GHz; 325 MHz around 163 GHz; 250 MHz around 211.1 GHz; and 225 MHz around 275.25 GHz; and a 9 GHz (319.3–328.3 GHz) gap to avoid the telluric water line at 325 GHz. Although still covered by ALCHEMI, data in the frequency range around the 183-GHz telluric water line is badly contaminated. This affects, among other things, the $7_{-1} \rightarrow 6_0 - E$ methanol line at 181.3 GHz, expected to be masing by our non-LTE models (see Appendix C for details).

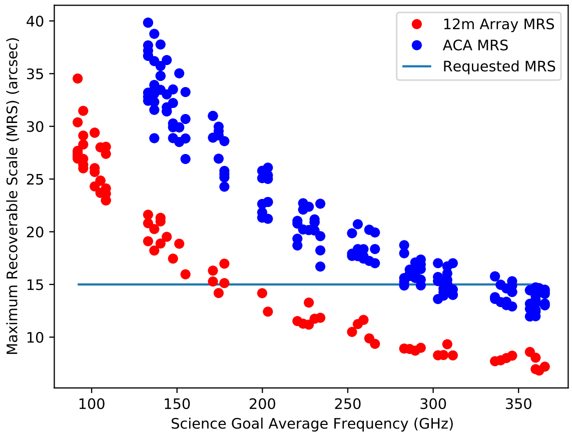

Figure 1.29: The ALCHEMI maximum recoverable scale (MRS) estimated for each array configuration. There are four points per spectral window, centered at the mean frequency with two spectral windows per sideband (see Appendix D.4). The horizontal blue line indicates the targeted MRS of 15”. Figure taken from Martín et al. (2021).

A total of 372 datacubes with 1.6” angular resolution were created. They have, when applicable, a frequency overlap of 100-200 MHz between adjacent tunings, allowing for an inspection of relative amplitude calibration.

1.4 Results

The main findings of this thesis can be summarized as follows. Regarding the first topic, we have found that the decreasing trend of the ^{32}S/^{34}S abundance ratio towards the Galactic nucleus is halted somewhere between 1 kpc and ~130 pc from the Galactic center, to increase again in the inner ~130 pc regions of our Galaxy and reach a ^{32}S/^{34}S column density ratio of $16.3^{+2.1}_{-1.7}$ and an integrated intensity ratio of $18.6^{+2.2}_{-1.8}$ (Humire et al., 2020b). This value is lower than the one found in the solar system (^{32}S/^{34}S=22.6; Yu et al. 2020) and similar to those found at ~5 kpc from the Galactic center (Humire et al., 2020b). This indicates that the metallicity in the central parts of our Galaxy is similar to the one encountered at the outer edge of the large-scale bar, of about 4.6 kpc extension (Wegg et al., 2015). The broken ^{32}S/^{34}S slope as a function of Galactic center distance differs from the uninterrupted relation found in stellar nucleosynthesis tracers of less massive stars, such as carbon, oxygen, and nitrogen isotope ratios. We have also calculated a carbon ^{12}C/^{13}C ratio of $22.1^{+3.3}_{-2.4}$ for the inner ~3 pc of the Milky Way.

It is important to highlight that our ^{32}S/^{34}S abundance ratios have been measured to a very high level of confidence, with the best value of $16.3^{+2.1}_{-1.7}$. The critical requirement for our measurements is the identification of the ^{13}C^{34}S isotopologue line in the +50 km s^{-1} Cloud, located at only $\sim$3 pc from the GC. We present the first observation of this line in that object, giving way to the best and most centrally located estimation of the ^{32}S/^{34}S ratio in the GC. Our results are in very good agreement with the ones obtained through the double isotopologue method, namely: $\frac{^{12}\mathrm{C}}{^{13}\mathrm{C}} \times \frac{^{13}\mathrm{C}^{32}\mathrm{S}}{^{12}\mathrm{C}^{34}\mathrm{S}}$, that delivers a ^{32}S/^{34}S ratio of $16.3^{+3.0}_{-2.4}$.

Independent studies based on optical observations suggest that the Galactic bar can transfer material from its outer limits toward the inner region of our Galaxy (e.g., Davies et al., 2009). This would explain the similarities in metallicities at both bar edges, one at $\sim$4.6 kpc and the other at the outskirts of the Galactic CMZ and deeper into the GC (inner 200 pc). Therefore, our sulfur isotope measurements can complement optical results.

Since sulfur is produced in massive stars, primarily in SNe Type II explosions (Clayton, 2007), and ^{34}S correlates with metallicity (Woosley & Weaver, 1995), ^{32}S/^{34}S changes should be anti-correlated with respect to metallicity resulting from massive star yields. We have found that, while ^{32}S/^{34}S ratios indeed nicely anti-correlate with metallicities measured by [Fe/H] (Genovali et al., 2014; Kovtyukh et al., 2019) they are not followed by [O/H] metallicities (Henry & Worthey, 1999). Interestingly, metallicities measured by [O/H] relate well with the inverse slope of ^{12}C/^{13}C, ^{14}N/^{15}N, and ^{18}O/^{17}O isotope ratios across Galactocentric distance (Yang et al., 2019; Chen et al., 2021; Zhang et al., 2020). On the other hand, there are similarities between ^{16}O/^{18}O and ^{32}S/^{34}S ratios across the Milky Way (Polehampton et al., 2005; Humire et al., 2020b), and this can be naturally explained in the sense that both ^{16}O and ^{18}O are primarily synthesized in massive ($>10\,M_{\odot}$; Clayton 2007) stars, in the same way as sulfur (Woosley & Weaver, 1995; Clayton, 2007). Updated models relate oxygen production with SNe II and Fe mainly with SN Ia (Kobayashi et al., 2020), but this seems in contradiction with the observations we carried out (Humire et al., 2020b), although new results my help to reconcile this discrepancy (Yan, Y. T., submitted).

With respect to the second topic, we have found that Class I methanol masers (pumped by shocks) are the brightest in extragalactic objects, being detected where Class II methanol masers (pumped by IR radiation) do not show up. We also report a first tentative detection of the maser at 36 GHz in Maffei 2 (Humire et al., 2020a), which was recently confirmed by Chen et al. (2022). Using ALCHEMI data, we detected a lack of methanol maser emission in the $J_{-1} \rightarrow (J-1)_0 - E$ line series (at 84, 132, 229, and 278 GHz) at the very central regions of the CMZ of NGC 253, while this is not the case for methanol masers belonging to the $J_0 \rightarrow (J-1)_1 - A^+$ series (those at 95, 146, and 198 GHz), emerging also in the central regions of the CMZ. The conditions required to produce Class I methanol masers in the $J_{-1} \rightarrow (J-1)_0 - E$ line series require weak shocks, generated where entrained material by spiral arms interacts with the nuclear bar. Complementary, dissociating UV radiation is the most likely explanation for the lack of Class I methanol masers in the mentioned series at the very center of NGC 253 (Humire et al., 2022). The latter can be concluded thanks to a mixture of high resolution and frequency coverage available from the ALCHEMI collaboration. An estimation of shock strength has been carried out using SiO and HNCO line ratios, while photodissociation regions were measured through CN and C^{17}O line ratios, following Meier et al. (2015). This is summarized in Figure 1.30. Quantitatively speaking, we have increased the amount of known galaxies hosting methanol masers beyond the local group, including Maffei 2. Furthermore, we have expanded the number of extragalactic methanol maser transitions detected so far from 5 to 11.

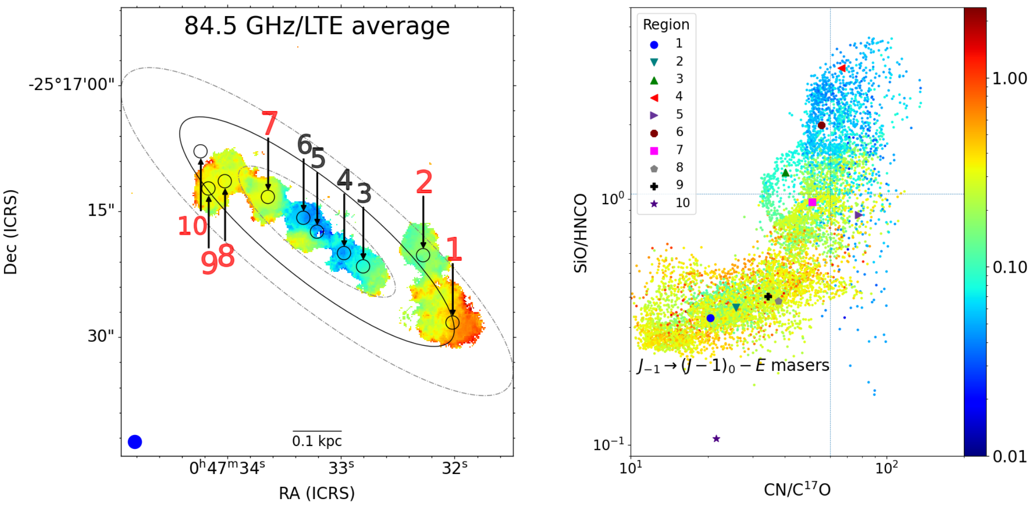

Figure 1.30: Methanol maser emission in the $J_{-1} \longrightarrow (J-1)_0 - E$ line series as a function of CRIR and shocks. Left: Maser emission distribution per spaxel as observed by dividing integrated intensities of the maser methanol line at 84.5 GHz by the mean intensity value of the surrounding (in terms of $E_{\rm up}$/k) methanol lines in LTE at 218.4 and 310.1 GHz. A 3σ clipping was applied in all the transitions involved to produce the figure. The center and edges of the inner Lindblad resonance from Iodice et al. (2014) are marked with a black ellipse and dash-dotted gray ellipses, respectively. Regions where we observe methanol maser emission in the $J_{-1} \longrightarrow (J-1)_0 - E$ line series are labeled in red. Right: Same spaxels (with their values as colors) as in the figure to the left, but this time distributed according to their ratios in the SiO/HNCO (y-axis) and CN/C^{17}O line ratio maps in ALMA band 3. A logarithmic stretch has been applied in both panels for an easy visualization. Colors are in common for both panels. Our threshold of $> 3\sigma$ above LTE conditions corresponds to an intensity ratio of >0.1244 between the 84 GHz line and the average of the 218.4 and 310.1 GHz lines.

CHAPTER 2

Sulphur and carbon isotopes towards Galactic centre clouds (Summary)

This chapter is a summary of the homologous article published in Astronomy and Astrophysics (A&A) under the reference code:

- Humire, P.K., Thiel, V., Henkel, C., Belloche, A., Loison, J. -C., Pillai, T., Riquelme, D., Wakelam, V., Langer, N., Hernández-Gómez, A., Mauersberger, R., and Menten, K. M. 2020A&A, 642A, 222H,

which is granted for non-exclusive right of republication by the author. The refereed article can be found in `https://doi.org/10.1051/0004-6361/202038216` and in the Appendix A of this document, while the fully open access ArXiv version is presented in `https://arxiv.org/pdf/2009.07306.pdf`.

2.1 Context

Measuring isotopic ratios is a sensitive technique used to obtain information on stellar nucleosynthesis and chemical evolution. Since sulfur traces late evolutionary stages of massive stars, any variance with respect to C, N, or O isotope ratios (see Fig. 2.1), which give information on CNO and helium burning (Chin et al., 1996), will tell us about the distribution and life cycle of massive stars in contrast to lower-mass stars.

Due to their short lives, the star formation rate of massive stars can be traced by their supernova (SN) rate. Although the amount of ^{34}S compared to ^{32}S is related to metallicity, which decreases with increasing galactocentric radius (e.g., as observed from oxygen, Henry & Worthey, 1999), the production of ^{34}S is mostly related to SNe II, which show a dip in the inner regions of our Galaxy and other spiral galaxies (Anderson & James, 2009). This is in good agreement with the increase of ^{32}S/^{34}S in the Galactic center (Humire et al., 2020b), since ^{32}S is formed in the same proportion in massive stars as all over the Galaxy. However, those results are still under debate (see, e.g. Hakobyan et al., 2009) and more work is needed.

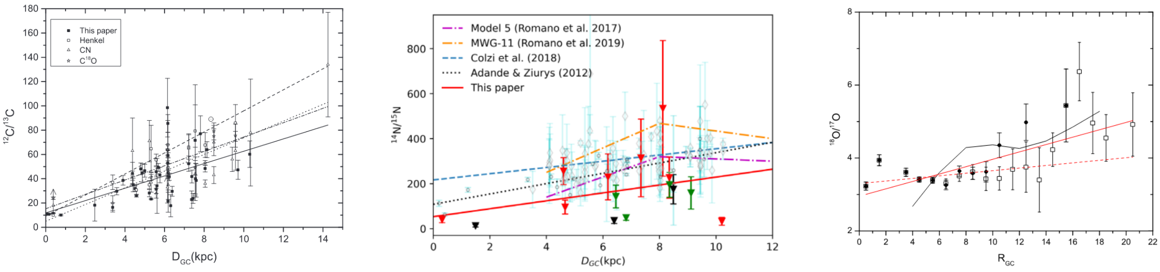

Figure 2.1: Carbon, nitrogen, and oxygen isotope ratios showing a decreasing trend towards the Galactic nucleus. Left: Carbon ^{12}C/^{13}C isotope ratios obtained from formaldehyde as a function of galactocentric radius ($D_{\rm GC}$). Figure from Yan et al. (2019). Middle: Nitrogen ^{14}N/^{15}N isotope ratios obtained from ammonia as a function of $D_{\rm GC}$. Figure from Chen et al. (2021). Right: Oxygen ^{18}O/^{17}O isotope ratios obtained from C^{18}O and C^{17}O as a function of galactocentric radius, defined as $R_{\rm GC}$ in this figure taken from Zhang et al. (2020).

2.2 Aims

We present measurements of the carbon and sulfur abundances in the interstellar medium of the central region of our Galaxy. The selected targets are the +50km s^{-1} Cloud and several line-of-sight clouds towards Sgr B2(N) as well as the envelope of Sgr B2(N) itself.

2.3 Methods

Towards the +50 km s^{-1} Cloud, we observed the J=2–1 rotational transitions of ^{12}C^{32}S, ^{12}C^{34}S, ^{13}C^{32}S, ^{12}C^{33}S, and ^{13}C^{34}S, and the J=3–2 transitions of ^{12}C^{32}S and ^{12}C^{34}S with the IRAM-30 m telescope, as well as the J=6–5 transitions of ^{12}C^{34}S and ^{13}C^{32}S with the APEX 12 m telescope, all in emission. The J=2–1 rotational transitions of ^{12}C^{32}S, ^{12}C^{34}S, ^{13}C^{32}S, and ^{13}C^{34}S were observed with ALMA in the envelope of Sgr B2(N), with those of ^{12}C^{32}S and ^{12}C^{34}S also observed in the line-of-sight clouds towards Sgr B2(N), all in absorption.

2.4 Results

In the +50 km s^{-1} Cloud, we derive a ^{12}C/^{13}C isotopic ratio of $22.1^{+3.3}_{-2.4}$, that leads, with the measured ^{13}C^{32}S/^{12}C^{34}S line intensity ratio, to a ^{32}S/^{34}S ratio of $16.3^{+3.0}_{-2.4}$. We also derive the ^{32}S/^{34}S isotopic ratio more directly from the two isotopologues ^{13}C^{32}S and ^{13}C^{34}S, which leads to independent ^{32}S/^{34}S estimations of $16.3^{+2.1}_{-1.7}$ and 17.9±5.0 for the +50 km s^{-1} Cloud and Sgr B2(N), respectively. We also obtain a ^{34}S/^{33}S ratio of 4.3±0.2 in the +50 km s^{-1} Cloud.

2.5 Conclusions

Previous studies observed a decreasing trend in the ^{32}S/^{34}S isotopic ratios when approaching the Galactic center. Our results indicate a termination of this tendency at least at a galactocentric distance of 130^{+60}_{-30} pc. This is at variance with findings based on ^{12}C/^{13}C, ^{14}N/^{15}N and ^{18}O/^{17}O isotope ratios, where the above-mentioned trend is observed to continue right to the central molecular zone (see Fig. 2.1). This can indicate a drop in the production of massive stars at the Galactic center, in line with recent metallicity gradient ([Fe/H]) studies (Kovtyukh et al., 2019), and opens the work towards a comparison with Galactic and stellar evolution models (Kobayashi et al., 2011).

The main finding of this work is summarized in Fig. 2.2, where we present sulfur isotope ^{32}S/^{34}S ratio variations when accounting for different carbon ^{12}C/^{13}C ratios as a function of galactocentric radius, $D_{\rm GC}$ (e.g. Wilson & Rood, 1994; Halfen et al., 2017; Milam et al., 2005; Yan et al., 2019). The ^{32}S/^{34}S values beyond 2 kpc from the Galaxy nucleus were calculated using ^{13}C^{32}S/C^{34}S values obtained by Chin et al. (1996) after applying the mentioned ^{12}C/^{13}C ratios, as indicated in the figure legend. In Fig. 2.2 we also indicate the ^{32}S/^{34}S ratios obtained in this work. They are labeled in orange, cyan, and light green. All ratios were deduced from integrated intensity ratios. Possible differences between integrated column density ratios and line intensity ratios for the mean values in Sgr B2(N) fall inside the error bars. For the case of the GC l.o.s. clouds towards Sgr B2(N), their distances are uncertain and they are believed to be located within 1 kpc from the GC (see Sect. 3 of Appendix A). As described in Sect. 5 of Appendix A, the purple and yellow hatched-shaded loci are derived from [Fe/H] vs $D_{\rm GC}$ relations obtained by Bovy et al. (2014) and Genovali et al. (2014), after accounting for the models of Kobayashi et al. (2011); hatched-only loci correspond to an extrapolation of those relations, following Inno et al. (2019). Finally, we include two additional ^{32}S/^{34}S ratios inferred from metallicities ([Fe/H]) measured in the central 30 pc of the Galaxy by Davies et al. (2009) and Najarro et al. (2009) utilizing the models of (Kobayashi et al., 2011), which relate metallicities with sulfur as ^{32}S/^{34}S = −19.8×[Fe/H]+23.2 (see Eq. 9 in Appendix A).

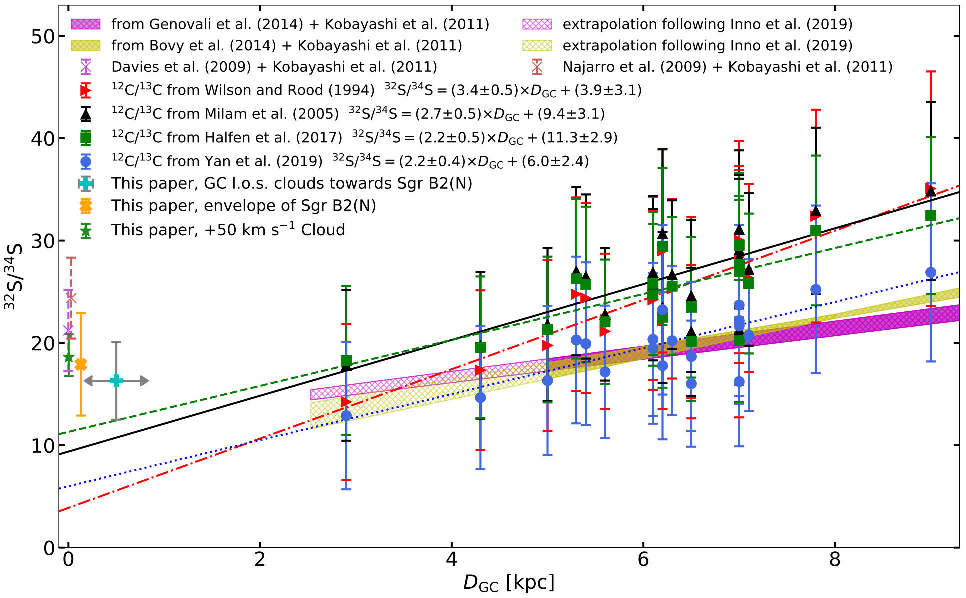

Figure 2.2: Sulfur isotope ^{32}S/^{34}S ratio variation when accounting for different carbon ^{12}C/^{13}C ratios as a function of galactocentric radius. The new values encountered in this work, in orange, cyan, and light green, demonstrate a termination of the decreasing trend in the ^{32}S/^{34}S isotopic ratios when getting near to the Galactic center as we approach the central molecular zone (CMZ) of out Galaxy. Adapted from Fig. 11 in Humire et al. (2020b).

CHAPTER 3

36GHz methanol lines from nearby galaxies: maser or quasi-thermal emission? (Summary)

This chapter corresponds to a summary of the homologous article published in Astronomy and Astrophysics (A&A) under the reference code:

- Humire, P. K., Henkel, C., Gong, Y., Leurini, S, Mauersberger, R., Levshakov, S. A., Winkel, B., Tarchi, A., Castangia, P., Malawi, A., Asiri, H., Ellingsen, S. P., McCarthy, T. P., Chen, X., and Tang, X. 2020A&A, 633A, 106H,

which is granted for non-exclusive right of republication by the author. The refereed article can be found in `https://doi.org/10.1051/0004-6361/201936330` and in the Appendix B of this document, while the fully open access ArXiv version is presented in `https://arxiv.org/pdf/1911.06776.pdf`.

3.1 Context

Methanol (CH_3OH) is one of the most abundant interstellar molecules (e.g. Kalenskii & Sobolev, 1994; Wang et al., 2004; Maffucci et al., 2018), exhibiting a plethora of lines at centimeter(cm)-, millimeter(mm)-, and sub-mm wavelengths (Schilke et al., 2001; Comito et al., 2005), including many maser lines. More than one thousand methanol masers are known in the Galaxy (e.g. Menten, 1991b; Pratap et al., 2008; Yusef-Zadeh et al., 2013; Cotton & Yusef-Zadeh, 2016; Yang et al., 2017; Yang et al., 2019; Ladeyschikov et al., 2019; Billington et al., 2020). However, in extragalactic targets, such maser lines are rarely observed. Following the detections of quasi-thermal methanol emission in nearby galaxies (Henkel et al., 1987), the large number of Galactic masers and the existence of even more luminous H_2O and OH "megamasers" (e.g. Lo, 2005) provided a strong motivation to search for class II 6.7 GHz maser emission towards extragalactic sources (Ellingsen et al., 1994a; Phillips et al., 1998; Darling et al., 2003). This yielded detections in absorption towards NGC 3079 and Arp 220 (Impellizzeri et al., 2008; Salter et al., 2008) and in emission towards the Large Magellanic Cloud (LMC; Sinclair et al., 1992; Ellingsen et al., 1994b; Beasley et al., 1996; Green et al., 2008; Henkel et al., 2018) and the Andromeda galaxy M 31 (Sjouwerman et al., 2010). The LMC also provided a 12.2 GHz class II maser detection, reported by Ellingsen et al. (2010).

Since none of the surveys for ultraluminous class II masers revealed detections of masers more luminous than in the Galaxy, searches for brighter analogs of the relatively inconspicuous Galactic class I masers were also carried out in nearby extragalactic sources. The detection of 36 GHz class I masers in NGC 253 by Ellingsen et al. (2014) revealed emission that is at least ten times more luminous than the widespread emission associated with the 300 pc × 100 pc central region of our Galaxy and 10^4 times more luminous than a typical individual Galactic 36 GHz maser. This demonstrates the existence of ultraluminous methanol masers (with respect to their Galactic counterparts). Follow-up observations confirmed this detection (Ellingsen et al., 2017; Gorski et al., 2017; Chen et al., 2018; Gorski et al., 2019), which was augmented by successful searches for the related class I maser transitions at 44 and 84 GHz in NGC 253 (Ellingsen et al., 2017; McCarthy et al., 2018b). Nevertheless, the search for additional sources turned out to be difficult. For some time, NGC 4945 was the only additional galaxy detected in the 36 GHz CH_3OH class I maser line beyond any reasonable doubt (at multiple epochs with more than one telescope; McCarthy et al., 2017, 2018a). More recently, 36 GHz emission was also reported from IC 342 and NGC 6946 (Gorski et al., 2018).

3.2 Aims

The main goal of this project is to search for Class I methanol masers, at 36 and 44 GHz, in nearby spiral galaxies such as Maffei 2 and IC 342, something that would greatly increase the number of galaxies beyond the local group known to host this kind of masers.

3.3 Methods

The 36 GHz measurements were carried out with the 100 m telescope at Effelsberg near Bonn, Germany, in early January and early February 2019. Complementary 44 GHz observations were taken in late March 2019. We obtained the data with a secondary focus Q-band receiver, sensitive in the range 33 – 50 GHz, providing both circular polarizations with an equivalent system temperature of ≈130 Jy on a flux density scale (≈1.6 K main beam brightness temperature per Jy) prior to averaging the two polarizations. Pointing observations were carried out every ∼40 minutes towards 3C 84 and NRAO 150 near Maffei 2 and towards W3(OH) near IC 342. The pointing accuracy was 4"±2" (the error is the standard deviation of an individual measurement) and never exceeded 10", while the beam size was ∼23" at both frequencies.

We employed a Fast Fourier Transform spectrometer backend with a bandwidth of 300 MHz. The number of channels was 65536, yielding a channel spacing of 0.038 km s^{-1} at 36 GHz and a velocity resolution of 0.044 km s^{-1} (see Klein et al., 2012). At 44 GHz, the corresponding values are 0.031 km s^{-1} and 0.036 km s^{-1}.

3.4 Results

In Figure 3.1 we report class I 36 GHz ($\lambda \approx 0.8$ cm) CH_3OH $4_{-1} \rightarrow 3_0$ E line emission from the nearby galaxies Maffei 2 ($D \approx 6$ Mpc) and IC 342 ($D \approx 3.5$ Mpc), measured with the Effelsberg telexcope at three different epochs within a time span of about five weeks.

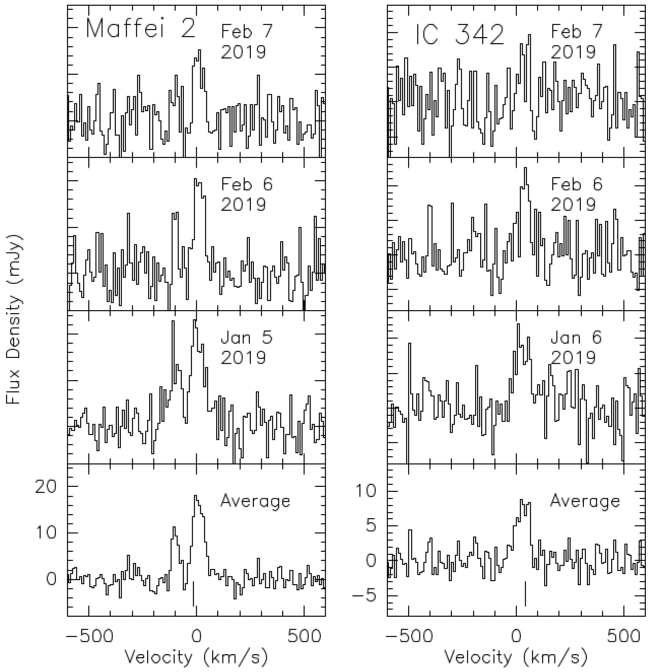

Figure 3.1: $4_{-1} \rightarrow 3_0$ E methanol spectra from Maffei 2 (left) and IC 342 (right). Spectra from a given source are all presented with the same amplitude and velocity scale. The adopted rest frequency is 36.169261 GHz, the coordinates are α_{J2000} = $2^{\mathrm{h}}\ 41^{\mathrm{m}}\ 55^{s}.2$, δ_{J2000} = $59^{\circ}\ 36'\ 12''$ (Maffei 2) and α_{J2000} = $3^{\mathrm{h}}\ 46^{\mathrm{m}}\ 48^{s}.6$, δ_{J2000} = $68^{\circ}\ 05'\ 46''$ (IC 342). The velocity scale is the local standard of rest. The spectra were smoothed by averaging 256 contiguous channels to a channel spacing of 9.7 km s^{-1}. The average spectrum was obtained, weighting individual subscans with the inverse square of their system temperature. The systemic local standard of rest velocity for Maffei 2 is –14±5 km s^{-1} and $V_{\mathrm{HEL}} = V_{\mathrm{LSR}}$ – 3.1 km s^{-1}. For IC 342, the corresponding values are +35±3 km s^{-1} and $V_{\mathrm{HEL}} = V_{\mathrm{LSR}}$ – 3.9 km s^{-1}. Vertical lines indicating the systemic velocities are included in the lower parts of the averaged spectra.

The 36 GHz methanol line of Maffei 2 is the second most luminous among the sources detected with certainty outside the Local Group of galaxies. This is not matched by the moderate infrared luminosity of Maffei 2. Higher-resolution data are required to check whether this is related to its prominent bar and associated shocks. Upper limits for M 82, NGC 4388, NGC 5728, and Arp 220 are also presented.

The previously reported detection of 36 GHz maser emission in Arp 220 is not confirmed. Nondetections are reported from the related class I 44 GHz ($\lambda \approx 0.7$ cm) methanol transition towards Maffei 2 and IC 342, indicating that this line is not stronger than its 36 GHz counterpart.

3.5 Conclusions

With Maffei 2 and IC 342 we present two 36 GHz class I methanol line emitters from galaxies outside the Local Group, while a previously reported detection of the ultraluminous infrared galaxy Arp 220 is not confirmed. The line luminosity of Maffei 2 is surprisingly high, which is possibly related to its prominent bar. As in the prototypical source NGC 253, upper limits indicate that the 44 GHz class I methanol line is not substantially stronger than its 36 GHz counterpart. Now there are five such well-confirmed sources with 36 GHz line detections beyond any reasonable doubt. In contrast to the two initially detected and still most prominent of these sources, NGC 253 and NGC 4945, it is difficult to directly prove that the detected signals from Maffei 2 and IC 342 (and NGC 6946) are caused by masers. The line profiles are compatible with those obtained from ammonia, where masers are rarely observed. Unlike NGC 253 and NGC 4945, which are starburst galaxies, the others are spiral galaxies that are about as active with respect to star formation as our Milky Way. Therefore, by analogy with the central part of our Galaxy, the most likely interpretation is that the detected features represent the superposition of a large number of spatially unresolved weak maser hotspots lacking a single dominant source. It is hard to imagine that more active galaxies, like for example NGC 253 and NGC 4945, do not also show such a population of weak masers. Therefore, a search for such a weak and broad underlying spatially widespread 36 GHz methanol emission would also be worthwhile in starburst galaxies, as well as interferometric studies with utmost sensitivity to unambiguously demonstrate that at least a part of the detected emission originates from maser sources. The latter would, however, be a very ambitious project, presumably only feasible with the future next-generation Very Large Array (ngVLA).

CHAPTER 4

Methanol masers in NGC 253 with ALCHEMI (Summary)

This chapter is a summary of the homologous article published in Astronomy and Astrophysics (A&A) under the reference code:

- P. K. Humire, C. Henkel, A. Hernández-Gómez, S. Martín, J. Mangum, N. Harada, S. Muller, K. Sakamoto, K. Tanaka, Y. Yoshimura, K. Nakanishi, S. Mühle, R. Herrero-Illana, D. S. Meier, E. Caux, R. Aladro, R. Mauersberger, S. Viti, L. Colzi, V. M. Rivilla, M. Gorski, K. M. Menten, K.-Y. Huang, S. Aalto, P. P. van der Werf, and K. L. Emig 2022A&A, 663A, 33H,

which is granted for non-exclusive right of republication by the author. The refereed article can be found in `https://doi.org/10.1051/0004-6361/202243384` and in the Appendix C of this document, while the fully open access ArXiv version is presented in `https://arxiv.org/pdf/2205.03281.pdf`.

4.1 Context

Methanol masers of Class I (collisionally pumped) and Class II (radiatively pumped) have been extensively studied in the Milky Way, where they are primarily associated with dense clumps, while the association with other potential tracers, like OH and H_2O, is less convincing (Billington et al., 2020). This demonstrates their usefulness to trace very recent massive star formation in dust embedded sources, something impossible at other wavelengths due to the high opacity (e.g., at optical and UV wavelengths). It is therefore expected that the study of methanol masers will increase in the years to come, accompanied by new facilities (e.g. MeerKat, FAST) and enhancements to those currently available such as the ngVLA and future ALMA cycles (Henkel et al., 2018).

Methanol possesses a large number of transitions at cm, sub-mm (see Fig. 1.10), and IR wavelengths (Schilke et al., 2001; Comito et al., 2005), a property that allows it to deliver information about the density and kinetic temperature of the ISM from where it is emitted. For example Leurini et al. (2007) found that the $J_2 \rightarrow J_1 - E$ transitions at ~25 GHz are sensitive to the density while the $2_k \rightarrow 1_k$ and the $5_k \rightarrow 4_k$ v_t =1 transitions (encompassing E– and A–CH_3OH types) at 96.5 and 241.2 GHz, respectively, are sensitive to the temperature. The methanol $J_{-1} \rightarrow (J-1)_0 - E$ line series has been found to mase at the interplay between the inner bar and spiral arms of nearby galaxies (Ellingsen et al., 2017; McCarthy et al., 2018b), highly perturbed regions where the gas is losing an important amount of angular momentum in order to move radially inwards through the bar or be stalled in a circumnuclear ring (Sellwood & Wilkinson, 1993).

In the Galaxy, Class II methanol masers are the strongest (e.g. Kalenskii et al., 2017), with the $5_1 \rightarrow 6_0 A^+$ transition at 6.7 GHz reaching flux densities of ∼5000 Jy (Menten, 1991a). In contrast, the strongest Galactic methanol maser transition of Class I type, the $7_0 \rightarrow 6_1 A^+$ line at 44 GHz, shows flux densities not higher than 800 Jy (Haschick et al., 1990). It is therefore interesting that Class I methanol masers remained as the only ones observed beyond the Local Group since their first dectection at 36 GHz in NGC 253 (Ellingsen et al., 2014) during eight years until a first tentative detection of a Class II methanol maser at 6.7 GHz by Chen et al. (2022).

4.2 Aims

NGC 253 is the extragalactic object beyond the Local Group where most methanol maser transitions have been reported so far, as can be inferred from Table 4.1. Contrary to what occurs in our own Galaxy, collisionally-pumped Class I methanol masers should be stronger than the radiatively-pumped Class II. This finding indicates that, at least at large scales, shocks conform the best phenomena to produce masers orders of magnitude stronger than in the Milky Way (Ellingsen et al., 2014; Chen et al., 2022). Within the Class I type, extragalactic maser detections have been achieved in two line series: The $J_0 \rightarrow (J-1)_1 - A$ and the $J_{-1} \rightarrow (J-1)_0 - E$ methanol line series. Contrary to the Class II sources, a significant continuum radiation level at mm wavelengths is not required to pump Class I methanol masers (e.g., Zeng et al., 2020).

While conditions for maser emission have been investigated early by theoretical studies (e.g. Cragg et al., 1992), an observational characterization is more difficult to achieve due to large telescope beams employed to observe small maser spots. Single dish observations produce beam dilution and subsequent intensity underestimations. Interferometric observations, on the other hand, can provide better estimations of maser spot sizes and intensities, with extended quasi-thermal emission being partially filtered out (Leurini et al., 2016; Cicone et al., 2021).

The main goal of this project is to search for methanol masers in the nuclear region of the nearby starburst galaxy NGC 253 using unprecedented synergy of frequency coverage, sensitivity, angular, and spectral resolution available from ALMA observations through the ALCHEMI collaboration (Martín et al., 2021). This will allow us to search for methanol maser transitions at higher frequencies than before in a target beyond the Local Group, and also to confirm previous detections. We also aim at deciphering the conditions where these masers are produced.

4.3 Methods

Covering a frequency range between 84 and 373 GHz (λ = 3.6 to 0.8 mm) at high angular (1.6"∼27 pc) and spectral (∼8–9 km s^{-1}) resolution with the ALMA large program ALCHEMI, we have probed different regions across the CMZ of NGC 253. The observed spectra from these regions are presented in Fig. 4.1. In this Figure we also show the atmospheric transmission calculated from the model developed by Pardo et al. (2001) and related works [1]. The model inputs represent in a good approximation the

---

[1] `https://cab.inta-csic.es/users/jrpardo/class_atm.html`

ambient conditions at the Chajnantor plain: a temperature of 270 K, a pressure of 560 millibar, a humidity of 20%, an altitude of 5000 m, and a precipitable water vapor column of 0.8 mm.

In order to look for methanol maser candidates, we employed the rotation diagram method and a set of radiative transfer models in each of the 10 regions presented in Fig. 4.1. We further separate between methanol A and E types, given their different transition frequencies and the possibility that they may arise in different physical environments.

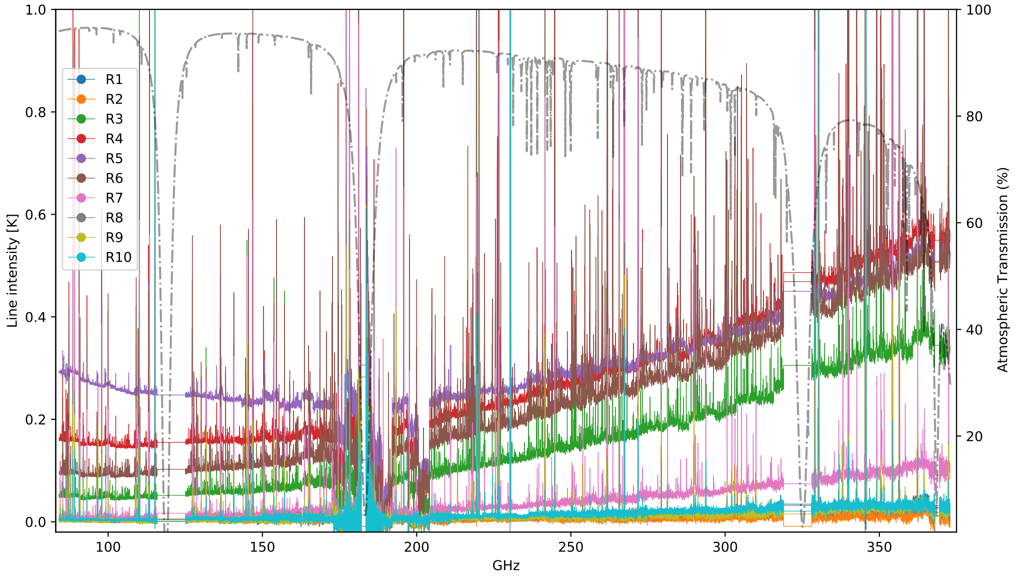

Figure 4.1: ALCHEMI spectra from 10 selected regions (see Table 1 of Appendix C) inside NGC 253's CMZ. The atmospheric transmission (dash-dotted gray lines) was calculated following the ATM model from Pardo et al. (2001), see Sect. 4.3 for model input parameters.

4.4 Results

We detect for the first time masers above 84 GHz in NGC 253, covering an ample portion of the $J_{-1} \rightarrow (J-1)_0 - E$ line series (at 84, 132, 229, and 278 GHz) and the $J_0 \rightarrow (J-1)_1 - A$ series (at 95, 146, and 198 GHz). This increases the number of methanol maser transitions in extragalactic objects from 5 to 11, as indicated in Table 4.1. We confirm the presence of the Class I maser line at 84 GHz, already reported by McCarthy et al. (2018b) but now being detected in more than one location. For the $J_{-1} \rightarrow (J-1)_0 - E$ line series, we observe a lack of Class I maser candidates in the central star-forming disk.

Table 4.1: Methanol masers in extragalactic objects

MM[a] transition (frequency)	Detected in	Class	reference(s) (first detection(s) only)
$5_1 \rightarrow 6_0 A^+$ (6.7 GHz)	LMC[b], M 31, Maffei 2(?)	II	(Sinclair et al., 1992; Sjouwerman et al., 2010; Chen et al., 2022)
$2_0 \rightarrow 3_{-1} E$ (12.1 GHz)	LMC	II	(Ellingsen et al., 2010)
$4_{-1} \rightarrow 3_0 E$ (36.2 GHz)	NGC 253, NGC 4945, IC342, NGC 6946, Maffei 2	I	(Ellingsen et al., 2014; McCarthy et al., 2017; Gorski et al., 2018; Humire et al., 2020a)
$7_0 \rightarrow 6_1 A^+$ (44.1 GHz)	NGC 253	I	(Ellingsen et al., 2017)
$5_{-1} \rightarrow 4_0 E$ (84.5 GHz)	NGC 253	I	(McCarthy et al., 2018b), Appendix C
$8_0 \rightarrow 7_1 A^+$ (95.1 GHz)	NGC 253	I	Appendix C
$6_{-1} \rightarrow 5_0 E$ (132.9 GHz)	NGC 253	I	Appendix C
$9_0 \rightarrow 8_1 A^+$ (146.6 GHz)	NGC 253	I	Appendix C
$10_0 \rightarrow 9_1 A^+$ (198.4 GHz)	NGC 253	I	Appendix C
$8_{-1} \rightarrow 7_0 E$ (229.8 GHz)	NGC 253	I	Appendix C
$9_{-1} \rightarrow 8_0 E$ (278.3 GHz)	NGC 253	I	Appendix C

Notes: [a] Methanol maser. [b] Large Magellanic Cloud.

4.5 Conclusions

The physical conditions for maser excitation in the $J_{-1} \rightarrow (J-1)_0 - E$ line series can be weak shocks and cloud-cloud collisions as suggested by shock tracers (SiO and HNCO) located in the outskirts of the CMZ. On the other hand, the presence of photodissociation regions due to a high star-formation rate would be needed to explain the lack of Class I masers in the very central regions.

CHAPTER 5

Concluding remarks and Outlook

5.1 Conclusions

Through the sub-millimeter (sub-mm) perspective of the central molecular zone (CMZ) of both our Galaxy (inner ~400 pc in diameter) and nearby galaxies such as Maffei 2 (inner ~850 pc) or NGC 253 (inner ~500 pc), to name a few, it is possible to unveil a largely unexplored side of the universe. One of the advantages that the radio and sub-mm regimes offer over other spectral windows is their immense frequency coverage available from Earth-based facilities. Sensitive facilities such as ALMA, NOEMA, and the IRAM 30 m telescope are making the detection of new molecules routine. Another advantage is the degree of depth at which radio wavelengths can emerge, allowing us to trace infalling material in the inner layers of molecular clouds. The sub-mm regime is also a privileged window where we can witness the rotational and vibrational movement of molecules embedded in the cold universe, at temperatures as low as 5–10 K. This is especially gratifying when we consider that the ionized gas detected by optical mirrors traces only one part in 10^{5-7} with respect to the cold material detected by radio and (sub-)millimeter antennas (Dale et al., 2005), in terms of mass. On the other hand, the detailed knowledge of the physical and chemical properties of molecules, on a quantum mechanical level, allows us to determine the conditions of the interstellar (ISM) and intergalactic medium (IGM), where these molecules emit or absorb radiation. Finally, thanks to aperture synthesis, unbeatable resolutions of a few μarcsec. are reachable. All of the above allows radio astronomers a better understanding of the universe, which complements the knowledge reached from other frequency regimes of the electromagnetic spectrum.

Based on previous findings related to sulfur bearing species complemented with updated trends of carbon ^{12}C/^{13}C ratios across the Galactic disk, the first part of this thesis, as presented in Appendix A, resulted in the discovery that the decreasing trend of ^{32}S/^{34}S ratios toward the Galaxy nucleus is halted somewhere between ~130 pc and 1 kpc from the Galactic center (GC) and increases in the nuclear ($\lesssim$130 pc) region (see Fig. 2.2). Since the ^{32}S/^{34}S ratio is inversely proportional to the metallicity, our results, summarized in Table 5.1, can be understood in the sense that the metallicity in the Galactic CMZ is similar to the large-scale disk at ~4–7 kpc from the nucleus (Fig. 1.8). This seems to contradict the widely accepted framework where our Galaxy forms initially in the GC and then grew up in diameter, something known as the inside-out growth scenario with rising isotope ratios in case of primary versus secondary nuclei with rising galactocentric radius.

The enrichment for most metals in the ISM mainly comes from massive star yields through supernovae type II events. It is thus surprising that a region such as the CMZ, with massive star formation, presents a metallicity similar to the one supposedly much younger solar vicinity (Kovtyukh et al., 2019). It may be that a hypothetical SN Type II prior to our Sun, and therefore the reason for the current solar chemical abundances (Cameron & Truran, 1977; Cook et al., 2021; Boss, 2022), conforms best to the conditions in the CMZ, leading to similar metallicities. However, this latter still does not explain the decreasing trend of ^{32}S/^{34}S from 9 down to 1 kpc from the GC, as summarized in our Fig. 1.6, adapted from Humire et al. (2020b).

It can be that cloud-cloud collisions constitute the preferred way to produce massive stars at the outskirts of the CMZ (~200 pc). These collisions are expected to lie at x_1/x_2 orbit interactions and also around the outer Lindblad resonance, at ~4 kpc from the GC, where the Galactic bar ends (e.g., Benjamin et al., 2005). Therefore, this last option would increase the observed ^{34}S abundance toward lower distances from the CMZ. Following the evidence in favor of bars channeling material toward the inner regions (see, e.g., Sect. 3.2 in Henshaw et al., 2022), we can reconcile that, further into the Galactic nucleus, the lack of resonances and cloud-cloud collisions may show up as an ISM environment resulting from the mixed material fueled by the bar. This will result in a chemical composition, namely ^{32}S/^{34}S ratios, in between the one observed at ~4 kpc and more distant regions ($> D_{\rm GC}$), explaining what we observe in Fig. 5 of Humire et al. (2020b). This latter should also lead to a high dispersion, including lower ^{32}S/^{34}S ratios that the ones reported by us in the CMZ, something that agrees with later findings (Yang, Y. T., submitted).

Another frame to account for the higher-than-expected ^{32}S/^{34}S ratios in the CMZ comes from considerations of the dust in the inner Galactic regions; that is to say, the CMZ is expected to have metal-richer dust grains compared to the Galactic Disk. This is due to a larger number of stars that did explode over the years, releasing metals to the ISM. Those metals, such as iron or silicon, are preferably bonded to dust over the gas. Our CMZ observations presented in Humire et al. (2020b) can then be affected by high amounts of iron in that region. If that is the case, oxygen metallicities ([O/H]) should be similar to iron ones ([Fe/H]). Unfortunately, oxygen measures in the CMZ are scarce (e.g., Mollá et al., 2019), and only a single point in the [O/H] vs. $D_{\rm GC}$ plot (see Fig. 6 in Wenger et al. 2019) agrees with distribution of [Fe/H] vs. $D_{\rm GC}$ (Fig. 1.8).

Finally, an alternative –albeit less likely– explanation would be that the CMZ, being older than the rest of the Galaxy, has consumed its fuel to produce massive stars. The reduction of massive stars compared to previous times will lead to a more than expected bottom heavy initial mass function, decreasing the amount of ^{34}S if the chemical memory of sulfur is short enough. The variation in the number of massive stars at galaxy nuclei is possibly a cyclic process, as observed in more evolved/lenticular systems (Allard et al., 2006).

A good method to trace collisions, such as the ones produced by x_1/x_2 orbit interactions, consists in the search for Class I methanol masers. Examples of them have been found at the outskirts of the CMZs of external galaxies, where they possess luminosities tens to thousand of times higher than their Galactic analogous. However, there are not many objects known to host methanol masers beyond the Local Group. It is thus important to extend the sample and that was the aim of our work presented in Appendix B, where we extended the number of galaxies undoubtedly known to host Class I methanol maser beyond the Local Group from 5 to 6 (this considering that the methanol maser in NGC 1068 (Wang et al., 2014) would be real). That is, previous to this thesis methanol masers were found with certainty in NGC 253, NGC 4945, NGC 6946, and IC 342, only. Thanks to our observations with the Effelsberg telescope, now the sample also includes Maffei 2.

In our initial search for extragalactic Class I methanol maser emission, we have detected the

Table 5.1: Isotopic ratios of sulfur. Data taken from Mauersberger et al. (2004), Müller et al. (2006), and Appendix A (in boldface). For ^{32}S/^{33}S we have taken the product of our measured ^{32}S/^{34}S and ^{34}S/^{33}S ratios.

Region	^{32}S/^{34}S	^{32}S/^{33}S	^{32}S/^{36}S	^{34}S/^{33}S	^{34}S/^{36}S
Solar system	22.64(0.00)	126.95(0.05)	6519(20)	5.606(0.002)	288(1)
Galactic center	$16.3^{+2.1}_{-1.7}$	$70.1^{+12.7}_{-10.2}$	–	4.3(0.2)	–
Local ISM	19(8)	–	–	–	–
ISM	24.4(5)	~150	3280(760)	6.3(1)	115(17)
IRC+10216	21.8(2.6)	121(15)	2700(600)	5.6(.3)	107(15)
z=0.89	10±1	–	–	–	–
LMC	18±6	–	–	–	–
NGC 253	8±2	–	–	–	–
NGC 4945	13.5±2.5	–	–	–	–

$4_{-1} \rightarrow 3_0 - E$ transition at 36 GHz likely to be masing in Maffei 2 and IC 342, and provided upper limits for the $7_0 \rightarrow 6_1 - A^+$ transition at 44 GHz in these targets. The most likely explanation for this, following previous studies in NGC 253 with the same results, is that the transition at 44 GHz may arise from more confined regions than the ones at 36 GHz, given that A−CH$_3$OH (e.g. at 44 GHz) needs higher temperatures than E−CH$_3$OH (e.g., at 36 GHz) to mase (Pratap et al., 2008).

Another explanation for the lack of maser emission at 44 GHz is that lines belonging to the $J_0 \rightarrow (J-1)_1 - A^+$ series are pumped by a different mechanism than the ones in the $J_{-1} \rightarrow (J-1)_0 - E$ line series (e.g., the methanol line at 36 GHz). It can be that the lines conforming the first series, such as the one at 44 GHz, require a minimum level of continuum emission to be inverted, in addition to collisional excitation. Following this argument, the lines at 36 GHz, detected to mase for a region devoid of an appreciable radio continuum (e.g., Zeng et al., 2020), would show a higher number of maser spots at the bar edges of Maffei 2 and IC 342, allowing its detection with single-dish facilities. On the other hand, the line at 44 GHz would be less widespread and its components less numerous, being smeared out in the telescope beam. Furthermore, E–type methanol transitions quench faster at increasing densities compared to its A relatives (McEwen et al., 2014), and masers in the $J_0 \rightarrow (J-1)_1 - A^+$ are known to emerge at higher gas temperatures ($T_{\rm kin} = 80 - 200$ K) and densities than those in the $J_{-1} \rightarrow (J-1)_0 - E$ line series ($T_{\rm kin} < 100$ K) (Pratap et al., 2008). The latter provides a good explanation for the ubiquitous detection of maser action in the $8_0 \rightarrow 7_1 - A^+$ transition at 95 GHz in the CMZ of NGC 253, including regions where $J_{-1} \rightarrow (J-1)_0 - E$ transitions are thermal (Humire et al., 2022).

The following work, using interferometric observations of NGC 253, may give us clues that this explanation is incorrect, or at least not enlightening. Utilizing an ample frequency coverage, from 84 GHz until 274 GHz, we were able to detect many transitions in the $J_{-1} \rightarrow (J-1)_0 - E$ line series (at 84, 132, 229, and 278 GHz) and the $J_0 \rightarrow (J-1)_1 - A$ series (at 95, 146, and 198 GHz). This extends the amount of methanol maser transitions detected in external galaxies from 5 to 11, paving the way to future radiative transfer modeling capable to extract the environmental conditions in which this amplification occurs.

Connecting this with the previous results in Maffei 2 and IC 342, we do detect maser emission in the $J_0 \rightarrow (J-1)_1 - A$ series, and we find this series to be more equally distributed along the CMZ of NGC 253 than the $J_{-1} \rightarrow (J-1)_0 - E$ line series. For example, the $8_0 \rightarrow 7_1 - A^+$ transition at 95 GHz is observed both in the nuclear regions as well as at the outskirts of the CMZ of NGC 253. On the other hand, all the transition lines belonging to the $J_{-1} \rightarrow (J-1)_0 - E$ line series are masing in the outskirts of the CMZ only, under a mean sensitivity of 14.8 mK (Martín et al., 2021). Additionally, the $9_0 \longrightarrow 8_1 - A^+$ transition line at 146 GHz is the one that differs the most from local thermodynamic equilibrium (LTE) among the studied maser transitions conditions. This is measured in a region (region 1; see Appendix C) strongly affected by weak collisions (Meier et al., 2015) and devoid of a strong sub-mm continuum and stellar formation (Bendo et al., 2015).

We also found that the inner ∼100 pc of the CMZ of NGC 253 possess stronger shocks than its outskirts. The detection of masers in the $J_0 \longrightarrow (J-1)_1 - A$ line series also in these nuclear regions may indicate a greater resistance to these more violent conditions in comparison with the $J_{-1} \longrightarrow (J-1)_0 - E$ line series.

We can conclude from the above that maser emission in the $J_{-1} \longrightarrow (J-1)_0 - E$ line series depends strongly on weak gas collisions such as cloud-cloud interactions, similar to those observed at the interface between x_1 and x_2 orbits in the CMZ of our Galaxy. Given that extragalactic Class I methanol masers are stronger than their Galactic counterparts, weak shocks at the edges of the CMZ of galaxies arise as one of the best pumping mechanisms for methanol masers.

5.2 Outlook

We find that the decreasing trend of ^{32}S/^{34}S ratios stops at a distance of 1 kpc or less from the Galactic center. This ratio is inversely proportional to the metallicity measured through iron (Eq. 1.12) and may indicate a lack of metal-rich massive stars in the Galactic center as compared to regions located toward the outer half of the large-scale Galactic bar (∼3–5 kpc; see Wegg et al. 2015 for bar extension and the ^{32}S/^{34}S slope presented in Fig. 2.2). On the other hand, the CMZ ^{32}S/^{34}S ratios are similar to the ones measured at 5–7 kpc from the GC. Further away, the ^{32}S/^{34}S ratios increase up to values of about 20–30, indicating lower metallicities in agreemen with [Fe/H] (Kovtyukh et al., 2019).

Many open questions emerge from our findings. For example: Is there a connection between the CMZ and regions just outside the galactic bar? Is the bar transferring material from its outskirts to the CMZ? Is the ^{32}S/^{34}S behavior similar in other galaxies? Would the presence or absence of bars and their strength affect the distribution of massive stars? How is this ratio distributed across starbursts and quiescent galaxies in the Local Group? How does this isotope ratio change over cosmological scales?

Among Class I methanol masers, the transitions belonging to the $J_{-1} \longrightarrow (J-1)_0 - E$ line series are highly dependent on collisions and are exclusively located at the edges of the CMZ of NGC 253. Further studies are required to check this in other environments, such as more quiescent galaxies like Maffei 2 and IC 342. Now that we know the presence of Class I methanol maser emission at 36 GHz ($J=4$) in these two galaxies (Gorski et al., 2018; Chen et al., 2022), one step forward would be to detect maser emission at higher resolution. If the disposition of maser spots is confirmed to also be at the CMZ outskirts of galaxies, independently of their star formation rate (SFR), the detection of Class I masers in the $J_{-1} \longrightarrow (J-1)_0 - E$ family can be used to trace the edges of the CMZ of nearby galaxies. Connecting this to the sulfur ratios, it would be possible to additionally check for a dip in the ^{32}S/^{34}S ratios at the outer limits of extragalactic CMZs. Although the more reliable isotopologues to obtain the ^{32}S/^{34}S ratio, namely ^{13}C^{32}S and ^{13}C^{34}S, are hardly detected above the noise level obtainable for external galaxies, making use of the double isotopologue method: $\frac{^{12}\mathrm{C}}{^{13}\mathrm{C}} \times \frac{^{13}\mathrm{C}^{32}\mathrm{S}}{^{12}\mathrm{C}^{34}\mathrm{S}}$ we will likely obtain similar results, given the low fractionation level of sulfur (as demonstrated in Appendix A). The application of the double isotopologue method will constitute a useful tool for the determination of extragalactic sulfur isotopologue ratios.

As mentioned earlier, the nuclear region of NGC 253 shows a high level of line confusion. This issue was especially harmful when we required a clear distinction between thermal and maser lines in the spectral domain. The clearest example of this is the largely unexplored methanol $7_{-1} \rightarrow 6_0 - E$ transition at 181.295 GHz (see Subsect. 4.2.2 in Appendix C), which belongs to the $J_{-1} \rightarrow (J-1)_0 - E$ line series. This series seems prone to mase in soft-shock and moderate UV radiation environments (see discussion in Appendix C). While all the other transitions covered by ALCHEMI in this line series are masing (Fig. 5 in Appendix C), the line at 181.295 GHz is completely blended by the J =2–1 HNC line at 181.324 GHz. According to our detailed non-LTE model in region 8 (Appendix C, complementary material), this transition has a negative optical depth (-2.4). The above mentioned arguments leave little doubt about the maser status of the $7_{-1} \rightarrow 6_0 - E$ transition.

As suggested by Zeng et al. (2018), and references therein (see also Sect.1.3.1 and Appendix D.3), the G+0.693-0.027 Galactic quiescent cloud has similar characteristics to those found at the edges of the CMZ of NGC 253. This is a good motivation to explore in this object the same relations observed in one of the closest nuclear starbursts, among other things, the appearance of Class I masers in regions with soft shocks and a moderate cosmic ray ionization rate (CRIR). The higher spectral and spatial resolution achievable in Galactic objects should be enough to spectrally distinguish between J =2–1 HNC and the $7_{-1} \rightarrow 6_0 - E$ CH_3OH transition lines. With the avoidance of strong beam smearing, radiative transfer models performed for G+0.693-0.027 will finally unveil the conditions required to pump Class I methanol masers[1], explaining, for instance, why these are stronger than Class II methanol masers in extragalactic objects.

Although photodissociation may be one of the main reasons why methanol masers are not observed in the central regions of NGC 253, thermal transitions of CH_3OH show a higher column density there. Fractional abundance calculations might shed light on this, indicating whether methanol is effectively more abundant there or not.

---

[1] at least those in the $J_{-1} \rightarrow (J-1)_0 - E$ line series

Bibliography

Aharonian F., Yang R., de Oña Wilhelmi E., 2019, Nature Astronomy, 3, 561

Aladro R., Martín-Pintado J., Martín S., Mauersberger R., Bayet E., 2011, A&A, 525, A89

Alissandrakis C. E., Bastian T. S., Nindos A., 2022, A&A, 661, L4

Allard E. L., Knapen J. H., Peletier R. F., Sarzi M., 2006, MNRAS, 371, 1087

Allen V., van der Tak F. F. S., Walsh C., 2018, A&A, 616, A67

Anand G. S., Tully R. B., Rizzi L., Karachentsev I. D., 2019, ApJL, 872, L4

Anderson J. P., James P. A., 2009, MNRAS, 399, 559

André P., Ward-Thompson D., Barsony M., 1993, ApJ, 406, 122

André P., Könyves V., Arzoumanian D., Palmeirim P., 2014, in The Labyrinth of Star Formation. p. 225, doi:10.1007/978-3-319-03041-8_43

Ao Y., et al., 2013, A&A, 550, A135

Armstrong J. T., Barrett A. H., 1985, ApJS, 57, 535

Arnett W. D., 1974, ApJ, 194, 373

Baan W. A., An T., Henkel C., Imai H., Kostenko V., Sobolev A., 2022, Nature Astronomy,

Bagdonaite J., Daprà M., Jansen P., Bethlem H. L., Ubachs W., Muller S., Henkel C., Menten K. M., 2013, Phys. Rev. Lett., 111, 231101

Ball J. A., Gottlieb C. A., Lilley A. E., Radford H. E., 1970, ApJL, 162, L203

Bally J., Stark A. A., Wilson R. W., Henkel C., 1988, ApJ, 324, 223

Barrett A. H., Schwartz P. R., Waters J. W., 1971, ApJL, 168, L101

Batrla W., Matthews H. E., Menten K. M., Walmsley C. M., 1987, Nature, 326, 49

Bayet E., Aladro R., Martín S., Viti S., Martín-Pintado J., 2009, ApJ, 707, 126

Bayet E., Williams D. A., Hartquist T. W., Viti S., 2011, MNRAS, 414, 1583

Beasley A. J., Ellingsen S. P., Claussen M. J., Wilcots E., 1996, ApJ, 459, 600

Beck R., 2015, A&A, 578, A93

Becklin E. E., Gatley I., Matthews K., Neugebauer G., Sellgren K., Werner M. W., Wynn-Williams C. G., 1980, ApJ, 236, 441

Belloche A., Müller H. S. P., Menten K. M., Schilke P., Comito C., 2013, A&A, 559, A47

Belloche A., Müller H. S. P., Garrod R. T., Menten K. M., 2016, A&A, 587, A91

Belloche A., Garrod R. T., Müller H. S. P., Menten K. M., Medvedev I., Thomas J., Kisiel Z., 2019, A&A, 628, A10

Bendo G. J., Beswick R. J., D'Cruze M. J., Dickinson C., Fuller G. A., Muxlow T. W. B., 2015, MNRAS, 450, L80

Benjamin R. A., et al., 2005, ApJL, 630, L149

Billington S. J., et al., 2019, MNRAS, 490, 2779

Billington S. J., et al., 2020, MNRAS, 499, 2744

Böker T., Falcón-Barroso J., Schinnerer E., Knapen J. H., Ryder S., 2008, AJ, 135, 479

Bolatto A. D., et al., 2013, Nature, 499, 450

Bonfand M., Belloche A., Menten K. M., Garrod R. T., Müller H. S. P., 2017, A&A, 604, A60

Bonnell I. A., Clarke C. J., Bate M. R., Pringle J. E., 2001, MNRAS, 324, 573

Boss A. P., 2022, ApJ, 933, 1

Bouscasse L., Csengeri T., Belloche A., Wyrowski F., Bontemps S., Güsten R., Menten K. M., 2022, A&A, 662, A32

Bovy J., et al., 2014, ApJ, 790, 127

Breen S. L., Ellingsen S. P., Contreras Y., Green J. A., Caswell J. L., Stevens J. B., Dawson J. R., Voronkov M. A., 2013, MNRAS, 435, 524

Breen S. L., Contreras Y., Dawson J. R., Ellingsen S. P., Voronkov M. A., McCarthy T. P., 2019, MNRAS, 484, 5072

Brogan C. L., et al., 2019, ApJL, 881, L39

Burrows A., et al., 1997, ApJ, 491, 856

Cameron A. G. W., Truran J. W., 1977, Icarus, 30, 447

Carey S. J., et al., 2009, PASP, 121, 76

Carter M., et al., 2012, A&A, 538, A89

Caswell J. L., et al., 2010, MNRAS, 404, 1029

Ceccarelli C., 2004, in Johnstone D., Adams F. C., Lin D. N. C., Neufeeld D. A., Ostriker E. C., eds, Astronomical Society of the Pacific Conference Series Vol. 323, Star Formation in the Interstellar Medium: In Honor of David Hollenbach. p. 195

Chabrier G., Baraffe I., 2000, ARA&A, 38, 337

Chen X., Ellingsen S. P., Baan W. A., Qiao H.-H., Li J., An T., Breen S. L., 2015, ApJL, 800, L2

Chen X., Ellingsen S. P., Shen Z.-Q., McCarthy T. P., Zhong W.-Y., Deng H., 2018, ApJL, 856, L35

Chen X., et al., 2020a, Nature Astronomy, 4, 1170

Chen X., et al., 2020b, ApJL, 890, L22

Chen J. L., et al., 2021, ApJS, 257, 39

Chen X., Yang T., Ellingsen S. P., McCarthy T. P., Ren Z.-Y., 2022, ApJ, 926, 48

Chevance M., et al., 2022, MNRAS, 509, 272

Chin Y. N., Henkel C., Whiteoak J. B., Langer N., Churchwell E. B., 1996, A&A, 305, 960

Churchwell E., et al., 2009, PASP, 121, 213

Cicone C., et al., 2014, A&A, 562, A21

Cicone C., et al., 2021, A&A, 654, L8

Clayton D., 2007, Handbook of Isotopes in the Cosmos. Cambridge Planetary Science

Cohen D. P., Turner J. L., Consiglio S. M., 2020, MNRAS, 493, 627

Comito C., Schilke P., Phillips T. G., Lis D. C., Motte F., Mehringer D., 2005, ApJS, 156, 127

Cook D. L., Meyer B. S., Schönbächler M., 2021, ApJ, 917, 59

Cotton W. D., Yusef-Zadeh F., 2016, ApJS, 227, 10

Cragg D. M., Johns K. P., Godfrey P. D., Brown R. D., 1992, MNRAS, 259, 203

Cragg D. M., Sobolev A. M., Godfrey P. D., 2005, MNRAS, 360, 533

Cyganowski C. J., Brogan C. L., Hunter T. R., Churchwell E., 2009, ApJ, 702, 1615

Cyganowski C. J., Hannaway D., Brogan C. L., Hunter T. R., Zhang Q., 2018, in Tarchi A., Reid M. J., Castangia P., eds, Vol. 336, Astrophysical Masers: Unlocking the Mysteries of the Universe. pp 281–282, doi:10.1017/S1743921317010717

Dahmen G., Huttemeister S., Wilson T. L., Mauersberger R., 1998, A&A, 331, 959

Dale D. A., Sheth K., Helou G., Regan M. W., Hüttemeister S., 2005, AJ, 129, 2197

Dale D. A., et al., 2009, ApJ, 703, 517

Dale J. E., Kruijssen J. M. D., Longmore S. N., 2019, MNRAS, 486, 3307

Darling J., Goldsmith P., Li D., Giovanelli R., 2003, AJ, 125, 1177

Davies B., Origlia L., Kudritzki R.-P., Figer D. F., Rich R. M., Najarro F., 2009, ApJ, 694, 46

Destree J. D., Snow T. P., Black J. H., 2009, ApJ, 693, 804

van Dishoeck E. F., Blake G. A., 1998, ARA&A, 36, 317

Domínguez Sánchez H., et al., 2011, MNRAS, 417, 900

Dos Santos P. M., Lepine J. R. D., 1979, Nature, 278, 34

Draine B. T., 2011. Princeton University Press

Drdla K., Knapp G. R., van Dishoeck E. F., 1989, ApJ, 345, 815

Duan Y.-B., McCoy A., 2001, Quantum Mechanical Simulation of Vibration-Torsion-Rotation Levels of Methanol. Springer Berlin Heidelberg, Berlin, Heidelberg

Duan Y.-B., Wang R., Mukhopadhyay I., 2002, Chemical Physics, 280, 119

Ekström S., 2021, Frontiers in Astronomy and Space Sciences, 8, 53

Ellingsen S. P., 2006, ApJ, 638, 241

Ellingsen S. P., Norris R. P., Whiteoak J. B., Vaile R. A., McCulloch P. M., Price M. G., 1994a, MNRAS, 267, 510

Ellingsen S. P., Whiteoak J. B., Norris R. P., Caswell J. L., Vaile R. A., 1994b, MNRAS, 269, 1019

Ellingsen S. P., Voronkov M. A., Cragg D. M., Sobolev A. M., Breen S. L., Godfrey P. D., 2007, in Chapman J. M., Baan W. A., eds, Vol. 242, Astrophysical Masers and their Environments. pp 213–217 (`arXiv:0705.2906`), doi:10.1017/S1743921307012999

Ellingsen S. P., Breen S. L., Caswell J. L., Quinn L. J., Fuller G. A., 2010, MNRAS, 404, 779

Ellingsen S. P., Breen S. L., Voronkov M. A., Caswell J. L., Chen X., Titmarsh A., 2012, arXiv e-prints, p. arXiv:1210.2139

Ellingsen S. P., Chen X., Qiao H.-H., Baan W., An T., Li J., Breen S. L., 2014, ApJL, 790, L28

Ellingsen S. P., Chen X., Breen S. L., Qiao H. H., 2017, MNRAS, 472, 604

Engels D., 1979, A&AS, 36, 337

Esplugues G. B., Viti S., Goicoechea J. R., Cernicharo J., 2014, A&A, 567, A95

Evans Neal J. I., 1999, ARA&A, 37, 311

Evans Neal I., 2003, in Curry C. L., Fich M., eds, SFChem 2002: Chemistry as a Diagnostic of Star Formation. p. 157 (`arXiv:astro-ph/0211526`)

Ferrière K., 2012, A&A, 540, A50

Figer D. F., et al., 2002, ApJ, 581, 258

Fingerhut R. L., Lee H., McCall M. L., Richer M. G., 2007, ApJ, 655, 814

Fish V. L., Muehlbrad T. C., Pratap P., Sjouwerman L. O., Strelnitski V., Pihlström Y. M., Bourke T. L., 2011, ApJ, 729, 14

Fontani F., Commerçon B., Giannetti A., Beltrán M. T., Sánchez-Monge Á., Testi L., Brand J., Tan J. C., 2018, A&A, 615, A94

Forrey R. C., Babb J. F., Stancil P. C., McLaughlin B. M., 2018, MNRAS, 479, 4727

Friberg P., Madden S. C., Hjalmarson A., Irvine W. M., 1988, A&A, 195, 281

Genovali K., et al., 2014, A&A, 566, A37

Ginsburg A., Goddi C., 2019, AJ, 158, 208

Ginsburg A., et al., 2016, A&A, 586, A50

Ginsburg A., et al., 2018, ApJ, 853, 171

Goldsmith P. F., Langer W. D., 1999, ApJ, 517, 209

Gómez-Ruiz A. I., et al., 2015, MNRAS, 446, 3346

Gómez J. L., et al., 2022, ApJ, 924, 122

Gorski M., Ott J., Rand R., Meier D. S., Momjian E., Schinnerer E., 2017, ApJ, 842, 124

Gorski M., Ott J., Rand R., Meier D. S., Momjian E., Schinnerer E., 2018, ApJ, 856, 134

Gorski M. D., Ott J., Rand R., Meier D. S., Momjian E., Schinnerer E., Ellingsen S. P., 2019, MNRAS, 483, 5434

Green J. A., et al., 2008, MNRAS, 385, 948

Greene T., 2001, American Scientist, 89, 316

Greene T. P., Wilking B. A., André P., Young E. T., Lada C. J., 1994, ApJ, 434, 614

Grudić M. Y., Hopkins P. F., Faucher-Giguère C.-A., Quataert E., Murray N., Kereš D., 2018, MNRAS, 475, 3511

Güsten R., Henkel C., 1983, A&A, 125, 136

Güsten R., Walmsley C. M., Ungerechts H., Churchwell E., 1985, A&A, 142, 381

Güsten R., Nyman L. Å., Schilke P., Menten K., Cesarsky C., Booth R., 2006, A&A, 454, L13

Haasler D., et al., 2022, A&A, 659, A158

Hakobyan A. A., Mamon G. A., Petrosian A. R., Kunth D., Turatto M., 2009, A&A, 508, 1259

Halfen D. T., Woolf N. J., Ziurys L. M., 2017, ApJ, 845, 158

Harada N., Sakamoto K., Martín S., Watanabe Y., Aladro R., Riquelme D., Hirota A., 2019, ApJ, 884, 100

Harada N., et al., 2021, ApJ, 923, 24

Haschick A. D., Baan W. A., 1993, ApJ, 410, 663

Haschick A. D., Menten K. M., Baan W. A., 1990, ApJ, 354, 556

Hastings W. K., 1970, Biometrika, 57, 97

Hatchfield H. P., Sormani M. C., Tress R. G., Battersby C., Smith R. J., Glover S. C. O., Klessen R. S., 2021, ApJ, 922, 79

Hawkins I., Jura M., 1987, ApJ, 317, 926

Henkel C., Jacq T., Mauersberger R., Menten K. M., Steppe H., 1987, A&A, 188, L1

Henkel C., Mauersberger R., Peck A. B., Falcke H., Hagiwara Y., 2000, A&A, 361, L45

Henkel C., Tarchi A., Menten K. M., Peck A. B., 2004, A&A, 414, 117

Henkel C., Greene J. E., Kamali F., 2018, in Tarchi A., Reid M. J., Castangia P., eds, Vol. 336, Astrophysical Masers: Unlocking the Mysteries of the Universe. pp 69–79 (`arXiv:1802.04727`), doi:10.1017/S1743921318000753

Henry R. B. C., Worthey G., 1999, PASP, 111, 919

Henshaw J. D., et al., 2016, MNRAS, 457, 2675

Henshaw J. D., Barnes A. T., Battersby C., Ginsburg A., Sormani M. C., Walker D. L., 2022, arXiv e-prints, p. arXiv:2203.11223

Herbst E., van Dishoeck E. F., 2009, ARA&A, 47, 427

Herbst E., Messer J. K., De Lucia F. C., Helminger P., 1984, Journal of Molecular Spectroscopy, 108, 42

Herzberg G., 1945, Molecular spectra and molecular structure. Vol.2: Infrared and Raman spectra of polyatomic molecules

Heywood I., et al., 2022, ApJ, 925, 165

Holdship J., et al., 2021, A&A, 654, A55

Huang K. Y., et al., 2022, arXiv e-prints, p. arXiv:2202.05005

Hughes G. L., Gibson B. K., Carigi L., Sánchez-Blázquez P., Chavez J. M., Lambert D. L., 2008, MNRAS, 390, 1710

Humire P. K., et al., 2020a, A&A, 633, A106

Humire P. K., et al., 2020b, A&A, 642, A222

Humire P. K., et al., 2022, A&A, 663, A33

Hunter I., Lennon D. J., Dufton P. L., Trundle C., Simón-Díaz S., Smartt S. J., Ryans R. S. I., Evans C. J., 2008, A&A, 479, 541

Hurt R. L., Turner J. L., Ho P. T. P., 1996, ApJ, 466, 135

Ikeda M., Ohishi M., Nummelin A., Dickens J. E., Bergman P., Hjalmarson Å., Irvine W. M., 2001, ApJ, 560, 792

Impellizzeri C. M. V., Henkel C., Roy A. L., Menten K. M., 2008, A&A, 484, L43

Inno L., et al., 2019, MNRAS, 482, 83

Iodice E., Arnaboldi M., Rejkuba M., Neeser M. J., Greggio L., Gonzalez O. A., Irwin M., Emerson J. P., 2014, A&A, 567, A86

Ishizuki S., Kawabe R., Ishiguro M., Okumura S. K., Morita K.-I., 1990, Nature, 344, 224

Izumi T., et al., 2013, PASJ, 65, 100

Jansen P., Bethlem H. L., Ubachs W., 2014, J. Chem. Phys., 140, 010901

Jarrett T. H., Chester T., Cutri R., Schneider S. E., Huchra J. P., 2003, AJ, 125, 525

Johnston K. J., Gaume R., Stolovy S., Wilson T. L., Walmsley C. M., Menten K. M., 1992, ApJ, 385, 232

Johnston E. J., Aragón-Salamanca A., Merrifield M. R., 2014, MNRAS, 441, 333

Jørgensen J. K., Belloche A., Garrod R. T., 2020, ARA&A, 58, 727

Kalenskii S. V., Sobolev A. M., 1994, Astronomy Letters, 20, 91

Kalenskii S. V., Johansson L. E. B., Bergman P., Kurtz S., Hofner P., Walmsley C. M., Slysh V. I., 2010, MNRAS, 405, 613

Kalenskii S. V., Kurtz S., Hofner P., 2017, Astronomical and Astrophysical Transactions, 30, 161

Kelly G., Viti S., Bayet E., Aladro R., Yates J., 2015, A&A, 578, A70

Kennicutt R. C., Evans N. J., 2012, ARA&A, 50, 531

Kim J., et al., 2021, MNRAS, 504, 487

Kirk H., Johnstone D., Tafalla M., 2007, ApJ, 668, 1042

Klein B., Hochgürtel S., Krämer I., Bell A., Meyer K., Güsten R., 2012, A&A, 542, L3

Klein T., et al., 2014, IEEE Transactions on Terahertz Science and Technology, 4, 588

Kobayashi C., Karakas A. I., Umeda H., 2011, MNRAS, 414, 3231

Kobayashi C., Karakas A. I., Lugaro M., 2020, ApJ, 900, 179

Koehler J. S., Dennison D. M., 1940, Physical Review, 57, 1006

Kovtyukh V. V., Andrievsky S. M., Martin R. P., Korotin S. A., Lepine J. R. D., Maciel W. J., Keir L. E., Panko E. A., 2019, MNRAS, 489, 2254

Krieger N., et al., 2017, ApJ, 850, 77

Kruijssen J. M. D., Dale J. E., Longmore S. N., 2015, MNRAS, 447, 1059

Krumholz M. R., Kruijssen J. M. D., 2015, MNRAS, 453, 739

Kuno N., Nakanishi K., Sorai K., Shibatsuka T., 2008, PASJ, 60, 475

Kurtz S., Hofner P., Álvarez C. V., 2004, ApJS, 155, 149

Laas J. C., Caselli P., 2019, A&A, 624, A108

Lada C. J., Shu F. H., 1990, Science, 248, 564

Ladeyschikov D. A., Bayandina O. S., Sobolev A. M., 2019, AJ, 158, 233

Lamb J. B., Oey M. S., Werk J. K., Ingleby L. D., 2010, ApJ, 725, 1886

Langer W. D., Velusamy T., Morris M. R., Goldsmith P. F., Pineda J. L., 2017, A&A, 599, A136

Laporte N., Zitrin A., Ellis R. S., 2021, MNRAS, 505, 4838

Larson R. B., 1969, MNRAS, 145, 271

Law C. J., Yusef-Zadeh F., Cotton W. D., Maddalena R. J., 2008, ApJS, 177, 255

Lees R. M., 1973, ApJ, 184, 763

Leitherer C., Ekström S., Meynet G., Schaerer D., Agienko K. B., Levesque E. M., 2014, ApJS, 212, 14

Leroy A. K., et al., 2015, ApJ, 801, 25

Leroy A. K., et al., 2018, ApJ, 869, 126

Leurini S., Schilke P., Menten K. M., Flower D. R., Pottage J. T., Xu L. H., 2004, A&A, 422, 573

Leurini S., Schilke P., Wyrowski F., Menten K. M., 2007, A&A, 466, 215

Leurini S., Menten K. M., Walmsley C. M., 2016, A&A, 592, 31

Levshakov S. A., Centurión M., Molaro P., Kostina M. V., 2006, A&A, 447, L21

Levshakov S. A., Agafonova I. I., Henkel C., Kim K.-T., Kozlov M. G., Lankhaar B., Yang W., 2022, MNRAS, 511, 413

Liechti S., Wilson T. L., 1996, A&A, 314, 615

Lin Y., Wyrowski F., Liu H. B., Izquierdo A. F., Csengeri T., Leurini S., Menten K. M., 2022, A&A, 658, A128

Linke R. A., Goldsmith P. F., 1980, ApJ, 235, 437

Lique F., Spielfiedel A., Cernicharo J., 2006, A&A, 451, 1125

Lis D. C., Goldsmith P. F., 1990, ApJ, 356, 195

Lo K. Y., 2005, ARA&A, 43, 625

Loinard L., Menten K. M., Güsten R., Zapata L. A., Rodríguez L. F., 2012, ApJL, 749, L4

Loison J.-C., et al., 2019, MNRAS, 485, 5777

Lucas R., Liszt H. S., 2002, A&A, 384, 1054

Luhman K. L., 2012, ARA&A, 50, 65

MacLeod G. C., et al., 2019, MNRAS, 489, 3981

Maffucci D. M., Wenger T. V., Le Gal R., Herbst E., 2018, ApJ, 868, 41

Mangum J. G., Shirley Y. L., 2015, PASP, 127, 266

Mangum J. G., Ginsburg A. G., Henkel C., Menten K. M., Aalto S., van der Werf P., 2019, ApJ, 871, 170

Mao R.-Q., Schulz A., Henkel C., Mauersberger R., Muders D., Dinh-V-Trung 2010, ApJ, 724, 1336

Martín-Pintado J., Bachiller R., Thum C., Walmsley M., 1989, A&A, 215, L13

Martín S., Mauersberger R., Martín-Pintado J., Henkel C., García-Burillo S., 2006, ApJS, 164, 450

Martín S., Martín-Pintado J., Blanco-Sánchez C., Rivilla V. M., Rodríguez-Franco A., Rico-Villas F., 2019, A&A, 631, A159

Martín S., et al., 2021, A&A, 656, A46

Martins F., Hillier D. J., Paumard T., Eisenhauer F., Ott T., Genzel R., 2008, A&A, 478, 219

Mauersberger R., Henkel C., Wilson T. L., Harju J., 1989, A&A, 226, L5

Mauersberger R., Henkel C., Langer N., Chin Y. N., 1996, A&A, 313, L1

Mauersberger R., Henkel C., Weiß A., Peck A. B., Hagiwara Y., 2003, A&A, 403, 561

Mauersberger R., Ott U., Henkel C., Cernicharo J., Gallino R., 2004, A&A, 426, 219

McCarthy T. P., Ellingsen S. P., Chen X., Breen S. L., Voronkov M. A., Qiao H.-h., 2017, ApJ, 846, 156

McCarthy T. P., Ellingsen S. P., Breen S. L., Henkel C., Voronkov M. A., Chen X., 2018a, MNRAS, 480, 4578

McCarthy T. P., Ellingsen S. P., Breen S. L., Voronkov M. A., Chen X., 2018b, ApJL, 867, L4

McCarthy T. P., Ellingsen S. P., Breen S. L., Voronkov M. A., Chen X., Qiao H. h., 2020, MNRAS, 491, 4642

McEwen B. C., Pihlström Y. M., Sjouwerman L. O., 2014, ApJ, 793, 133

McKee C. F., Tan J. C., 2002, Nature, 416, 59

Meier D. S., Turner J. L., 2012, ApJ, 755, 104

Meier D. S., Turner J. L., Hurt R. L., 2008, ApJ, 675, 281

Meier D. S., et al., 2015, ApJ, 801, 63

Menten K. M., 1991a, in Haschick A. D., Ho P. T. P., eds, Astronomical Society of the Pacific Conference Series Vol. 16, Atoms, Ions and Molecules: New Results in Spectral Line Astrophysics. pp 119–136

Menten K. M., 1991b, ApJ, 380, L75

Menten K. M., 2012, in Booth R. S., Vlemmings W. H. T., Humphreys E. M. L., eds, Vol. 287, Cosmic Masers - from OH to H0. pp 506–515 (`arXiv:1204.5865`), doi:10.1017/S1743921312007624

Menten K. M., Lundgren A., Belloche A., Thorwirth S., Reid M. J., 2008, A&A, 477, 185

Menten K. M., Wilson R. W., Leurini S., Schilke P., 2009, ApJ, 692, 47

Messineo M., Habing H. J., Sjouwerman L. O., Omont A., Menten K. M., 2002, A&A, 393, 115

Meyer M. J., et al., 2004, MNRAS, 350, 1195

Milam S. N., Savage C., Brewster M. A., Ziurys L. M., Wyckoff S., 2005, ApJ, 634, 1126

Millar T. J., Herbst E., 1990, A&A, 231, 466

Mills E. A. C., Morris M. R., 2013, ApJ, 772, 105

Mills E., Morris M. R., Lang C. C., Cotera A., Dong H., Wang Q. D., Stolovy S., 2011, in Morris M. R., Wang Q. D., Yuan F., eds, Astronomical Society of the Pacific Conference Series Vol. 439, The Galactic Center: a Window to the Nuclear Environment of Disk Galaxies. p. 125 (`arXiv:1002.1115`)

Molinari S., et al., 2010, PASP, 122, 314

Molinari S., et al., 2011, ApJL, 735, L33

Molinari S., et al., 2014, in Beuther H., Klessen R. S., Dullemond C. P., Henning T., eds, Protostars and Planets VI. p. 125 (`arXiv:1402.6196`), doi:10.2458/azu_uapress_9780816531240-ch006

Mollá M., Díaz Á. I., Cavichia O., Gibson B. K., Maciel W. J., Costa R. D. D., Ascasibar Y., Few C. G., 2019, MNRAS, 482, 3071

Möller T., Endres C., Schilke P., 2017, A&A, 598, A7

Montaigne H., et al., 2005, ApJ, 631, 653

Moré J. J., 1978, in , Vol. 630, Lecture Notes in Mathematics, Berlin Springer Verlag. pp 105–116, doi:10.1007/BFb0067700

Morris M., Serabyn E., 1996, ARA&A, 34, 645

Motte F., Bontemps S., Louvet F., 2018, ARA&A, 56, 41

Müller H. S. P., Schlöder F., Stutzki J., Winnewisser G., 2005, Journal of Molecular Structure, 742, 215

Müller S., Guélin M., Dumke M., Lucas R., Combes F., 2006, A&A, 458, 417

Muller S., et al., 2013, A&A, 551, A109

Mumma M. J., et al., 2001, Science, 292, 1334

Najarro F., Figer D. F., Hillier D. J., Geballe T. R., Kudritzki R. P., 2009, ApJ, 691, 1816

Nakagawa K., Tsunekawa S., Kojima T., 1987, Journal of Molecular Spectroscopy, 126, 329

Nemmich M. A., Fatima D., Slimane M., 2018, p. 10

Nesterenok A. V., 2022, MNRAS, 509, 4555

Newton K., 1980, MNRAS, 191, 615

Nilsson A., Hjalmarson Å., Bergman P., Millar T. J., 2000, A&A, 358, 257

Oka T., Geballe T. R., 2020, ApJ, 902, 9

Orr M. E., et al., 2021, ApJL, 908, L31

Pardo J. R., Cernicharo J., Serabyn E., 2001, IEEE Transactions on Antennas and Propagation, 49, 454

Patel S. G., et al., 2013, ApJ, 766, 15

Paulson S. T., Pandian J. D., 2020, MNRAS, 492, 1335

Pei C. C., Liu S.-Y., Snyder L. E., 2000, ApJ, 530, 800

Pence W. D., 1980, ApJ, 239, 54

Pérez-Beaupuits J. P., Güsten R., Harris A., Requena-Torres M. A., Menten K. M., Weiß A., Polehampton E., van der Wiel M. H. D., 2018, ApJ, 860, 23

Pérez L. M., et al., 2016, Science, 353, 1519

Pham D., Ghanbarzadeh A., KoÃ§ E., Otri S., Rahim S., Zaidi M., 2006, Proceedings of IPROMS 2006 Conference

Phillips C. J., Norris R. P., Ellingsen S. P., Rayner D. P., 1998, MNRAS, 294, 265

Pickett H. M., Poynter R. L., Cohen E. A., Delitsky M. L., Pearson J. C., Müller H. S. P., 1998, J. Quant. Spect. ¨and Microw. Spect. Phys., 60, 883

Pignatari M., et al., 2016, ApJS, 225, 24

Pihlström Y. M., Sjouwerman L. O., Frail D. A., Claussen M. J., Mesler R. A., McEwen B. C., 2014, AJ, 147, 73

Plambeck R. L., Menten K. M., 1990, ApJ, 364, 555

Polehampton E. T., Baluteau J. P., Swinyard B. M., 2005, A&A, 437, 957

Pratap P., Shute P. A., Keane T. C., Battersby C., Sterling S., 2008, AJ, 135, 1718

Rabli D., Flower D. R., 2010, MNRAS, 406, 95

Regan M. W., Teuben P., 2003, ApJ, 582, 723

Reid M. J., 2007, in Chapman J. M., Baan W. A., eds, Vol. 242, Astrophysical Masers and their Environments. pp 522–529, doi:10.1017/S1743921307013701

Reid M. J., Moran J. M., 1981, ARA&A, 19, 231

Reid M. J., Menten K. M., Zheng X. W., Brunthaler A., Xu Y., 2009, ApJ, 705, 1548

Reipurth B., Bally J., 2001, ARA&A, 39, 403

Rekola R., Richer M. G., McCall M. L., Valtonen M. J., Kotilainen J. K., Flynn C., 2005, MNRAS, 361, 330

Requena-Torres M. A., Martín-Pintado J., Martín S., Morris M. R., 2008, ApJ, 672, 352

Riechers D. A., Weiss A., Walter F., Carilli C. L., Cox P., Decarli R., Neri R., 2022, Nature, 602, 58

Ritchey A. M., Federman S. R., Lambert D. L., 2011, ApJ, 728, 36

Rivilla V. M., et al., 2022, ApJL, 929, L11

Rosen A. L., Krumholz M. R., 2020, AJ, 160, 78

Rosen A. L., Li P. S., Zhang Q., Burkhart B., 2019, ApJ, 887, 108

Rosenberg M. J. F., Kazandjian M. V., van der Werf P. P., Israel F. P., Meijerink R., Weiß A., Requena-Torres M. A., Güsten R., 2014, A&A, 564, A126

Rosenthal M. J., Zaw I., 2020, MNRAS, 499, 1233

Ryle M., Hewish A., 1960, MNRAS, 120, 220

Sabín-Sanjulián C., et al., 2017, A&A, 601, A79

Sakamoto K., 2014,] 10.1017/S1743921314000453, 303, 159

Sakamoto K., et al., 2006, ApJ, 636, 685

Sakamoto K., Mao R.-Q., Matsushita S., Peck A. B., Sawada T., Wiedner M. C., 2011, ApJ, 735, 19

Sakamoto K., Martín S., Wilner D. J., Aalto S., Evans A. S., Harada N., 2021, ApJ, 923, 240

Salii S. V., Sobolev A. M., Kalinina N. D., 2002, Astronomy Reports, 46, 955

Salter C. J., Ghosh T., Catinella B., Lebron M., Lerner M. S., Minchin R., Momjian E., 2008, AJ, 136, 389

Sánchez-Monge Á., et al., 2017, A&A, 604, A6

Sandqvist A., et al., 2008, A&A, 482, 849

Sarzi M., Allard E. L., Knapen J. H., Mazzuca L. M., 2007, MNRAS, 380, 949

Schilke P., Benford D. J., Hunter T. R., Lis D. C., Phillips T. G., 2001, ApJS, 132, 281

Schinnerer E., Böker T., Meier D. S., Calzetti D., 2008, ApJL, 684, L21

Schmiedeke A., et al., 2016, A&A, 588, A143

Schwörer A., et al., 2019, A&A, 628, A6

Scoville N. Z., 1972, ApJL, 175, L127

Sellwood J. A., Wilkinson A., 1993, Reports on Progress in Physics, 56, 173

Semenov V. A., Kravtsov A. V., Caprioli D., 2021, ApJ, 910, 126

Shirley Y. L., 2015, PASP, 127, 299

Shu F. H., 1977, ApJ, 214, 488

Shu F. H., Adams F. C., Lizano S., 1987, ARA&A, 25, 23

Simpson J. M., et al., 2014, ApJ, 788, 125

Sinclair M. W., Carrad G. J., Caswell J. L., Norris R. P., Whiteoak J. B., 1992, MNRAS, 256, 33P

Sjouwerman L. O., Murray C. E., Pihlström Y. M., Fish V. L., Araya E. D., 2010, ApJL, 724, L158

Sobolev A. M., 1992, Soviet Ast., 36, 590

Sobolev A. M., 1993, Astronomy Letters, 19, 293

Sobolev A. M., Cragg D. M., Godfrey P. D., 1997, A&A, 324, 211

Sobolev A. M., et al., 2007, in Chapman J. M., Baan W. A., eds, Vol. 242, Astrophysical Masers and their Environments. pp 81–88 (`arXiv:0706.3117`), doi:10.1017/S1743921307012616

Sormani M. C., Treß R. G., Ridley M., Glover S. C. O., Klessen R. S., Binney J., Magorrian J., Smith R., 2018, MNRAS, 475, 2383

Sormani M. C., Tress R. G., Glover S. C. O., Klessen R. S., Battersby C. D., Clark P. C., Hatchfield H. P., Smith R. J., 2020, MNRAS, 497, 5024

Spiegel D. S., Burrows A., Milsom J. A., 2011, ApJ, 727, 57

Strickland D. K., Heckman T. M., Weaver K. A., Dahlem M., 2000, AJ, 120, 2965

Sukhbold T., Ertl T., Woosley S. E., Brown J. M., Janka H. T., 2016, ApJ, 821, 38

Szczepanski J. C., Ho P. T. P., Haschick A. D., Baan W. A., 1989, in Morris M., ed., Vol. 136, The Center of the Galaxy. p. 383

van der Tak F. F. S., Black J. H., Schöier F. L., Jansen D. J., van Dishoeck E. F., 2007, A&A, 468, 627

Taylor G. B., Carilli C. L., Perley R. A., 1999, Synthesis Imaging in Radio Astronomy II. Astronomical Society of the Pacific Conference Series Vol. 180

Thiel V., 2019, PhD thesis, University of Bonn

Thiel V., et al., 2019, A&A, 623, A68

Thielemann F. K., Arnett W. D., 1985, ApJ, 295, 604

Tikhonov N. A., Galazutdinova O. A., 2018, Astrophysical Bulletin, 73, 279

Timmes F. X., Woosley S. E., Weaver T. A., 1995, ApJS, 98, 617

Tress R. G., Sormani M. C., Glover S. C. O., Klessen R. S., Battersby C. D., Clark P. C., Hatchfield H. P., Smith R. J., 2020, MNRAS, 499, 4455

Tsuboi M., Handa T., Inoue M., Inatani J., Ukita N., 1989, in Morris M., ed., Vol. 136, The Center of the Galaxy. p. 135

Tsuboi M., Miyazaki A., Okumura S. K., 2009, PASJ, 61, 29

Tsuboi M., Miyazaki A., Uehara K., 2015, PASJ, 67, 109

Turner B. E., 1985, ApJ, 299, 312

Turner J. L., Ho P. T. P., 1985, ApJ, 299, L77

Turner B. E., Gordon M. A., Wrixon G. T., 1972, ApJ, 177, 609

Uehara K., Tsuboi M., Kitamura Y., Miyawaki R., Miyazaki A., 2019, ApJ, 872, 121

Urquhart J. S., et al., 2015, MNRAS, 446, 3461

Vasyunina T., Linz H., Henning T., Zinchenko I., Beuther H., Voronkov M., 2011, A&A, 527, A88

de Vaucouleurs G., de Vaucouleurs A., Corwin H. G. J., 1976, Second reference catalogue of bright galaxies. Containing information on 4,364 galaxies with references to papers published between 1964 and 1975.

de Vaucouleurs G., de Vaucouleurs A., Corwin Herold G. J., Buta R. J., Paturel G., Fouque P., 1991, Third Reference Catalogue of Bright Galaxies

Vidal T. H. G., Loison J.-C., Jaziri A. Y., Ruaud M., Gratier P., Wakelam V., 2018, MNRAS, 469, 435

Viti S., 2016, in Jablonka P., André P., van der Tak F., eds, IAU Symposium Vol. 315, From Interstellar Clouds to Star-Forming Galaxies: Universal Processes?. pp 17–25 (`arXiv:1603.09105`), doi:10.1017/S1743921316007195

Voronkov M. A., Caswell J. L., Ellingsen S. P., Sobolev A. M., 2010, MNRAS, 405, 2471

Voronkov M. A., Caswell J. L., Ellingsen S. P., Green J. A., Breen S. L., 2014, MNRAS, 439, 2584

Walsh A. J., Hyland A. R., Robinson G., Burton M. G., 1997, MNRAS, 291, 261

Walsh A. J., Burton M. G., Hyland A. R., Robinson G., 1998, MNRAS, 301, 640

Walsh A. J., Bertoldi F., Burton M. G., Nikola T., 2001, MNRAS, 326, 36

Wang M., Henkel C., Chin Y. N., Whiteoak J. B., Hunt Cunningham M., Mauersberger R., Muders D., 2004, A&A, 422, 883

Wang K. S., Bourke T. L., Hogerheijde M. R., van der Tak F. F. S., Benz A. O., Megeath S. T., Wilson T. L., 2013, A&A, 558, A69

Wang J., Zhang J., Gao Y., Zhang Z.-Y., Li D., Fang M., Shi Y., 2014, Nature Communications, 5, 5449

Wegg C., Gerhard O., Portail M., 2015, MNRAS, 450, 4050

Wenger T. V., Balser D. S., Anderson L. D., Bania T. M., 2019, ApJ, 887, 114

Wheeler J. C., Sneden C., Truran James W. J., 1989, ARA&A, 27, 279

Williams J. P., Blitz L., McKee C. F., 2000, in Mannings V., Boss A. P., Russell S. S., eds, Protostars and Planets IV. p. 97 (`arXiv:astro-ph/9902246`)

Williams B. A., et al., 2022, MNRAS, 514, 578

Wilson W. J., Barrett A. H., 1972, A&A, 17, 385

Wilson T. L., Matteucci F., 1992, A&A Rev., 4, 1

Wilson T. L., Rood R., 1994, ARA&A, 32, 191

Wilson T. L., Ruf K., Walmsley C. M., Martin R. N., Pauls T. A., Batria W., 1982, A&A, 115, 185

Woosley S. E., Weaver T. A., 1995, ApJS, 101, 181

Yan Y. T., et al., 2019, ApJ, 877, 154

Yang K., et al., 2017, The Astrophysical Journal, 846, 160

Yang K., et al., 2019, ApJS, 241, 18

Yang W. J., et al., 2022, A&A, 658, A192

Yorke H. W., Bodenheimer P., 1999, ApJ, 525, 330

Young J. S., Allen L., Kenney J. D. P., Lesser A., Rownd B., 1996, AJ, 112, 1903

Yu H. Z., et al., 2020, ApJ, 899, 145

Yusef-Zadeh F., Cotton W., Viti S., Wardle M., Royster M., 2013, ApJL, 764, L19

Zeng S., et al., 2018, MNRAS, 478, 2962

Zeng S., et al., 2020, MNRAS, 497, 4896

Zhang Q., Wang K., Lu X., Jiménez-Serra I., 2015, ApJ, 804, 141

Zhang J. S., et al., 2020, ApJS, 249, 6

Zhao G.-Y., et al., 2022, ApJ, 932, 72

Zinnecker H., Yorke H. W., 2007, ARA&A, 45, 481

APPENDIX A

Sulphur and carbon isotopes towards Galactic centre clouds

A&A 642, A222 (2020)
https://doi.org/10.1051/0004-6361/202038216

Astronomy & Astrophysics

Sulphur and carbon isotopes towards Galactic centre clouds*

P. K. Humire[1], V. Thiel[1], C. Henkel[1,2,3], A. Belloche[1], J.-C. Loison[4], T. Pillai[1,5], D. Riquelme[1], V. Wakelam[6], N. Langer[1,7], A. Hernández-Gómez[1], R. Mauersberger[1], and K. M. Menten[1]

[1] Max-Planck-Institut für Radioastronomie, Auf dem Hügel 69, 53121 Bonn, Germany
e-mail: phumire@mpifr-bonn.mpg.de
[2] Department of Astronomy, King Abdulaziz University, PO Box 80203, Jeddah 21589, Saudi Arabia
[3] Xinjiang Astronomical Observatory, Chinese Academy of Sciences, 830011 Urumqi, PR China
[4] Institut des Sciences Moléculaires (ISM), CNRS, Univ. Bordeaux, 351 cours de la Libération, 33400 Talence, France
[5] Institute for Astrophysical Research, 725 Commonwealth Avenue, Boston University Boston, MA 02215, USA
[6] Laboratoire d'astrophysique de Bordeaux, CNRS, Univ. Bordeaux, B18N, allée Geoffroy Saint-Hilaire, 33615 Pessac, France
[7] Argelander-Institut für Astronomie, Universität Bonn, Auf dem Hügel 71, 53121 Bonn, Germany

Received 20 April 2020 / Accepted 30 August 2020

ABSTRACT

Context. Measuring isotopic ratios is a sensitive technique used to obtain information on stellar nucleosynthesis and chemical evolution.

Aims. We present measurements of the carbon and sulphur abundances in the interstellar medium of the central region of our Galaxy. The selected targets are the +50 km s^{-1} Cloud and several line-of-sight clouds towards Sgr B2(N).

Methods. Towards the +50 km s^{-1} Cloud, we observed the $J = 2$–1 rotational transitions of ^{12}C^{32}S, ^{12}C^{34}S, ^{13}C^{32}S, ^{12}C^{33}S, and ^{13}C^{34}S, and the $J = 3$–2 transitions of ^{12}C^{32}S and ^{12}C^{34}S with the IRAM-30 m telescope, as well as the $J = 6$–5 transitions of ^{12}C^{34}S and ^{13}C^{32}S with the APEX 12 m telescope, all in emission. The $J = 2$–1 rotational transitions of ^{12}C^{32}S, ^{12}C^{34}S, ^{13}C^{32}S, and ^{13}C^{34}S were observed with ALMA in the envelope of Sgr B2(N), with those of ^{12}C^{32}S and ^{12}C^{34}S also observed in the line-of-sight clouds towards Sgr B2(N), all in absorption.

Results. In the +50 km s^{-1} Cloud we derive a ^{12}C/^{13}C isotopic ratio of $22.1^{+3.3}_{-2.4}$, that leads, with the measured ^{13}C^{32}S/^{12}C^{34}S line intensity ratio, to a ^{32}S/^{34}S ratio of $16.3^{+3.0}_{-2.4}$. We also derive the ^{32}S/^{34}S isotopic ratio more directly from the two isotopologues ^{13}C^{32}S and ^{13}C^{34}S, which leads to an independent ^{32}S/^{34}S estimation of $16.3^{+2.1}_{-1.7}$ and 17.9 ± 5.0 for the +50 km s^{-1} Cloud and Sgr B2(N), respectively. We also obtain a ^{34}S/^{33}S ratio of 4.3 ± 0.2 in the +50 km s^{-1} Cloud.

Conclusions. Previous studies observed a decreasing trend in the ^{32}S/^{34}S isotopic ratios when approaching the Galactic centre. Our result indicates a termination of this tendency at least at a galactocentric distance of 130^{+60}_{-30} pc. This is at variance with findings based on ^{12}C/^{13}C, ^{14}N/^{15}N, and ^{18}O/^{17}O isotope ratios, where the above-mentioned trend is observed to continue right to the central molecular zone. This can indicate a drop in the production of massive stars at the Galactic centre, in the same line as recent metallicity gradient ([Fe/H]) studies, and opens the work towards a comparison with Galactic and stellar evolution models.

Key words. Galaxy: centre – submillimetre: ISM – Galaxy: formation – Galaxy: evolution – stars: atmospheres – submillimetre: general

1. Introduction

Studying stellar nucleosynthesis and chemical enrichment of rare isotopes of a given element at optical wavelengths is difficult because the observed atomic isotope lines are usually affected by blending (e.g. Hawkins & Jura 1987; Levshakov et al. 2006; Ritchey et al. 2011). However, at radio and (sub)millimetre wavelengths, transitions from rare isotopic substitutions of a given molecular species, called isotopologues, are well separated in frequency from their main species, typically by a few percent of their rest frequency.

While the relative abundances of C, N, and O isotopes provide information on carbon–nitrogen–oxygen (CNO) and helium burning, sulphur isotopes allow us to probe late evolutionary stages of massive stars and supernovae (SNe) of Type Ib/c and II (oxygen-burning, neon-burning, and s-process nucleosynthesis) (Wilson & Rood 1994; Chin et al. 1996; Mauersberger et al. 1996), filling a basic gap in our understanding of stellar nucleosynthesis and the chemical evolution of the Universe (e.g. Wang et al. 2013).

In the interstellar medium (ISM), atomic sulphur is thought to freeze out on dust grain mantles and to be later released from the grains due to shocks, leading to the formation of several molecular species in the gas phase, such as OCS, SO$_2$, H$_2$S, and H$_2$CS (Millar & Herbst 1990), which serve as both shock and high-mass star formation tracers in starburst galaxies (Bayet et al. 2008).

Among the sulphur-bearing compounds, CS (carbon monosulfide) is the most accessible molecular species: its lines are ubiquitous in the dense ISM and tend to be strong at sites of massive star formation in the spiral arms of our Galaxy, in the Galactic centre (GC) region and in external galaxies (e.g. Linke & Goldsmith 1980; Mauersberger et al. 1989; Bayet et al. 2009; Kelly et al. 2015).

---

* The reduced spectra and datacubes are only available at the CDS via anonymous ftp to cdsarc.u-strasbg.fr (130.79.128.5) or via http://cdsarc.u-strasbg.fr/viz-bin/cat/J/A+A/642/A222

Open Access funding provided by Max Planck Society.

Sulphur has four stable isotopes: ^{32}S, ^{33}S, ^{34}S, and ^{36}S. Their solar system fractions are 95.018:0.750:4.215:0.017 (Lodders 2003), respectively. In the ISM, Chin et al. (1996) found a relation between ^{32}S/^{34}S isotope ratios and their galactocentric distance ($D_{\rm GC}$) of ^{32}S/^{34}S = $(3.3 \pm 0.5)(D_{\rm GC}/{\rm kpc}) + (4.1 \pm 3.1)$ by using a linear least-squares fit to the unweighted data, with a correlation coefficient of 0.84, while no correlation was obtained between ^{34}S/^{33}S ratios and $D_{\rm GC}$. However, most of the sources observed in that study are located within the galactocentric distance range $5.5 \leq D_{\rm GC} \leq 7.0$ kpc, with the minimum distance at 2.9 kpc from the Galactic centre. Therefore, it is important to also cover the inner region of the Milky Way to find out whether the trend proposed by Chin et al. (1996) is also valid for the inner Galaxy as has been reported for the ^{12}C/^{13}C (see e.g. Yan et al. 2019), ^{14}N/^{15}N (Adande & Ziurys 2012) and ^{18}O/^{17}O (Wouterloot et al. 2008; Zhang et al. 2015) isotopic ratios.

The GC region harbours one of the most intense and luminous sites of massive star formation in the Galaxy, Sgr B2 (Molinari et al. 2014; Ginsburg et al. 2018). It provides an extreme environment in terms of pressure, turbulent Mach number, and gas temperature (Ginsburg et al. 2016) over a much more extended region than encountered in star-forming regions throughout the Galactic disc (Morris & Serabyn 1996; Ginsburg et al. 2016; Schwörer et al. 2019; Dale et al. 2019). These conditions are comparable to those in starburst galaxies (Belloche et al. 2013; Schwörer et al. 2019). We therefore expect unique results in this GC study from sulphur ratios, which are a tool for tracing stellar processing (see Sect. 6). For a compilation of sulphur ratios determined in our Milky Way, we refer to Tables 2 and 7 in Mauersberger et al. (2004) and Müller et al. (2006), respectively.

As is true for our Galaxy, detections of ^{34}S in extragalactic objects remain scarce. Some observations, also accounting for ^{12}C/^{13}C ratios (using the double-isotope ratio method, Sect. 4.1.1) led to values of ~16–25 and 13.5 ± 2.5 for the ^{32}S/^{34}S ratio in the nuclear starbursts of NGC 253 and NGC 4945, respectively (Wang et al. 2004; Henkel et al. 2014), although the value for NGC 4945 might be underestimated due to saturation of the CS lines (Martín et al. 2010). A ratio of 20 ± 5 was obtained for N159 in the Large Magellanic Cloud (Johansson et al. 1994). At redshift $z = 0.89$, a ^{32}S/^{34}S ratio of 10 ± 1 has been derived using absorption lines from the spiral arm of a galaxy located along the line of sight (l.o.s.) towards a radio loud quasar (Müller et al. 2006).

In the present study we focus on the $J = 2$–1 transitions of ^{12}C^{32}S (hereafter CS), ^{12}C^{34}S (hereafter C^{34}S), ^{13}C^{32}S (hereafter ^{13}CS), ^{12}C^{33}S (hereafter C^{33}S), and ^{13}C^{34}S, the $J = 3$–2 transitions of CS and C^{34}S, and the $J = 6$–5 transitions of C^{34}S and ^{13}CS, all observed together towards the Sgr A Complex (see, e.g., Sandqvist et al. 2015). We have also studied absorption features caused by the envelope of Sgr B2(N) in the $J = 2$–1 rotational transition of CS, C^{34}S, ^{13}CS and ^{13}C^{34}S, as well as CS and C^{34}S absorption features caused by l.o.s. clouds towards Sgr B2(N). These absorption and emission profiles allow us to obtain ^{12}C/^{13}C and the missing ^{32}S/^{34}S ratios close to the Galactic nucleus. Expanding the database for sulphur isotope ratios in the GC region is important in order to constrain models of stellar interiors as well as models of the chemical evolution of the Galaxy (e.g. Kobayashi et al. 2011).

The paper is organized as follows. In Sect. 2, we describe the observations. In Sect. 3, we describe in detail our targets. In Sect. 4, we present measured opacities and isotopologue ratios from CS species, the modelling of our Sgr B2(N) data, and a comprehensive study of CS fractionation. In Sect. 5, we compare our results with previous studies. In Sect. 6, we discuss the results in the context of trends with galactocentric distance and give some explanations for our findings, before summarizing and concluding in Sect. 7.

2. Observations

2.1. +50 km s^{-1} Cloud

The +50 km s^{-1} Cloud observations were conducted with the IRAM 30 m and the APEX 12 m telescopes over a period of 1.5 yr, from 2015 May to 2016 September, under varying weather conditions. The observed position was EQ J2000: 17$^{\rm h}$45$^{\rm m}$50.20$^{\rm s}$, −28°59′41.1″ for both telescopes, and the representative spectral resolution was 0.6 km s^{-1}. With the IRAM 30 m telescope, three frequency set-ups were observed with the E090 and E150 receivers in combination with the Fast Fourier Transform Spectrometer (FFTS, at 195 kHz resolution mode[1]). For the observations presented in this paper, we covered the 93.2–100.98 GHz frequency range (CS, C^{34}S, and C^{33}S $J = 2$–1) in one set-up with the E090 receiver. In a separate E090 set-up, our tuning covered the frequency range 85.5–93.3 GHz (^{13}CS and ^{13}C^{34}S $J = 2$–1), while simultaneously the E150 receiver covered the frequency range from 143.5 to 151.3 GHz (for CS and C^{34}S $J = 3$–2). The observations were conducted in total power position switching mode. No spectral contamination was found in our off-source reference position (17$^{\rm h}$46$^{\rm m}$10.4$^{\rm s}$, −29°07′08″). The main beam efficiencies for our IRAM 30 m measurements were computed using the Ruze formalism (Ruze 1966). Adopted values were 0.8 and 0.7 at 98 and 147 GHz, respectively[2]. We discarded data taken under poor weather conditions (precipitable water vapor content (pwv) > 7 mm) by discarding data taken with system temperatures > 500 K. The representative half-power beam widths (HPBW) values are about 25″ at 98 GHz and 17″ at 147 GHz for the IRAM 30 m observations.

The Atacama Pathfinder Experiment 12 m telescope (APEX) 12 m (Güsten et al. 2006) was used for observations of the $J = 6$–5 lines of the CS, ^{13}CS, and ^{13}C^{34}S isotopologues at roughly 280 GHz. The measurements were conducted simultaneously using the FLASH345 (Klein et al. 2014) receiver connected to the extended FFTS (XFFTS) backend. These observations were also executed in total power position switching mode and the same off-source reference position, which was found to be clean. The HPBW was about 22″ at the observed frequency and the adopted main beam efficiency was 0.7.

All line intensities are reported in main beam brightness temperature units ($T_{\rm MB}$). While the spectral resolution was instrument dependent (between 0.4 and 0.6 km s^{-1} for the IRAM and 0.08 km s^{-1} for the APEX data), all spectra were smoothed to a resolution of 3 km s^{-1} for analysis.

The data were reduced with the GILDAS package[3] and required minimal flagging, followed by a baseline subtraction of order two.

2.2. Line-of-sight clouds towards Sgr B2(N)

For Sgr B2(N), we used the Exploring Molecular Complexity with ALMA (EMoCA) survey (Belloche et al. 2016) that was performed with the Atacama Large Millimetre/submillimetre

---

[1] `http://www.iram.es/IRAMES/mainWiki/Backends`

[2] Calculated following the table in `https://www.iram.fr/GENERAL/calls/w08/w08/node20.html`

[3] `https://www.iram.fr/IRAMFR/GILDAS`

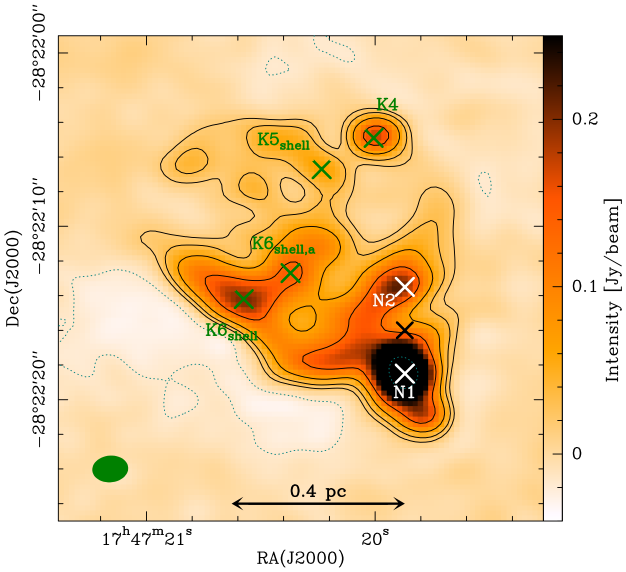

Fig. 1. ALMA continuum map of Sgr B2(N) at 85 GHz. The black contour lines show the flux density levels at 3σ, 6σ, 12σ, and 24σ and the dotted lines indicate -3σ, where σ is the rms noise level of 5.4 mJy beam^{-1}. The white crosses denote the positions of the two main hot cores, Sgr B2(N1) and Sgr B2(N2). The black cross, located between the white ones, indicates the phase centre. The green crosses show peaks of continuum emission selected for our absorption study. They label the ultra-compact H II region K4, two peaks in the shell of the H II region K6 and one peak in the shell of the H II region K5 (Gaume et al. 1995). The green ellipse in the lower left corner shows the size of the synthesized beam of ~1.″6 (see Table 1).

Array (ALMA) in the direction of this source. The centre of the observed field (see Fig. 1) lies in the middle (EQ J2000: $17^h47^m19.87^s, -28°22′16″$) between the two main hot cores, N1 and N2, which are separated by 4.″9 along the north–south direction, or around 0.19 pc in projection assuming a distance to the Galactic centre, Sgr A*, of 8.122 kpc (Gravity Collaboration 2018). The survey covers the frequency range from 84.1 to 114.4 GHz, which includes carbon monosulfide $J = 2–1$ lines, with a spectral resolution of 488 kHz (1.7 to 1.3 km s^{-1}) at a median angular resolution of 1.″6, or ~0.06 pc. The average noise level is ~3 mJy beam^{-1} per channel. Details of the calibration and deconvolution of the data are reported in Belloche et al. (2016, Sect. 2.2). For this work, we corrected the data for primary beam attenuation. Several isotopologues of CS are detected in the EMoCA survey. To determine the ^{32}S/^{34}S and ^{12}C/^{13}C isotopic ratios, we use four isotopologues: CS, C^{34}S, ^{13}CS, and ^{13}C^{34}S.

A list of the observed transitions of CS isotopologues and some associated parameters is given in Table 1.

3. Sources

The +50 km s^{-1} Cloud (also known as M–0.02–0.07, although the +50 km s^{-1} Cloud could include additional molecular knots on its positive-longitude side; Ferrière 2012), observed here with IRAM and APEX, is a giant molecular cloud (GMC) of hook or indented-sphere shape, considered to be one of the most prominent high-mass star formation sites in the GC. It has a mass of $\sim 5 \times 10^5\,M_\odot$; a density of 10^4–10^5 cm^{-3}; a gas temperature of 80–100 K (from NH$_3$, CH$_3$CN, and CH$_3$CCH; Güsten et al. 1985), ~190 K (from H$_2$CO, Ao et al. 2013), or 410 ± 10 K (from NH$_3$, Mills & Morris 2013); and a dust temperature of 20–30 K (Sandqvist et al. 2008). The energetics of at least a part of the +50 km s^{-1} Cloud are influenced by the supernova (SN) remnant Sgr A East (Ferrière 2012; Uehara et al. 2019). In CS emission, its dense core peaks at a l.o.s. distance of 3 ± 3 pc relative to the Galactic centre (Ferrière 2012), coincident with 1.2 mm observations (Vollmer et al. 2003, and references therein), and peaks at $(\Delta\alpha, \Delta\delta) \approx (3.'0, 1.'5)$ with respect to Sgr A*, corresponding to ≈7 ± 3 pc to the east along the Galactic plane and 4.5 ± 3 pc to the south from the Galactic plane (see the explanation for galactocentric Cartesian coordinates in Ferrière 2012, and their Table 1).

With ALMA we have observed Sgr B2(N)orth, one of the sites of massive star formation associated with Sgr B2, the most massive cloud in our Galaxy. The whole Sgr B2 complex has a total mass of $10^7\,M_\odot$ (Goldsmith et al. 1990) and gas temperatures of at least 50 K (from p–H$_2$CO in Ginsburg et al. 2016, their Sect. 5.8). Most of the mass in Sgr B2(N) (~73%) is contained in one single core (AN01) (Sánchez-Monge et al. 2017). The densities and column densities of the hot cores in Sgr B2(N) are high ($>10^6$ cm^{-3} and $>10^{23}$ cm^2; Sánchez-Monge et al. 2017; Bonfand et al. 2019).

Sgr B2(N) is located at a galactocentric distance of 130^{+60}_{-30} pc from Sgr A* (from Reid et al. 2009, considering the projected distance of 100 pc as lower limit) or ~8 kpc from us. Its diameter is ~0.8 pc (Lis & Goldsmith 1990; Schmiedeke et al. 2016). Several diffuse and translucent clouds are detected in absorption along the l.o.s. to Sgr B2(N) (see e.g. Greaves & Williams 1994; Thiel et al. 2019). The exact locations of the different velocity components of the l.o.s. clouds towards Sgr B2(N) are not yet fully constrained. In the case of our observations (see Table 4), we can only suggest that the lines with negative velocities arise from l.o.s. clouds between the Expanding Molecular Ring (with a galactocentric radius of 200–300 pc, Whiteoak & Gardner 1979) and the 1 kpc disc, while the lines with positive velocities arise from the envelope of Sgr B2(N) (Greaves & Williams 1994; Wirström et al. 2010; Thiel et al. 2019). Specifically, our lines in the range −105 to −70 km s^{-1} are believed to be located within 1 kpc of the GC (Corby et al. 2018, and references therein), and our lines with velocities around +60 km s^{-1} are associated with the envelope of Sgr B2(N) (Wirström et al. 2010).

This massive star-forming region harbours five hot cores, namely Sgr B2(N1–N5), with kinetic temperatures ranging from ~130 to 150 K for N3–N5, between 150 and 200 K for N2, and between 160 and 200 K for N1, assuming LTE conditions in all these cases (Belloche et al. 2016, 2019; Bonfand et al. 2017). In addition, there are 20 ~1.3 mm continuum sources associated with dense clouds in Sgr B2(N) that exhibit a rich chemistry (Sánchez-Monge et al. 2017; Schwörer et al. 2019). Recently, Ginsburg et al. (2018) detected 271 compact continuum sources at ~3 mm in the extended Sgr B2 cloud, thought to be high-mass protostellar cores, representing the largest cluster of high-mass young stellar objects reported to date in the Galaxy.

4. Results

In the following we first discuss the measured profiles towards the +50 km s^{-1} Cloud, and provide the equations used to determine peak opacities and the carbon isotope ratio (Sect. 4.1). Then we determine the ^{32}S/^{34}S isotope ratio in two different ways (Sects. 4.1.1 and 4.1.2) from the $J = 2–1$ lines of the different detected CS isotopologues. The $J = 3–2$ opacities and the ^{34}S/^{33}S ratio are the topics of Sects. 4.1.3 and 4.1.4. Sgr B2(N) data are analysed in Sect. 4.2, while the relation between the ^{32}S/^{34}S

Table 1. Some observational and physical parameters for the five measured CS isotopologue transitions in the +50 km s^{-1} Cloud and the four transitions from the l.o.s. clouds towards Sgr B2(N), which are also located in the Galactic centre region.

Target	Telescope	Isotopologue	Transition	ν_0 $^{(a)}$ (GHz)	E_{up}/k $^{(b)}$ (K)	$A_{u,l}$ $^{(c)}$ (s^{-1})	$HPBW$ $^{(d)}$ (″)
+50 Cloud	IRAM 30 m	$^{13}C^{34}S$	2–1	90.9260260	6.55	1.19×10^{-5}	27.0
+50 Cloud	IRAM 30 m	^{13}CS	2–1	92.4943080	6.66	1.41×10^{-5}	26.6
+50 Cloud	IRAM 30 m	$C^{34}S$	2–1	96.4129495	6.25	1.60×10^{-5}	25.5
+50 Cloud	IRAM 30 m	$C^{33}S$	2–1	97.1720639	7.00	1.63×10^{-5}	25.3
+50 Cloud	IRAM 30 m	CS	2–1	97.9809533	7.05	1.67×10^{-5}	25.1
+50 Cloud	IRAM 30 m	$C^{34}S$	3–2	144.6171007	11.80	5.74×10^{-5}	17.0
+50 Cloud	IRAM 30 m	CS	3–2	146.9690287	14.10	6.05×10^{-5}	16.6
+50 Cloud	APEX 12 m	^{13}CS	6–5	277.4554050	46.60	4.40×10^{-4}	22.1
+50 Cloud	APEX 12 m	$C^{34}S$	6–5	289.2090684	38.19	4.81×10^{-4}	21.2
Sgr B2(N)	ALMA	$^{13}C^{34}S$	2–1	90.9260260	6.55	1.19×10^{-5}	1.8 × 1.6
Sgr B2(N)	ALMA	^{13}CS	2–1	92.4943080	6.66	1.41×10^{-5}	2.9 × 1.5
Sgr B2(N)	ALMA	$C^{34}S$	2–1	96.4129549	6.25	1.60×10^{-5}	1.9 × 1.4
Sgr B2(N)	ALMA	CS	2–1	97.9809533	7.05	1.67×10^{-5}	1.8 × 1.3

Notes. The spectroscopic information for each molecule is taken from the Cologne Database for Molecular Spectroscopy (CDMS, Müller et al. 2005; Endres et al. 2016). $^{(a)}$Rest frequency. $^{(b)}$Upper energy level. $^{(c)}$Einstein coefficient for spontaneous emission from upper u to lower l level. $^{(d)}$Half-power beam width. For the IRAM sources it was calculated following Eq. (1) in `http://www.iram.es/IRAMES/telescope/telescopeSummary/telescope_summary.html`.

Table 2. Line parameters for the nine measured CS isotopologue transitions in the +50 km s^{-1} Cloud.

Isotopologue	Transition	$\int T_{mb} dV$ (K km s^{-1})	Peak velocity (km s^{-1})	$FWHM$ (km s^{-1})	T_{mb}^{peak} (K)	$\tau^{(a)}$
$^{13}C^{34}S^{(b)}$	2–1	1.25 ± 0.12	48.44 ± 0.92	20.99 ± 2.24	0.06 ± 0.005	–
^{13}CS	2–1	23.28 ± 0.28	46.94 ± 0.12	22.28 ± 0.29	0.98 ± 0.01	$0.08^{+0.05}_{-0.04}$
$C^{34}S$	2–1	32.61 ± 0.41	46.45 ± 0.13	23.07 ± 0.32	1.33 ± 0.02	–
$C^{33}S$	2–1	7.73 ± 0.31	47.05 ± 0.45	27.61 ± 1.14	0.26 ± 0.01	–
$CS^{(+)}$	2–1	250.00 ± 6.66	48.10 ± 0.11	27.56 ± 0.51	8.52 ± 0.16	$1.9^{+1.1}_{-0.8}$
$CS^{(-)}$	2–1	-37.62 ± 6.13	48.09 ± 0.19	10.85 ± 0.82	-3.26 ± 0.32	–
$C^{34}S$	3–2	21.19 ± 0.19	45.95 ± 0.09	22.39 ± 0.22	0.89 ± 0.01	0.05–0.15
$CS^{(+)}$	3–2	250.00 ± 14.22	47.87 ± 0.10	25.59 ± 0.61	9.18 ± 0.73	1.0–2.8
$CS^{(-)}$	3–2	-78.71 ± 14.69	48.45 ± 0.12	13.97 ± 0.77	-5.29 ± 0.71	–
^{13}CS	6–5	2.39 ± 0.12	43.94 ± 0.43	18.61 ± 1.04	0.120 ± 0.005	–
$C^{34}S$	6–5	3.32 ± 0.10	44.42 ± 0.26	18.51 ± 0.62	0.169 ± 0.005	–

Notes. $^{(a)}$Peak opacity. $^{(b)}$A CH_3OCH_3 (see Sect. 4.1 and Fig. 2) contribution was subtracted before performing a single Gaussian fit to this line. $^{(+)}$Positive component (in blue in Fig. 2). $^{(-)}$Negative component (in green in Fig. 2).

isotope ratios from CS and the actual interstellar $^{32}S/^{34}S$ values is the topic of Sect. 4.3. Generally, the analysis assumes that lines with the same rotational quantum numbers, related to different CS isotopologues, are co-spatial. We present a summary of our results in Table 3.

4.1. Peak opacities and column density ratios in the +50 km s^{-1} Cloud

The CS emission lines observed towards the +50 km s^{-1} Cloud are presented in Fig. 2. All lines show peaks in agreement with the local standard of rest (LSR) velocity of the system, ~50 km s^{-1} (Sandqvist et al. 2008; Requena-Torres et al. 2008). In addition to the CS $J = 2$–1 isotopologue lines, there are probably weak features of cyanoformaldehyde (NCCHO) and ethanol (C_2H_5OH) at 96.4260958 GHz and 96.4273380 GHz, respectively, on the blue-shifted side (~0 km s^{-1}) of $C^{34}S$; dimethyl ether (CH_3OCH_3) at 90.9375080 GHz or ~10 km s^{-1} on the blue-shifted side dominates the $^{13}C^{34}S$ spectrum. Those molecules have been observed already in Sgr B2 (Zuckerman et al. 1975; Nummelin et al. 1998; Martín-Pintado et al. 2001; Remijan et al. 2008; Belloche et al. 2013).

Moreover, the CS $J = 2$–1 and $J = 3$–2 line profiles show double-peaked profiles, which are readily explained by self-absorption, cantered at the systemic velocity of the cloud in the $J = 2$–1 transition and with a self-absorption marginally redshifted (by ~0.4 km s^{-1}) in the $J = 3$–2 transition. The CS parameters allowed to vary freely and obtained from single- or double-component Gaussian fitting are summarized in Table 2. They were obtained using a series of Python codes, mainly within the lmfit package[4].

---

[4] `https://lmfit.github.io/lmfit-py/intro.html`

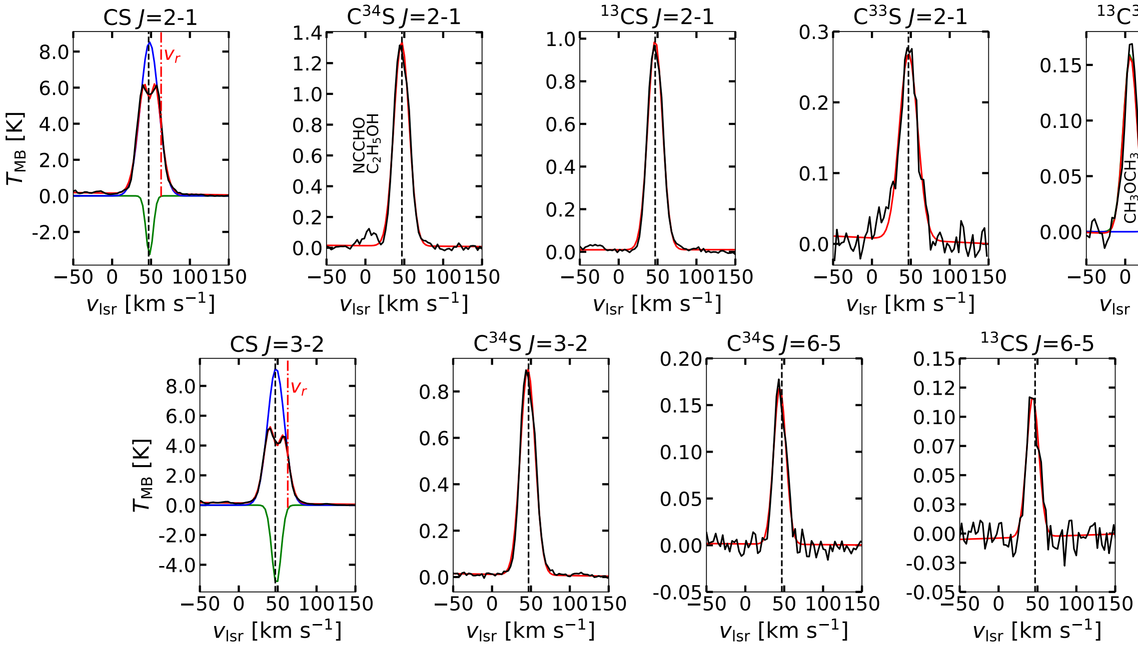

Fig. 2. *From left to right and top to bottom*: observed line profiles of the $J = 2$–1 transitions of CS, $C^{34}S$, ^{13}CS, $C^{33}S$, and $^{13}C^{34}S$, the $J = 3$–2 transitions of CS and $C^{34}S$, and the $J = 6$–5 transitions of $C^{34}S$ and ^{13}CS, in the +50 km s^{-1} Cloud (EQ J2000: $17^h45^m50.20^s$, $-28°59'41.1''$). Measured profiles are shown in black; the resulting Gaussian fitting is presented in red. For the CS $J = 2$–1 and $J = 3$–2 lines, a double Gaussian fitting was performed to account for the self-absorbed component (in green) in an attempt to retrieve the undisturbed emission line (in blue) (see Sect. 4.1). All the other lines are well fitted by a single component. In the case of $^{13}C^{34}S$ $J = 2$–1, the companion line is subtracted because of its relatively strong emission and potential contamination. The dashed vertical lines denote the ^{13}CS $J = 2$–1 peak position (46.94 km s^{-1}, see Table 2). Dash-dotted red lines denote the redshifted velocity ($v_r = 63$ km s^{-1}) at which the CS $J = 2$–1 and $J = 3$–2 transition lines are not affected by self-absorption (see Sect. 4.1). Nearby lines likely observed are labelled.

As can be seen in Fig. 2, for the CS $J = 2$–1 and $J = 3$–2 lines, we have fitted a double Gaussian considering a positive (in blue) and a negative (in green) Gaussian component each. Their parameters are summarized in Table 2, where the uncertainties were taken directly from the lmfit package (for details see Appendix D).

Given that CS $J = 2$–1 and $J = 3$–2 show double-peaked profiles, while the rare isotopologues exhibit a single peak in between, the CS lines are likely optically thick. This was also suggested by Tsuboi et al. (1999) who find that CS $J = 1$–0 is moderately optically thick in this object, with an opacity (τ) of around 2.8. Then, we can further assume as a first approximation that $C^{34}S$ $J = 2$–1 is optically thin in the expected case that $^{32}S/^{34}S \gg 3$ (see Sect. 4.1.2 for a confirmation of this assumption; see also Frerking et al. 1980 and Corby et al. 2018). In this case $^{13}C^{34}S$ $J = 2$–1 is definitively optically thin.

In the following, we consider an excitation temperature range of 9.4–300 K for our column density computations in order to obtain conservative estimates. Our column density values were calculated using Eq. (80) in Mangum & Shirley (2015) assuming a filling factor of unity. We then deduce from the integrated line intensities of $C^{34}S$ $J = 2$–1 and $^{13}C^{34}S$ $J = 2$–1, converted to column densities, a $^{12}C/^{13}C$ ratio of $22.1^{+3.3}_{-2.4}$. This value is used in Eqs. (1) and (2) (denoted R_C), and it agrees with previous observations in the GC within the uncertainties (~17–25; e.g. Frerking et al. 1980; Corby et al. 2018), and with the values derived from many transitions of complex organic molecules (COMs) in the hot core Sgr B2(N2) (Belloche et al. 2016; Müller et al. 2016), indicating that our approach is correct and confirming that $C^{34}S$ is indeed optically thin.

Assuming equal excitation temperatures (see Appendix B) and beam filling factors for ^{12}CS and ^{13}CS, the ^{13}CS $J = 2$–1 peak opacity $\tau(^{13}CS)$ can then be determined from

$$\frac{T_{MB}(^{12}CS)}{T_{MB}(^{13}CS)} = \frac{1 - e^{-\tau(^{13}CS)R_C}}{1 - e^{-\tau(^{13}CS)}}, R_C = \frac{^{12}C}{^{13}C}. \tag{1}$$

However, as there is a self-absorption feature at the centre of the ^{12}CS $J = 2$–1 and $J = 3$–2 profiles, we measure the line temperatures of both ^{12}CS and ^{13}CS at a redshifted velocity, $v_r = 63$ km s^{-1}, where the line shape is not affected by self-absorption. We can then retrieve the opacity at the systemic velocity, assumed to be the ^{13}CS $J = 2$–1 peak velocity, $v_{sys} = 46.94$ km s^{-1}, by considering a Gaussian distribution. First, we compute the opacities at v_r in the following way:

$$\frac{T_{MB}(^{12}CS_{v_r})}{T_{MB}(^{13}CS_{v_r})} = \frac{1 - e^{-\tau(^{13}CS_{v_r})R_C}}{1 - e^{-\tau(^{13}CS_{v_r})}}, R_C = \frac{^{12}C}{^{13}C}, \tag{2}$$

$$\frac{4.26 \pm 0.11}{0.24 \pm 0.11} = \frac{1 - e^{-22.1^{+3.3}_{-2.4}\tau(^{13}CS_{v_r})}}{1 - e^{-\tau(^{13}CS_{v_r})}}. \tag{3}$$

Here, $T_{MB}(^{12}CS_{v_r})$ and $T_{MB}(^{13}CS_{v_r})$ are the main-beam brightness temperatures of CS and ^{13}CS $J = 2$–1 at v_r. This results in $\tau(^{13}CS_{v_r}) = 0.02 \pm 0.01$, considering the same uncertainties for the peak temperatures as those obtained by performing a single Gaussian fit in those lines. We can now retrieve the opacity at the systemic velocity as

$$\tau(^{13}CS_{v_{sys}}) = \frac{\tau(^{13}CS_{v_r})}{e^{-(v_r - v_{sys})^2/2\sigma^2}}, \tag{4}$$

where σ is the full width at half maximum (FWHM) of $^{13}CS_{v_{sys}}$ divided by $\sqrt{8\ln(2)}$ (FWHM/$\sqrt{8\ln(2)}$ $= 9.46 \pm 0.12$ km s^{-1}) and

$\upsilon_{\rm sys} = 46.942 \pm 0.118$ km s^{-1}. We obtain $\tau(^{13}{\rm CS}_{v_{sys}}) = 0.08^{+0.05}_{-0.04}$. Multiplying this by $R_{\rm C}$, we obtain $\tau(^{13}{\rm CS}_{v_{sys}})R_{\rm C} = \tau({\rm CS}_{v_{sys}}) = 1.9^{+1.1}_{-0.8}$, consistent with previous observations ($\tau({\rm CS}_{v_{sys}})$ ~2.8; Tsuboi et al. 1999). The uncertainty on $\upsilon_{\rm sys}$ corresponds to a 0.15% variation in the $\tau({\rm CS}_{v_{sys}})$ value in the worst case. Therefore, it is ignored in the following.

4.1.1. A ^{32}S/^{34}S ratio obtained through the double isotope method

As we have seen, CS must be moderately optically thick. Then, the ^{32}S/^{34}S isotope ratios cannot be determined from the observed $N(^{12}{\rm CS})/N({\rm C}^{34}{\rm S})$ ratio. Instead, we can use the column densities of ^{13}CS and C^{34}S by realistically assuming that those lines are optically thin (see Sect. 4.1). Therefore, we have derived the values for ^{32}S/^{34}S making use of the carbon isotope ratio mentioned above, in the following way:

$$\frac{^{32}{\rm S}}{^{34}{\rm S}} = \frac{^{12}{\rm C}}{^{13}{\rm C}} \frac{N(^{13}{\rm CS})}{N({\rm C}^{34}{\rm S})}. \tag{5}$$

From Eq. (5) we obtain a ^{32}S/^{34}S $J = 2$–1 ratio of $16.3^{+3.0}_{-2.4}$. By using the ^{13}CS and C^{34}S $J = 6$–5 transitions, we obtain a ^{32}S/^{34}S $J = 6$–5 ratio of $15.8^{+4.2}_{-3.4}$. This agreement within the uncertainties can be taken as another argument in favour of the low opacity of C^{34}S and the subsequent validity of our assumptions and calculations. If some of the C^{34}S lines in the rotational ladder were not optically thin, we would expect different $N(^{13}{\rm CS})/N({\rm C}^{34}{\rm S})$ ratios in the $J = 2$–1 and 6–5 transitions due to photon trapping leading to higher excitation temperatures in the more abundant isotopologue, which is not observed.

4.1.2. ^{32}S/^{34}S ratio from direct observations

As we have measured the ^{13}C^{34}S $J = 2$–1 transition, we can also obtain the ^{32}S/^{34}S ratio directly from

$$\frac{^{32}{\rm S}}{^{34}{\rm S}} = \frac{N(^{13}{\rm CS})}{N(^{13}{\rm C}^{34}{\rm S})}. \tag{6}$$

Using this we obtain a ^{32}S/^{34}S $J = 2$–1 ratio of $16.3^{+2.1}_{-1.7}$, consistent with the ratio obtained through the double-isotope method in Eq. (5) and again indicating that our initial assumptions concerning line saturation were correct. In the following, we use the latter value for our analysis because it was determined in the most direct way. In order to estimate the opacity of CS from C^{34}S (see Sect. 4.1.3), we use this C^{32}S/C^{34}S $J = 2$–1 ratio of $16.3^{+2.1}_{-1.7}$ as the sulphur isotopic ratio ^{32}S/^{34}S and call it $R_{\rm S}$.

To compare our results with those of Chin et al. (1996), we also derived a sulphur ratio from the integrated intensities: $^{32}{\rm S}/^{34}{\rm S} \sim I(^{13}{\rm CS})/I(^{13}{\rm C}^{34}{\rm S})$. This results in a ^{32}S/^{34}S value of $18.6^{+2.2}_{-1.8}$. The differences between the column density and integrated intensity ratios are due to the rotational partition functions, rotational constants, and Einstein A-coefficients for spontaneous emission of radiation that slightly differ for the different isotopologues.

4.1.3. CS and C^{34}S $J = 3$–2 opacities

Now we are able to determine the opacities of CS and C^{34}S $J = 3$–2 by proceeding in the same way as in Eqs. (2) and (4), but considering this time the sulphur ratio. Here, as in Eq. (2), we also assume equal excitation temperatures (see Appendix B) and beam filling factors, this time for ^{12}CS and C^{34}S $J = 3$–2:

Table 3. Summary for our carbon and sulphur column density ratio calculations in the +50 km s^{-1} Cloud.

$^{12}{\rm C}/^{13}{\rm C}\,^{(a)}$ $J = 2$–1	$^{32}{\rm S}/^{34}{\rm S}\,^{(b)}$ $J = 2$–1/$J = 6$–5	$^{32}{\rm S}/^{34}{\rm S}\,^{(c)}$ $J = 2$–1	$^{34}{\rm S}/^{33}{\rm S}\,^{(d)}$ $J = 2$–1
$22.1^{+3.3}_{-2.4}$	$16.3^{+3.0}_{-2.4}/15.8^{+4.2}_{-3.4}$	$16.3^{+2.1}_{-1.7}$	4.3 ± 0.2

Notes. $^{(a)}$From $N({\rm C}^{34}{\rm S})/N(^{13}{\rm C}^{34}{\rm S})$ $J = 2$–1 lines, as described in Sect. 4.1. $^{(b)}$Through the double isotope method in Sect. 4.1.1. $^{(c)}$From direct observations in Sect. 4.1.2. $^{(d)}$Sect. 4.1.4.

$$\frac{T_{\rm MB}(^{12}{\rm CS}_{v_r})}{T_{\rm MB}({\rm C}^{34}{\rm S}_{v_r})} = \frac{1 - {\rm e}^{-\tau({\rm C}^{34}{\rm S}_{v_r}){\rm R_S}}}{1 - {\rm e}^{-\tau({\rm C}^{34}{\rm S}_{v_r})}}, R_{\rm S} = \frac{^{32}{\rm S}}{^{34}{\rm S}}. \tag{7}$$

From Eq. (7), $\tau({\rm C}^{34}{\rm S}_{v_r}) = 0.01$–0.03. Following the formalism in Eq. (4), we obtain a $\tau({\rm C}^{34}{\rm S}_{v_{\rm sys}})$ value of 0.05–0.15. Entering this value and replacing $\tau({\rm C}^{34}{\rm S}_{v_{\rm sys}})R_{\rm S}$ by $\tau({\rm CS}_{v_{\rm sys}})$, the ${\rm CS}_{v_{\rm sys}}$ opacity results in a proper range of 1.0–2.8, considering throughout this calculation that this latter value cannot lie below unity, since CS shows clear signs of optical thickness (see Sect 4.1). This is consistent with previous observations (Tsuboi et al. 1999). All the derived opacities are summarized in Table 2.

4.1.4. ^{34}S/^{33}S ratio from direct observations

The C^{33}S $J = 2$–1 line was also observed. This offers the possibility of obtaining the ^{34}S/^{33}S ratio for the GC. Since C^{33}S is less abundant than C^{34}S, we can expect a clearly optically thin profile. This ratio is easily obtained by

$$\frac{^{34}{\rm S}}{^{33}{\rm S}} = \frac{N({\rm C}^{34}{\rm S})}{N({\rm C}^{33}{\rm S})}. \tag{8}$$

We obtain a ^{34}S/^{33}S ratio of 4.3 ± 0.2 for the +50 km s^{-1} Cloud. If we take the integrated intensities instead of the column densities, this ratio would be 4.2 ± 0.2, consistent with the lower end of the range of ratios obtained by Chin et al. (1996), who derived ^{34}S/^{33}S ratios between 4.38 and 7.53, irrespective of Galactic radius. Whether this is a first hint of a gradient remains to be seen. Better data from the Galactic disc are necessary to tackle this question.

4.2. Modelling the Sgr B2(N) data

Here, we rely on the modelling of the absorption profiles of the isotopologues of CS carried out by Thiel (2019) using the EMoCA survey, following the same method as Thiel et al. (2019). They used the software Weeds (Maret et al. 2011) to model the absorption profiles. Their work assumes that all transitions of a molecule have the same excitation temperature and that the beam filling factor is unity, which is a reasonable assumption given that most absorption features are extended on scales of 15″ or beyond in the ALMA maps (see Thiel et al. 2019, their Sect. 5.4), while the beam size is 1.″6 (see Sect. 2.2, Fig. 1, and Table 1). The fitted parameters were the column density, line width, and the centroid velocity, under the assumption that the excitation temperature is equal to the temperature of the cosmic microwave background (2.73 K).

We selected four continuum peaks inside Sgr B2(N) (Fig. 1). We excluded the two strong continuum peaks at which the

Table 4. Isotopic ratios determined in the envelope of Sgr B2(N) (^{13}CS/^{13}C^{34}S and C^{34}S/^{13}C^{34}S) and in GC clouds along the line of sight to Sgr B2(N) (CS/C^{34}S) using absorption lines of CS isotopologues.

Isotopic ratios determined in the envelope of Sgr B2(N)

$\Delta x^{(a)}$ (″)	$\Delta y^{(a)}$ (″)	$V_{\rm LSR}$ (km s^{-1})	N(C^{34}S)$^{(b)}$ (10^{12} cm^{-2})	N(^{13}CS)$^{(b)}$ (10^{12} cm^{-2})	N(^{13}C^{34}S)$^{(b)}$ (10^{12} cm^{-2})	FWHM$^{(c)}$ (km s^{-1})	^{13}CS/^{13}C^{34}S	C^{34}S/^{13}C^{34}S
1.8	11.1	71.6	70.0 ± 1.1	35.0 ± 1.2	2.5 ± 0.6	4.0	14.0 ± 3.3	28.0 ± 6.6
1.8	11.1	65.8	120.0 ± 1.6	90.0 ± 2.2	3.5 ± 0.7	5.0	25.7 ± 5.3	34.3 ± 7.1
1.8	11.1	61.1	65.0 ± 1.1	38.0 ± 1.4	2.6 ± 0.7	5.0	14.6 ± 4.1	25.0 ± 7.0
9.3	1.8	71.1	39.0 ± 0.9	30.0 ± 0.9	1.2 ± 0.4	4.0	25.0 ± 8.8	32.5 ± 11.4
9.3	1.8	63.8	200.0 ± 2.3	160.0 ± 2.1	8.2 ± 0.8	7.5	19.5 ± 2.0	24.4 ± 2.4
4.8	9.3	80.6	94.0 ± 3.1	74.0 ± 3.7	7.0 ± 1.9	9.0	10.6 ± 3.0	13.4 ± 3.7
4.8	9.3	61.3	280.0 ± 6.5	120.0 ± 4.7	8.0 ± 2.0	9.5	15.0 ± 3.8	35.0 ± 8.8
6.6	3.3	64.2	420.0 ± 4.5	280.0 ± 4.3	15.0 ± 1.5	12.5	18.7 ± 1.8	28.0 ± 2.7
average							17.9 ± 5.0	27.6 ± 6.5

Isotopic ratios determined in GC clouds along the line of sight to Sgr B2(N)

$\Delta x^{(a)}$ (″)	$\Delta y^{(a)}$ (″)	$V_{\rm LSR}$ (km s^{-1})	N(CS)$^{(b)}$ (10^{12} cm^{-2})	N(C^{34}S)$^{(b)}$ (10^{12} cm^{-2})	FWHM$^{(c)}$ (km s^{-1})	CS/C^{34}S
1.8	11.1	−73.3	26.0 ± 0.7	1.4 ± 0.5	3.5	18.6 ± 6.3
1.8	11.1	−81.2	45.0 ± 0.9	2.5 ± 0.6	5.0	18.0 ± 4.0
1.8	11.1	−104.2	58.0 ± 1.0	3.0 ± 0.6	5.0	19.3 ± 3.6
9.3	1.8	−82.5	16.0 ± 0.7	1.4 ± 0.4	2.5	11.4 ± 3.7
9.3	1.8	−92.6	20.0 ± 0.7	1.2 ± 0.5	2.5	16.7 ± 7.3
9.3	1.8	−104.7	63.0 ± 1.1	3.0 ± 0.7	6.5	21.0 ± 4.9
6.6	3.3	−71.8	65.0 ± 1.5	7.2 ± 0.8	5.5	9.0 ± 1.0
6.6	3.3	−79.8	29.0 ± 1.0	1.8 ± 0.6	4.0	16.1 ± 5.8
Average						16.3 ± 3.8

Notes. $^{(a)}$The offset positions (Δx, Δy) in units of arcseconds: (1.8, 11.1), (9.3, 1.8), (4.8,9.3), and (6.6, 3.3), correspond to K4, K6$_{\rm shell}$, K5$_{\rm shell}$, and K6$_{\rm shell,a}$, in Fig. 1, respectively. See the caption to Fig. 1 and the green crosses in the image. $^{(b)}$Column densities determined using Weeds. $^{(c)}$It is assumed that all isotopologues have the same FWHM. The average isotope ratios presented by the lowest line of each panel are unweighted and provide the standard deviation of an individual measurement (without dividing by the square root of the number of ratios).

main hot cores N1 and N2 are located because at these positions the spectra are full of emission lines of organic molecules (e.g. Bonfand et al. 2017) contaminating the carbon monosulfide absorption features. The offsets to the centre of the observed field are (1″.8, 11″.1), (9″.3, 1″.8), (4″.8, 9″.3), and (6″.6, 3″.3) (see Fig. 1 and Table 4). The observed absorption profiles and the corresponding Weeds models for the four isotopologues and the four positions are shown in Fig. 3. Using their results for the column densities, we determined the isotopic ratios CS/C^{34}S, ^{13}CS/^{13}C^{34}S, and C^{34}S/^{13}C^{34}S. We determined those ratios separately for the envelope of Sgr B2(N) and some GC clouds along the l.o.s. to Sgr B2(N), the latter with velocities lower than −50 km s^{-1}. We only determine the ratio CS/C^{34}S in those cases where the absorption caused by CS is not optically thick.

The resulting unweighted average values of the isotopic ratios are listed in Table 4, namely a ^{32}S/^{34}S isotope ratio of 16.3 ± 3.8 in the GC l.o.s. clouds towards Sgr B2(N) and 17.9 ± 5.0 in the envelope of Sgr B2(N). For this envelope we obtain a ^{12}C/^{13}C ratio of 27.6 ± 6.5. It should be noted that our uncertainties correspond to the standard deviation for independent measurements, i.e. without dividing it by the square root of the number of studied spectral components.

4.3. Discussion on the validity of using C^{32}S/C^{34}S as a proxy for ^{32}S/^{34}S

Chin et al. (1996) estimated that sulphur fractionation is marginal for CS isotopic ratios. If the bulk of the CS emission, which allows us to measure rare isotopes, arises from the densest parts of the molecular clouds only, the heating from the massive stars should inhibit significant fractionation (Chin et al. 1996). In that case, CS emission can be used directly to determine sulphur isotope ratios from such sources.

In their oxygen fractionation study, Loison et al. (2019) analyse sulphur fractionation including CS. Some sulphur fractionation is induced at low temperature by the ^{34}S^{+} + CS → S^{+} + C^{34}S reaction. To determine the potential fractionation of sulphur, we used the network from Loison et al. (2019) in the +50 km s^{-1} Cloud, the l.o.s. clouds towards Sgr B2(N) and the envelope of Sgr B2(N), with realistic physical conditions for these objects, in particular a much higher value of the cosmic-ray ionization rate (CRIR) than the usual value in more local dense molecular clouds. Some typical results are shown in Fig. 4 and are described below.

In the simulations, all elements with an ionization potential below the maximum energy of ambient UV photons (13.6 eV)

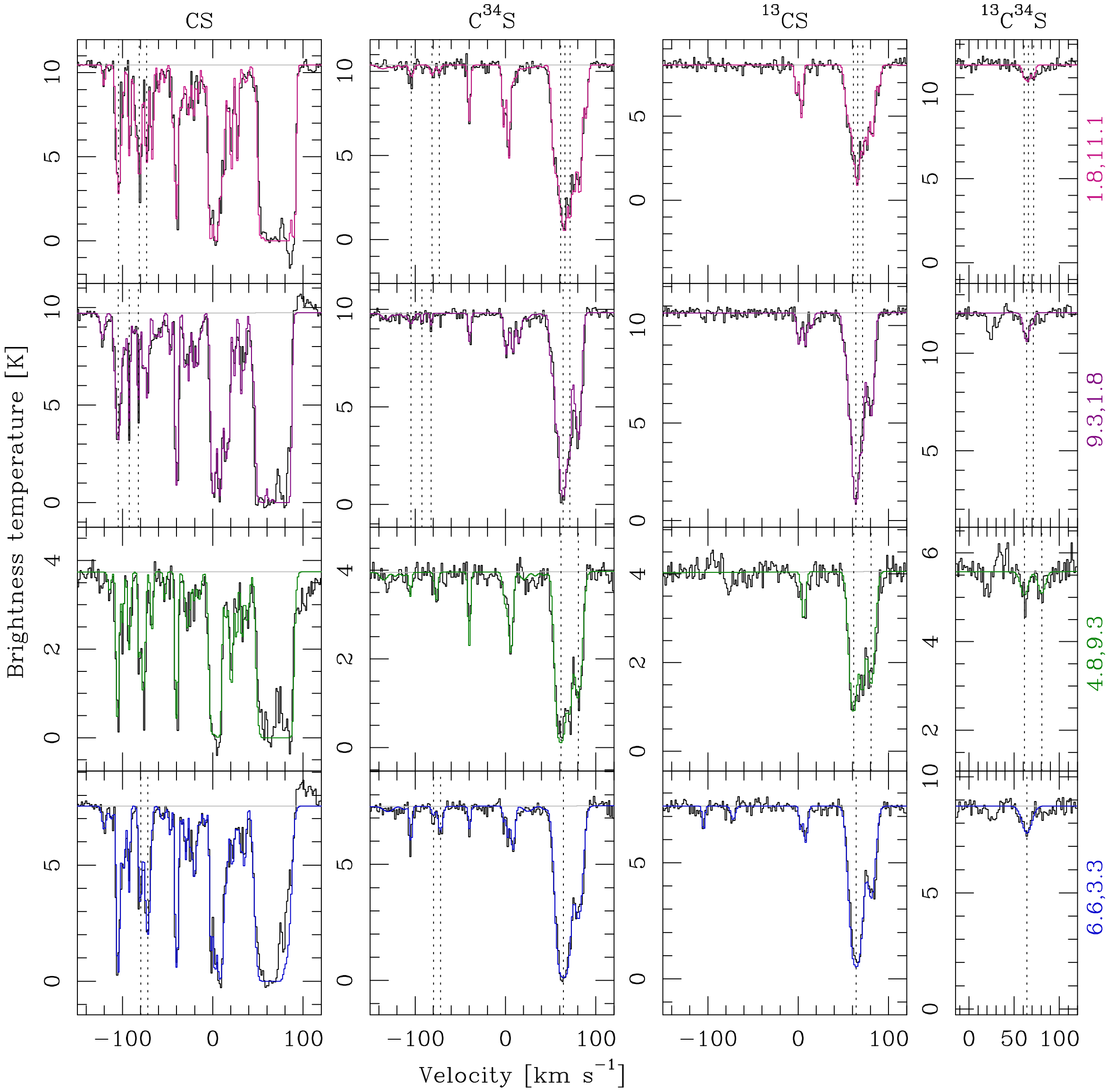

Fig. 3. EMoCA absorption spectra of four isotopologues of CS towards four positions in Sgr B2(N). The offsets (in units of arcseconds, see Table 4 and Fig. 1) from the phase centre are indicated at the right of each row. The observed spectra are shown in black and the synthetic spectra in magenta, purple, green, and blue, depending on the position. The synthetic spectra were obtained by Thiel (2019). The dotted vertical lines indicate the velocities at which we determined the isotopic ratios using the corresponding isotopologue. The velocities are listed in Table 4. The grey horizontal lines show the continuum level.

are assumed to be initially in an atomic, singly ionized state. We considered all sulphur in the S$^+$ form without depletion, and we performed some tests to quantify the effect of depletion, which is low (see below). Hydrogen, with its high degree of self-shielding, is taken to be entirely molecular. The initial abundances are similar to those in Table 1 of Hincelin et al. (2011), the C/O elemental ratio being equal to 0.7 in our study. We verified that the initial state of carbon and nitrogen (C$^+$ versus CO and N versus N$_2$) have very little influence on sulphur fractionation (less than 4% for the typical ages considered: 10^{5-6} yr). The estimation of the dense cloud ages is deduced from clouds with similar density (10^4 to a few 10^5 cm^{-3}) for which the age is given by the best agreement between calculations and observations for key species given by the so-called distance of disagreement (Wakelam et al. 2006). By key species we mean species typically encountered in molecular clouds such as HCN, HNC, CN, CH, C2H, *c*–C3H, *c*–C3H2, CO, H$_2$CO, CH$_3$OH, NO, SO, CS, HCS$^+$, and H$_2$CS (see e.g. Wakelam et al. 2010; Agúndez & Wakelam 2013; Agúndez et al. 2019).

For Fig. 4a, which represents conditions in the +50 km s^{-1} Cloud, we adopted a density of 10^5 cm^{-3} and a CRIR of $\zeta^{\mathrm{H}_2} = 7 \times 10^{-16}$ s^{-1} based on measurements in hot cores of Sgr B2(N) by using COMs (Bonfand et al. 2019). For Figs. 4b and c, which represent the conditions for the envelope of Sgr B2(N) and the l.o.s. clouds towards Sgr B2(N), respectively, we chose a density of 10^4 cm^{-3}, an upper limit for the volume density in those regions (see Thiel et al. 2019, their Table 12), in order to avoid possible UV heating in our models. Due to this high density, we have adopted a CRIR of $\zeta^{\mathrm{H}_2} = 3 \times 10^{-15}$ s^{-1}, i.e. one order of magnitude lower than the value usually obtained in the l.o.s. of translucent and diffuse clouds towards the Galactic centre, but within the range obtained for the nuclear ~100 pc of our Galaxy (Indriolo et al. 2015; Le Petit et al. 2016). The ^{32}S/^{34}S isotope ratio chosen for each simulation is that obtained from

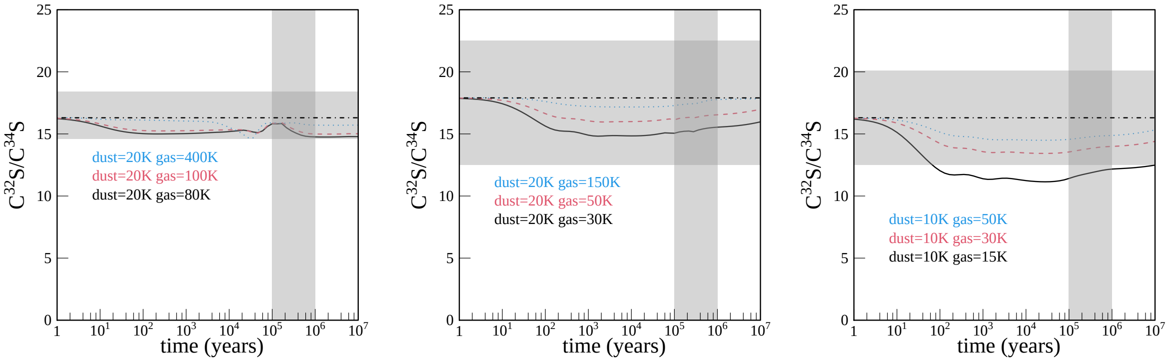

(a) (b) (c)

Fig. 4. Calculated abundance ratios of gas phase species $C^{32}S/C^{34}S$ as a function of cloud age for conditions in (*a*) the +50 km s^{-1} Cloud, (*b*) the envelope of Sgr B2(N), and (*c*) l.o.s. clouds towards Sgr B2(N) (see Sect. 4.2 for details). Low values for the gas temperatures were chosen to illustrate an upper limit for fractionation. The vertical grey loci represent values given by the most probable chemical age. The observational results from this study are illustrated as horizontal light grey rectangles (including the uncertainties).

our measurements, namely $16.3^{+2.1}_{-1.7}$, 17.9 ± 5.0, and 16.3 ± 3.8 for Figs. 4a, b, and c, respectively.

Despite the limited literature on the subject, according to models from Laas & Caselli (2019), the +50 km s^{-1} Cloud is the only object in this study that could show signs of sulphur depletion. However, for a depletion level of up to 90%, our models give results consistent with no sulphur depletion (which is the case for the results shown in Fig. 4) because of the high temperatures that prevent any efficient fractionation. It should be noted that if this cloud's chemistry was determined in an earlier colder evolutionary period with possibly significant sulphur fractionation, CS, in contrast to CO, could not accumulate because it would have been destroyed by protonation as the dissociative recombination of HCS^+ leads mainly to S + CH and not to CS + H (see Appendix A). Therefore, the memory effect for the CS fractionation of such a dense cloud is small. For the l.o.s. clouds towards Sgr B2(N) and the envelope of Sgr B2(N), some runs (those shown in Fig. 4) give some sulphur fractionation when the gas temperature is low. This is due to the combination of low density limiting the depletion of sulphur and a high CRIR ($\zeta^{H_2} = 3 \times 10^{-15}$ s^{-1}). These characteristics induce an elevated concentration of S^+ in the gas phase and then a ^{34}S enrichment through the $^{34}S^+ + CS \rightarrow S^+ + C^{34}S$ reaction (see Table 2 in Loison et al. 2019). It should be noted that the cases with some ^{34}S enrichment only concern low kinetic temperatures, and that this relatively low enrichment will be even lower with some sulphur depletion. This depletion is not well constrained in the +50 km s^{-1} Cloud, the l.o.s. clouds towards Sgr B2(N), and the envelope of Sgr B2(N), but it is high for some cold dense molecular clouds (between 10 and 25 for the dark cloud L1544 Barnard 1b (Fuente et al. 2016) and even up to 200 for the dark cloud L1544 (Vastel et al. 2018).

The extremely low gas temperature cases in our models (black lines in Fig. 4) are shown to demonstrate the dependence of sulphur depletion on gas temperature. Since Galactic centre molecular cloud temperatures are higher (Ginsburg et al. 2016), CS shows likely very little fractionation in ^{34}S for the purposes of this study and our measurements of the $C^{32}S/C^{34}S$ ratio are a good approximation to the $^{32}S/^{34}S$ ratio (even if the values thus obtained may be slightly underestimated when considering the results of the models). We can then expect a $\lesssim$10% increase in the $^{32}S/^{34}S$ ratios obtained for the +50 km s^{-1} Cloud in Fig. 4a and slightly more for the l.o.s. clouds towards Sgr B(N) and its envelope ($\lesssim$15%), considering the conditions labelled in red and blue in Figs. 4b and c.

Some measurements using the double-isotope ratio method (see Sect. 4.1.1), which take the $^{12}C/^{13}C$ ratio into account, may induce a bias since CS may show a non-negligible fractionation into ^{13}C. There is no specific study of the ^{13}C fractionation of CS, but the reactivity of C^+ and C, in particular with CO and CN (but also with CS), can induce an enrichment or depletion in ^{13}C of carbonaceous species including CS (Smith & Adams 1980; Roueff et al. 2015). In that case, the good agreement between the sulphur fractionation measurements using $C^{32}S/C^{34}S$ and the values obtained using the double-isotope method also suggests a low ^{13}C fractionation of CS. This result is interesting and could initiate future studies on the modelling of ^{13}C fractionation in CS.

5. Our results in the light of previous studies

If we assume that the gradient proposed by Chin et al. (1996) would also be valid in the Galactic centre region, the $^{32}S/^{34}S$ ratio would decrease to values of 4.1 ± 3.1 at the centre of our Galaxy, i.e. to a very low value, only 1/4 of the solar system ratio. This value is less than one fourth of the value derived from integrated intensities in this work, $18.6^{+2.2}_{-1.8}$.

This difference can be explained in terms of the $^{12}C/^{13}C$ ratios assumed in Chin et al. (1996), required to obtain the $^{32}S/^{34}S$ ratio through the double-isotope method by using the formalism of Eq. (5) (although using intensities instead of column densities). The $^{12}C/^{13}C$ ratios were derived from the relation found by Wilson & Rood (1994) of $^{12}C/^{13}C = (7.5 \pm 1.9)$ $(D_{GC}/\mathrm{kpc}) + (7.6 \pm 12.9)$ that gives a value of $7.6^{+12.9}_{-7.6}$ for the Galactic centre, although the authors claimed a value of ~20 near the Galactic nucleus (Wilson & Rood 1994, Sect 5.1). This provides an idea of the large uncertainty in this relation.

On the other hand, we are confident about our $^{12}C/^{13}C$ ratio of $22.1^{+3.3}_{-2.4}$ (Sect. 4.1) for two reasons: first, the agreement between the $^{32}S/^{34}S$ ratio obtained through the double-isotope method (Sect. 4.1.1), which makes use of the $^{12}C/^{13}C$ ratio, and the $^{32}S/^{34}S$ ratio obtained directly from $^{13}CS/^{13}C^{34}S$ (Sect. 4.1.2), i.e. independently of the carbon ratio (this also indicates that the carbon fractionation is low, as described in Sect. 4.3) and second, its proximity to the ratio obtained through decades of observations in the nuclear regions of our Galaxy ($^{12}C/^{13}C$ = 17–25, Frerking et al. 1980; Wilson & Rood 1994; Milam et al. 2005; Müller et al. 2008; Corby et al. 2018), including LTE modelling of complex organic molecules

(Belloche et al. 2016; Müller et al. 2016). There is no abrupt redirection in the $^{12}C/^{13}C$ ratio (e.g. Henkel et al. 1985).

Recently, Corby et al. (2018) found $^{32}S/^{34}S$ ratios mostly in the 5–10 range, based on $C^{32}S$ and $C^{34}S$ $J = 1–0$ absorption lines from diffuse clouds near the GC, with a resolution of ∼15″. Considering their data in the –73 to –106 km s^{-1} velocity range, corresponding to our GC l.o.s. clouds towards Sgr B2(N), their observations reach values between 6.6 ± 6 and 29 ± 14, consistent with our values between 9.0 ± 1.0 and 21.0 ± 4.9 (Table 4, lower panel).

In addition, Armijos-Abendaño et al. (2015), with a resolution of ∼30″–38″ , found values of ≳22 and 8.7 ± 1.3 for $^{32}S/^{34}S$ isotope ratios in l.o.s. clouds towards Sgr A and Sgr B2, respectively, consistent with previous estimations (Frerking et al. 1980). However, their sulphur ratios were obtained from OCS/OC^{34}S, with OCS being potentially optically thick and OC^{34}S spectra being badly affected by band pass ripples, possibly providing only tentative detections. So we propose a more conservative lower limit for the l.o.s. clouds towards Sgr A of ∼10 and we suggest that the uncertainty for their ratio in Sgr B2 was underestimated.

Both Corby et al. (2018) and Armijos-Abendaño et al. (2015) employed integrated column density ratios, so we should compare those measurements with our normal $^{32}S/^{34}S$ isotope ratio estimation, that is $16.3^{+2.1}_{-1.7}$ for the +50 km s^{-1} Cloud (as an approximation for their l.o.s. clouds towards Sgr A) and 16.3 ± 3.8 for the l.o.s. clouds towards Sgr B2 (see Table 4). Our data represent a significant improvement in terms of accuracy and precision with respect to those previous observations. In addition, our estimation of 17.9 ± 5.0 for the envelope of Sgr B2(N) agrees with both estimations for the +50 km s^{-1} Cloud and also with previous calculations for the whole Sgr B2 region: ∼16, from the OCS/OC^{34}S ratio, which is claimed to be derived from optically thin lines (Goldsmith & Linke 1981).

Cutting-edge model calculations performed by Kobayashi et al. (2011) relate sulphur isotope ratios ($^{32}S/^{33,34,36}S$) with metallicity ([Fe/H][5]). We can use this relation in combination with a given metallicity gradient along the Milky Way ([Fe/H] versus D_{GC}/kpc), to derive a $^{32}S/^{34}S$ versus D_{GC}/kpc relation and compare it with our measurements.

Table 3 of Kobayashi et al. (2011) gives values for the $^{32}S/^{34}S$ ratio as a function of [Fe/H] over the range $-0.5 \leq \mathrm{[Fe/H]} \leq 0.0$. We can derive the following relation by interpolating their data:

$$\frac{^{32}S}{^{34}S} = -19.8 \times \mathrm{[Fe/H]} + 23.2. \tag{9}$$

Extrapolating up to $\mathrm{[Fe/H]} \leq 0.85$, we can account for the inner part of our Galaxy. Then, to relate $^{32}S/^{34}S$ to the galactocentric distance, we can make use of the relations obtained by Bovy et al. (2014) and Genovali et al. (2014), valid for $5 \leq D_{GC}/\mathrm{kpc} \leq 14–19$, respectively:

$$\mathrm{[Fe/H]} = (-0.09 \pm 0.01) \times (D_{GC}/\mathrm{kpc} - 8) + 0.03 \pm 0.01, \tag{10}$$

$$\mathrm{[Fe/H]} = (-0.06 \pm 0.002) \times D_{GC}/\mathrm{kpc} + 0.57 \pm 0.02, \tag{11}$$

and combine them with Eq. (9), to obtain the following relations:

$$\frac{^{32}S}{^{34}S} = (1.8 \mp 0.2) \times (D_{GC} - 8\,\mathrm{kpc}) + 22.6 \mp 0.2, \tag{12}$$

$$\frac{^{32}S}{^{34}S} = (1.2 \mp 0.04) \times D_{GC} + 11.9 \mp 0.4. \tag{13}$$

Equations (12) and (13) are plotted in Fig. 5 as hatched-shaded regions. As described in the legend, their extrapolations down to 2.53 kpc, following Inno et al. (2019, their Fig. 11), for both Eqs. (10) and (11), are indicated as hatched regions only.

Additionally, we have accounted for iron abundances obtained from high-resolution near-infrared observations by Davies et al. (2009) and Najarro et al. (2009) in the inner 30 pc of the Galaxy (see also Kovtyukh et al. 2019). Their measurements are [Fe/H] = 0.1 ± 0.2 and −0.06 ± 0.2, respectively, and we converted them to $^{32}S/^{34}S$ ratios of 21.2 ± 4 and 24.4 ± 4 by applying Eq. (9).

In summary, the relations of both Bovy et al. (2014) and Genovali et al. (2014), through Eq. (9), give results closer to those obtained from the double-isotope method (Eq. (5)), considering $^{12}C/^{13}C$ ratios by Yan et al. (2019) in combination with the $^{13}C^{32}S/C^{34}S$ ratios from Chin et al. (1996), as can be seen in Fig. 5 (dotted blue line). In the nuclear region of the Galaxy the Davies et al. (2009) and Najarro et al. (2009) observations, when accounting for Eq. (9), are both consistent with our measurements for the +50 km s^{-1} Cloud and the envelope of Sgr B2(N).

6. Discussion

Among the four stable sulphur isotopes (^{32}S, ^{33}S, ^{34}S, and ^{36}S), ^{32}S is a primary nucleus which could be synthesized in a single generation of massive stars. ^{32}S is mostly formed during stages of hydrostatic and explosive oxygen-burning (Wilson & Matteucci 1992) either preceding a Type II supernova event or in a Type Ia supernova, where two ^{16}O nuclei collide to form ^{28}Si and ^{4}He, with these products subsequently fusing to yield ^{32}S. Type II supernovae synthesize around ten times more ^{32}S than Type I supernovae, and occur roughly 5 times as often as those of Type I (Hughes et al. 2008). ^{33}S is partly a secondary isotope because it can be formed by neutron capture from newly made ^{32}S if the star not only has hydrogen and helium, but also carbon and oxygen in its initial composition (Clayton 2007). It is synthesized in hydrostatic and explosive oxygen- and neon-burning, also produced in massive stars. ^{34}S is partly a secondary product because it can be formed from newly made ^{32}S and ^{33}S by neutron capture, but also during oxygen burning in supernovae like the primary isotope, ^{32}S (Hughes et al. 2008, and references therein). While the comprehensive calculations of Woosley & Weaver (1995) identify ^{32}S as a primary isotope, the same study also found that ^{34}S is not a clean primary isotope; its yields decrease with decreasing metallicity. However, they identify ^{33}S as a primary isotope, in contradiction with later findings (Clayton 2007). ^{36}S is probably the only purely secondary sulphur isotope, being produced by s-process nucleosynthesis in massive stars (Thielemann & Arnett 1985; Mauersberger et al. 1996) and also by explosive C and He burning and via direct neutron capture from ^{34}S, according to models (Pignatari et al. 2016). ^{36}S could be the only S isotope not only produced from massive stars but also, to a lesser extent, from AGB stars (Pignatari et al. 2016). However, lines from $C^{36}S$ are too weak to be detected in this study. Massive stars, as well as Type Ib/c and II supernovae, appear to slightly overproduce ^{34}S and underproduce ^{33}S compared to ^{32}S, relative to the solar vicinity (Timmes et al. 1995).

The main result of our study is that the previous trend observed by Chin et al. (1996) is broken near the centre of our Galaxy. In other words, the increase in $^{32}S/^{34}S$ with D_{GC} is not valid in the Galactic centre region. The values of $16.3^{+2.1}_{-1.7}$ from the +50 km s^{-1} Cloud and 16.3 ± 3.8 and 17.9 ± 5.0

---

[5] Where $\mathrm{[Fe/H]} = \log_{10}([N_{Fe}/N_{H}])_{star} - \log_{10}([N_{Fe}/N_{H}])_{sun}$.

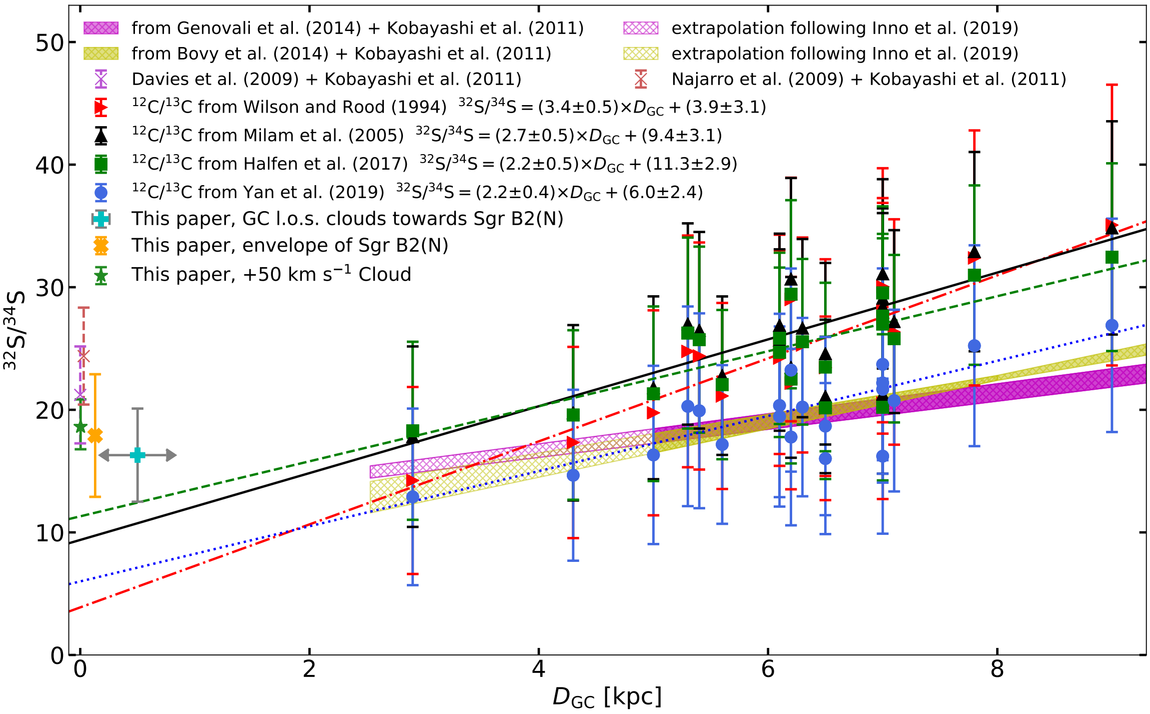

Fig. 5. Sulphur isotope $^{32}S/^{34}S$ ratio variation when accounting for different carbon $^{12}C/^{13}C$ ratios as a function of galactocentric radius, D_{GC} (e.g. Wilson & Rood 1994; Halfen et al. 2017; Milam et al. 2005; Yan et al. 2019) (for the implemented $^{13}C^{32}S/C^{34}S$ ratios, see Chin et al. 1996). The $^{32}S/^{34}S$ to D_{GC} relations obtained from a linear least-squares fit to weighted data (taken as $1/\sigma$, see Sect. 5) are shown and plotted as lines with different styles (see legend). The $^{32}S/^{34}S$ ratios from this work are shown in orange, cyan, and light green. All ratios were gleaned from integrated intensity ratios except for Sgr B2(N) (see Fig. 3), where our derived integrated column density ratios are used. Possible differences between integrated column density ratios and line intensity ratios for the mean values in Sgr B2(N) fall inside the error bars. For the case of the GC l.o.s. clouds towards Sgr B2(N), their distances are uncertain and they are believed to be located within 1 kpc from the GC (see Sect. 3). As described in Sect. 5, the purple and yellow hatched-shaded loci are derived from [Fe/H] vs D_{GC} relations obtained by Bovy et al. (2014) and Genovali et al. (2014), after accounting for the models of Kobayashi et al. (2011); hatched-only loci correspond to an extrapolation of those relations, following Inno et al. (2019). Using the same models, two $^{32}S/^{34}S$ ratios are included. These ratios are derived from iron abundances measured in the central 30 pc of the Galaxy by Davies et al. (2009) and Najarro et al. (2009). A zoom on the results of our study displayed in the left part of the figure is shown in Fig. C.1.

from the GC l.o.s. clouds towards Sgr B2(N) and its envelope, respectively, contrast with the expected ∼5–10 regardless of the value of $^{12}C/^{13}C$ adopted (see Fig. 5) when accounting for the $^{13}C^{32}S/C^{34}S$ ratios used in Chin et al. (1996). It is also worth mentioning that our $^{32}S/^{34}S$ isotope ratios derived from absorption lines from diffuse or translucent clouds (Sgr B2(N)) are consistent with values derived from emission lines from a prominent star-forming region with dense molecular gas (the +50 km s^{-1} Cloud), even though the chemistry for CS formation is completely different in those regions (see Appendix A).

Frerking et al. (1980), even before the $^{32}S/^{34}S$ slope was found, suggested values for $^{32}S/^{34}S$ of ∼22 for the Galactic centre. Therefore, the sulphur ratio seems to be constant, or even increases with decreasing D_{GC}, within the inner 2.9 kpc of the Milky Way, in contrast to $^{12}C/^{13}C$ (e.g. Yan et al. 2019), $^{14}N/^{15}N$ (e.g. Adande & Ziurys 2012), and $^{18}O/^{17}O$ (Wouterloot et al. 2008; Zhang et al. 2015). Intriguingly, $^{32}S/^{34}S$ behaves in a similar way to $^{16}O/^{18}O$ (Polehampton et al. 2005), two nuclei with the bulk of their formation taking place in massive stars ($\geq 10\,M_{\odot}$) (Clayton 2007). This is surprising because ^{34}S is a tracer of secondary processing as ^{13}C and ^{15}N, and therefore its abundance is expected to increase in the same manner as observed for those isotopes.

The fact that sulphur traces late evolutionary stages of massive stars can give a clue to this difference in comparison to C and N, which give information on CNO and helium burning (Chin et al. 1996). Due to their short lives, the star formation rate of massive stars can be traced by their SN rate. Although the amount of ^{34}S is related to metallicity, which decreases with increasing galactocentric radius especially in spiral galaxies (e.g. as observed from oxygen, Henry & Worthey 1999), leading to a trend similar to C and N, the production of ^{34}S is mostly related to SNe II, which show a dip in the inner regions of our Galaxy and other spiral galaxies (Anderson & James 2009), in good agreement with our higher than expected $^{32}S/^{34}S$ ratios in the Galactic centre. However, these results are still under debate (see e.g. Hakobyan et al. 2009) and more observations are needed.

Another argument in favour of the above could be that metallicities traced by iron (Genovali et al. 2014; Kovtyukh et al. 2019) instead of oxygen (Henry & Worthey 1999) show a trend in good agreement with our observations (after converting [Fe/H] to D_{GC}/kpc not only outside the central 2.53 kpc as in Fig. 5, but also in the GC region itself). This could also indicate a drop in the production of massive stars at the Galactic centre compared to the rest of the Galaxy and to less massive stars.

Our $^{32}S/^{34}S$ isotope ratio of $16.3^{+2.1}_{-1.7}$ can constrain opacity estimates of sulphur-bearing molecules in the Galactic centre region and will considerably augment the confidence in theoretical modelling of dense molecular clouds (e.g. Loison et al. 2019). Such results can then be used as initial inputs to reproduce hot core conditions (Charnley 1997; Viti et al. 2004; Vidal et al. 2018).

Our new value for this ratio can also improve synthetic spectral fitting and subsequent line identification, giving better estimations to sulphur-bearing molecules. As a prime example, we mention the recent work of Zakharenko et al. (2019): the canonical ratio of $^{32}S/^{34}S = 22.5$ (Frerking et al. 1980) is insufficient to reproduce their data, as can be seen in their Fig. 4. Our value of $16.3^{+2.1}_{-1.7}$ leads to an enhancement of the ^{34}S isotopologue by a factor of 1.4 in their fit (red line), better reproducing the lines detected at 99.512 and 99.520 GHz, and thus increasing the confidence in the identification of $CH_3{}^{34}SH$ in the hot core Sgr B2(N2).

7. Summary and conclusions

From our analysis of the emission line profiles of CS, ^{13}CS, $C^{34}S$, $^{13}C^{34}S$ $J=2$–1, of CS and $C^{34}S$ $J=3$–2, and of ^{13}CS and $C^{34}S$ $J=6$–5 in the +50 km s^{-1} Cloud and CS, ^{13}CS, $C^{34}S$, $^{13}C^{34}S$ $J=2$–1 observed in absorption towards Sgr B2(N), we obtain the following main results:

- From measurements of the $J=2$–1 lines of $^{12}C^{34}S$ $J=2$–1 and $^{13}C^{34}S$ $J=2$–1, we have obtained a $^{12}C/^{13}C$ isotope ratio of $22.1^{+3.3}_{-2.4}$ near the centre of our Galaxy, in good agreement with previous estimations.
- For the +50 km s^{-1} Cloud we obtain a $^{34}S/^{33}S$ ratio of 4.3 ± 0.2, derived from $C^{34}S$ $J=2$–1 and $C^{33}S$ $J=2$–1 column densities. If we take the integrated intensities instead, this ratio would be 4.2 ± 0.2, consistent with the lower end of the range of ratios obtained by Chin et al. (1996), who derived $^{34}S/^{33}S$ ratios between 4.38 and 7.53, irrespective of Galactic radius. This might be a first indication of a gradient with rising ratios as a function of increasing galactocentric distance, but data from the Galactic disc have to become more precise for a definite result.
- From the $J=2$–1 ^{13}CS and $^{13}C^{34}S$ emission lines in the +50 km s^{-1} Cloud, we derive, for the first time in a direct way, a $^{32}S/^{34}S$ column density ratio of $16.3^{+2.1}_{-1.7}$, which is consistent with the $^{32}S/^{34}S$ ratio derived from the $J=6$–5 and $J=2$–1 ^{13}CS and $C^{34}S$ isotopologues when accounting for the above-mentioned $^{12}C/^{13}C$ ratio. Due to possible CS fractionation, the above ratio might be underestimated by less than ~10%.
- We were able to directly obtain a $^{32}S/^{34}S$ ratio of 17.9 ± 5.0 for the envelope of Sgr B2(N), from the isotopologues ^{13}CS and $^{13}C^{34}S$ in the $J=2$–1 lines. Moreover, we have obtained a $^{32}S/^{34}S$ ratio of 16.3 ± 3.8 for the GC l.o.s. clouds towards Sgr B2(N) through the CS and $C^{34}S$ $J=2$–1 isotopologue lines, when CS is not optically thick. Those ratios are prone to increase by up to ~15%, when taking CS fractionation effects into account.
- Making use of the network presented in Loison et al. (2019), we significantly improved CS fractionation estimations under conditions similar to those taking place in massive molecular clouds, young stellar objects, and diffuse or translucent cold molecular clouds.
- Comparing the sulphur ratios from this work with data available in the literature that were obtained from larger distances to Sgr A* and showed a decrease in $^{32}S/^{34}S$ towards the Galactic centre, we can confidently establish that this decrease terminates at least at a distance of 100 pc to Sgr A*, at the position of Sgr B2(N) (Reid et al. 2009). This is different from trends previously reported for $^{12}C/^{13}C$, $^{14}N/^{15}N$, and $^{18}O/^{17}O$.
- Our improved $^{32}S/^{34}S$ isotope ratio will considerably augment the confidence in theoretical modelling for hot cores and in synthetic spectral fitting and subsequent line identification, giving better constraints for the intensities of sulphur-bearing molecules.

Overall, our results suggest that processes occurring at late evolutionary stages of massive stars could be better traced by sulphur isotopologues instead of the most commonly studied CNO isotopes. Further observations targeting isotopologue ratios with distinct nucleogenesis like $^{32}S/^{34}S$ (i.e. primary species versus secondary isotopologues) produced in advanced massive stars and SNe II can lead to a better understanding of environmental discrepancies between the solar neighbourhood and the inner Galaxy. This will allow, for example, a connection between metallicity gradients traced by iron (Genovali et al. 2014; Kovtyukh et al. 2019) and observations of SNe II (Anderson & James 2009). The above could be also extrapolated to external galaxies, especially with the advent of a new generation of facilities.

Acknowledgements. We appreciate the important suggestions by the anonymous referee that helped to express this research in a clearer and more comprehensive way. PH is a member of and received financial support for this research from the International Max Planck Research School (IMPRS) for Astronomy and Astrophysics at the Universities of Bonn and Cologne. This work makes use of the following ALMA data: ADS/JAO.ALMA#2011.0.00017.S, ADS/JAO.ALMA#2012.1.00012.S. ALMA is a partnership of ESO (representing its member states), NSF (USA) and NINS (Japan), together with NRC (Canada), NSC and ASIAA (Taiwan), and KASI (Republic of Korea), in cooperation with the Republic of Chile. The Joint ALMA Observatory is operated by ESO, AUI/NRAO and NAOJ. The interferometric data are available in the ALMA archive at `https://almascience.eso.org/aq/`. This paper is partly based on data acquired with the Atacama PathfinderEXperiment (APEX). APEX is a collaboration between the Max Planck Institute for Radio Astronomy, the European Southern Observatory, and the Onsala Space Observatory. Part of this work is based on observations carried out with the IRAM 30-m telescope. IRAM is supported by INSU/CNRS (France), MPG (Germany) and IGN (Spain). We acknowledge the IRAM staff for the support and help offered during all the applicable observational runs.

References

Adande, G. R., & Ziurys, L. M. 2012, ApJ, 744, 194
Adriaens, D. A., Goumans, T. P. M., Catlow, C. R. A., & Brown, W. A. 2010, J. Phys. Chem. C, 114, 1892
Agúndez, M., & Wakelam, V. 2013, Chem. Rev., 113, 8710
Agúndez, M., Marcelino, N., Cernicharo, J., Roueff, E., & Tafalla, M. 2019, A&A, 625, A147
Anderson, J. P., & James, P. A. 2009, MNRAS, 399, 559
Ao, Y., Henkel, C., Menten, K. M., et al. 2013, A&A, 550, A135
Armijos-Abendaño, J., Martín-Pintado, J., Requena-Torres, M. A., Martín, S., & Rodríguez-Franco, A. 2015, MNRAS, 446, 3842
Bayet, E., Viti, S., Williams, D. A., & Rawlings, J. M. C. 2008, ApJ, 676, 978
Bayet, E., Aladro, R., Martín, S., Viti, S., & Martín-Pintado, J. 2009, ApJ, 707, 126
Belloche, A., Müller, H. S. P., Menten, K. M., Schilke, P., & Comito, C. 2013, A&A, 559, A47
Belloche, A., Müller, H. S. P., Garrod, R. T., & Menten, K. M. 2016, A&A, 587, A91
Belloche, A., Garrod, R. T., Müller, H. S. P., et al. 2019, A&A, 628, A10
Bonfand, M., Belloche, A., Menten, K. M., Garrod, R. T., & Müller, H. S. P. 2017, A&A, 604, A60
Bonfand, M., Belloche, A., Garrod, R. T., et al. 2019, A&A, 628, A27
Bovy, J., Nidever, D. L., Rix, H.-W., et al. 2014, ApJ, 790, 127
Charnley, S. B. 1997, ApJ, 481, 396
Chin, Y. N., Henkel, C., Whiteoak, J. B., Langer, N., & Churchwell, E. B. 1996, A&A, 305, 960
Clayton, D. 2007, Handbook of Isotopes in the Cosmos (Cambridge: Cambridge University Press)
Corby, J. F., McGuire, B. A., Herbst, E., & Remijan, A. J. 2018, A&A, 610, A10
Dale, J. E., Kruijssen, J. M. D., & Longmore, S. N. 2019, MNRAS, 486, 3307
Davies, B., Origlia, L., Kudritzki, R.-P., et al. 2009, ApJ, 694, 46
Drdla, K., Knapp, G. R., & van Dishoeck, E. F. 1989, ApJ, 345, 815
Endres, C. P., Schlemmer, S., Schilke, P., Stutzki, J., & Müller, H. S. P. 2016, J. Mol. Spectr., 327, 95

Ferrière, K. 2012, A&A, 540, A50

Frerking, M. A., Wilson, R. W., Linke, R. A., & Wannier, P. G. 1980, ApJ, 240, 65

Fuente, A., Cernicharo, J., Roueff, E., et al. 2016, A&A, 593, A94

Gaume, R. A., Claussen, M. J., de Pree, C. G., Goss, W. M., & Mehringer, D. M. 1995, ApJ, 449, 663

Genovali, K., Lemasle, B., Bono, G., et al. 2014, A&A, 566, A37

Ginsburg, A., Henkel, C., Ao, Y., et al. 2016, A&A, 586, A50

Ginsburg, A., Bally, J., Barnes, A., et al. 2018, ApJ, 853, 171

Goldsmith, P. F., & Linke, R. A. 1981, ApJ, 245, 482

Goldsmith, P. F., Lis, D. C., Hills, R., & Lasenby, J. 1990, ApJ, 350, 186

González, M., Hijazo, J., Novoa, J. J., & Sayós, R. 1996, J. Chem. Phys., 105, 10999

Gravity Collaboration (Abuter, R., et al.) 2018, A&A, 615, L15

Greaves, J. S., & Williams, P. G. 1994, A&A, 290, 259

Güsten, R., Walmsley, C. M., Ungerechts, H., & Churchwell, E. 1985, A&A, 142, 381

Güsten, R., Nyman, L. Å., Schilke, P., et al. 2006, A&A, 454, L13

Hakobyan, A. A., Mamon, G. A., Petrosian, A. R., Kunth, D., & Turatto, M. 2009, A&A, 508, 1259

Halfen, D. T., Woolf, N. J., & Ziurys, L. M. 2017, ApJ, 845, 158

Hawkins, I., & Jura, M. 1987, ApJ, 317, 926

Henkel, C., Guesten, R., & Gardner, F. F. 1985, A&A, 143, 148

Henkel, C., Asiri, H., Ao, Y., et al. 2014, A&A, 565, A3

Henry, R. B. C., & Worthey, G. 1999, PASP, 111, 919

Hincelin, U., Wakelam, V., Hersant, F., et al. 2011, A&A, 530, A61

Hughes, G. L., Gibson, B. K., Carigi, L., et al. 2008, MNRAS, 390, 1710

Indriolo, N., Neufeld, D. A., Gerin, M., et al. 2015, ApJ, 800, 40

Inno, L., Urbaneja, M. A., Matsunaga, N., et al. 2019, MNRAS, 482, 83

Johansson, L. E. B., Olofsson, H., Hjalmarson, A., Gredel, R., & Black, J. H. 1994, A&A, 291, 89

Kelly, G., Viti, S., Bayet, E., Aladro, R., & Yates, J. 2015, A&A, 578, A70

Klein, T., Ciechanowicz, M., Leinz, C., et al. 2014, IEEE Trans. Terahertz Sci. Technol., 4, 588

Kobayashi, C., Karakas, A. I., & Umeda, H. 2011, MNRAS, 414, 3231

Kovtyukh, V. V., Andrievsky, S. M., Martin, R. P., et al. 2019, MNRAS, 489, 2254

Laas, J. C., & Caselli, P. 2019, A&A, 624, A108

Le Petit, F., Ruaud, M., Bron, E., et al. 2016, A&A, 585, A105

Levshakov, S. A., Centurión, M., Molaro, P., & Kostina, M. V. 2006, A&A, 447, L21

Lilenfeld, H. V., & Richardson, R. J. 1977, J. Chem.Phys., 67, 3991

Linke, R. A., & Goldsmith, P. F. 1980, ApJ, 235, 437

Lique, F., Spielfiedel, A., & Cernicharo, J. 2006, A&A, 451, 1125

Lis, D. C., & Goldsmith, P. F. 1990, ApJ, 356, 195

Lodders, K. 2003, ApJ, 591, 1220

Loison, J.-C., Wakelam, V., Gratier, P., et al. 2019, MNRAS, 485, 5777

Lucas, R., & Liszt, H. S. 2002, A&A, 384, 1054

Mangum, J. G., & Shirley, Y. L. 2015, PASP, 127, 266

Maret, S., Hily-Blant, P., Pety, J., Bardeau, S., & Reynier, E. 2011, A&A, 526, A47

Martín, S., Aladro, R., Martín-Pintado, J., & Mauersberger, R. 2010, A&A, 522, A62

Martín-Pintado, J., Rizzo, J. R., de Vicente, P., Rodríguez-Fernández, N. J., & Fuente, A. 2001, ApJ, 548, L65

Mauersberger, R., Henkel, C., Wilson, T. L., & Harju, J. 1989, A&A, 226, L5

Mauersberger, R., Henkel, C., Langer, N., & Chin, Y. N. 1996, A&A, 313, L1

Mauersberger, R., Ott, U., Henkel, C., Cernicharo, J., & Gallino, R. 2004, A&A, 426, 219

Milam, S. N., Savage, C., Brewster, M. A., Ziurys, L. M., & Wyckoff, S. 2005, ApJ, 634, 1126

Millar, T. J., & Herbst, E. 1990, A&A, 231, 466

Mills, E. A. C., & Morris, M. R. 2013, ApJ, 772, 105

Molinari, S., Bally, J., Glover, S., et al. 2014, in Protostars and Planets VI, eds. H. Beuther, R. S. Klessen, C. P. Dullemond, & T. Henning, 125

Montaigne, H., Geppert, W. D., Semaniak, J., et al. 2005, ApJ, 631, 653

Morris, M., & Serabyn, E. 1996, ARA&A, 34, 645

Müller, H. S. P., Schlöder, F., Stutzki, J., & Winnewisser, G. 2005, J. Mol. Struct., 742, 215

Müller, S., Guélin, M., Dumke, M., Lucas, R., & Combes, F. 2006, A&A, 458, 417

Müller, H. S. P., Belloche, A., Menten, K. M., Comito, C., & Schilke, P. 2008, J. Mol. Spectr., 251, 319

Müller, H. S. P., Belloche, A., Xu, L.-H., et al. 2016, A&A, 587, A92

Najarro, F., Figer, D. F., Hillier, D. J., Geballe, T. R., & Kudritzki, R. P. 2009, ApJ, 691, 1816

Nummelin, A., Bergman, P., Hjalmarson, Å., et al. 1998, ApJS, 117, 427

Pignatari, M., Herwig, F., Hirschi, R., et al. 2016, ApJS, 225, 24

Polehampton, E. T., Baluteau, J. P., & Swinyard, B. M. 2005, A&A, 437, 957

Reid, M. J., Menten, K. M., Zheng, X. W., Brunthaler, A., & Xu, Y. 2009, ApJ, 705, 1548

Remijan, A. J., Hollis, J. M., Lovas, F. J., et al. 2008, ApJ, 675, L85

Requena-Torres, M. A., Martín-Pintado, J., Martín, S., & Morris, M. R. 2008, ApJ, 672, 352

Ritchey, A. M., Federman, S. R., & Lambert, D. L. 2011, ApJ, 728, 36

Roueff, E., Loison, J. C., & Hickson, K. M. 2015, A&A, 576, A99

Ruze, J. 1966, IEEE Proc., 54, 633

Sánchez-Monge, Á., Schilke, P., Schmiedeke, A., et al. 2017, A&A, 604, A6

Sandqvist, A., Larsson, B., Hjalmarson, Å., et al. 2008, A&A, 482, 849

Sandqvist, A., Larsson, B., Hjalmarson, Å., et al. 2015, A&A, 584, A118

Schmiedeke, A., Schilke, P., Möller, T., et al. 2016, A&A, 588, A143

Schwörer, A., Sánchez-Monge, Á., Schilke, P., et al. 2019, A&A, 628, A6

Smith, D., & Adams, N. G. 1980, ApJ, 242, 424

Thiel, V. 2019, PhD thesis, University of Bonn, Germany

Thiel, V., Belloche, A., Menten, K. M., et al. 2019, A&A, 623, A68

Thielemann, F. K., & Arnett, W. D. 1985, ApJ, 295, 604

Timmes, F. X., Woosley, S. E., & Weaver, T. A. 1995, ApJS, 98, 617

Tsuboi, M., Handa, T., & Ukita, N. 1999, ApJS, 120, 1

Uehara, K., Tsuboi, M., Kitamura, Y., Miyawaki, R., & Miyazaki, A. 2019, ApJ, 872, 121

van der Tak, F. F. S., Black, J. H., Schöier, F. L., Jansen, D. J., & van Dishoeck, E. F. 2007, A&A, 468, 627

van Dishoeck, E. F., & Blake, G. A. 1998, ARA&A, 36, 317

Vastel, C., Quénard, D., Le Gal, R., et al. 2018, MNRAS, 478, 5519

Vidal, T. H. G., Loison, J.-C., Jaziri, A. Y., et al. 2018, MNRAS, 469, 435

Viti, S. 2016, IAU Symp., 17

Viti, S., Collings, M. P., Dever, J. W., McCoustra, M. R. S., & Williams, D. A. 2004, MNRAS, 354, 1141

Vollmer, B., Duschl, W. J., & Zylka, R. 2003, Astron. Nachr. Suppl., 324, 613

Wakelam, V., Herbst, E., & Selsis, F. 2006, A&A, 451, 551

Wakelam, V., Smith, I. W. M., Herbst, E., et al. 2010, Space Sci. Rev., 156, 13

Wang, M., Henkel, C., Chin, Y. N., et al. 2004, A&A, 422, 883

Wang, K. S., Bourke, T. L., Hogerheijde, M. R., et al. 2013, A&A, 558, A69

Whiteoak, J. B., & Gardner, F. F. 1979, MNRAS, 188, 445

Wilson, T. L., & Matteucci, F. 1992, A&ARv, 4, 1

Wilson, T. L., & Rood, R. 1994, ARA&A, 32, 191

Wirström, E. S., Bergman, P., Black, J. H., et al. 2010, A&A, 522, A19

Woosley, S. E., & Weaver, T. A. 1995, ApJS, 101, 181

Wouterloot, J. G. A., Henkel, C., Brand, J., & Davis, G. R. 2008, A&A, 487, 237

Yan, Y. T., Zhang, J. S., Henkel, C., et al. 2019, ApJ, 877, 154

Zakharenko, O., Lewen, F., Ilyushin, V. V., et al. 2019, A&A, 627, A41

Zhang, J. S., Sun, L. L., Riquelme, D., et al. 2015, ApJS, 219, 28

Zuckerman, B., Turner, B. E., Johnson, D. R., et al. 1975, ApJ, 196, L99

Appendix A: Chemical aspects

In diffuse clouds, it has been suggested that CS forms mainly by exothermic ion-molecule reactions of S^+ with CH and C_2 (Drdla et al. 1989; van Dishoeck & Blake 1998). However, these species require to be one order of magnitude more abundant than currently observed in order to reproduce the observed quantities of CS (Lucas & Liszt 2002). Currently, CS formation is believed to be dominated by the exothermic reaction (Drdla et al. 1989; Lucas & Liszt 2002; Montaigne et al. 2005; Laas & Caselli 2019)

$$HCS^+ + e^- \rightarrow CS + H. \tag{A.1}$$

Subsequently, the dominant destruction route of CS is photodissociation, with destruction by He^+ being only significant in denser clouds (Drdla et al. 1989).

At higher densities, CS is mainly produced through neutral–neutral reactions with atomic sulfur such as (Fuente et al. 2016; Vidal et al. 2018; Laas & Caselli 2019)

$$S + CH \rightarrow CS + H, \tag{A.2a}$$

$$S + C_2 \rightarrow CS + C, \text{ and} \tag{A.2b}$$

$$SO + C \rightarrow CS + O. \tag{A.2c}$$

The dissociative recombination (DR) of HCS^+ becomes the main path for CS destruction at low temperatures because HCS^+ is mainly produced through protonation of CS and its DR leads mainly to S+CH and not to CS+H (Montaigne et al. 2005).

At higher temperatures, such as in hot cores and hot corinos for which recent models suggest some changes in sulfur chemistry (Vidal et al. 2018), CS is also destroyed by atomic oxygen:

$$CS + O \rightarrow CO + S. \tag{A.3}$$

This reaction is supposed to be negligible at low temperature due to the presence of a barrier (Lilenfeld & Richardson 1977; González et al. 1996). However the value of the barrier is questionable (Adriaens et al. 2010) so that this reaction may not be completely negligible at low temperature. Apart from this reaction, and despite the recent advances in the investigation of sulfur species in the interstellar medium (Fuente et al. 2016; Vidal et al. 2018; Laas & Caselli 2019), there are still large uncertainties with respect to CS and HCS^+ chemistry.

Recent studies agree with the above reactions, but indicate that the dominant mechanism also depends on the cosmic ray ionization rates (CRIR). At high CRIR, which may be typical of the central parts of giant spiral galaxies, reactions (A.2c) and (A.3) dominate CS formation and destruction, but at lower CRIR the following reaction (route (A.4)) becomes dominant for the destruction of CS (Kelly et al. 2015; Viti 2016):

$$H_3O^+ + CS \rightarrow HCS^+ + H_2O. \tag{A.4}$$

In hot cores and corinos, recent models suggest some deviations from the above-mentioned routes of sulfur chemistry (Vidal et al. 2018). Specifically for CS, the main paths for its formation and destruction continue being Eqs. (A.2c) and (A.3), respectively. CS is initially destroyed by atomic oxygen (Eq. (A.3)) both at 100 and 300 K, on timescales of 10^4 and 10^3 yr, respectively. Nevertheless, CS is then also produced by

$$S + CH_2 \rightarrow HCS \xrightarrow{S} CS_2 \xrightarrow{H} CS. \tag{A.5}$$

Appendix B: Excitation temperatures

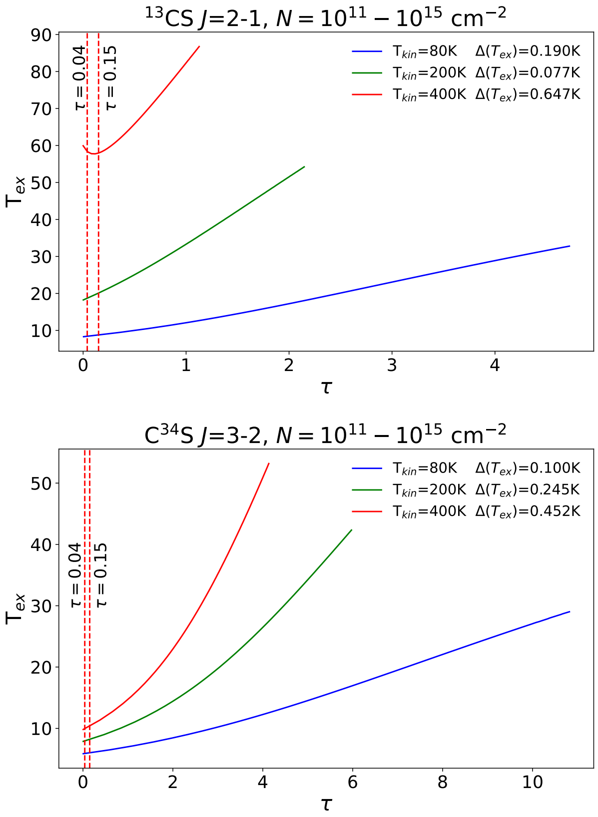

Fig. B.1. Excitation temperatures ($T_{\rm ex}$) as a function of opacity (τ) for ^{13}CS $J = 2$–1 (*top*) and C^{34}S $J = 3$–2 (*bottom*). Molecular column densities range between 10^{11} and 10^{15} cm^{-2}, and the kinetic temperature is 80, 200, and 400 K, represented by blue, green, and red lines, respectively. $\Delta(T_{\rm ex})$ refers to the $T_{\rm ex}$ maximum variation between $\tau = 0.04$ and 0.15 (delineated by dashed vertical red lines).

As mentioned in Sects. 4.1 and 4.1.3, we assumed the same excitation temperatures ($T_{\rm ex}$) in all our opacity calculations. This is argued by the low opacity of the isotopologues used to make such calculations.

Let us take an opacity (τ) ranging between 0.04 and 0.15 (see Table 2) for both ^{13}CS $J = 2$–1 and C^{34}S $J = 3$–2 with which we obtained the opacity for ^{12}CS $J = 2$–1 and $J = 3$–2, respectively. As can be seen in Fig. B.1, the variations in $T_{\rm ex}$ within this range falls below 0.64 K. Considering that this temperature will be inside an exponential as denominator of a fraction and, furthermore, multiplied by the Boltzmann constant (see Eq. (80) in Mangum & Shirley 2015), is reasonable to assume that $T_{\rm ex}$ variations are negligible for the scope of this work.

Calculations were done with a python version[6] of RADEX (van der Tak et al. 2007), a statistical equilibrium molecular radiative transfer code. Our inputs were a kinetic temperature of 80, 200, and 400 K; 100 equally spaced values for the column density from 10^{11} to 10^{15} cm^{-2}; and a H_2 volumetric density of 5×10^4 cm^{-3}, in an attempt to emulate the conditions of the +50 km s^{-1} Cloud (see Sect. 3). ^{13}CS and C^{34}S collision rates were taken from the Leiden Atomic and Molecular Database (LAMDA, Schwörer et al. 2019), which in turn uses calculations made by Lique et al. (2006).

---

[6] See `https://pypi.org/project/ndradex/` for a full description. We have used the Grid RADEX run option.

Appendix C: Zoom in for Fig. 5

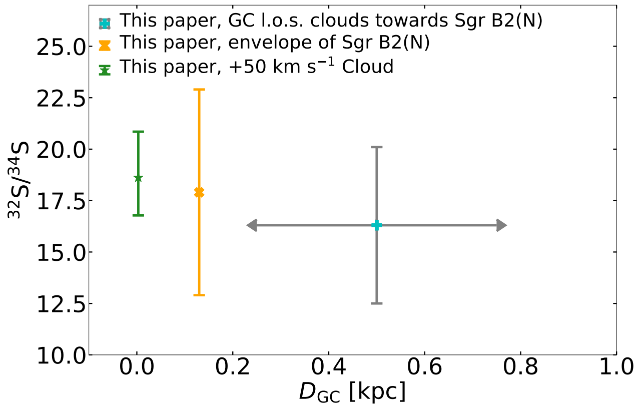

Fig. C.1. Sulphur isotope ^{32}S/^{34}S ratio for the new data presented in this paper as a function of galactocentric radius, D_{GC}.

We plot our own data from Fig. 5 in a magnified way. Data values for the l.o.s. clouds towards Sgr B2(N) and its envelope are given in Table 4. The integrated intensity ^{32}S/^{34}S ratio of the +50 km s^{-1} Cloud ($18.6^{+2.2}_{-1.8}$) comes from Sect. 4.1.2.

Appendix D: Gaussian fitting

We preferred to use the lmfit package instead of Gildas[7], for example, because the former has some improvements related to uncertainty calculations. While both use minimization, Simplex and Gradient methods, because of the use of the Minimize package[8], lmfit has additional functions and packages to ensure a proper uncertainty estimation "even in the most difficult cases"[9]. We compared the uncertainties from Gildas and lmfit; those derived based on Gildas are lower than those from lmfit by a small percentage (well within the uncertainties), and at the same time the use of Gildas results in a less successful fit in certain cases (not shown). Given the rich available documentation for lmfit, we opted for the lmfit-based fitting and associated uncertainty determination.

---

[7] https://www.iram.fr/IRAMFR/GILDAS

[8] https://lmfit.github.io/lmfit-py/fitting.html#the-minimize-function

[9] https://lmfit.github.io/lmfit-py/

APPENDIX B

36 GHz methanol lines from nearby galaxies: maser or quasi-thermal emission?

A&A 633, A106 (2020)
https://doi.org/10.1051/0004-6361/201936330

Astronomy & Astrophysics

36 GHz methanol lines from nearby galaxies: maser or quasi-thermal emission?[⋆]

P. K. Humire[1], C. Henkel[1,2,3], Y. Gong[1], S. Leurini[4,1], R. Mauersberger[1], S. A. Levshakov[5,6,7], B. Winkel[1], A. Tarchi[4], P. Castangia[4], A. Malawi[2], H. Asiri[2], S. P. Ellingsen[8], T. P. McCarthy[8,9], X. Chen[10,11], and X. Tang[3,12]

[1] Max-Planck-Institut für Radioastronomie, Auf dem Hügel 69, 53121 Bonn, Germany
e-mail: `chenkel@mpifr-bonn.mpg.de`
[2] Astronomy Department, Faculty of Science, King Abdulaziz University, PO Box 80203, Jeddah 21589, Saudi Arabia
[3] Xinjiang Astronomical Observatory, Chinese Academy of Sciences, 830011 Urumqi, PR China
[4] INAF-Osservatorio Astronomico di Cagliari, Via della Scienza 5, 09047 Selargius, CA, Italy
[5] Ioffe Physical-Technical Institute, 194021 St. Petersburg, Russia
[6] Electrotechnical University "LETI", 197376 St. Petersburg, Russia
[7] Petersburg Nuclear Physics Institute, 188300 Gatchina, Russia
[8] School of Natural Sciences, University of Tasmania, Hobart, TAS 7001, Australia
[9] Australia Telescope National Facility, CSIRO, PO Box 76, Epping, NSW 1710, Australia
[10] Center for Astrophysics, GuangZhou University, Guangzhou 510006, PR China
[11] Shanghai Astronomical Observatory, Chinese Academy of Sciences, Shanghai 200030, PR China
[12] Key Laboratory of Radio Astronomy, Chinese Academy of Sciences, 830011 Urumqi, PR China

Received 17 July 2019 / Accepted 12 November 2019

ABSTRACT

Methanol (CH_3OH) is one of the most abundant interstellar molecules, offering a vast number of transitions to be studied, including many maser lines. However, while the strongest Galactic CH_3OH lines, the so-called class II masers, show no indications for the presence of superluminous counterparts in external galaxies, the less luminous Galactic class I sources appear to be different. Here we report class I 36 GHz ($\lambda \approx 0.8$ cm) CH_3OH $4_{-1} \rightarrow 3_0$ E line emission from the nearby galaxies Maffei 2 ($D \approx 6$ Mpc) and IC 342 ($D \approx 3.5$ Mpc), measured with the 100 m telescope at Effelsberg at three different epochs within a time span of about five weeks. The 36 GHz methanol line of Maffei 2 is the second most luminous among the sources detected with certainty outside the Local Group of galaxies. This is not matched by the moderate infrared luminosity of Maffei 2. Higher-resolution data are required to check whether this is related to its prominent bar and associated shocks. Upper limits for M 82, NGC 4388, NGC 5728 and Arp 220 are also presented. The previously reported detection of 36 GHz maser emission in Arp 220 is not confirmed. Nondetections are reported from the related class I 44 GHz ($\lambda \approx 0.7$ cm) methanol transition towards Maffei 2 and IC 342, indicating that this line is not stronger than its 36 GHz counterpart. In contrast to the previously detected 36 GHz CH_3OH emission in NGC 253 and NGC 4945, our 36 GHz profiles towards Maffei 2 and IC 342 are similar to those of previously detected nonmasing lines from other molecular species. However, by analogy to our Galactic center region, it may well be possible that the 36 GHz methanol lines in Maffei 2 and IC 342 are composed of a large number of faint and narrow maser features that remain spatially unresolved. In view of this, a search for a weak broad 36 GHz line component would also be desirable in NGC 253 and NGC 4945.

Key words. masers – galaxies: spiral – galaxies: individual: IC 342 – galaxies: individual: Maffei 2 – galaxies: ISM – radio lines: galaxies

1. Introduction

Methanol (CH_3OH) is one of the most abundant interstellar molecules (e.g., Kalenski & Sobolev 1994; Wang et al. 2004; Maffucci et al. 2018) exhibiting a plethora of lines at centimeter (cm), millimeter (mm), and submillimeter (submm) wavelengths. To provide an example, Schilke et al. (2001) and Comito et al. (2005) reported the detection of a total of ≈650 methanol transitions from Orion-KL. Some of these lines show inverted level populations and significant optical depths. Such methanol maser lines form two distinct families exhibiting clearly nonthermal emission in quite specific but different transitions: class I masers are often separated from the main sources of star forming activity (between 0.1 and 1.0 pc from UC HII regions, OH and H_2O masers according to Gómez-Ruiz et al. 2016), whereas class II masers are closely associated with such sites. The 6.7 GHz transition (Menten 1991) has become the prototypical class II maser line, exhibiting particularly strong emission in regions of intense radiation from warm dust and relatively cool gas (Cragg et al. 2005). Sources characterized by class I emission are encountered in regions not necessarily devoid of far infrared radiation but requiring collisional excitation – they appear to be associated with weak shocks, possibly related to outflows from young stellar objects interacting with the dense ambient interstellar medium (e.g., Kurtz et al. 2004; Leurini et al. 2016). In such regions, the $4_{-1} \rightarrow 3_0$ E and $7_0 \rightarrow 6_1$ A^+ transitions at 36 and 44 GHz, respectively, become most prominent. Apparently, the 36 GHz line is strongest towards

---

[⋆] A copy of the reduced spectra is available at the CDS via anonymous ftp to `cdsarc.u-strasbg.fr` (`130.79.128.5`) or via `http://cdsarc.u-strasbg.fr/viz-bin/cat/J/A+A/633/A106`

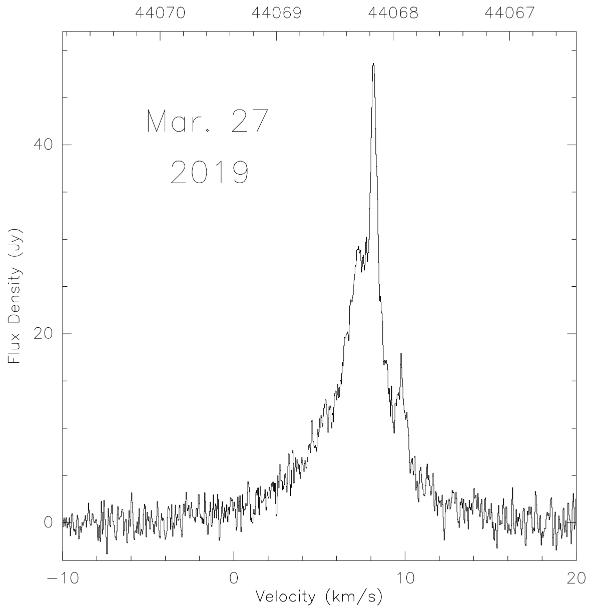

Fig. 1. $7_0 \rightarrow 6_1$ A^+ methanol spectrum from Orion-KL. The adopted rest frequency is 44.069367 GHz, the beam size is 23″ and the coordinates are $\alpha_{J2000} = 5^h35^m14\overset{s}{.}2$, $\delta_{J2000} = -5°22'30''$. The velocity scale is the local standard of rest and the channel spacing is 0.31 km s^{-1} after averaging eight contiguous channels.

sources with kinetic temperatures of $T_{kin} \lesssim 100$ K, where signs of high-mass star formation are not yet seen. The 44 GHz masers are closer to ultracompact (UC)-HII-regions and mm wave continuum sources and may be excited at $T_{kin} \gtrsim 100$ K. With respect to required densities, optimal conditions for 36 GHz masers appear to include densities that are an order of magnitude higher than those at 44 GHz (e.g., Pratap et al. 2008; McEwen et al. 2014; Nesterenok 2016; Leurini et al. 2016).

More than one thousand methanol masers are known in the Galaxy (e.g., Menten 1991; Pratap et al. 2008; Yusef-Zadeh et al. 2013; Cotton & Yusef-Zadeh 2016; Yang et al. 2017, 2019). However, in extragalactic targets, such maser lines are rarely observed. Following the detections of quasi-thermal methanol emission in nearby galaxies (Henkel et al. 1987), the large number of Galactic masers and the existence of even more luminous H_2O and OH "megamasers" (e.g., Lo 2005) provided strong motivation to search for class II 6.7 GHz maser emission towards extragalactic sources (Ellingsen et al. 1994a; Phillips et al. 1998; Darling et al. 2003). This yielded detections in absorption towards NGC 3079 and Arp 220 (Impellizzeri et al. 2008; Salter et al. 2008) and in emission towards the Large Magellanic Cloud (LMC; Sinclair et al. 1992; Ellingsen et al. 1994b; Beasley et al. 1996; Green et al. 2008; Henkel et al. 2018a) and the Andromeda galaxy M 31 (Sjouwerman et al. 2010). The LMC also provided a 12.2 GHz class II maser detection, reported by Ellingsen et al. (2010). However, the intrinsic brightness of all these emission lines turned out to be similar to those of their stronger Galactic counterparts.

Since none of the surveys for ultraluminous class II masers revealed positive results, searches for brighter analogs of the relatively inconspicuous Galactic class I masers were also carried out in nearby extragalactic sources. The detection of 36 GHz class I masers in NGC 253 by Ellingsen et al. (2014) revealed emission that is more than ten times more luminous than the widespread emission associated with the 300 pc × 100 pc central region of our Galaxy and 10^4 times more luminous than a typical individual Galactic 36 GHz maser. This demonstrates the existence of ultraluminous methanol masers (with respect to their Galactic counterparts). Follow-up observations confirmed this detection (Ellingsen et al. 2017; Gorski et al. 2017, 2019; Chen et al. 2018), which was augmented by successful searches for the related class I maser transitions at 44 and 84 GHz in NGC 253 (Ellingsen et al. 2017; McCarthy et al. 2018a). Nevertheless, the search for additional sources turned out to be difficult. For some time, NGC 4945 was the only additional galaxy detected in the 36 GHz CH_3OH class I maser line beyond any reasonable doubt (at multiple epochs with more than one telescope; see McCarthy et al. 2017, 2018b). More recently, 36 GHz emission was also reported from IC 342 and NGC 6946 (Gorski et al. 2018). Chen & Ellingsen (2018) very briefly mentioned a Jansky Very Long Baseline Array (JVLA) detection of Maffei 2. In the following we report clear single-dish detections of Maffei 2, a particularly luminous emitter of 36 GHz line radiation, and IC 342 in the 36.169261 GHz (Endres et al. 2016) $4_{-1,4} \rightarrow 3_{0,3}$ E transition of methanol, thus providing additional strong evidence for the widespread existence of such emission in nearby galaxies. This report also includes a number of nondetections, most notably the nondetection of Arp 220.

2. Observations

2.1. Front- and backends

The 36 GHz measurements were carried out with the 100 m telescope at Effelsberg[1] near Bonn, Germany, in early January and early February 2019. Complementary 44 GHz observations were taken in late March 2019. We obtained the data with a secondary focus Q-band receiver, sensitive in the range 33–50 GHz, providing both circular polarizations with an equivalent system temperature of ≈130 Jy on a flux density scale (≈1.6 K main beam brightness temperature per Jy) prior to averaging the two polarizations. Pointing observations were carried out every ≈40 min towards 3C 84 and NRAO 150 near Maffei 2 and towards W3(OH) near IC 342. The pointing accuracy was 4″ ± 2″ (the error is the standard deviation of an individual measurement) and never exceeded 10″, while the beam size was ≈23″ at both frequencies.

Near the start of each 36 GHz observing session, we targeted the well-known HC_3N $J = 4 \rightarrow 3$ (36.392 GHz) and SiS $J = 2 \rightarrow 1$ (36.310 GHz) lines of IRC+10216 to make sure the system was working. At 44.069 GHz, we chose the CH_3OH $7_0 \rightarrow 6_1$ A^+ line towards Orion-KL (Fig. 1) as a system check that may be used for future projects focusing on issues related to maser variability. For the measurements towards the targets themselves we used a position-switching mode, with 2 min off- and on-source integration times, respectively, and with offsets in right ascension alternating between +10′ and –10′ to remove elevation-dependent effects. We employed a Fast Fourier Transform spectrometer backend with a bandwidth of 300 MHz. The number of channels was 65536, yielding a channel spacing of 0.038 km s^{-1} at 36 GHz and a velocity resolution of 0.044 km s^{-1} (see Klein et al. 2012). At 44 GHz, the corresponding values are 0.031 km s^{-1} and 0.036 km s^{-1}.

2.2. Calibration

We established flux density scales by performing continuum cross scans through 3C 286 and NGC 7027 (see Ott et al. 1994),

---

[1] This publication is based on observations with the 100 m telescope of the MPIfR (Max-Planck-Institut für Radioastronomie) at Effelsberg.

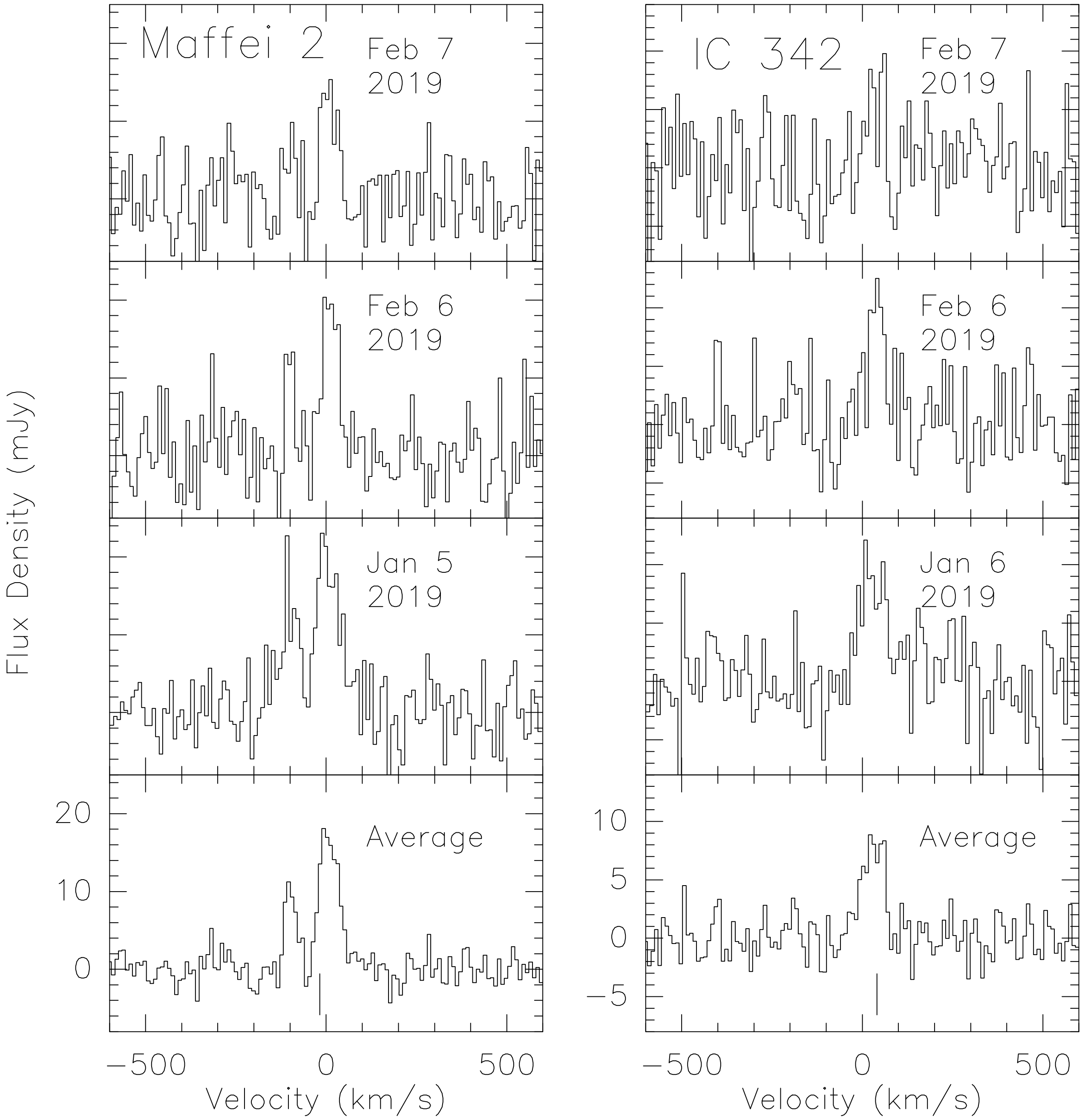

Fig. 2. $4_{-1} \rightarrow 3_0$ E methanol spectra from Maffei 2 (*left*) and IC 342 (*right*). Spectra from a given source are all presented with the same amplitude and velocity scale. The adopted rest frequency is 36.169261 GHz, the coordinates are $\alpha_{\rm J2000} = 2^{\rm h}41^{\rm m}55\overset{\rm s}{.}2$, $\delta_{\rm J2000} = 59° \ 36' \ 12''$ (Maffei 2) and $\alpha_{\rm J2000} = 3^{\rm h}46^{\rm m}48\overset{\rm s}{.}6$, $\delta_{\rm J2000} = 68° \ 05' \ 46''$ (IC 342). The velocity scale is the local standard of rest. The spectra were smoothed by averaging 256 contiguous channels to a channel spacing of 9.7 km s^{-1}. The average spectrum was obtained, weighting individual subscans with the inverse square of their system temperature. The systemic local standard of rest velocity for Maffei 2 is –14 ± 5 km s^{-1} and $V_{\rm HEL} = V_{\rm LSR} - 3.1$ km s^{-1}. For IC 342, the corresponding values are +35 ± 3 km s^{-1} and $V_{\rm HEL} = V_{\rm LSR} - 3.9$ km s^{-1}. Vertical lines indicating the systemic velocities are included in the lower parts of the averaged spectra.

also accounting for gain variations of the telescope as a function of elevation and for a 0.6% yr^{-1} secular decrease in intensity in the case of NGC 7027. Accounting for pointing errors and scatter in the measured signals, we estimate that the calibration uncertainty is ±15%.

3. Results

Figure 2 shows 36 GHz methanol spectra taken towards the centers of Maffei 2 and IC 342. Following initial detections in early January 2019, which looked very promising but not fully convincing, we reobserved the sources a month later. With profiles from a total of three epochs, each showing signals above 3σ and a total of order 10σ (see Table 1), there is no doubt that the detections are real. However, we note that the lines obtained at the individual epochs are weak and relatively noisy. Therefore, differences with respect to peak flux density and line shape cannot be reliably interpreted in terms of variability. Instead, the differences are more likely caused by slightly varying average pointing offsets and, most likely, by different weather conditions, which included occasional light rain during the last observing night. This is consistent with the fact that the best single epoch

Table 1. Methanol line parameters.

Source	$\alpha_{\rm J2000}$	$\delta_{\rm J2000}$	Transition	ν (GHz)	$\int S\,{\rm d}V$ (mJy km s^{-1})	$V_{\rm LSR}$ (km s^{-1})	$\Delta V_{1/2}$ (km s^{-1})	$S_{\rm peak}$ (mJy)	$L_{\rm CH_3OH}$ ($L_\odot$)
Maffei 2	02:41:55.2	+59:36:12	$4_{-1} \rightarrow 3_0$	36.169261	422 ± 45	–99.3 ± 1.9	35.0 ± 3.9	11.3 ± 1.9	0.53 ± 0.06
			$4_{-1} \rightarrow 3_0$	36.169261	1181 ± 60	7.5 ± 1.5	61.1 ± 3.4	18.1 ± 1.5	1.47 ± 0.07
			$7_0 \rightarrow 6_1$	44.069419				<12.0	
IC 342	03:46:48.6	+68:05:46	$4_{-1} \rightarrow 3_0$	36.169261	641 ± 64	29.7 ± 3.6	70.6 ± 8.0	8.5 ± 1.4	0.26 ± 0.03
			$7_0 \rightarrow 6_1$	44.069419				<10.0	
M 82	09:55:52.2	+69:40:47	$4_{-1} \rightarrow 3_0$	36.169261				<4.4	
NGC 4388	12:25:46.7	+12:39:41	$4_{-1} \rightarrow 3_0$	36.169261				<4.6	
NGC 5728	14:42:23.9	–17:15:11	$4_{-1} \rightarrow 3_0$	36.169261				<4.5	
Arp 220	15:34:57.3	+23:30:11	$4_{-1} \rightarrow 3_0$	36.169261				<4.2	

Notes. Obtained from Gaussian fits to the average spectra displayed in Fig. 2. Column 1: sources; Cols. 2 and 3: J2000 coordinates; Col. 4: methanol transition; Col. 5: rest frequency; Cols. 6–8: integrated flux densities, local standard of rest velocities, and full width at half power line widths. Given errors include standard deviations from Gaussian fits but do not include the calibration uncertainty (Sect. 2.2); Col. 9: peak flux densities; Col. 10: methanol line luminosities. Adopted distances: 5.73 Mpc for Maffei 2 and 3.28 Mpc for IC 342 (see Sect. 4). For M 82, NGC 4388, NGC 5728, and Arp 220, 1σ upper limits are given for 9.7 km s^{-1} wide channels. For the 44 GHz transition towards Maffei 2 and IC 342, 1σ upper limits are given for 8.0 km s^{-1} wide channels. To convert the local standard of rest velocities given here into heliocentric values, use $V_{\rm HEL} = V_{\rm LSR} - 3.1$ km s^{-1} for Maffei 2 and $V_{\rm HEL} = V_{\rm LSR} - 3.9$ km s^{-1} for IC 342.

spectra are from January 2019, while the latest spectra show the lowest signal-to-noise ratios.

Table 1 provides Gaussian fit parameters to the average spectra from Maffei 2 and IC 342. In Maffei 2 we find two well-separated spectral components, while IC 342 exhibits one component and overall weaker emission, with lower peak and velocity integrated flux density. The CH_3OH line luminosities in the last column of Table 1, assuming isotropic radiation, were calculated using

$$L/L_\odot = 0.038 \times \,(S_\nu \Delta V_{1/2}/{\rm Jy\,km\,s^{-1}}) \times \,(D/{\rm Mpc})^2, \qquad (1)$$

with S_ν, $\Delta V_{1/2}$ and D representing flux density, full width to half power line width and distance. Upper limits are provided for four additional galaxies as well as also for the 44 GHz line of methanol towards Maffei 2 and IC 342.

4. Discussion

4.1. Detected lines

The two originally detected 36 GHz galaxies outside the Local Group, NGC 253 and NGC 4945 (Ellingsen et al. 2014; McCarthy et al. 2017) show overall properties that are quite different from the galaxies detected by us. Both NGC 253 and NGC 4945 host ongoing starbursts and are characterized by infrared luminosities a few times higher than those of the Milky Way, Maffei 2 or IC 342. NGC 4945 also hosts an active galactic nucleus. NGC 253 and NGC 4945 are both highly inclined giant spiral galaxies ($i \approx 75°$; e.g., Iodice et al. 2014; Henkel et al. 2018b). Furthermore, with outflowing gas in their nuclear regions (Turner 1985; Bolatto et al. 2013; Henkel et al. 2018b), they also provide an environment in which shocks potentially leading to class I methanol maser emission may be ubiquitous. It is remarkable, that the various maser components in NGC 253 occur not right at the center but at offsets of a few hundred parsecs from the nucleus (Ellingsen et al. 2017). The same also holds in the case of NGC 4945, where the (southeastern) front side of the galaxy shows a single but relatively strong maser spot, presumably also arising at a distance of a few hundred parsecs from the nucleus (McCarthy et al. 2018b).

Maffei 2 and IC 342, located behind the Galactic plane, are different. To evaluate their global properties, the first notable parameter is distance. While IC 342 is located at about the same distance as NGC 253 and NGC 4945 (here we adopt 3.28 Mpc; Karachentsev et al. 2013), Maffei 2 may be located at a significantly greater distance. Wu et al. (2014) estimated distances of 3.4–3.5 Mpc for both Maffei 2 and IC 342 using the tip of the red giant branch method. However, Tikhonov & Galazutdinova (2018) re-evaluated their *Hubble* Space Telescope (HST) images. They applied stellar photometry at infrared and optical spectral ranges and compared the resulting Hertzprung-Russel diagrams. In particular the red giant branches, with their upper luminosity boundaries and color indices, were analyzed and compared with data from galaxies being much less obscured by Galactic dust. These latter authors obtained extinctions of $A_{\rm v} = 3\overset{\rm m}{.}65$ and $0\overset{\rm m}{.}9$ for Maffei 2 and IC 342, respectively. While their resulting distance to IC 342 is consistent with previously obtained values, their distance to Maffei 2 becomes 6.7 ± 0.5 Mpc. Reanalyzing near infrared photometry from the HST, Anand et al. (2019) confirm a larger distance for Maffei 2 and propose $D = 5.73 \pm 0.40$ Mpc, which is adopted in the following (see also Table 1 for both Maffei 2 and IC 342).

A common feature of Maffei 2 and IC 342 is, as already briefly mentioned, their location behind the plane of the Milky Way. While IC 342 is displaced from the plane by $10\overset{\circ}{.}6$, Maffei 2 is almost exactly on this plane ($b^{\rm II} = -0\overset{\circ}{.}3$), which led to its very late discovery (Maffei 1968). With respect to infrared luminosity and therefore also to star formation, making use of the more recent distance estimates to Maffei 2, both galaxies have luminosities of $L_{\rm IR} \approx 10^{10}\,L_\odot$. Not hosting an AGN, they are about as active as our own Galaxy ($L_{\rm FIR} \approx 1.2 \times 10^{10}\,L_\odot$; e.g., Misiriotis et al. 2004, 2006), forming on average a few solar masses of new stars per year (see, e.g., Kennicutt 1998 for the correlation between infrared luminosity and star formation rate and Chomiuk & Povich 2011 for uncertainties related to estimates of Galactic star formation rates). Both galaxies host two spiral arms terminating on a central ring with vigorous massive star formation (e.g., Meier & Turner 2012). Therefore, chemically, Maffei 2 may be considered to some extent as a more inclined copy of IC 342 and may not (as before) be considered as a particularly small spiral galaxy. However, one major difference remains: it is the kiloparsec-sized bar in Maffei 2 that is possibly causing widespread shocks favoring 36 GHz methanol maser emission (see Ellingsen et al. 2017 and below). A similar structure is not found in IC 342.

The previously obtained 36 GHz methanol maser detections in NGC 253 and NGC 4945 (Ellingsen et al. 2014; McCarthy et al. 2017) have something in common: the detected profiles are much narrower than those obtained when measuring quasi-thermal line emission from areas covering their entire central molecular zones. This is different with respect to our lines shown in Fig. 2. Galactic foreground emission (Maffei 2 and IC 342 are located behind the Perseus arm) cannot cause this effect. The two line peaks detected towards Maffei 2 are not compatible with molecular velocities of the Perseus arm (Cohen et al. 1980) and must therefore be of extragalactic origin. The 36 GHz methanol velocity components are also seen, with similar spectral profiles but with lower signal-to-noise ratios, in other tracers of dense molecular gas, the integrated ammonia (NH_3) $(J, K) = (1, 1)$ and (likely) (2,2) profiles near 24 GHz (Lebrón et al. 2011). The global ammonia profiles from IC 342 also show similar shapes and radial velocities to those presented in Fig. 2 and cannot be interpreted in terms of Galactic origin, since Galactic molecular clouds in this region show smaller radial velocities (Cohen et al. 1980; Lo et al. 1984; Tarchi et al. 2002). Both 36 GHz methanol (e.g., Leurini et al. 2016) and 24 GHz ammonia (e.g., Lebrón et al. 2011) may trace similarly dense molecular gas because rates for spontaneous emission are not far apart (1.48 and 1.67×10^{-7} s^{-1}, the latter for the $(J, K) = (1,1)$ ammonia transition; e.g., Schöier et al. 2005 and references therein). Therefore, the agreement in line shapes does not directly hint at 36 GHz maser emission in our two detected galaxies, but this is further discussed below in relation to what is known from the central region of the Milky Way.

Following the nomenclature of Lebrón et al. (2011), used for their ammonia (NH_3) observations with a beam size of $\approx 3\farcs5$, the blueshifted component we recognize in Maffei 2 (Fig. 2 and Table 1) must arise from their regions C and D, located in the southern part of the galaxy. The component near zero velocity is related to the northern part, represented by molecular complexes A and B. In Fig. 2 of Lebrón et al. (2011), sources B and C are dominant and, with their separation of 10″–15″ (280–415 pc), they should also dominate the 36 GHz methanol emission inside our 23″ beam. In the para-NH_3 (1,1) ground state inversion transition, the redshifted component is stronger than the blueshifted one, by a factor of roughly 1.6. The corresponding line intensity ratio we see in our 36 GHz methanol transition is 2.8 ± 0.3 in favor of this more redshifted component. While this difference is clearly compatible with quasi-thermal emission in both NH_3 (where this is expected) and CH_3OH, although suggesting slightly different physical or chemical conditions, we nevertheless note that the blueshifted CH_3OH component may be narrower than the one seen in ammonia.

Toward IC 342, our line widths and velocities of methanol are comparable, within the errors, to the ammonia lines from Lebrón et al. (2011). Very recently, Gorski et al. (2018) reported JVLA measurements of the central kiloparsec of IC 342 with 1″ and 7 km s^{-1} resolution. These latter authors detected six spatially resolved 36 GHz CH_3OH sites in IC 342 located along a northeast-southwest axis (position angle ≈30°) with a length of 20″ (300 pc). Interestingly, their strongest four sources peak at velocities clearly redshifted (≈50 km s^{-1}) with respect to the galaxy's systemic local standard of rest velocity of 35 km s^{-1}. A similar trend is also seen in the NH_3 (1,1) emission from Lebrón et al. (2011; their Fig. 1, lower right panel). However, our Table 1 instead indicates a peak velocity of the overall emission at systemic or slightly blueshifted velocities. Since the Gorski et al. (2018) data encompass the entire central region of IC 342 giving rise to emission from high-density molecular tracers, this discrepancy cannot be explained in terms of spatial regions not being covered by their measurements. This also holds for our data. Missing flux in the interferometric measurements might instead be the cause of the difference. However, adding the luminosities given in their Table 6 leads to a total luminosity of $0.315\,L_\odot$, which is (within 2σ, see, e.g., Sect. 2.2) compatible with our luminosity of $(0.26 \pm 0.03)\,L_\odot$ (Table 1). While we cannot explain the difference in radial velocities, the apparent lack of missing flux suggests that the bulk of the 36 GHz methanol emission is originating from compact spatially unresolved regions, compatible with maser emission.

In the folllowing text we use the definition of starburst galaxies as outlined by Mao et al. (2010; their Fig. 1), where the optical isophotal diameter D_{25} (25^m/arcsec^2) is applied to obtain the ratio $\log\,[(L_{\rm IR}/L_\odot)/(D_{25}^2/{\rm kpc}^2)]$. Here, in almost all cases the value 7.25 separates galaxies commonly identified as starburst from nonstarburst galaxies. With Maffei 2, IC 342 and NGC 6946 not being starburst galaxies like NGC 253 and NGC 4945 (according to our definition), but showing infrared luminosities and likely star forming rates similar to those of the Milky Way, there may be similarities between the conditions in Maffei 2, IC 342, and NGC 6946 and the central molecular zone (CMZ) of our Galaxy. Haschick et al. (1990) provided data from our Galactic center region, showing 36 GHz and 44 GHz methanol spectra from Sgr A-A ≈1′ northeast of the Galactic center and Sgr A-F, ≈3′ south of the Galactic center (their Fig. 9). These latter authors find narrow 36 GHz spikes, likely due to maser emission, on top of a broad component, possibly of quasi-thermal origin. For these two Galactic sources, the 36 GHz methanol lines show quite a number of narrow spikes, while only one such spike is seen in the corresponding 44 GHz methanol line.

More recently, Yusef-Zadeh et al. (2013) and Cotton & Yusef-Zadeh (2016) find a widespread population of more than 2000 compact 36 GHz methanol maser sources within the central degree of our Galaxy. The lines are narrow (≈1 km s^{-1}). Such a widespread distribution with a huge number of individual maser components covering the full radial velocity range of the nuclear environment could mimic a total profile, that is quite undistinguishable from quasi-thermal emission as long as the masers are spatially unresolved and no individual source stands out.

Figure 3 correlates 36 GHz line methanol luminosities with infrared luminosities obtained from IRAS (the Infrared Astronomical Satellite) and therefore with the star forming rates of their respective parent galaxies. While the number of sources is small and while both 36 GHz line and infrared continuum luminosities may be uncertain, it is clear that there is no good correlation. NGC 253 with its high infrared luminosity shows the most luminous 36 GHz methanol emission. However, NGC 4945, almost as luminous in the infrared, is comparatively weak with respect to the 36 GHz methanol line. Outflowing gas in its nuclear region (Henkel et al. 2018b), leading to shocks, is possibly not quite as prominent as in NGC 253 (Turner 1985; Bolatto et al. 2013). Maffei 2 also stands out with respect to methanol emission, even though its infrared luminosity is modest. While we did not resolve the sources, the explanation may be the prominent nuclear bar in Maffei 2 (e.g., Meier & Turner 2012), that may cause shocks throughout its central region, enhancing 36 GHz methanol emission above its normal level. Higher-resolution observations to study the spatial connection between the bar and the 36 GHz methanol emission would be desirable.

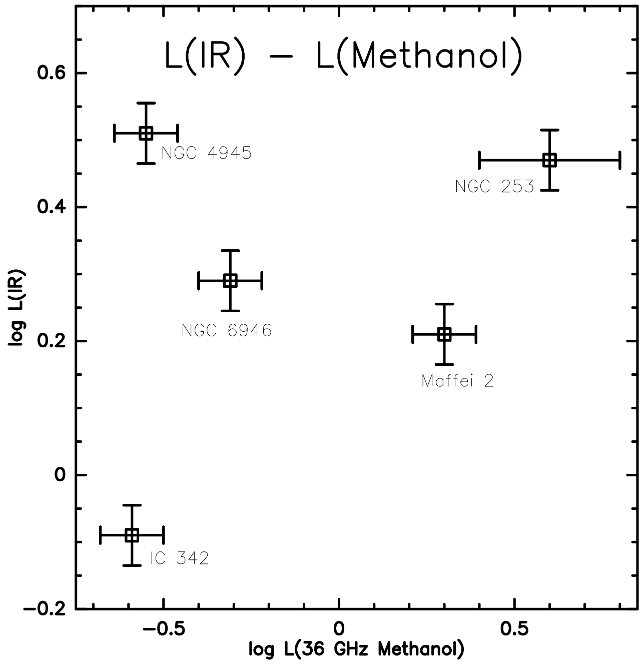

Fig. 3. 36 GHz methanol line luminosities in solar units vs. infrared luminosities in units of 10^{10} $L_{\odot}$, obtained from IRAS data, on logarithmic scales. For the former, ±20% (see Sect. 2.2, we added 5% due to limited signal-to-noise ratios) and for the latter ±10% error bars have been taken. The exception is NGC 253, where a larger error bar has been chosen for the 36 GHz methanol luminosity (see below). Adopted distances to the galaxies are 3.28 Mpc for IC 342 (Sect. 4), 5.73 Mpc for Maffei 2 (Sect. 4), 5.98 Mpc for NGC 6946 (Gorski et al. 2018), 3.5 Mpc for NGC 253 (Gorski et al. 2018) and 3.8 Mpc for NGC 4945 (Henkel et al. 2018b). The methanol line luminosities were calculated with Eq. (1). There exist huge discrepancies in total 36 GHz methanol flux density in the case of NGC 253, with Ellingsen et al. (2014) finding ≈0.3 $L_{\odot}$, Ellingsen et al. (2017) reporting ≈3 $L_{\odot}$ and Gorski et al. (2017) suggesting 6.4 $L_{\odot}$. We chose 4 $L_{\odot}$. For NGC 4945, McCarthy et al. (2017) report 0.14 $L_{\odot}$, while McCarthy et al. (2018b) find 2.8 $L_{\odot}$. We have taken the latter value, suspecting that the lower luminosity values are due to missing flux (e.g., Chen et al. 2018) and that variability might also play a role.

As already mentioned, it is noteworthy that toward the nonstarbursting galaxies we see line profiles compatible with the line profiles of other dense molecular gas tracers (for NH_3, see the discussion above; for HNCO, see Gorski et al. 2017, 2018). Toward the two detected starburst galaxies, however, we see emission from highly confined regions, the strongest such region being located in NGC 4945. We may therefore ask whether these galaxies also contain a component similar to the one in the less active galaxies Maffei 2, IC 342, and NGC 6946, only being less conspicuous in view of the outstanding maser peaks already encountered in these starburst environments. We advocate searches for such an underlying smoother 36 GHz emission component also in these galaxies. We note however that by analogy with our Galactic center region (e.g., Yusef-Zadeh et al. 2013), it is likely that this component is also representing maser emission.

4.2. Undetected lines

It may be argued that our lack of detected 44 GHz methanol in Maffei 2 and IC 342 is caused by the different levels of excitation, with the 36 GHz upper level (4_{-1}) 21 K and the 44 GHz upper level (7_0) 65 K above the ground state (the equivalent energy of the photons is only ≈2 K). However, we note that our 44 GHz measurements show rms values that are about three times larger than those at 36 GHz. Therefore, our nondetections at 44 GHz toward Maffei 2 and IC 342 merely indicate that the 44 GHz emission is not stronger than that at 36 GHz, which is consistent with the conditions in NGC 253 (Ellingsen et al. 2017) and appears to be a typical signature of extragalactic methanol class I emission.

With respect to our 36 GHz nondetections, the Arp 220 result is particularly interesting. Chen et al. (2015) reported several areas with emission in the outskirts of the merger with flux densities of order 10–20 mJy and our beam size is large enough to incorporate most of these regions. However, our upper limit given in Table 1 (last line) corresponds to a 5σ level of ≈4 mJy for a feature of 300 km s^{-1} in width. In view of its extreme infrared flux density, M 82 was an obvious target (it is one of the most prolific extragalactic infrared emitters of the entire sky; e.g., Henkel et al. 1986). Instead, NGC 4388 and NGC 5728 were observed because Chen et al. (2016) had published tentative 36 GHz class I methanol signals. We were not able to confirm their tentative features but note that our data are of similar sensitivity, and so in these cases, unlike for Arp 220, the situation remains unclear.

5. Conclusions

With Maffei 2 and IC 342 we present two 36 GHz class I methanol line emitters from galaxies outside the Local Group, while a previously reported detection of the ultraluminous infrared galaxy Arp 220 is not confirmed. The line luminosity of Maffei 2 is surprisingly high, which is possibly related to its prominent bar. As in the prototypical source, NGC 253, upper limits indicate that the 44 GHz class I methanol line is not substantially stronger. Now there are five such well-confirmed sources with 36 GHz line detections beyond any reasonable doubt. In contrast to the two initially detected and still most prominent of these sources, NGC 253 and NGC 4945, it is difficult to directly prove that the detected signals from Maffei 2 and IC 342 (and NGC 6946) are caused by masers. The line profiles are compatible with those obtained from ammonia, where masers are rarely observed. Unlike NGC 253 and NGC 4945, which are starburst galaxies, the others are spiral galaxies that are about as active with respect to star formation as our Milky Way. Therefore, by analogy with the central part of our Galaxy, the most likely interpretation is that the detected features represent the superposition of a large number of spatially unresolved weak maser hotspots lacking a single dominant source. It is hard to imagine that more active galaxies, like for example NGC 253 and NGC 4945, do not also show such a population of weak masers. Therefore, a search for such a weak and broad underlying spatially widespread 36 GHz methanol emission would also be worthwhile in starburst galaxies, as well as interferometric studies with utmost sensitivity to unambiguously demonstrate that at least a part of the detected emission originates from maser sources. The latter would, however, be a very ambitious project, presumably only feasible with the future next generation Very Large Array (ngVLA).

Acknowledgements. We wish to thank K.-M. Menten and an anonymous referee for valuable comments as well as the staff at Effelsberg for their great support, in particular the operators and A. Kraus. S. A. L. acknowledges funding through RSF grant No. 19-12-00157. This research has made use of NASA's Astrophysical Data System and of the NASA/IPAC Extragalactic Database.

References

Anand, G. S., Tully, R. B., Rizzi, L., & Karachentsev, I. D. 2019, ApJ, 872, l4

Beasley, A. J., Ellingsen, S. P., Claussen, M. J., & Wilcots, E. 1996, ApJ, 459, 600

Bolatto, A. D., Warren, S. R., Leroy, A. K., et al. 2013, Nature, 499, 450

Chen, X., & Ellingsen, S. P. 2018, in Astrophysical Masers: Unlocking the Mysteries of the Universe, eds. A. Tarchi, M. J. Reid, & P. Castangia, IAU Symp., 336, 99

Chen, X., Ellingsen, S. P., Baan, W. A., et al. 2015, ApJ, 800, L2

Chen, X., Ellingsen, S.-P., Zhang, J.-S., et al. 2016, MNRAS, 459, 357

Chen, X., Ellingsen, S. P., Shen, Z.-Q., et al. 2018, ApJ, 856, L35

Chomiuk, L., & Povich, M. S. 2011, AJ, 142, 197

Cohen, R. S., Cong, H., Dame, T. M., & Thaddeus, P. 1980, ApJ, 239, L53

Comito, C., Schilke, P., Phillips, T. G., et al. 2005, ApJS, 156, 127

Cotton, W. D., & Yusef-Zadeh, F. 2016, ApJS, 227, 10

Cragg, D. M., Sobolev, A. M., & Godfrey, P. D. 2005, MNRAS, 360, 533

Darling, J., Goldsmith, P., Li, D., & Giovanelli, R. 2003, AJ, 125, 1177

Ellingsen, S. P., Norris, R. P., Whiteoak, J. B., et al. 1994a, MNRAS, 267, 510

Ellingsen, S. P., Whiteoak, J. B., Norris, R. P., Caswell, J. L., & Vaile, R. A. 1994b, MNRAS, 269, 1019

Ellingsen, S. P., Breen, S. L., Caswell, J. L., Quinn, L. J., & Fuller, G. A. 2010, MNRAS, 404, 779

Ellingsen, S. P., Chen, X., Qiao, H.-H., et al. 2014, ApJ, 790, L28

Ellingsen, S. P., Chen, X., Breen, S. L., & Qiao, H.-H. 2017, MNRAS, 472, 604

Endres, C. P., Schlemmer, S., Schilke, P., Stutzki, J., & Müller, H. S. P. 2016, J. Mol. Spectr., 327, 95

Gómez-Ruiz, A. I., Kurtz, S. E., Araya, E. D., Hofner, P., & Loinard, L. 2016, ApJS, 222, 18

Gorski, M., Ott, J., Rand, R., et al. 2017, ApJ, 842, 124

Gorski, M., Ott, J., Rand, R., et al. 2018, ApJ, 856, 134

Gorski, M., Ott, J., Rand, R., et al. 2019, MNRAS, 483, 5434

Green, J. A., Caswell, J. L., Fuller, G. A., et al. 2008, MNRAS, 385, 948

Haschick, A. D., Menten, K. M., & Baan, W. A. 1990, ApJ, 354, 556

Henkel, C., Wouterloot, J. G. A., & Bally, J. 1986, A&A, 155, 193

Henkel, C., Jacq, T., Mauersberger, R., Menten, K. M., & Steppe, H. 1987, A&A, 188, L1

Henkel, C., Greene, J. E., & Kamali, F. 2018a, in Astrophysical Masers: Unlocking the Mysteries of the Universe, eds. A. Tarchi, M. J. Reid, & P. Castangia, IAU Symp., 336, 69

Henkel, C., Mühle, S., Bendo, G., et al. 2018b, A&A, 615, A155

Impellizzeri, C. M. V., Henkel, C., Roy, A. L., & Menten, K. M. 2008, A&A, 484, L43

Iodice, E., Arnaboldi, M., Rejkuba, M., et al. 2014, A&A, 567, A86

Kalenski, S. V., & Sobolev, A. M. 1994, Astron. Lett., 20, 91

Karachentsev, I. D., Makarov, D. I., & Kaisina, E. I. 2013, AJ, 145, 101

Kennicutt, R. C. 1998, ARA&A, 36, 189

Klein, B., Hochgürtel, S., Krämer, I., et al. 2012, A&A, 542, L3

Kurtz, S., Hofner, P., & Álvarez, C. V. 2004, ApJS, 155, 149

Lebrón, M., Mangum, J. G., Mauersberger, R., et al. 2011, A&A, 534, A56

Leurini, S., Menten, K. M., & Walmsley, C. M. 2016, A&A, 592, A31

Lo, K. Y. 2005, ARA&A, 43, 625

Lo, K. Y., Berge, G. L., Claussen, M. J., et al. 1984, ApJ, 282, L59

Maffei, P. 1968, PASP, 80, 618

Maffucci, D. M., Wenger, T. V., Le Gal, R., & Herbst, E. 2018, ApJ, 868, 41

Mao, R.-Q., Schulz, A., Henkel, C., et al. 2010, ApJ, 724, 1336

McCarthy, T. P., Ellingsen, S. P., Chen, X., et al. 2017, ApJ, 846, 156

McCarthy, T. P., Ellingsen, S. P., Breen, S. L., Voronkov, M. A., & Chen, X. 2018a, ApJ, 867, L4

McCarthy, T. P., Ellingsen, S. P., Breen, S. L., et al. 2018b, MNRAS, 480, 4578

McEwen, B. C., Pihlström, Y. M., & Sjouwerman, L. O. 2014, ApJ, 793, 133

Meier, D. S., & Turner, J. L. 2012, ApJ, 755, 104

Menten, K. M. 1991, ApJ, 380, L75

Misiriotis, A., Papadakis, I. E., Kylafis, N. D., & Papamastorakis, J. 2004, A&A, 417, 39

Misiriotis, A., Xilouris, E. M., Papamastorakis, J., Boumis, P., & Goudis, C. D. 2006, A&A, 459, 113

Nesterenok, A. V. 2016, MNRAS, 455, 3978

Ott, M., Witzel, A., Quirrenbach, A., et al. 1994, A&A, 284, 331

Phillips, C. J., Norris, R. P., Ellingsen, S. P., & Rayner, D. P. 1998, MNRAS, 294, 265

Pratap, P., Shute, P. A., Keane, T. C., Battersby, C., & Sterling, S. 2008, AJ, 135, 1718

Salter, C., Ghosh, T., Catinella, B., et al. 2008, AJ, 136, 389

Schilke, P., Benford, D. J., Hunter, T. R., Lis, D. C., & Phillips, T. G. 2001, ApJS, 132, 281

Schöier, F. L., van der Tak, F. F. S., van Dishoeck, E. F., & Black, J. H. 2005, A&A, 432, 369

Sinclair, M. W., Carrad, G. J., Caswell, J. L., Norris, R. P., & Whiteoak, J. B. 1992, MNRAS, 256, 33

Sjouwerman, L. O., Murray, C. E., Pihlström, Y. M., Fish, V. L., & Araya, E. D. 2010, ApJ, 724, L158

Tarchi, A., Henkel, C., Peck, A. B., & Menten, K. M. 2002, A&A, 385, 1049

Tikhonov, N. A., & Galazutdinova, O. A. 2018, Astrophys. Bull., 73, 279

Turner, B. E. 1985, ApJ, 299, 312

Wang, M., Henkel, C., Chin, Y.-N., et al. 2004, A&A, 422, 883

Wu, P. F., Tully, R. B., & Rizzi, L. 2014, AJ,148, 7

Yang, K., Chen, X., Shen, Z.-Q., et al. 2017, ApJ, 846, 160

Yang, K., Chen, X., Shen, Z.-Q., et al. 2019, ApJS, 241, 18

Yusef-Zadeh, F., Cotton, W., Viti, S., Wardle, M., & Royster, M. 2013, ApJ, 764, L19

APPENDIX C

Methanol masers in NGC 253 with ALCHEMI

A&A 663, A33 (2022)
https://doi.org/10.1051/0004-6361/202243384

Astronomy & Astrophysics

Methanol masers in NGC 253 with ALCHEMI

P. K. Humire[1], C. Henkel[1,2,3], A. Hernández-Gómez[1], S. Martín[4,5], J. Mangum[6], N. Harada[7,8,9], S. Muller[10], K. Sakamoto[8], K. Tanaka[11], Y. Yoshimura[12], K. Nakanishi[7,9], S. Mühle[13], R. Herrero-Illana[4,14], D. S. Meier[15,16], E. Caux[17], R. Aladro[1], R. Mauersberger[1], S. Viti[18,19], L. Colzi[20], V. M. Rivilla[20], M. Gorski[10], K. M. Menten[1], K.-Y. Huang[18], S. Aalto[10], P. P. van der Werf[18], and K. L. Emig[6,⋆]

(Affiliations can be found after the references)

Received 21 February 2022 / Accepted 5 May 2022

ABSTRACT

Context. Methanol masers of Class I (collisionally pumped) and Class II (radiatively pumped) have been studied in great detail in our Galaxy in a variety of astrophysical environments such as shocks and star-forming regions and are they are helpful to analyze the properties of the dense interstellar medium. However, the study of methanol masers in external galaxies is still in its infancy.

Aims. Our main goal is to search for methanol masers in the central molecular zone (CMZ; inner 500 pc) of the nearby starburst galaxy NGC 253.

Methods. Covering a frequency range between 84 and 373 GHz ($\lambda = 3.6$–0.8 mm) at high angular ($1''.6 \sim 27$ pc) and spectral ($\sim$8–9 km s^{-1}) resolution with ALCHEMI (ALMA Comprehensive High-resolution Extragalactic Molecular Inventory), we have probed different regions across the CMZ of NGC 253. In order to look for methanol maser candidates, we employed the rotation diagram method and a set of radiative transfer models.

Results. We detect for the first time masers above 84 GHz in NGC 253, covering an ample portion of the $J_{-1} \rightarrow (J-1)_0 - E$ line series (at 84, 132, 229, and 278 GHz) and the $J_0 \rightarrow (J-1)_1 - A$ series (at 95, 146, and 198 GHz). This confirms the presence of the Class I maser line at 84 GHz, which was already reported, but now being detected in more than one location. For the $J_{-1} \rightarrow (J-1)_0 - E$ line series, we observe a lack of Class I maser candidates in the central star-forming disk.

Conclusions. The physical conditions for maser excitation in the $J_{-1} \rightarrow (J-1)_0 - E$ line series can be weak shocks and cloud-cloud collisions as suggested by shock tracers (SiO and HNCO) in bi-symmetric shock regions located in the outskirts of the CMZ. On the other hand, the presence of photodissociation regions due to a high star-formation rate would be needed to explain the lack of Class I masers in the very central regions.

Key words. galaxies: spiral – galaxies: starburst – masers – submillimeter: galaxies – radio lines: galaxies

1. Introduction

Methanol (CH_3OH) is a molecule prone to population inversion under specific excitation conditions in the interstellar medium (ISM) (e.g., Cragg et al. 1992), causing maser emission. In particular, methanol masers are unique tools for studying physical properties of dense gas associated with young stellar objects (YSOs). Given their brightness and compactness (Menten 1991), their positions can be determined with high precision astrometry (i.e., at milli-arcsecond accuracy with very long baseline interferometry) and over vast distances.

Thousands of such methanol masers have been detected in the Milky Way (Cotton & Yusef-Zadeh 2016; Green et al. 2017; Yang et al. 2019). However, in nearby galaxies we can only account for a handful of successful detections (e.g., McCarthy et al. 2020). In particular, the brightest Galactic methanol maser transition at 6.7 GHz (Breen et al. 2015), remains elusive in extragalactic objects outside the Local Group (Ellingsen et al. 1994; Darling et al. 2003), with the only exception being NGC 3079 (Impellizzeri et al. 2008), and possibly Arp220 (Salter et al. 2008), where this line is detected in absorption.

The early discovery that methanol masers can be divided into two classes, a collisionally pumped Class I and a radiatively pumped Class II (Batrla et al. 1987; Menten 1991), allows us to trace either stellar-induced outflows (Class I) or ultracompact H II regions (Class II). Class I methanol masers have been observed toward high and low-mass stars (Kalenskii et al. 2006, 2010; Rodríguez-Garza et al. 2017), while Class II masers have been observed only toward high-mass YSOs (Breen et al. 2013). Unlike H_2O and OH masers, Class II methanol masers seem to be exclusively correlated with star-forming regions (Walsh et al. 2001; Breen et al. 2013).

Because Class II masers are usually brighter than Class I masers in our Galaxy, the former type of masers have been studied in great detail, leading to surveys targeting exclusively their relation with the surrounding conditions (Yang et al. 2017; Billington et al. 2020). However, outside our Galaxy, Class II masers were only detected in the Magellanic Clouds (Sinclair et al. 1992; Green et al. 2008; Ellingsen et al. 2010) and the Andromeda galaxy (Sjouwerman et al. 2010), with luminosities not surpassing those in our Galaxy. On the other hand, extragalactic Class I masers can be more luminous than those of Class II, and have been successfully observed beyond the Local Group, particularly in nearby barred spiral galaxies such as NGC 253, IC 342, or NGC 4945 (e.g., Ellingsen et al. 2014; McCarthy et al. 2017; Gorski et al. 2018).

There are two types of methanol. For *E*-type methanol, one of the protons in the hydrogen atoms of the methyl (CH_3) group has an antiparallel nuclear spin with respect to the others, analogous to the case of para-NH_3. In *A*-type methanol, the nuclear spins of the three protons in the methyl group are parallel, as in the case of ortho-NH_3. As the two methanol types have different transition frequencies and may arise in different physical environments, we decided to analyze them separately.

[⋆] Jansky Fellow of the National Radio Astronomy Observatory.

Hereafter we use the conventional notation for A^+ and A^- introduced by Lees & Baker (1968), related to a combination between the A–CH_3OH overallparity and Mulliken symbols[1] A_1 and A_2. This is done to discriminate between splitted $+K$ and $-K$ levels (doublets), with K being the projection of the angular momentum along the molecular symmetry axis. Furthermore, $+K$ and $-K$ levels are torsionally degenerate for the case of A-type methanol, contrary to the case of E-type methanol (see also Cragg et al. 1993).

As shown by Lees (1973), among E-type methanol transitions (E–CH_3OH) Class I population inversion is favored in the $K = -1$ relative to the $K = 0$ or $K = -2$ ladders. This leads to the prominence of the $J_{-1} \rightarrow (J-1)_0 - E$ series (see, e.g., Leurini et al. 2016, their Fig. 3). Indeed, the $4_{-1} \rightarrow 3_0 - E$ (36.2 GHz) and $5_{-1} \rightarrow 4_0 - E$ (84.5 GHz) lines have been recently discovered to be masing in one extragalactic object, NGC 253 (Ellingsen et al. 2014; McCarthy et al. 2018). For A-type methanol, population inversion in the $K = 0$ relative to the $K = 1$ ladder is favored, playing out in the $J_0 \rightarrow (J-1)_1 - A^+$ series, of which the 44.1 GHz line, at $J = 7$, has been also detected in NGC 253 (Ellingsen et al. 2017). The emission of Galactic Class II methanol masers are more compact than those of their Galactic Class I cousins (Moscadelli et al. 2003; Matsumoto et al. 2014), and that could make Class II methanol masers more difficult to detect at extragalactic distances. In addition, Class I masers require lower densities and temperatures than Class II masers (Menten 2012), making them more numerous. Specifically for the $J_{-1} \rightarrow (J-1)_0 - E$ series with $J = 4$ and 5, their intensities were predicted to be on the order of 50 mJy in the case of NGC 253 (Sobolev 1993).

Class I methanol masers may be associated with a variety of phenomena, such as supernova remnants (Plambeck & Menten 1990; Pihlström et al. 2014), massive protostellar induced outflows (Cyganowski et al. 2018), and interactions of expanding H II regions with surrounding molecular gas (Voronkov et al. 2010), namely regions where shocks compress and heat the gas. In the central molecular zone (CMZ) of our Galaxy (i.e., the inner ~200 pc in radius; Morris & Serabyn 1996), cosmic ray interactions with molecular clouds have been claimed to be an additional source of methanol production. While a high methanol abundance alone is certainly not sufficient to trigger maser emission, there seems to be indeed a clear enhancement of Class I masers in this region (Yusef-Zadeh et al. 2013; Cotton & Yusef-Zadeh 2016; Ladeyschikov et al. 2019). In particular, extended strong emission showing characteristics of maser action had been found by Haschick & Baan (1993) and Salii et al. (2002) in the G1.6−0.025 region at the periphery of the CMZ and by Szczepanski et al. (1989) and Liechti & Wilson (1996) in a region in which the supernova remnant Sgr A East interacts with a Giant Molecular Cloud (GMC). Noteworthy, CMZ conditions in the Milky Way should provide some guidance to the central regions of starburst galaxies (Belloche et al. 2013).

Class I methanol masers at 36, 44, and 84 GHz have already been reported in NGC 253 by Ellingsen et al. (2014, 2017), and McCarthy et al. (2018), respectively. The former, at 36 GHz, has been also observed in NGC 4945, IC 342, NGC 6946, and Maffei 2 (McCarthy et al. 2017; Gorski et al. 2018; Humire et al. 2020). A 84 GHz mega-maser ($\geq 10^6$ times more luminous than typical Galactic masers; Lo 2005) has been reported in NGC 1068 (Wang et al. 2014), but a confirmation would be needed to put this onto a firm basis. Although a tentative detection of methanol mega-maser emission was claimed in Arp 220 (Chen et al. 2015), later studies ruled it out (Humire et al. 2020; McCarthy et al. 2020). Making use of the unprecedented spectral coverage available by the Atacama Large Millimeter/sub-millimeter Array (ALMA) Large Program ALCHEMI (Martín et al. 2021), we have been able to make a comprehensive study toward one of the best candidates to search for extragalactic maser emission, the Sculptor galaxy NGC 253.

NGC 253 is a nearby (D ~ 3.5 Mpc, Rekola et al. 2005) highly inclined (i ~ 70°–79°, Pence 1980; Iodice et al. 2014) SAB(s)c galaxy (de Vaucouleurs et al. 1991) with a systemic heliocentric velocity ($\upsilon_{\rm sys}$) of ~258.8 km s^{-1} (Meyer et al. 2004). Its large-scale bar feeds the nuclear region producing stars at an approximate rate of ~1.7 $M_\odot$ yr^{-1} (Bendo et al. 2015) within the central $20'' \times 10''$, where $1''$ corresponds to ~17 pc. The position angle (PA) of the large-scale bar is 51° (Pence 1980). The PA continues till the central ~170 parsecs. Further into the core, the isovelocity contours of the gas change their orientation by about 90° due to the existence of a nuclear bar (Cohen et al. 2020). Like our Galaxy, NGC 253 is characterized by a particularly strong and diverse molecular emission in its central 500 pc (Sakamoto et al. 2006), which we therefore identify as its CMZ. Previous studies do not suggest that an Active Galactic Nucleus (AGN) is important for the properties of the molecular gas in the CMZ of NGC 253 (Müller-Sánchez et al. 2010).

This paper is organized as follows: our observations are described in Sect. 2. In Sect. 3 we show the selected regions to be studied in the CMZ of NGC 253. In Sect. 4 we introduce the two methods used to identify methanol masers. In Sect. 5 we discuss the results and provide a number of conditions to explain maser emission. We finally draw the conclusions of our findings in Sect. 6.

2. Observations

We use ALMA observations of NGC 253 taken in Cycles 5 and 6 as part of the large program ALCHEMI (ALMA Comprehensive High-resolution Extragalactic Molecular Inventory, 2017.1.00161.L, followed up by program 2018.1.00162.S, see Martín et al. 2021). The central region of the galaxy ($50'' \times 20'' = 850 \times 340$ pc, with a position angle of 65°) was covered in bands 3–7 (84.2–373.2 GHz), with both the 12 m and 7 m antenna arrays, achieving a final homogeneous angular resolution of $1''.6$. The mentioned region was covered with a single pointing in band 3, with a primary beam ranging between $57''$ and $68''$, and Nyquist-sampled mosaic patterns of 5 up to 19 pointings for the remaining bands, ensuring a homogeneous sensitivity across the selected region[2]. The phase center of the observations is $\alpha = 00^{\rm h}47^{\rm m}33^{\rm s}.26$, $\delta = -25^\circ17'17''.7$ (ICRS[3]).

The absolute flux calibration accuracy is on the order of 15% for all ALMA bands, since most percentages are lower across individual bands. The flux density RMS noise ranges from 0.18 to 5.0 mJy beam^{-1}, and the averaged sensitivity is 14.8 mK. For more details about the data reduction procedures and image processing, see Martín et al. (2021).

---

[1] `https://mathworld.wolfram.com/CharacterTable.html`

[2] ALMA sets up by default a hexagonal Nyquist sampled pattern to ensure homogeneous sensitivity across the mapped region. Furthermore, mosaic images are primary beam corrected, in our case this includes the studied 850×340 pc region. For more information about mosaicing, we refer the reader to Sect. 7.7 in the ALMA technical Handbook (`https://almascience.eso.org/documents-and-tools/cycle9/alma-technical-handbook`).

[3] International Celestial Reference System, equivalent to J2000 within a few milli-arcseconds (Ma et al. 1998).

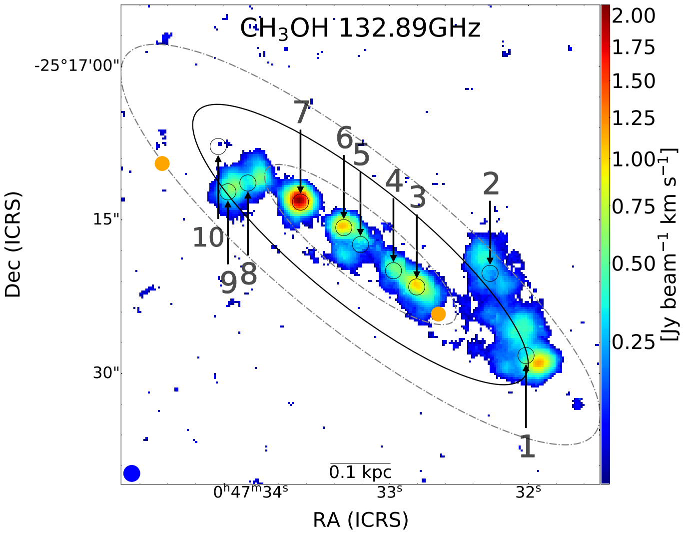

Fig. 1. Integrated intensity map for the $6_{-1} \rightarrow 5_0 - E$ methanol line at 132.9 GHz (within a velocity interval of $\upsilon_{\rm sys} \lesssim \pm 200\,{\rm km\,s^{-1}}$). Selected positions for spectral extraction (Sect. 3) are encircled in beam-sized apertures and numbered from 1 to 10. The center and edges of the inner Lindblad resonance from Iodice et al. (2014) are denoted with a black ellipse and dash-dotted gray ellipses, respectively. Superbubbles identified by Sakamoto et al. (2006) are indicated as orange circles. The ALMA beam (1$''$.6) is shown in blue in the bottom left corner.

3. Selected positions

In Fig. 1, we show the integrated intensity map of the $6_{-1} \rightarrow 5_0 - E$ methanol emission (132.9 GHz rest frequency) using a 3σ clip threshold and applying the formalism suggested by Mangum & Shirley (2015, their Appendix C) to obtain the uncertainties. The selection of this methanol line is motivated by its high signal-to-noise ratio (S/N), the absence of notable blending candidates, and maser emission in some regions (see below). In NGC 253, the inner Lindblad resonance (ILR) was found to be cospatial with its circumnuclear ring (CNR) by Iodice et al. (2014). The total ILR extension measured by them is 0.3 ± 0.1–0.4 ± 0.1 kpc (deprojected size). We draw concentric ellipses at 0.2 and 0.5 kpc to denote the ILR limits in Fig. 1 (dash-dotted gray ellipses) as well as its center at 0.35 kpc (solid black ellipse). Along the text, we use the ILR position as a proxy to the x_2 orbit in NGC 253 (see Sect. 5).

The presence of methanol masers depends on the physical conditions prevailing across the CMZ of NGC 253. We decided to select ten distinct positions within the CMZ (see Fig. 1 and Table 1). These positions were established based on intensity peaks of the CS $J = 2-1$ and H^{13}CN $J = 1-0$ transitions, applying a GMC identification approach based on Leroy et al. (2015), that is to say, using the CPROPS software (Rosolowsky & Leroy 2006). Our region coordinates are not exactly the same as those used by Leroy et al. (2015), even though our numbering is close to theirs. We preferred to use those GMC locations instead of the peak intensities of our methanol lines at a given frequency, because the peak location varies depending on the chosen transition (see also, Zinchenko et al. 2017; McCarthy et al. 2018). We list the coordinates and velocities of all these positions in Table 1. The velocities were obtained from preliminary LTE radiative transfer models, similar to the ones described in Sect. 4.2, and averaged over each methanol symmetric type.

For each region, we extracted the full spectrum (84–373 GHz, see Sect. 4.2) from the data convolved to a common circular beam of 1$''$.6 diameter, equivalent to the maximum angular resolution of the observations (see Sect. 2). At higher resolution, however, GMCs further divide into molecular clumps with a size range of 0$''$.07–0$''$.25 (1.2–4.3 pc; Leroy et al. 2018). Contrary to the spectrum of the other nine studied regions, we have found a very complex spectrum in region 5 located next to the dynamical center of the galaxy (Müller-Sánchez et al. 2010). Radio recombination line observations revealed an S-shaped pattern with complex kinematics including a counter-rotating core in the inner 2$''$ suggestive of a secondary bar (Anantharamaiah & Goss 1996) and evidencing a black hole mass of $\sim 10^7\,M_\odot$ (Cohen et al. 2020). This highly-perturbed environment is likely causing the crowded spectrum observed in region 5. In this position, the broad line emission, with a full width at half maximum (FWHM) above 100 km s^{-1}, prevents an accurate Gaussian line fitting for the rotation diagram analysis in Sect. 4.1, but can be used for the radiative transfer modeling in Sect. 4.2. In addition, toward region 5 and mostly in the low frequency range (~84–163 GHz, ALMA bands 3 and 4) we observe absorption components.

Methanol lines in absorption or self-absorption (in the case of the line at 358.6 GHz) along the entire ALCHEMI spectral coverage are observed in at least one region for the following four transitions: the $3_1 \rightarrow 4_0 - A^+$ line at 107.0 GHz, the $4_{-2} \rightarrow 4_{-0} - E$ line at 190.1 GHz, the $5_{-2} \rightarrow 5_{-0} - E$ line at 190.3 GHz (in absorption in region 10 only), and the $4_1 \rightarrow 3_0 - E$ line at 358.6 GHz. They are shown in Fig. 2.

Table 1. Selected regions.

Region	$\alpha_{\rm ICRS}$ [00$^{\rm h}$:47$^{\rm m}$:–$^{\rm s}$]	$\delta_{\rm ICRS}$ [−25°:17′:–″]	$\upsilon_{\rm LSR}$ [km s^{-1}]
R1	32.02	28.3	304
R2	32.28	20.2	330
R3	32.81	21.6	286
R4	32.97	20.0	252
R5	33.21	17.4	231
R6	33.33	15.8	180
R7	33.64	13.3	174
R8	34.02	11.4	205
R9	34.17	12.3	201
R10	34.24	7.8	144

Notes. The Local Standard of Rest (LSR) velocities were obtained by fitting a local thermodynamic equilibrium model (LTE) to the spectra and averaging between the *A*– and *E*–CH$_3$OH symmetry species. Our spectral resolution of ~8–9 km s^{-1} dominates the velocity uncertainty.

4. Methanol maser emission identification

In some[4] cases, it can be difficult to assess whether a given line is excited under thermal or maser conditions. Methanol maser lines in Galactic star-forming regions are usually very bright (in the sense of brightness temperature) and narrow. However, in the case of extragalactic objects, beam dilution makes them apparently weaker and less distinguishable from thermal emission due to line blending from surrounding gas. In the spectral dimension this also complicates a proper line identification since the contribution of other species might affect the true brightness of the putative maser lines (see the last column of Table A.1).

---

[4] `https://web-archives.iram.fr/IRAMFR/ARN/may95/node4.html`

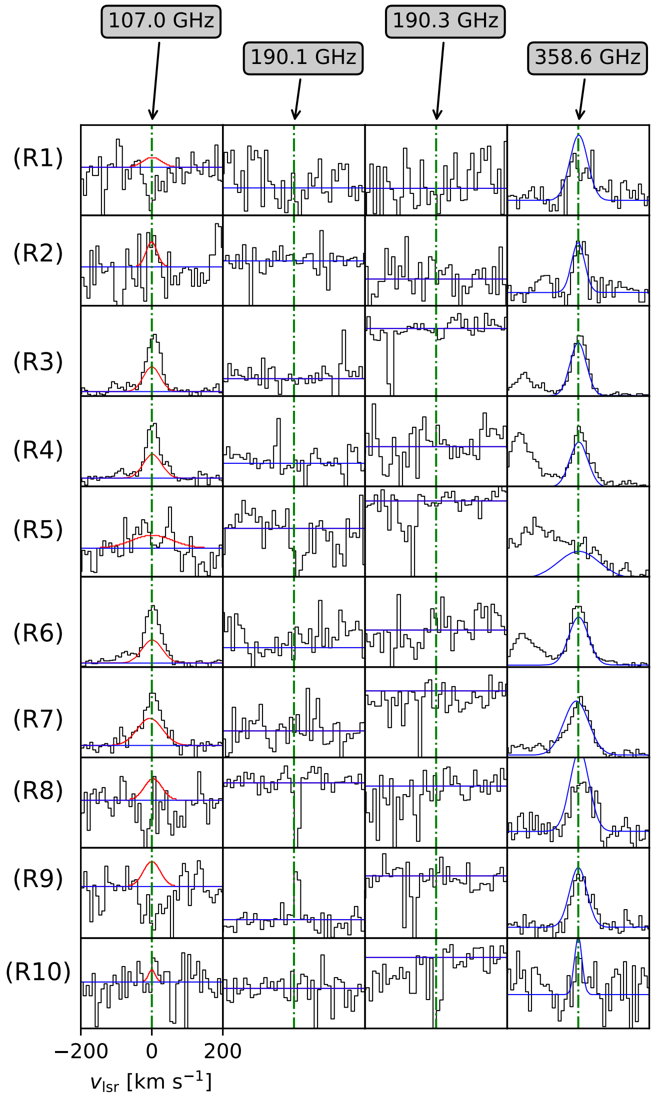

Fig. 2. Methanol lines observed in absorption or self-absorption in one or more of the selected regions (Table 1). Red and blue lines are synthetic spectra for methanol *A*- and *E*- type, respectively (see Sect. 4.2). Line frequencies are labeled in the top of the figure, while the velocity range (in km s^{-1}, after applying the radio convention (`https://web-archives.iram.fr/IRAMFR/ARN/may95/node4.html`) and subtracting the $v_{\rm LSR}$ velocities from Table 1) is indicated in the bottom-left corner. Regions 1–10 are ordered from *top to bottom* as indicated in the *leftmost panel* (*y*-axis: *R* from "Region" plus the corresponding number). For the location of the regions, see Fig. 1 and Table 1.

In this section we explore two methods to identify methanol emission lines outside local thermodynamic equilibrium (LTE) as an indicator of potential maser emission, namely rotation diagram analysis and comparisons with synthetic spectra from radiative transfer modeling. For both methods, we constrained the upper energy above the ground level ($E_{\rm up}/k$) of the lines to ≤150 K, since the entirety of lines above that limit are blended with other methanol transitions below that limit, and are likely not contributing significantly to the overall emission (see the analysis in Sect. 4.2).

In this study, we consider as LTE conditions those reached when a single excitation temperature, $T_{\rm ex}$, characterizing the energy level population according to the Boltzmann distribution, is sufficient to explain the line emission of methanol along all its observed transitions. Namely, an equivalency between kinetic ($T_{\rm kin}$) and excitation temperatures is not strictly required.

4.1. Rotation diagram

As a first approach, we use the rotation diagram method to compare the relative intensities of methanol lines in NGC 253. The details of this method can be found in Goldsmith & Langer (1999) and are also summarized in our Appendix A.

Since this method assumes that the gas is under LTE conditions and that the lines are optically thin, any transition deviating from a straight-line fit in the rotation diagram indicates that, for values below the fitted line, opacities are not low and that, for values above the fitted line, maser emission may be a suitable explanation.

If a given line is affected by blending, we could overestimate its integrated intensity, which would lead to a wrongly classified maser line. Therefore, after identifying all the methanol transitions in our observations and before performing the rotation diagrams, we have initially searched both in the CDMS (Müller et al. 2005) and JPL (Pickett et al. 1998) databases for potentially contaminating lines from other molecular species (last column in Table A.1). Special care was taken on previously reported molecules in NGC 253 (e.g., Martín et al. 2006; Meier et al. 2015; Ando et al. 2017), as well as preliminary line identification performed on the 1″.6 resolution ALCHEMI data (Martín et al., in prep.). Blended nonmethanol line candidates are required to fall inside the FWHM of the given methanol line, which varies for each symmetric type and region.

To produce the rotation diagrams we have used the CASSIS[5] software. In particular, we have used the spectroscopic VASTEL database, which comes from the JPL catalog[6], since it distinguishes between *A* and *E* methanol forms. Covering transitions with $E_{\rm up}/k < 150$ K, we did not consider methanol lines separated from each other by less than their FWHM. Because of that, we did not include in our analysis the $J_K \rightarrow (J-1)_K$ line series at ~96.7 GHz ($J = 2$), ~145.1 GHz ($J = 3$), ~193.5 GHz ($J = 4$), ~241.8 GHz ($J = 5$), and ~290.1 GHz ($J = 6$).

A summary of the considered transitions for each region is shown in Table A.1, where line parameters were taken from the CDMS database (the same holds for the other tables throughout this work). For each of the selected lines, we have obtained the integrated line intensity $\int T_{\rm mb} {\rm d}v$ by fitting a single Gaussian profile. The resulting rotation diagrams are presented in Fig. 3, for *A*– and *E*–CH$_3$OH symmetry species separately and for each studied region (Table 1), where we conservatively assumed a flux calibration uncertainty of 15%, as recommended by Martín et al. (2021). This uncertainty plus Gaussian fitting uncertainties were added in quadrature for each line.

The rotation diagram method assumes the Rayleigh–Jeans (RJ) approximation (see Appendix A). In our case, given the low $T_{\rm ex}$ measured by the rotation diagrams in certain regions (see Table A.2), the RJ approximation is not a good assumption for high-frequency transitions, leading to an overestimation of ~40% for the upper level population of some transitions in the worst case scenario. As explained in Appendix A, applying a correction factor to all our transitions, as an attempt to go beyond the RJ approximation, we obtain slight changes in $T_{\rm ex}$ but total column densities decrease by up to ~40% in extreme cases. The value that would be derived from the Planck function for the corresponding transition assuming the same $T_{\rm ex}$ originally derived

---

[5] `http://cassis.irap.omp.eu`

[6] `http://cassis.irap.omp.eu/?page=catalogs-vastel`

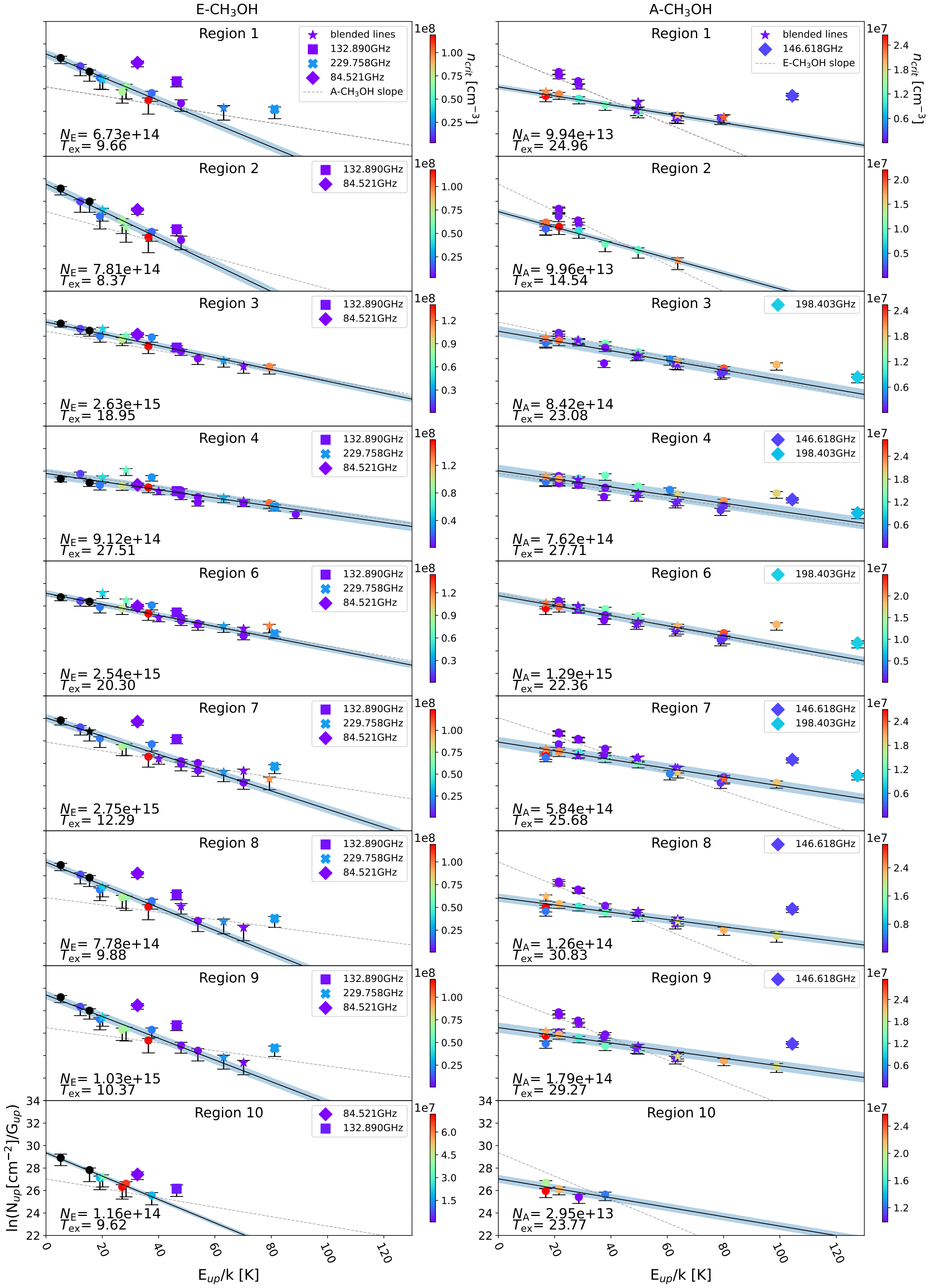

Fig. 3. Rotation diagrams based on our selected methanol transitions (Table A.1) and separated by methanol symmetric type (E–CH$_3$OH and A–CH$_3$OH). Straight black lines represent our best fits to the data considering only methanol lines not blended with other methanol lines (see Sect. 4.1) and following LTE conditions. Dotted gray lines are the slopes of the complementary methanol symmetric type in the same region. Maser candidates (see Sect. 4.1) are labeled with symbols. Points are color-coded depending on their critical densities (in units of cm^{-3}), as indicated by the color bar to their right (transitions with unavailable critical densities are in black). In the bottom left corner of each panel, the column density ($N_{E\text{–CH}_3\text{OH}}$ and $N_{A\text{–CH}_3\text{OH}}$, in cm^{-2}) and the excitation temperature ($T_{\rm ex}$, in Kelvin) derived from the fit are indicated. Non-blended lines in LTE are marked by circles, while methanol lines blended with other methanol lines (at $E_{\rm up}/k$ > 150 K) are assigned by stars. Shaded areas represent 1σ uncertainties (see Sect. 4.1).

Table 2. Outliers in the rotation diagrams.

Maser candidate						τ [a]	Blended [b]					Maser [c]	Location [d]
Transition	ν [GHz]	A/E	Class	E_{up}/k [K]	A_{ij} [s^{-1}]	[$\times10^{-4}$]	Transition	ν [GHz]	A/E	E_{up}/k [K]	A_{ij} [s^{-1}]	[K]	
$5_{-1} \rightarrow 4_0$	84.521172	E	I	32.49	1.97×10^{-6}	−236.6	$12_{10} \rightarrow 12_{11}$	84.531123	E	1085.97	7.72×10^{-7}	Yes	1,2,7–10
$2_1 \rightarrow 1_1$	95.914310	A^+	–	21.44	2.49×10^{-6}	12.5	Not-blended	–	–	–	–	No	
$2_1 \rightarrow 1_1$	97.582798	A^-	–	21.56	2.63×10^{-6}	3.8	Not-blended	–	–	–	–	No	
$6_{-1} \rightarrow 5_0$	132.890759	E	I	46.41	7.74×10^{-6}	−67.7	Not-blended	–	–	–	–	Yes	1,2,7–10
$3_1 \rightarrow 2_1$	143.865795	A^+	–	28.35	1.07×10^{-5}	7.8	Not-blended	–	–	–	–	No	
$3_1 \rightarrow 2_1$	146.368328	A^-	–	28.59	1.13×10^{-5}	6.5	Not-blended	–	–	–	–	No	
$9_0 \rightarrow 8_1$	146.618697	A^+	I	104.41	8.03×10^{-6}	−0.1	$14_1 \rightarrow 13_2$	146.617429	A^+	256.02	6.6×10^{-6}	Yes	1,7–9
$2_1 \rightarrow 3_0$	156.602395	A^+	–	21.44	1.78×10^{-5}	162.3	Not-blended	–	–	–	–	No	
$10_0 \rightarrow 9_1$	198.403067	A^+	I	127.60	4.10×10^{-5}	−0.01	Not-blended	–	–	–	–	Yes	3,6,7
$8_{-1} \rightarrow 7_0$	229.758756	E	I	81.20	4.19×10^{-5}	−2.1	Not-blended	–	–	–	–	Yes	2,7–9
$2_{-1} \rightarrow 1_{-0}$	261.805675	E	–	28.01	5.57×10^{-5}	402.3	$20_5 \rightarrow 21_3$	261.800288	E	611.06	9.85×10^{-9}	No	
$6_2 \rightarrow 5_1$	315.266861	E	–	63.10	1.18×10^{-4}	6.7	$37_{-6} \rightarrow 36_{-7}$	315.237555	E	1808.32	5.73×10^{-5}	No	
$8_1 \rightarrow 8_0$	318.318919	A^{-+}	II [e]	98.82	1.79×10^{-4}	1.5	Not-blended	–	–	–	–	No	
$7_{-0} \rightarrow 6_{-0}$	338.124488	E	–	78.08	1.70×10^{-4}	10.9	$38_{12} \rightarrow 37_{10}$	338.117653	E	2425.29	7.38×10^{-8}	No	
$4_{-0} \rightarrow 3_1$	350.687662	E	–	36.33	8.67×10^{-5}	1205.0	$18_{-3} \rightarrow 18_{-2}$	350.723878	E	812.46	4.17×10^{-5}	No	
$4_1 \rightarrow 3_0$	358.605799	E	–	44.26	1.32×10^{-4}	224.1	Not-blended	–	–	–	–	No	
$7_2 \rightarrow 6_1$	363.739868	E	–	79.36	1.70×10^{-4}	1.7	$23_6 \rightarrow 22_9$	363.680652	E	1327.80	1.78×10^{-7}	No	

Notes. [a]Optical depth according to our non-LTE model of region 8 (see Appendix C). [b]Methanol lines next to the frequency given in Col. (2). Their frequency is given in Col. (9). [c]Maser candidates based on the discussion in Sect. 4.1.1. [d]Regions where the transition is masing. [e]According to the classification of the $J_1 - J_0A^{-+}$ line series in Zinchenko et al. (2017). The dash (–) symbol indicates no information/detection. For more information about the columns see Sect. 4.1.

with the RJ approximation for each region and methanol symmetric type, is shown inside the error bars in Fig. 3. The application of the Planck formula increases the lower-limit uncertainty as a function of the T_{ex} (see Eq. (A.3)) found for each region through RJ and the individual frequency of each transition and therefore mostly affects the regions where T_{ex} is lower than 12 K, i.e., regions 1, 2, and 8–10 in E–CH$_3$OH. The parameters derived after applying this correction are also included in the uncertainties presented in Table A.2.

In Fig. 3 we also indicate the critical densities of the different transitions shown in the rotation diagrams. To this end, we have used the most recently available collisional rates (C_{ij}), interpolating their values, given in steps of 10 K by Rabli & Flower (2010), by the corresponding T_{ex} obtained through the rotation diagrams in each region and for each methanol symmetric type. The critical densities thus obtained, in units of cm^{-3} are then indicated by colors in the rotation diagrams (Fig. 3; transitions with unavailable C_{ij} are in black).

We started including all the considered transitions (Table A.1) below a certain E_{up}/k (see below) to perform our rotation diagrams and obtain the best linear fit. However, we soon realized that some transitions did not fall on the linear fit line derived from the ensemble of methanol integrated intensities. We excluded these lines that do not follow LTE conditions but are not likely to correspond to masers, see Appendix B, to perform, in a second iteration, a linear fit to the remaining data in order to estimate the column density and T_{ex}. Our fit results are shown at the bottom of each rotation diagram in Fig. 3 with outliers indicated in the legends when they correspond to maser candidates (see below). Column densities and T_{ex} with their uncertainties are listed in Table A.2. In general, the distribution of the data points can be well described by a single T_{ex}.

Without considering the outliers, the standard deviations (1σ) of the residuals of the data points from the fitted lines are of a difference $(\ln(N_{\mathrm{up,\,data\,points}}) - \ln(N_{\mathrm{up,\,bestfit}}))$ between 0.2 (E–CH$_3$OH in region 10) and 0.5 (A–CH$_3$OH in region 4). These values translate into a factor $(N_{\mathrm{up,\,data\,points}}/N_{\mathrm{up,\,bestfit}})$ between $\exp(0.2) = 1.2$ and $\exp(0.5) = 1.7$.

We conservatively rounded up the average standard deviation ($\sigma = 0.35$–0.4) and obtained a factor of 3.3 scatter, in the exponential scale of our rotation diagrams ($\exp(3\sigma)$). We then classify as outliers all methanol transitions surpassing by more than a factor of 3.3 the expected value from LTE conditions.

These outliers are listed in Table 2, where their transitional quantum numbers, frequencies, symmetry types, maser classes, E_{up}/k, A_{ij}, and optical depths are indicated in Cols. (1)–(7), respectively. In this table we also provide information about possible line blending with other methanol transitions falling within the FWHM of the main transition; they possess higher E_{up}/k and lower A_{ij}, implying a lower contribution to the observed spectrum due to the need for more extreme conditions to be emitted. In Table 2, the information given for these lines is the transition, frequency, symmetric type, E_{up}/k, and A_{ij} along Cols. (8)–(12), respectively.

Deviations from LTE are expected in the ISM, in particular for complex level diagrams and if radiative and collisional excitation and de-excitation compete. But in general, given the success in the fitting, it can be inferred that potential blending lines in Table A.1 are, in most cases, not significantly contaminating.

We wish to emphasize that a sophisticated model, including hundreds or thousands of transitions from many molecules, would be needed to determine methanol line blending with transitions of other species in a thorough way, providing a percentage of contamination to methanol made from other species. Since this is clearly beyond the scope of this paper (but we sometimes quote initial results from region 5, obtained from Martin et al., in prep.), we refer in the following to the case of blending of methanol with other methanol lines, unless contamination with other species is explicitly mentioned.

Based on the line width, CASSIS is able to discriminate between unblended methanol lines and those which are contaminated by adjacent lines of methanol. In Fig. 3 we represent unblended lines with circles and blended lines with stars. Since line widths change per region, the same transition may be denoted by circles or stars depending on the region. Besides of that, we have found that some methanol lines presented in Fig. 3 are blended with other highly energetic methanol lines ($E_{\mathrm{up}}/k \geq 1000$ K, see Table 2) and therefore significant blending is highly unlikely. However, we decided to show them also as blended lines (stars) in order to be impartial along all the regions and

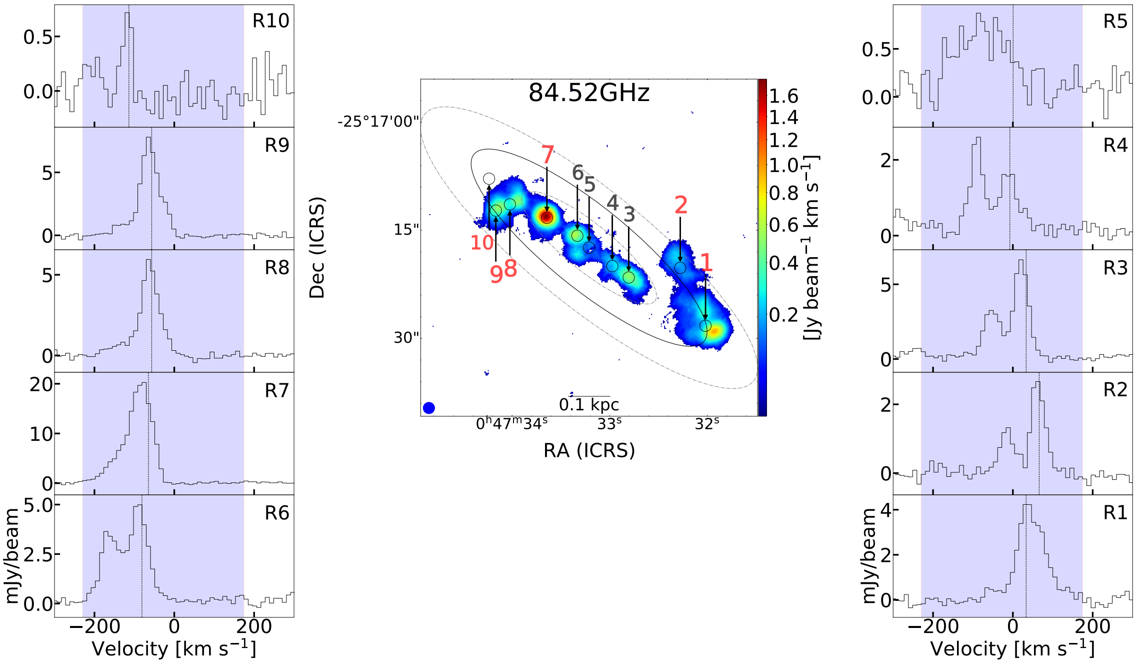

Fig. 4. *Central panel*: velocity integrated intensity of the $5_{-1} \rightarrow 4_0 - E$ methanol line at 84.5 GHz obtained by integrating the channels inside the colored areas shown in the side panels. Regions where we detect Class I maser emission in the $J_{-1} \rightarrow (J-1)_0 - E$ series (see Sect. 4.1.2) are labeled in red and with slightly larger numbers. *Side panels*: methanol spectra of the different regions as labeled in the top right corner of each panel (a $\upsilon_{\rm sys}$ of 258.8 km s^{-1} was subtracted). Vertical lines indicate the peak velocity of the ^{13}CO $J = 1-0$ line (110.2 GHz) extracted in each region, as a reference for the systemic velocity at that position. Coordinate system, beam size and other parameters are the same as in Fig. 1.

transitions. In addition, we note that lines with $E_{\rm up}/k \leq 150$ K, being blended with methanol transitions with $E_{\rm up}/k > 150$ K, are plotted with the lower $E_{\rm up}/k$ value in Fig. 3. Finally, the LTE slope is adjusted exclusively considering unblended and non-masing methanol lines (for a definition of the latter, see below).

4.1.1. Rotation diagram results

To distinguish maser candidates among outliers, that is, lines located beyond a 3σ scatter; the respective line must belong to known methanol maser line series already discovered in NGC 253 at lower frequencies. This is because maser action is more prominent at lower frequencies than the ones covered in this work: as A_{ij} is proportional to the cube of the frequency, lower A_{ij} leads to a longer time lapse to accumulate inverted populations. In addition, we also require that the candidate line shows maser behavior in more than one region.

In the following we measure the departure from LTE of the maser lines as the ratio between their nominal upper level column densities in the rotation diagrams ($N_{\rm up,maser}$) over the expected upper level column density in LTE ($N_{\rm up,LTE}$). In the computation of $N_{\rm up}$ one generally assumes a proportional relation with the integrated intensity (see Eq. (A.2)). For maser lines, however, intensities and abundances are not related, as their negative opacity amplifies radiation from the background. Therefore this $N_{\rm up,maser}/N_{\rm up,LTE}$ factor must be taken as an intensity difference instead of abundance difference.

4.1.2. *E*-type methanol masers

Among the E–CH$_3$OH maser line candidates belonging to the $J_{-1} \rightarrow (J-1)_0 - E$ series (at 84.5, 132.9, and 229.8 GHz), none of them were detected out of LTE in regions 3–6 (see Table 2), which are therefore excluded from the following analysis.

We present the spectra and velocity integrated intensity maps of the two transitions with the highest S/Ns ($5_{-1} \rightarrow 4_0 - E$ at 84.5 GHz and $6_{-1} \rightarrow 5_0 - E$ at 132.9 GHz) in Figs. 4 and 5.

The $5_{-1} \rightarrow 4_0 - E$ line at 84.5 GHz departs from LTE by factors ($N_{\rm up,maser}/N_{\rm up,LTE}$) ranging from 4.2 ± 1.3 to 13.2 ± 1.2 in regions 10 and 1, respectively (see Fig. 3). This is the first detection of the 84.5 GHz maser line in more than one position, after its first discovery by McCarthy et al. (2018). The higher J masers in the $J_{-1} \rightarrow (J-1)_0 - E$ series are usually observed to originate in the same regions, suggesting similar distributions and pumping mechanism.

The $6_{-1} \rightarrow 5_0 - E$ line at 132.9 GHz departs from its expected integrated intensity in LTE by factors ranging from 4.6 ± 1.2 to 10.6 ± 1.2, in regions 2 and 1, respectively. Contrary to the previous transition at 84.5 GHz, it is not blended with other methanol lines.

The $8_{-1} \rightarrow 7_0 - E$ line at 229.8 GHz is observed to mase in the same regions as the ones at 84.5 and 132.9 GHz except in regions 2 and 10, which display the lowest LTE fitted $T_{\rm ex}$ in the E-type methanol species and also the lowest S/Ns. In these couple of regions, the emission is too weak to be classified as a maser. The $8_{-1} \rightarrow 7_0 - E$ line is the highest frequency transition detected as a maser by the rotation diagram method; its intensity departs from LTE by 9.8 ± 1.2, in region 7 and up to 32.0 ± 1.2 in region 1.

4.1.3. *A*-type methanol masers

With respect to A–CH$_3$OH, maser line candidates are part of the $J_0 \rightarrow (J-1)_1 - A^+$ series ($9_0 \rightarrow 8_1 - A^+$ and $10_0 \rightarrow 9_1 - A^+$ transitions). We note that a lower J (and lower frequency)

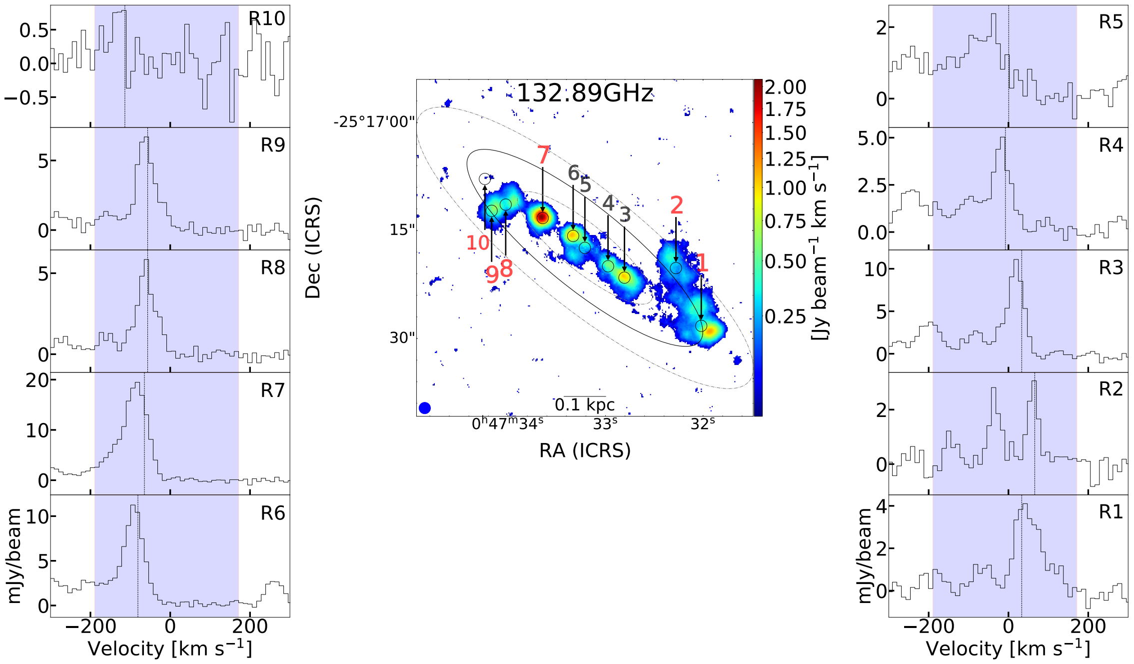

Fig. 5. Same as for Fig. 4, but for the $6_{-1} \rightarrow 5_0 - E$ methanol line at 132.9 GHz.

transition in this series is the $7_0 \rightarrow 6_1 - A^+$ line at 44.1 GHz, which is the strongest Galactic Class I maser.

The $9_0 \rightarrow 8_1 - A^+$ line at 146.618 GHz departs from LTE by factors in the range of 8.4 ± 1.2 (in region 8) to 29.8 ± 1.2 (in region 1), excluding region 4 because of line blending (see Appendix B). This maser transition has been suggested to be part of the Class I family of methanol masers (e.g., Yang et al. 2020, and references therein).

The $10_0 \rightarrow 9_1 - A^+$ line at 198.4 GHz departs from LTE in regions 3, 6, and 7, being the only masing line candidate for regions 3 and 6. In those regions, this line departs from LTE by factors of 4.3 ± 1.3, 3.6 ± 1.2, and 8.5 ± 1.2, respectively.

We have found that all our maser candidates, except the $10_0 \rightarrow 9_1 - A^+$ line at 198.4 GHz, are masers at the outskirts of the CMZ of NGC 253 (see Table 2). The physical conditions in the regions giving rise to those masers are characterized (see Fig. 6) by total column densities for A–CH$_3$OH lower than 6×10^{14} cm^{-2}, an excitation temperature lower than 15 K in E–CH$_3$OH, and differences between A– and E–CH$_3$OH excitation temperatures larger than 5.0 K. Conversely, we do not see a correlation between the presence of masers and total column densities in E-type methanol, the temperature described by A–CH$_3$OH, or differences between column densities of the two methanol types.

With the exception of the line at 198.4 GHz, it is worth noting that all the regions where we detect Class I maser emission lie inside the Lindblad resonances (see, e.g., Fig. 4), with the only exception being region 7. We further explore this point in Sect. 5.2.

Based on LTE modeling, we have also found other transitions that are possibly experiencing maser activity. They will be described below.

4.2. Radiative transfer modeling

In comparison with the rotation diagram method, synthetic spectra offer a number of improvements, such as the possibility to reproduce line profiles both in LTE and out of LTE, which may also subtly indicate the number of gas components present in the observed source (see, e.g., Fig. C.1). Also, as the lines are observed on a linear scale, the effect of slight changes in the assumed gas conditions are noticed in more detail compared with the logarithmic scale used in the rotation diagram method. Apart from those advantages, radiative transfer modeling allows us to fit not only single methanol lines, but also blended ones, as their spectra are summed up when trying to obtain the desired intensities. Alternatively, this provides an estimate for the degree of contamination caused by other species. This allows us to include many more lines, increasing the sample size. In fact, as we see below, there are 57 lines used for the fitting in our radiative transfer models, in contrast to the 39 finally used in the rotation diagrams (see Sect. 4.1.1).

The possibility to perform non-LTE modeling helps us to discard maser line candidates in case negative optical depths are not required to reproduce their emission. Finally, the nature of blended methanol lines with other methanol lines at known maser frequencies, such as the transitions at 95.169 and 278.305 GHz, could not be unveiled through the rotation diagram method. As mentioned in Sect. 4.1, we use the term blending to refer to contamination of methanol lines with other methanol transitions, unless contamination by other species is explicitly mentioned.

We have computed synthetic spectra for each of the 10 selected regions in NGC 253, covering the entire ALCHEMI frequency range (~84–373 GHz, see Sect. 2), by using the CASSIS software, capable of producing LTE and non-LTE spectral modeling. For the non-LTE case, CASSIS is used as a wrapper of RADEX (van der Tak et al. 2007), a one-dimensional non-LTE radiative transfer code based on the escape probability formulation. In CASSIS it is possible to create a physical model defined by 6 parameters: column density of the species (N(Sp)), excitation ($T_{\rm ex}$, LTE case) or kinetic ($T_{\rm kin}$, non-LTE case) temperature, full width at half maximum (FWHM) of the lines, velocity of the source in the Local Standard of Rest ($V_{\rm LSR}$) system, size of

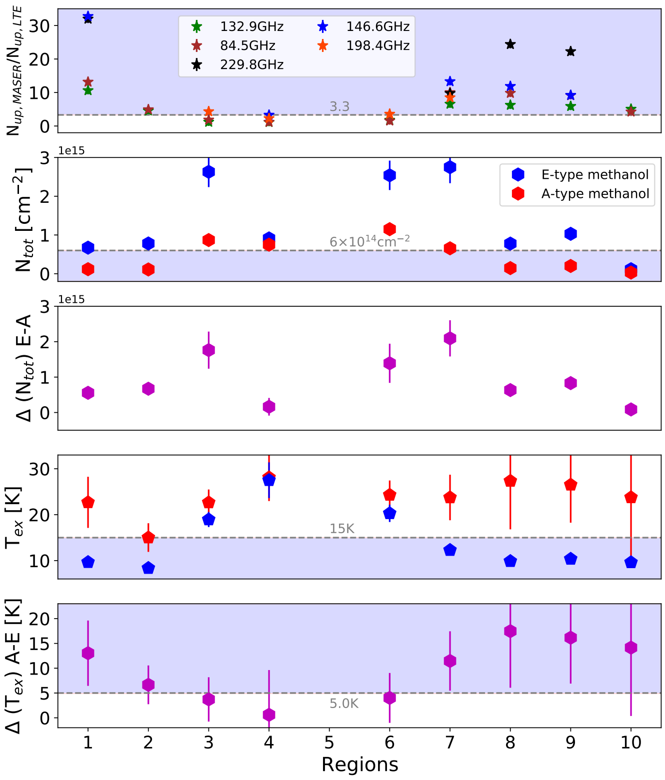

Fig. 6. Physical conditions for the methanol maser candidates (see Table 2) derived from our rotation diagrams. The x-axis indicates the number of the region. The y-axis represents, from *top to bottom*, (1) the ratio between the nominal upper level column densities of the lines $N_{\rm up,MASER}$ and the expected values from our best fit to LTE conditions $N_{\rm up}$,LTE, (2) the total column density, (3) the difference between total E– and A–type column densities, (4) the LTE excitation temperatures and (5) the difference between the A– and E–type excitation temperatures. Shaded areas highlight regions were maser emission in the $J_{-1} \rightarrow (J-1)_0 - E$ line series (at 84, 132, and 229 GHz), and the $J_0 \rightarrow (J-1)_1 - A^+$ line series (at 146 and 198.4 GHz), are observed, according to the *first panel*.

the source in arcseconds, and the H_2 volumetric density ($n_{\rm H2}$) in the case of non-LTE modeling. For simplicity, in this section we have considered that only a single physical component for each methanol type is responsible for the observed emission; for a more detailed analysis, see Appendix C. CASSIS makes use of the Monte Carlo Markov chain (MCMC) method (Hastings 1970) to explore a user-predefined range of values for each of the parameters previously mentioned. By means of the χ^2 minimization method, CASSIS is able to find the best ensemble of solutions. Computing the synthetic spectra we assumed a beam filling factor of one, by selecting a source size of $1\farcs6$ (~27 pc), and a slab geometry (appropriate for shocks, e.g., Leurini et al. 2016).

Model solutions could be strongly influenced by the initial conditions. Therefore we start by selecting unblended methanol lines to be fitted and then add blended lines whose total line profile is successfully reproduced with the starting models. This was achieved by exploring the success of CASSIS in reproducing the lines throughout our selected regions.

After our initial attempts to fit methanol lines along the entire ALCHEMI spectral coverage, assuming either LTE or non-LTE conditions, it became clear from our 10 regions that it is impossible to properly fit all the lines with a single physical set of parameters, even after separating between A– and E–CH_3OH flavors. This is especially important at frequencies below ~156 GHz, and it is possibly due to a couple of factors: the presence of a series of lines out of LTE, and the higher number of maser candidates.

Using our LTE model, we found that the $J_K \rightarrow (J-1)_K$ transitions (for both methanol symmetric types), which were avoided in Sect. 4.1 due to line blending, are not following LTE conditions. Within the ALCHEMI frequency coverage, these line series have the following frequencies: ~96.7 GHz (J = 2), ~145.1 GHz (J = 3), ~193.5 GHz (J = 4), ~241.8 GHz (J = 5), and ~290.1 GHz (J = 6). Performing a non-LTE model in region 8, they are satisfactorily reproduced, as can be seen in Fig. C.2 without invoking the presence of masers.

At frequencies below ~156 GHz we also cover four maser candidates, three of them reported in Sect. 4.1.2 plus an additional one that we see below (Sect. 4.2.1). Therefore, at lower frequencies our models fail to reproduce an important quantity of available, not blended, methanol lines.

We discard possible software issues by doing a sanity check with another radiative-transfer code capable of producing LTE models, MADCUBA (Martín et al. 2019). It shows similar results including convergence primarily toward lines above 156 GHz.

Having said the above, we do not include the mentioned $J_K \rightarrow (J-1)_K$ transition series nor the maser candidates in our LTE modeling. Even with this restriction, we observe that these series are well reproduced (>50%) in region 4 by merely fitting the other transitions, and this can be improved with a two-component LTE model (see Appendix C).

When inspecting and comparing the results for all regions between the LTE and non-LTE models, considering a single component for each methanol symmetric type, we observe that they are in agreement within an uncertainty of about 15% (although this agreement is not observed when we consider a two-component non-LTE model, see Appendix C). This is not surprising since high H_2 densities of $>10^7$ cm^{-3} are needed in the non-LTE models to reproduce most line profiles. At such densities collisions play a major role, tending to constrain the spread in excitation temperatures between different lines. Therefore, we conclude that the simpler LTE conditions are sufficient to represent the observed spectra in NGC 253. From now on, we therefore mainly refer to our LTE modeling, except in a few exceptional cases where this is explicitly mentioned.

As described in Sect. 4, we set an upper $E_{\rm up}/k$ threshold of 150 K for the synthetic spectra. This was determined through comparing observations to model fits with and without the higher energy levels ($E_{\rm up}/k$ > 150 K). A total of 600 LTE models for each individual spectrum, one per selected region (see Table 3), were computed, reaching a convergence after 300–400 iterations. We find that we only require models that include $E_{\rm up}/k$ < 150 K to fit the observed spectra. Thermal line emission with $E_{\rm up}/k$ > 150 K may be there, but is too faint to affect model fits or to be separated from line blends. In the Galaxy, methanol masers with levels around 150 K above the ground state are scarce. Within the ALCHEMI frequency coverage we can mention the case of the $11_{-1} \rightarrow 10_{-2} - E$ line at 104.3 GHz (Leurini & Menten 2018). However, this Class I maser is rarely seen (Voronkov et al. 2012). We do not obtain any strong emission at this frequency in NGC 253.

Best fit parameters determined from our LTE models for each region and methanol species are listed in Table 3. Differences between A– and E–CH_3OH symmetry species are present in terms of temperature and density. In velocity they differ by a few km s^{-1}, although this discrepancy never exceeds our spectral

Table 3. Best fit parameters from our LTE modeling.

	E–CH$_3$OH				A–CH$_3$OH				
Region	N(Sp) [$\times10^{14}$ cm^{-3}]	$T_{\rm ex}$ [K]	FWHM [km s^{-1}]	$V_{\rm LSR}$ [km s^{-1}]	N(Sp) [$\times10^{14}$ cm^{-3}]	$T_{\rm ex}$ [K]	FWHM [km s^{-1}]	$V_{\rm LSR}$ [km s^{-1}]	Mean $V_{\rm LSR}$ [km s^{-1}]
R1	$3.7^{+0.1}_{-0.1}$	$14.8^{+0.4}_{-0.6}$	$59.7^{+1.0}_{-2.5}$	$305.4^{+0.8}_{-1.0}$	$0.76^{+0.05}_{-0.04}$	$18.8^{+0.8}_{-0.7}$	$61.3^{+1.7}_{-0.4}$	$302.9^{+1.4}_{-0.8}$	304 ± 9
R2	$5.0^{+0.3}_{-0.2}$	$9.3^{+0.4}_{-0.4}$	$43.6^{+2.5}_{-1.5}$	$328.1^{+0.2}_{-0.7}$	$1.0^{+0.1}_{-0.1}$	$14.8^{+0.5}_{-0.9}$	$37.4^{+2.6}_{-2.9}$	$327.2^{+1.6}_{-1.1}$	328 ± 9
R3	$19.5^{+0.6}_{-0.5}$	$21.4^{+0.4}_{-0.5}$	$53.8^{+0.6}_{-0.9}$	$283.2^{+0.4}_{-0.4}$	$9.3^{+0.1}_{-0.2}$	$26.6^{+0.3}_{-0.6}$	$55.0^{+0.9}_{-0.3}$	$284.7^{+0.3}_{-0.5}$	283 ± 9
R4	$10.16^{+0.04}_{-0.03}$	$31.0^{+0.6}_{-1.2}$	$60.2^{+1.7}_{-1.5}$	$252.0^{+0.5}_{-0.6}$	$9.0^{+0.2}_{-0.2}$	$34.2^{+0.8}_{-0.9}$	$60.1^{+0.7}_{-1.3}$	$251.5^{+0.2}_{-0.6}$	252 ± 9
R5	$6.2^{+0.5}_{-0.4}$	$32.2^{+1.8}_{-1.7}$	$136.0^{+8.4}_{-7.9}$	$217.2^{+4.5}_{-3.3}$	$3.2^{+0.3}_{-0.2}$	$32.2^{+1.8}_{-1.7}$	$136.0^{+8.4}_{-7.9}$	$217.2^{+4.5}_{-3.3}$	217 ± 10
R6	$22.32^{+0.07}_{-0.03}$	$24.8^{+0.5}_{-0.4}$	$65.3^{+0.9}_{-0.4}$	$179.9^{+0.4}_{-0.5}$	$14.1^{+0.2}_{-0.2}$	$31.0^{+0.4}_{-0.6}$	$66.0^{+0.7}_{-0.9}$	$182.1^{+0.7}_{-0.3}$	181 ± 9
R7	$17.4^{+0.6}_{-0.4}$	$19.5^{+0.4}_{-0.5}$	$82.8^{+1.3}_{-1.4}$	$169.3^{+0.6}_{-0.9}$	$5.5^{+0.2}_{-0.1}$	$22.9^{+0.4}_{-0.5}$	$83.2^{+3.0}_{-2.9}$	$173.6^{+1.2}_{-1.0}$	171 ± 9
R8	$5.9^{+0.2}_{-0.1}$	$14.8^{+0.3}_{-0.4}$	$63.7^{+0.9}_{-1.8}$	$204.2^{+1.3}_{-1.9}$	$1.2^{+0.1}_{-0.1}$	$19.5^{+0.4}_{-0.7}$	$59.1^{+3.7}_{-3.3}$	$205.2^{+1.3}_{-1.6}$	205 ± 9
R9	$5.6^{+0.3}_{-0.1}$	$13.9^{+0.5}_{-0.4}$	$57.4^{+2.2}_{-1.3}$	$202.7^{+1.1}_{-0.9}$	$1.5^{+0.1}_{-0.1}$	$19.2^{+0.6}_{-0.4}$	$56.3^{+2.6}_{-1.9}$	$201.4^{+1.1}_{-0.7}$	202 ± 9
R10	$1.0^{+0.1}_{-0.1}$	$12.3^{+0.7}_{-1.1}$	$24.9^{+1.8}_{-1.3}$	$143.9^{+1.0}_{-0.8}$	$0.27^{+0.03}_{-0.02}$	$27.36^{+3.1}_{-3.1}$	$22.8^{+3.9}_{-3.3}$	$146.4^{+1.1}_{-1.5}$	145 ± 9

Notes. From left to right columns are: selected region of the CMZ of NGC 253 (see Table 3), E-type methanol parameters: column density of the species (N(Sp)), excitation temperature ($T_{\rm ex}$), FWHM of the modeled methanol lines, and the local standard of rest velocity of the region $V_{\rm LSR}$. Columns (6)–(9) provide the same gas parameters for A–CH$_3$OH. Uncertainties are 1σ. An extra uncertainty of 15% should be added to N(Sp) (due to the flux calibration accuracy, see Sect. 2). In the last column we present the average velocity of the two methanol symmetric types. In this case our 1σ uncertainty is summed in quadrature with our velocity resolution of ∼8–9 km s^{-1}, which dominates.

resolution of ∼8–9 km s^{-1}. Thus, the averaged $V_{\rm LSR}$ of these two species is adopted as the velocity of the region, in the same way as it has been previously established in Table 1.

A comparison between synthetic and observed spectra allows us to perform a deep scan of the methanol lines, highlighting some lines that slightly deviate from LTE conditions in the rotation diagrams or that are blended with other methanol lines and that were previously not discussed. The result of this inspection is henceforth described.

4.2.1. LTE modeling results

As can be seen in our Fig. 7, our synthetic spectra fit reasonably well the observed spectra in most of the regions. Region 5 is the most difficult to reproduce due to the large FWHM (∼140 km s^{-1}) of the lines, with its spectrum almost reaching the confusion limit. Fortunately, based on the remaining regions, we selected a large number of lines that are reproduced (see Tables C.1 and C.2, and Fig. 7). We attempted to fit the same lines in region 5, preventing in this way false line identifications and subsequent erroneous fitting attempts.

The best solution for Region 5 was reached by fitting both methanol symmetric types simultaneously. When this is done in CASSIS, the whole set of parameters between A- and E-type methanol is forced to be equal, allowing to change only the ratio between their column densities. As can be seen in Table 3, the column density of E–CH$_3$OH is 2.1 times higher than that of A–CH$_3$OH. A lower column density E/A ratio leads us always to a worse fitting and is therefore not attempted to reach. We have also discarded from the initial fit the A–CH$_3$OH transitions between 303.3 and 309.2 GHz, as their inclusion always leads to an overestimation of a number of lines (e.g., transitions at 239.7, 241.9, 338.6, and 350.9 GHz, see Tables C.1 and C.2).

All the proposed maser candidates listed in Table 2 that were initially unveiled through the rotation diagrams were confirmed by our models.

In addition to the outliers previously detected (see Table 2), we found several transitions with intensities not reproduced by our synthetic spectra. Among those outliers, listed in Table 4, there are a couple of maser candidates. We describe them below.

4.2.2. Maser line candidates

Contrary to the remaining outliers found through the radiative transfer modeling (shown in Fig. 8 and described at some level in Appendix D), our maser candidates have negative optical depths, depart significantly from LTE (see below), and belong to the same transition series as the maser candidates detected previously through the rotation diagram method (Sect. 4.1.3), being Class I methanol masers.

The $8_0 \rightarrow 7_1 - A^+$ transition line at 95.2 GHz shows intensities >12.8 times stronger than predicted by the LTE modeling in all the regions but region 4, where it is three times stronger. This large departure in the inner regions of the CMZ remind us of the case of the $10_0 \rightarrow 9_1 - A^+$ methanol line at 198.4 GHz, which shows emission 3.3 times larger than expected in regions 3 and 6.

The $9_{-1} \rightarrow 8_0 - E$ line at 278.305 GHz is the last methanol transition in the $J_{-1} \rightarrow (J-1)_0 - E$ line series covered in this work. As previously mentioned in Sect. 4.1.2, it is strongly contaminated by the $2_{-2} \rightarrow 3_{-1} - E$ line at 278.342 GHz and was therefore excluded from the analysis with rotation diagrams. In regions 1, 7, 8, and 9, however, its line profile is clearly distinguished from the contaminating line when being checked by the synthetic models. According to our radiative transfer modeling, the companion line at 278.342 GHz is the only one that should be observed (while the masing line intensity should be negligible under LTE, see Fig. 9), with its peak velocity about 40 km s^{-1} lower than the maser line in region 9, a difference four times larger than our spectral resolution.

In summary, all the outliers in the LTE models have intensities above the expected one under LTE conditions, but most of them are likely able to be reproduced under non-LTE conditions if the results obtained for region 8 (Appendix C) are maintained for the other regions. The only clear maser candidates are the lines at 95.2 and 278.3 GHz.

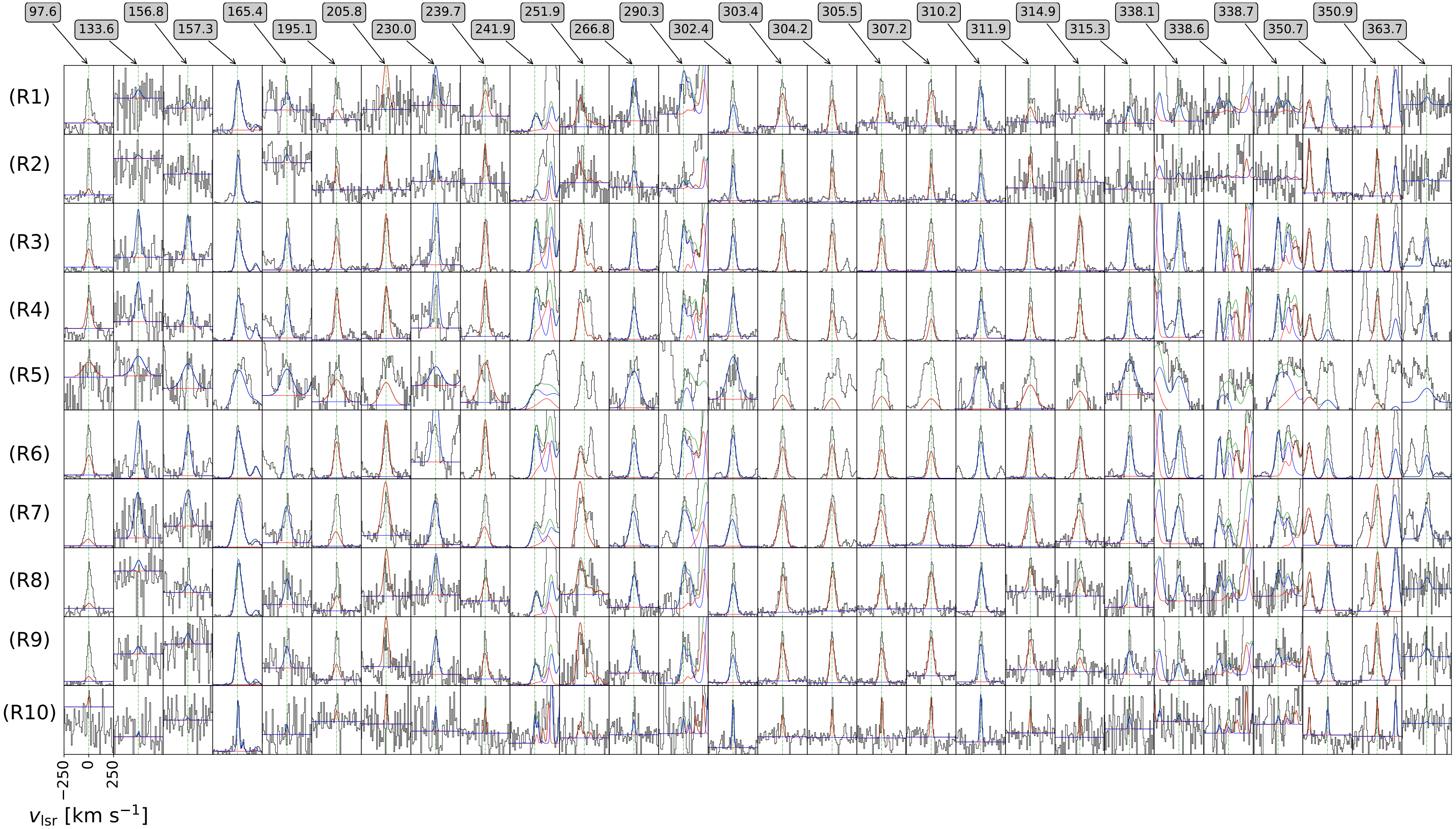

Fig. 7. Zoom into successfully fitted lines for each region, which can be considered to follow LTE conditions. Red and blue colors indicate methanol *A*- and *E*-type, respectively, while the superposition of the two types, the final fit, is indicated in green. Line frequencies (in GHz units) are labeled at the top of the figure and are also indicated as a green dashed vertical line inside panels, while the velocity range (in km s^{-1} with respect to the systemic velocity of the individual regions, see Fig. 4) is indicated in the bottom-left corner. Regions 1–10 are ordered from top to bottom as indicated in the leftmost panel (R from "Region" plus the corresponding number).

Table 4. Outliers in the LTE model.

Transition	ν [GHz]	A/E	$E_{\rm up}/k$ [K]	A_{ij} [s^{-1}]	τ [d] [$\times 10^{-5}$]	Maser [e]
$8_0 \rightarrow 7_1$	95.169391	A^+	83.54	2.13×10^{-6}	–6.5	I
$3_1 \rightarrow 4_0$	107.013831 [a]	A^+	28.35	3.06×10^{-6}	1021	No
$0_0 \rightarrow 1_{-1}$	108.893945	E	13.21	1.47×10^{-6}	16 590	No
$1_1 \rightarrow 1_0$	165.050175	E	15.47	2.35×10^{-5}	3423	No
$2_1 \rightarrow 2_0$	165.061130	E	20.11	2.35×10^{-5}	3801	No
$3_1 \rightarrow 3_0$	165.099240	E	27.08	2.35×10^{-5}	2579	No
$5_3 \rightarrow 5_2$	251.811956	A^{-+}	37.96	1.65×10^{-4}	–0.1	No
$2_0 \rightarrow 1_{-1}$	254.015377	E	12.19	1.90×10^{-5}	9522	No
$9_{-1} \rightarrow 8_0$	278.304512 [b]	E	102.07	7.67×10^{-5}	–2.5	I
$7_{-1} \rightarrow 6_{-1}$	338.344588	E	62.65	1.66×10^{-4}	1301	No
$J_K \rightarrow (J-1)_K$ [c]	97–290	A, E	–	–	>0.0	No

Notes. List of lines with intensities that exceed our LTE model. Their line intensities cannot be reproduced without a non-LTE model and there are no other lines subject to produce an important contribution if blended. [a]Blended with the methanol $34_5 \rightarrow 35_3 - A^-$ transition at 107.015820 GHz ($E_{\rm up}/k = 1515.904$ K, $A_{ij} = 1.00 \times 10^{-9}$ s^{-1}). [b]Blended with the methanol $2_{-2} \rightarrow 3_{-1} - E$ transition at 278.342261 GHz ($E_{\rm up}/k = 24.96$ K, $A_{ij} = 1.65 \times 10^{-5}$ s^{-1}). [c]The $J_K \rightarrow (J-1)_K$ line series is described in Appendices C and D. [d]Optical depth according to our non-LTE model in region 8 (see Appendix C). [e]Maser candidates based on the discussion in Sect. 4.2.2. If it is a candidate, then we add the classification Class I or II, according to Menten (1991).

Given the spatial resolution and software limitations (see van der Tak et al. 2007, their Sect. 3.6), we cannot account for a proper model to our maser candidates. Instead, we reproduce their line profiles and check whether negative optical depths are required or not. When no other results are plausible, we can assure that the transitions are effectively experiencing a population inversion. Unfortunately, as Class I maser emission arises from spot sizes on the order of 10^{-5}–10^{-3} pc (Voronkov et al. 2014; Matsumoto et al. 2014), any attempt to model our observations will be devoid of a real physical meaning. Negative optical depths are determined in the lines belonging to the $J_{-1} \rightarrow (J-1)_0 - E$ and $J_0 \rightarrow (J-1)_1 - A^+$ series (see Fig. 9) and they constitute our maser candidates. All of them are Class I methanol masers and, for the case of those belonging to the $J_{-1} \rightarrow (J-1)_0 - E$ line series, depart from LTE at the outskirts of the CMZ of NGC 253.

We summarize the observed methanol transitions along the entire ALCHEMI coverage in Fig. 10, where LTE lines are labeled in straight lines and maser candidates are in dashed lines. We indicate with colors the ALMA band for each transition. From Fig. 10 it becomes clear that the $7_{-1} \rightarrow 6_0 - E$ line at 181.295 GHz should be pumped by the same conditions than the other maser candidates in the $J_{-1} \rightarrow (J-1)_0 - E$ series. Our non-LTE models performed in region 8 yield a negative optical depth (−2.4) for this transition suggesting maser emission. Unfortunately, our spectral and angular resolution is not sufficient to discriminate between the 181.295 GHz line and the $J = 2-1$ HNC line at 181.324 GHz.

5. Discussion

5.1. Conditions for maser emission

Among all the lines proposed to be masers, the ones detected initially by our rotation diagrams are the most plausible ones. Here we focus on the Class I methanol masers in the $J_{-1} \rightarrow (J-1)_0 - E$ series (at 84, 132, 229, and 278 GHz), as they describe a very clear difference in maser occurrence: a complete LTE behavior in the central regions (3–6) and strong maser activity at the outskirts of the CMZ of NGC 253, where important $T_{\rm ex}$ differences between A- and E-type methanol take place (see Fig. 6), and also where Lindblad resonances are located (with the only exception of region 7).

Unfortunately, based on the rotation diagram method we do not have enough evidence to account for the presence of Class II masers. The only exception might be the $3_1 \rightarrow 4_0 - A^+$ transition line at 107 GHz ($E_{\rm up}/k = 28$ K), that follows LTE conditions in regions 2, 5, and 10 (∼1.5, ∼1.5, and 2σ, respectively). It is slightly above the fit in regions 3, 4, 6, and 7, and is present in absorption in regions 1 and 9 (3 and 2σ, respectively), and maybe also in region 8 (2σ); although in this region the line seems to exhibit emission in the middle of the absorption feature.

Maser activity by the line at 107 GHz was first discovered by Val'tts et al. (1995). They found this line either in absorption or showing quasi-thermal emission. In the first case, this line is spatially correlated with the $5_1 \rightarrow 6_0 - A^+$ Class II maser line at 6.7 GHz, that belongs to the same family of lines. Other lines in the $J_1 \rightarrow (J+1)_0 - A^+$ series are the transitions at 57 GHz ($J = 4$), 156.6 GHz ($J = 2$), and 205.8 GHz ($J = 1$). By means of the rotation diagram method, we note that the transition at 156.6 GHz is above the LTE trend in the same regions where the line at 107 GHz surpasses the LTE modeling (regions 3, 4, 6, and 7). However, as indicated in Appendix B, the line at 156.6 GHz may also follow the LTE conditions of A–CH$_3$OH.

In NGC 253, absorption against the continuum in region 5 is noticeably seen in the rotational ground state transitions of dense gas tracers such as the formyl cation (H^{13}CO$^+$; Harada et al. 2021). Absorption features are also very prominent in the $J = 2-1$ (e.g., Meier et al. 2015) and $J = 3-2$ transitions of silicon monoxide (SiO). All those features are uniquely observed in region 5, contrary to the case of the $3_1 \rightarrow 4_0 - A^+$ transition line at 107 GHz, that presents absorption mostly in regions 1 and 9.

Therefore, the edges of the CMZ, namely regions 1, 2, 7, 8, 9, and 10, appear to provide suitable conditions for Class I maser emission in the $J_{-1} \rightarrow (J-1)_0 - E$ line series. We are aware that these conclusions only refer to the average conditions in our selected regions, as our linear resolution is on the order of 27 pc, larger than typical clump sizes by a factor of 6–23 (see, e.g., Leroy et al. 2018, for estimations of clump sizes in the CMZ of NGC 253) but usually small enough to resolve GMCs.

Although Lindblad resonances (e.g., ellipses in Fig. 11) have been claimed as a good candidate for shocks (García-Burillo et al. 2000; Ellingsen 2018), for galaxies with a strong bar there is theoretical support against the existence of Lindblad resonances (Regan & Teuben 2003) or their relationship with the circumnuclear ring (CNR) position, which is more accurately defined by x_2 orbits (Kim et al. 2012; Li et al. 2015; Schmidt et al. 2019). The interplay between the nuclear dust/gas lanes and the CNR looks as a more likely explanation for the production of bi-symmetric shock/active regions: at the outskirts of the CMZ, where we find higher levels of HNCO as compared to SiO (regions 1, 2, and 7–10; see Fig. 11), in a similar way as in M 83 (Harada et al. 2019), leading to the appearance of methanol masers in the $J_{-1} \rightarrow (J-1)_0 - E$ line series. We should see maser action encircling the CMZ if they were caused by the ILR.

As an attempt to account for gas disturbances in the CMZ of NGC 253, we obtained line intensity ratios from two well-known shock tracers, SiO and HNCO. Their moment 0 maps, along with data reduction and a thorough analysis will be described in a forthcoming paper by Huang et al. (in prep.). Here our only interest is to relate the presence of shocks to methanol maser

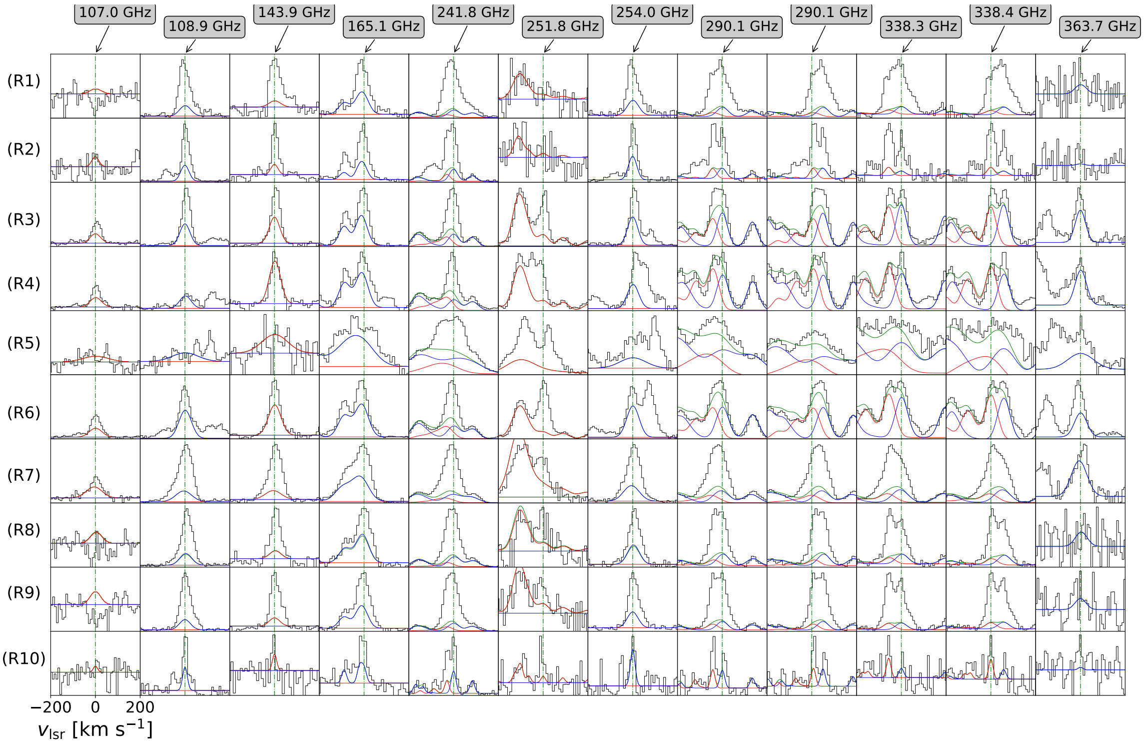

Fig. 8. Outliers to our LTE modeling (see Appendix D) with positive optical depths. The only exceptions are the $J_1 \rightarrow J_0A^{-+}$ line series, recently proposed to present methanol maser Class II activity by Zinchenko et al. (2017). Line frequencies are labeled at the top of the Figure. Most of the lines are unclassified so far. Labels and colors are the same as for Fig. 7.

emission in the $J_{-1} \rightarrow (J-1)_0 - E$ line series, which is mostly observed toward intersecting areas between the circumnuclear ring and leading-edge dust/gas lanes of the bar.

We selected transitions in the same ALMA bands (3 and 6) in order to reduce instrumental uncertainties. Based on previous studies, here we consider SiO as a tracer of strong shocks and HNCO as a tracer of weak shocks (e.g., Meier et al. 2015; Yu et al. 2018), and therefore the SiO/HNCO ratio may be used as an indicator of the shock strength (Kelly et al. 2017).

We note that HNCO ($4_{0,4}$–$3_{0,3}$), at 87.9 GHz, is enhanced in practically the same regions where we detect Class I maser activity in the $J_{-1} \rightarrow (J-1)_0 - E$ line series (at 84, 132, 229, and 278 GHz); this is also true for the previously detected methanol transition in this series, at 36 GHz, if we dismiss the weak maser candidate at the very center shown in Gorski et al. (2018). The resulting SiO $J = 2-1$/HNCO ($4_{0,4}$–$3_{0,3}$) ratios (see Fig. 11, left panel) are enhanced in the central regions, especially in regions 4 and 6, where no maser activity, in the $J_{-1} \rightarrow (J-1)_0 - E$ line series, is detected.

Considering the SiO and HNCO transitions at frequencies ~220 GHz (ALMA band 6), the largest SiO $J = 5-4$/HNCO ($10_{0,10}$–$9_{0,9}$) line ratios come from region 1 (see Fig. 11, right panel), the region where we see the largest departure between maser Class I emission in the $J_{-1} \rightarrow (J-1)_0 - E$ line series (and also in the A-type methanol line at 146.6 GHz) and LTE conditions (see Fig. 6). On the other hand, the lowest SiO $J = 5-4$/HNCO ($10_{0,10}$–$9_{0,9}$) ratios are observed in region 3 and this coincides with the lowest LTE departures of potential Class I masers in E–CH$_3$OH lines (see Fig. 6).

One, however, also needs to take into consideration the varying gas properties likely causing the highly varying trend of these SiO/HNCO ratios. A more complete investigation and further discussion upon the gas properties traced by HNCO and SiO is covered in a forthcoming paper (Huang et al., in prep.). In addition, there is something missing in describing the intermediate regions. For example, regions 4 and 6, where we do not see Class I maser emission in E–CH$_3$OH, present SiO $J = 5-4$/HNCO ($10_{0,10}$–$9_{0,9}$) ratios similar to regions 1, 2, 7, 8, and 9, where we do observe Class I maser emission in E–CH$_3$OH.

The missing element to be considered for the presence or absence of methanol masers can be the occurrence of photodissociation regions (PDRs), since photodissociation is the main mechanism for methanol destruction (see, e.g., Hartquist et al. 1995). We can use PDR tracers such as CN, whose abundance is found to be high in PDR regions (e.g., Fuente et al. 1993; Kim et al. 2020), to investigate whether PDRs may be dominant. As mentioned by Meier et al. (2015), the high rate of star production in the central regions of NGC 253 can be identified, for instance, by means of CN/C^{17}O line ratios, where C^{17}O traces dense molecular gas (e.g., Thomas & Fuller 2008).

We obtained the CN/C^{17}O line ratios by taking the ratio of moment 0 maps of the chosen molecules. A 3σ clipping was applied in the creation of those moment 0 and the resulting line ratio maps (see Fig. 12).

In Fig. 12 we also plot the Hα emission from recent MUSE[7] observations obtained from archival data (ID:0102.B-0078(A), PI:Laura Zschaechner) after continuum subtraction by means of the STATCONT software (Sánchez-Monge et al. 2018). The stronger Hα emission is related to the starburst induced outflow emerging from the nuclear bar, its morphology resembles the inner parts of previously observed outflows in X-rays (Strickland et al. 2000) as well as the OH plume to the northwest (Turner 1985). We created six red contours, on a linear scale, covering emission in the range (1–7) $\times 10^{-14}$ erg s^{-1} cm^{-2}. The CN/C^{17}O line ratios were obtained from ALMA band 3 and 6,

---

[7] Multi Unit Spectroscopic Explorer (MUSE; Bacon et al. 2017).

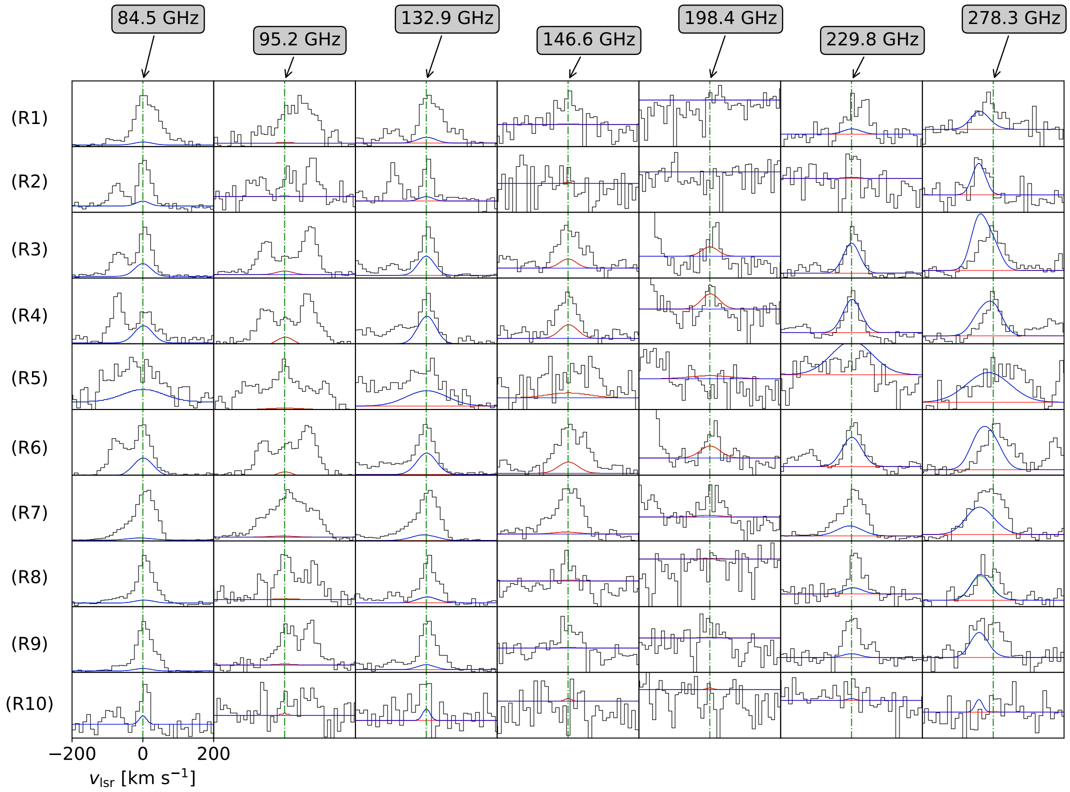

Fig. 9. Our proposed methanol masers belonging to previously known maser transitions. Labels and colors are the same that for Fig. 7.

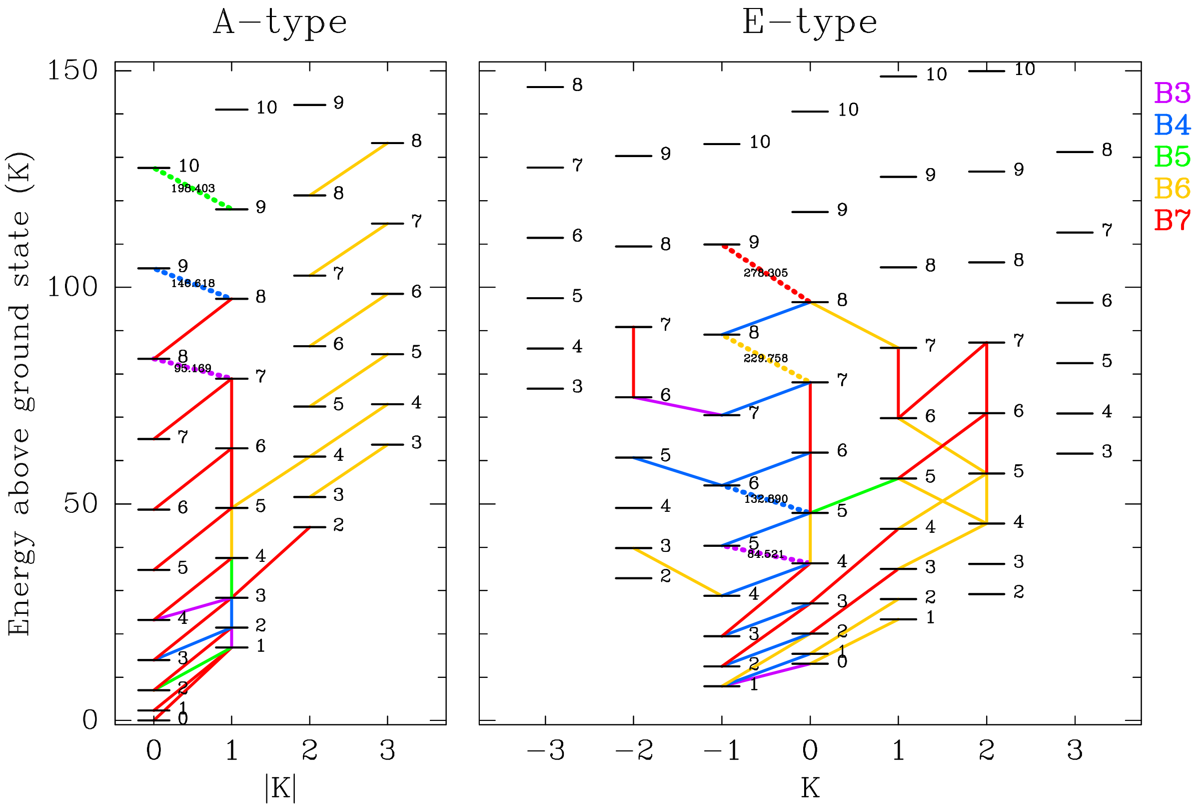

Fig. 10. Diagram of the energy levels for *A*-type (*left*) and *E*-type (*right*) methanol transitions covered by ALCHEMI. The *x*-axis gives the quantum number *K*, while the number for each level gives *J*. The transitions used in the analysis are indicated with a color code corresponding to ALMA bands, as given in the top right corner. The maser candidate lines are presented as dashed lines, with their frequency in GHz. We note the energy difference of 7.9 K between the ground state of *A* and *E*-type.

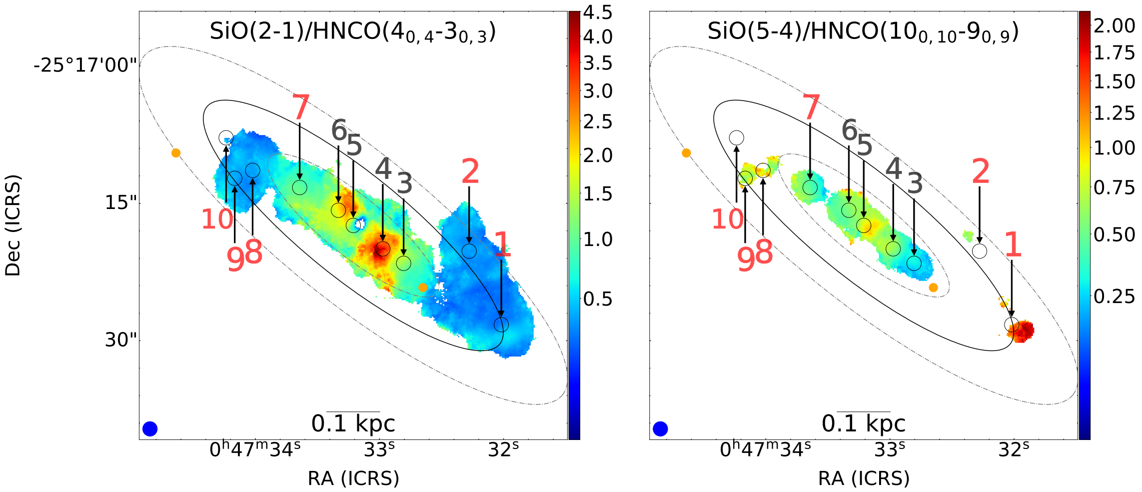

Fig. 11. Strong over weak shock tracers as accounted by SiO $J = 2-1$/HNCO ($4_{0,4}$–$3_{0,3}$) (*left*) and SiO $J = 5-4$/HNCO ($10_{0,10}$–$9_{0,9}$) (*right*) line ratios obtained from ALCHEMI data (Martín et al. 2021). A sigma clip of 3.0 was applied for both SiO and HNCO before obtaining the line ratios. Regions where we detect Class I maser emission in the $J_{-1} \rightarrow (J-1)_0 - E$ series (see Sect. 4.1.2) are labeled in red and with slightly larger numbers. The center and edges of the inner Lindblad resonance from Iodice et al. (2014) are denoted with a black ellipse and dash-dotted gray ellipses, respectively. A square root stretch has been applied for an easy visualization.

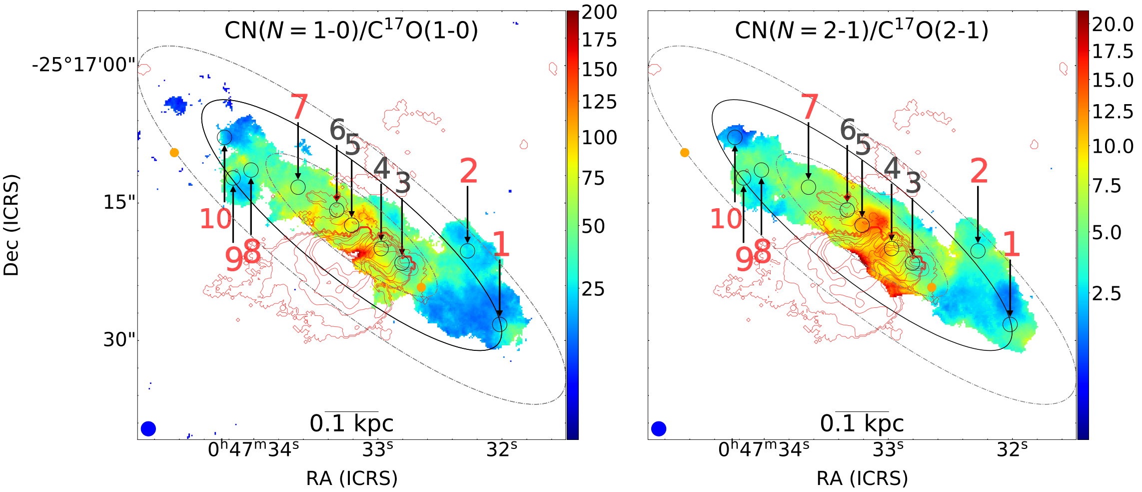

Fig. 12. CN ($N = 1-0$)/C^{17}O ($J = 1-0$) (*left*) and CN ($N = 2-1$)/C^{17}O ($J = 2-1$) (*right*) line ratios obtained from ALCHEMI data (Martín et al. 2021), indicating the presence of photodissociation regions. A 3σ clipping was applied. Red contours indicate the H$_\alpha$ emission in logarithmic scale from MUSE archival data (ID:0102.B-0078(A), PI:Laura Zschaechner). Regions where we detect Class I maser emission in the $J_{-1} \rightarrow (J-1)_0 - E$ series (see Sect. 4.1.2) are labeled in red and with slightly larger numbers. The center and edges of the inner Lindblad resonance from Iodice et al. (2014) are denoted with a black ellipse and dash-dotted gray ellipses, respectively. Higher ratios indicate a higher photodissociation level. A square root stretch has been applied for an easy visualization.

namely CN ($N = 1-0$)/C^{17}O ($J = 1-0$) and CN ($N = 2-1$)/C^{17}O ($J = 2-1$) ratios, respectively. These ratios are plotted in Fig. 12, where high values correspond to a high rate of photodissociation.

It can be noted from Fig. 12 that high values of CN/C^{17}O line intensity ratios are closely following the root of the large-scale outflowing gas. Overall, we note the highest level of photodissociation at the central regions of the CMZ (regions 4, 5, and 6), coinciding with regions where we observe a lack of methanol masers in the $J_{-1} \rightarrow (J-1)_0 - E$ line series, and also the A-type transition at 146.6 GHz, belonging to the $J_1 \rightarrow (J+1)_0 - A^+$ line series. The only exception involves the comparison between regions 3 and 7. Masers are observed in region 7, even though the CN/C^{17}O ratio is slightly higher than in region 3, where no maser emission is encountered.

Although region 7 is located away from the nuclear ring, it is associated with a hot core cluster indicating an active star formation activity, as deduced from an increment of Complex Organic Molecules (COMs) such as CH$_3$COOH (Ando et al. 2017). As tracers of YSO outflows, Class I methanol masers are expected to be detected in environments like our region 7. Additionally, region 7 is not showing a high level of photodissociation as compared to regions 4 or 5, where the star formation activity is further confirmed by the presence of the H40α line (Bendo et al. 2015).

In conclusion, the PDRs at some level can destroy methanol molecules in the central regions of NGC 253. This is one of the scenarios suggested by Ellingsen et al. (2017). Either starburst induced outflows and/or shocks where the leading-edge dust/gas lanes on the bar are connected to the circumnuclear ring, are causing the prevalence of Class I methanol masers in the $J_{-1} \rightarrow (J-1)_0 - E$ line series (at 84, 132, 229, and 278 GHz) to regions farther away from the core (regions 1, 2, 7, 8, 9, and 10). Region 7, although away from the resonances, presents a strong star formation but a rather moderate photodissociation level, giving way to the formation of methanol masers both in the $J_{-1} \rightarrow (J-1)_0 - E$ and the $J_0 \rightarrow (J-1)_1 - A^+$ line series.

5.2. Maser emission distribution

Based on our rotation diagrams, we selected a couple of E–CH_3OH lines that follow LTE conditions in all the studied regions and compare their averaged integrated intensities with the ones observed in the maser line at 84.5 GHz ($E_{up}/k = 32.5$ K) in each spaxel. The selected lines in LTE are the $4_2 \rightarrow 3_1 - E$ and $3_1 \rightarrow 2_0 - E$ transitions at 218.4 ($E_{up}/k = 37.6$ K) and 310.1 GHz ($E_{up}/k = 27.1$ K), respectively (see Table A.1). They are not blended with other methanol transitions and do not appear to be significantly contaminated by blending lines from other species (Table A.1), given their good fit in the rotation diagrams. Additionally, these two lines have E_{up}/k values around the one of the maser line at 84.5 GHz. The result of dividing the integrated intensity of the 84.5 GHz maser line by the averaged intensity of the two lines proposed to be in LTE (at 218.4 and 310.2 GHz) is presented in the left panel of Fig. 13. In this figure the spaxels with higher intensity ratios are in line with regions where we previously identified maser emission through the rotation diagram method. The distribution of maser emission we found is also in good agreement with latest detections of methanol maser emission at 36.2 GHz in NGC 253 (see McCarthy et al. 2020, their Fig. 2). We have further checked an equivalency between the intensity ratios and upper level column density ratios in our Appendix F. We find that a line intensity ratio of >0.1244 corresponds to regions with maser emission in the $J_1 \rightarrow (J-1)_0 - E$ line series (upper level column density ratios >3.3 with respect to LTE (Fig. 6, first panel)). This intensity ratio may appear low, but it is only because the spatially widespread thermal lines have higher intensities than the likely much less widespread nonthermal methanol transition at 84.5 GHz. Furthermore, it is important to emphasize that the maser's column densities are nominal and do not reflect column densities in a linear way due to amplification effects.

Taking into account the previous Sect. 5.1, we noticed that, in order to explain the lack of methanol maser emission in the $J_{-1} \rightarrow (J-1)_0 - E$ line series (Class I) in the central regions of NGC 253, it is necessary to invoke a combination of strong photodissociation in region 5 as well as strong rather than weak shocks in regions 3, 4, and 6. In other words, suitable conditions of Class I maser emission in these line series are weak shocks and low rates of photodissociation, the latter preventing methanol destruction. In the right panel of Fig. 13, we empirically determine a threshold for the two conditions previously mentioned as SiO/HNCO ratios lower than 1.05 and CN/$C^{17}O$ ratios lower than 60 in ALMA band 3 data.

In the right panel of Fig. 13, we also show the average values of the 10 selected regions (Table 3) derived from band 3 and they are distributed as expected: central regions fall where no maser emission is expected. We performed a similar diagram for ALMA band 6 data (not shown); in this case region 7 is difficult to separate from locations where LTE conditions are predominant, and regions 1, 2, and 8–10, are located where SiO/HNCO ratios are in the 0.4–1.2 range and CN/$C^{17}O$ ratios are lower than 4.75 (both ratios obtained from ALMA band 6 data).

A similar distribution for Class I methanol maser emission was previously found by Ellingsen et al. (2017) and Gorski et al. (2017, 2019) for the 36.2 GHz line, which also belongs to the $J_{-1} \rightarrow (J-1)_0 - E$ line series.

6. Summary and conclusions

Searching for methanol (CH_3OH) transitions, we have performed a spectral survey toward the archetypical starburst galaxy NGC 253 with the ALMA interferometer covering a frequency range between 84–373 GHz. We focus on ten regions inside the CMZ of this galaxy; those regions are centered at the position of giant molecular clouds.

After limiting our search to methanol lines with $E_{up}/k <$ 150 K, since above that limit lines are too weak to be detected, we identified all the methanol transitions of each region separately and used the rotation diagram method in order to determine which transitions deviate from LTE conditions. Assuming LTE conditions, we found that E–CH_3OH is more abundant at lower E_{up}/k and follows predominantly lower excitation temperatures than A–CH_3OH. We also find that including methanol lines with E_{up}/k<150 K is sufficient to fit the observed spectra.

We also performed LTE and non-LTE model calculations with CASSIS-RADEX to find maser candidates. A moderate difference of only about 15% in intensities between the LTE and non-LTE predictions is found in our data when we consider a single component for each methanol symmetric type (but this difference becomes important when we consider two components, see Appendix C).

Although most of the observed methanol lines can be reproduced by our LTE models, we found a number of outliers, of which 7 show maser properties. We have confidently identified a total of 3 A-type and 4 E-type methanol maser transitions, all of them classified as Class I.

We have also performed a more detailed non-LTE model in region 8 (Appendix C), where the $J_K \rightarrow (J-1)_K$ line series is better reproduced. From this model we obtained optical depths for the covered methanol transitions and these support the presence of masers indicating negative opacities for our best candidates.

Using rotation diagrams, we have confidently detected all but the last of the covered methanol lines in the $J_{-1} \rightarrow (J-1)_0 - E$ series to be masing, namely, methanol lines at 84.5, 132.9, and 229.8 GHz. The last available line in this series, at 278.3 GHz, is detected to depart from LTE when we compare the observed spectrum with the LTE synthetic spectrum, showing maser characteristics at the edges of the CMZ in NGC 253. Maser action in the 84.5 GHz line, previously reported by McCarthy et al. (2018), is now detected in more than one location for the first time.

An absorption line at 107 GHz was identified in the spectra of regions 1, 8 and 9, which are located at the outskirts of the CMZ of NGC 253. Interestingly, the position of these regions coincides with the position of the circumnuclear ring (cospatial with the Lindblad resonances according to Iodice et al. 2014, but see Sect. 5) and with Class I methanol maser emission in the $J_{-1} \rightarrow (J-1)_0 - E$ line series.

The increment of weak shocks in the interplay between dust/gas lanes and the circumnuclear ring is proposed to harbor favorable conditions to produce Class I masers in the $J_{-1} \rightarrow (J-1)_0 - E$ line series. This happens in regions 1, 2 and 8–10. These resonances are expected to create density waves and locally increase the amount of shocks where they are located, possibly creating favorable conditions to produce methanol masers. On

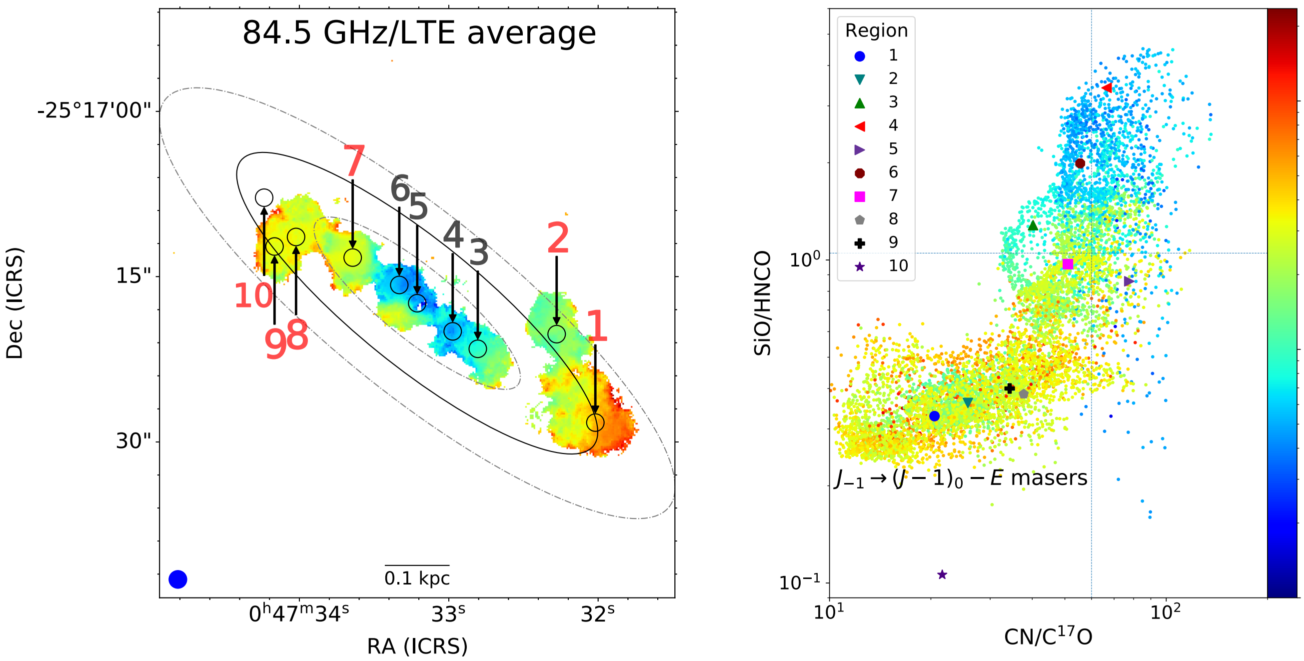

Fig. 13. *Left*: maser emission distribution per spaxel as observed by dividing integrated intensities of the maser methanol line at 84.5 GHz by the mean intensity value of the surrounding (in terms of $E_{\rm up}/k$) methanol lines in LTE at 218.4 and 310.1 GHz (see Sect. 5.2). A 3σ clipping was applied in all the transitions involved to produce the figure. The center and edges of the inner Lindblad resonance from Iodice et al. (2014) are denoted with a black ellipse and dash-dotted gray ellipses, respectively. Regions where we observe methanol maser emission in the $J_{-1} \rightarrow (J-1)_0 - E$ line series are labeled in red. *Right*: same spaxels (with their values as colors) as in the figure to the left, but this time distributed according to their ratios in the SiO/HNCO (y-axis) and CN/C^{17}O line ratio maps in ALMA band 3. A logarithmic stretch has been applied in both panels for an easy visualization. Colors are in common for both panels. Our threshold of 3.3 above the rotation diagram fit given in Fig. 6 (*first panel*) corresponds to an intensity ratio of >0.1244 (see Appendix F).

the other hand, considering the Class I masers belonging to the $J_0 \rightarrow (J-1)_1 - A$ line series (at 95, 146, and 198 GHz), we found the first of them ($J = 8$, at 95 GHz) departing at least by a factor of 3 (in region 4) from LTE in all the regions, and above a factor of 12 without considering region 4. The levels giving rise to the transition at 146 GHz are less populated, showing maser emission in regions 1, 7, 8 and 9. The last in the $J_0 \rightarrow (J-1)_1 - A$ series, at $J = 10$, departs from LTE by a factor higher than 3.3 in regions 3, 6, and 7, being the only one masing in the nuclear parts of the CMZ detected through the rotation diagram method.

We computed the SiO $J = 5-4$/HNCO ($10_{0,10}$–$9_{0,9}$) intensity ratios as a tracer of strong over weak shocks for all regions and found that region 1 and 3 have the highest and lowest values, respectively. When looking at the $J_{-1} \rightarrow (J-1)_0 - E$ series for those particular regions, we find that in region 1 maser lines deviate the most from the expected LTE behavior in the rotation diagram. This indicates that the transitions in region 1 are likely masing due to collisional excitation by shocks. For region 3, the emission seems to be completely in LTE since the transitions align almost perfectly in the rotation diagrams. When considering the SiO $J = 2-1$/HNCO ($4_{0,4}$–$3_{0,3}$) ratios, which cover much more spaxels and trace colder gas, we find an opposite picture, where HNCO is stronger than SiO at the outskirts of the CMZ, exactly where we observe methanol maser emission in the $J_{-1} \rightarrow (J-1)_0 - E$ line series, with the only exception of region 7, whose pumping mechanism might be dominated by star-forming processes, in agreement with latest findings in NGC 253 targeting the methanol $4_{-1} \rightarrow 3_0 - E$ transition at 36 GHz (Gorski et al. 2019).

For the regions in the center of the CMZ of NGC 253, we compared CN/C^{17}O ratios as a PDR tracer. We found out that regions 3, 4, and 5 show the highest levels of photodissociation. The implied strong ultraviolet radiation may lead to the destruction of methanol molecules in the central regions, preventing the appearance of methanol masers.

Although several scenarios are proposed to explain the presence or absence of methanol masers in all the regions in NGC 253, we cannot conclude which of them is dominant over all the regions along the CMZ. Higher angular resolution observations are needed to spatially resolve smaller regions and to differentiate between the proposed mechanisms that give rise to the formation of methanol masers.

Acknowledgements. PH is a member of and received financial support for this research from the International Max Planck Research School (IMPRS) for Astronomy and Astrophysics at the Universities of Bonn and Cologne. PH is grateful to Arnaud Belloche, Dario Colombo, Yu Gao, and Sudeep Neupane, for their constructive advice and fruitful discussions along a variety of aspects covered in this work. VMR is funded by the Comunidad de Madrid through the Atracción de Talento Investigador (Doctores con experiencia) Grant (COOL: Cosmic Origins Of Life; 2019–T1/TIC–15379), and from the Agencia Estatal de Investigación (AEI) through the Ramón y Cajal programme (grant RYC2020-029387-I). L.C. has received partial support from the Spanish State Research Agency (AEI; project number PID2019-105552RB-C41). KS thanks MOST grant 109-2112-M-001-020. NH acknowledges support from JSPS KAKENHI Grant Number JP21K03634. This work makes use of the following ALMA data: ADS/JAO.ALMA#2017.1.00161.L and ADS/JAO.ALMA#2018.1.00162.S. ALMA is a partnership of ESO (representing its member states), NSF (USA) and NINS (Japan), together with NRC (Canada), MOST and ASIAA (Taiwan), and KASI (Republic of Korea), in cooperation with the Republic of Chile. The Joint ALMA Observatory is operated by ESO, AUI/NRAO and NAOJ.

References

Anantharamaiah, K. R., & Goss, W. M. 1996, ApJ, 466, L13
Ando, R., Nakanishi, K., Kohno, K., et al. 2017, ApJ, 849, 81

Araya, E., Hofner, P., Kurtz, S., Bronfman, L., & DeDeo, S. 2005, ApJS, 157, 279

Bacon, R., Conseil, S., Mary, D., et al. 2017, A&A, 608, A1

Batrla, W., Matthews, H. E., Menten, K. M., & Walmsley, C. M. 1987, Nature, 326, 49

Belloche, A., Müller, H. S. P., Menten, K. M., Schilke, P., & Comito, C. 2013, A&A, 559, A47

Belloche, A., Garrod, R. T., Müller, H. S. P., et al. 2019, A&A, 628, A10

Bendo, G. J., Beswick, R. J., D'Cruze, M. J., et al. 2015, MNRAS, 450, L80

Billington, S. J., Urquhart, J. S., König, C., et al. 2020, MNRAS, 499, 2744

Breen, S. L., Ellingsen, S. P., Caswell, J. L., et al. 2011, ApJ, 733, 80

Breen, S. L., Ellingsen, S. P., Contreras, Y., et al. 2013, MNRAS, 435, 524

Breen, S. L., Fuller, G. A., Caswell, J. L., et al. 2015, MNRAS, 450, 4109

Chen, X., Ellingsen, S. P., Baan, W. A., et al. 2015, ApJ, 800, L2

Cohen, D. P., Turner, J. L., & Consiglio, S. M. 2020, MNRAS, 493, 627

Cotton, W. D., & Yusef-Zadeh, F. 2016, ApJS, 227, 10

Cragg, D. M., Johns, K. P., Godfrey, P. D., & Brown, R. D. 1992, MNRAS, 259, 203

Cragg, D. M., Mikhtiev, M. A., Bettens, R. P. A., Godfrey, P. D., & Brown, R. D. 1993, MNRAS, 264, 769

Cyganowski, C. J., Hannaway, D., Brogan, C. L., Hunter, T. R., & Zhang, Q. 2018, in Astrophysical Masers: Unlocking the Mysteries of the Universe, eds. A. Tarchi, M. J. Reid, & P. Castangia, 336, 281

Darling, J., Goldsmith, P., Li, D., & Giovanelli, R. 2003, AJ, 125, 1177

de Vaucouleurs, G., de Vaucouleurs, A., Corwin, H. G., et al. 1991, Third Reference Catalogue of Bright Galaxies (New York: Springer)

Ellingsen, S. P. 2018, in Astrophysical Masers: Unlocking the Mysteries of the Universe, eds. A. Tarchi, M. J. Reid, & P. Castangia, 336, 117

Ellingsen, S. P., Norris, R. P., Whiteoak, J. B., et al. 1994, MNRAS, 267, 510

Ellingsen, S. P., Breen, S. L., Caswell, J. L., Quinn, L. J., & Fuller, G. A. 2010, MNRAS, 404, 779

Ellingsen, S. P., Chen, X., Qiao, H.-H., et al. 2014, ApJ, 790, L28

Ellingsen, S. P., Chen, X., Breen, S. L., & Qiao, H. H. 2017, MNRAS, 472, 604

Fuente, A., Martin-Pintado, J., Cernicharo, J., & Bachiller, R. 1993, A&A, 276, 473

García-Burillo, S., Martín-Pintado, J., Fuente, A., & Neri, R. 2000, A&A, 355, 499

Goldsmith, P. F., & Langer, W. D. 1999, ApJ, 517, 209

Gorski, M., Ott, J., Rand, R., et al. 2017, ApJ, 842, 124

Gorski, M., Ott, J., Rand, R., et al. 2018, ApJ, 856, 134

Gorski, M. D., Ott, J., Rand, R., et al. 2019, MNRAS, 483, 5434

Green, J. A., Caswell, J. L., Fuller, G. A., et al. 2008, MNRAS, 385, 948

Green, J. A., Breen, S. L., Fuller, G. A., et al. 2017, MNRAS, 469, 1383

Harada, N., Sakamoto, K., Martín, S., et al. 2019, ApJ, 884, 100

Harada, N., Martín, S., Mangum, J. G., et al. 2021, ApJ, 923, 24

Hartquist, T. W., Menten, K. M., Lepp, S., & Dalgarno, A. 1995, MNRAS, 272, 184

Haschick, A. D., & Baan, W. A. 1993, ApJ, 410, 663

Hastings, W. K. 1970, Biometrika, 57, 97

Holdship, J., Viti, S., Martín, S., et al. 2021, A&A, 654, A55

Humire, P. K., Henkel, C., Gong, Y., et al. 2020, A&A, 633, A106

Impellizzeri, C. M. V., Henkel, C., Roy, A. L., & Menten, K. M. 2008, A&A, 484, L43

Iodice, E., Arnaboldi, M., Rejkuba, M., et al. 2014, A&A, 567, A86

Kalenskii, S. V., Slysh, V. I., & Val'tts, I. E. 2002, in Cosmic Masers: From Proto-Stars to Black Holes, eds. V. Migenes, & M. J. Reid, 206, 191

Kalenskii, S. V., Promyslov, V. G., Slysh, V. I., Bergman, P., & Winnberg, A. 2006, Astron. Rep., 50, 289

Kalenskii, S. V., Johansson, L. E. B., Bergman, P., et al. 2010, MNRAS, 405, 613

Kang, H., Kim, K.-T., Byun, D.-Y., Lee, S., & Park, Y.-S. 2015, ApJS, 221, 6

Kelly, G., Viti, S., García-Burillo, S., et al. 2017, A&A, 597, A11

Kim, W.-T., Seo, W.-Y., & Kim, Y. 2012, ApJ, 758, 14

Kim, W. J., Wyrowski, F., Urquhart, J. S., et al. 2020, A&A, 644, A160

Ladeyschikov, D. A., Bayandina, O. S., & Sobolev, A. M. 2019, AJ, 158, 233

Lees, R. M. 1973, ApJ, 184, 763

Lees, R. M., & Baker, J. G. 1968, J. Cosmol. Phys., 48, 5299

Leroy, A. K., Bolatto, A. D., Ostriker, E. C., et al. 2015, ApJ, 801, 25

Leroy, A. K., Bolatto, A. D., Ostriker, E. C., et al. 2018, ApJ, 869, 126

Leurini, S., & Menten, K. M. 2018, in Astrophysical Masers: Unlocking the Mysteries of the Universe, eds. A. Tarchi, M. J. Reid, & P. Castangia, 336, 17

Leurini, S., Menten, K. M., & Walmsley, C. M. 2016, A&A, 592, A31

Li, Z., Shen, J., & Kim, W.-T. 2015, ApJ, 806, 150

Liechti, S., & Wilson, T. L. 1996, A&A, 314, 615

Lo, K. Y. 2005, ARA&A, 43, 625

Ma, C., Arias, E. F., Eubanks, T. M., et al. 1998, AJ, 116, 516

Mangum, J. G., & Shirley, Y. L. 2015, PASP, 127, 266

Martín, S., Mauersberger, R., Martín-Pintado, J., Henkel, C., & García-Burillo, S. 2006, ApJS, 164, 450

Martín, S., Martín-Pintado, J., Blanco-Sánchez, C., et al. 2019, A&A, 631, A159

Martín, S., Mangum, J. G., Harada, N., et al. 2021, A&A, 656, A46

Matsumoto, N., Hirota, T., Sugiyama, K., et al. 2014, ApJ, 789, L1

McCarthy, T. P., Ellingsen, S. P., Chen, X., et al. 2017, ApJ, 846, 156

McCarthy, T. P., Ellingsen, S. P., Breen, S. L., Voronkov, M. A., & Chen, X. 2018, ApJ, 867, L4

McCarthy, T. P., Ellingsen, S. P., Breen, S. L., et al. 2020, MNRAS, 491, 4642

Meier, D. S., Walter, F., Bolatto, A. D., et al. 2015, ApJ, 801, 63

Menten, K. M. 1991, ApJ, 380, L75

Menten, K. M. 2012, in Cosmic Masers - from OH to H0, eds. R. S. Booth, W. H. T. Vlemmings, & E. M. L. Humphreys, 287, 506

Meyer, M. J., Zwaan, M. A., Webster, R. L., et al. 2004, MNRAS, 350, 1195

Morris, M., & Serabyn, E. 1996, ARA&A, 34, 645

Moscadelli, L., Menten, K. M., Walmsley, C. M., & Reid, M. J. 2003, ApJ, 583, 776

Müller, H. S. P., Schlöder, F., Stutzki, J., & Winnewisser, G. 2005, J. Mol. Struc., 742, 215

Müller-Sánchez, F., González-Martín, O., Fernández-Ontiveros, J. A., Acosta-Pulido, J. A., & Prieto, M. A. 2010, ApJ, 716, 1166

Oike, T., Kawaguchi, K., Takano, S., & Nakai, N. 2004, PASJ, 56, 431

Pence, W. D. 1980, ApJ, 239, 54

Pickett, H. M., Poynter, R. L., Cohen, E. A., et al. 1998, J. Quant. Spec. Radiat. Transf., 60, 883

Pihlström, Y. M., Sjouwerman, L. O., Frail, D. A., et al. 2014, AJ, 147, 73

Plambeck, R. L., & Menten, K. M. 1990, ApJ, 364, 555

Rabli, D., & Flower, D. R. 2010, MNRAS, 406, 95

Regan, M. W., & Teuben, P. 2003, ApJ, 582, 723

Rekola, R., Richer, M. G., McCall, M. L., et al. 2005, MNRAS, 361, 330

Rodríguez-Garza, C. B., Kurtz, S. E., Gómez-Ruiz, A. I., et al. 2017, ApJS, 233, 4

Rosolowsky, E., & Leroy, A. 2006, PASP, 118, 590

Sakamoto, K., Ho, P. T. P., Iono, D., et al. 2006, ApJ, 636, 685

Salii, S. V., Sobolev, A. M., & Kalinina, N. D. 2002, Astron. Rep., 46, 955

Salter, C. J., Ghosh, T., Catinella, B., et al. 2008, AJ, 136, 389

Sánchez-Monge, Á., Schilke, P., Ginsburg, A., Cesaroni, R., & Schmiedeke, A. 2018, A&A, 609, A101

Schmidt, E. O., Mast, D., Díaz, R. J., et al. 2019, AJ, 158, 60

Sinclair, M. W., Carrad, G. J., Caswell, J. L., Norris, R. P., & Whiteoak, J. B. 1992, MNRAS, 256, 33

Sjouwerman, L. O., Murray, C. E., Pihlström, Y. M., Fish, V. L., & Araya, E. D. 2010, ApJ, 724, L158

Sobolev, A. M. 1993, Astron. Lett., 19, 293

Strickland, D. K., Heckman, T. M., Weaver, K. A., & Dahlem, M. 2000, AJ, 120, 2965

Szczepanski, J. C., Ho, P. T. P., Haschick, A. D., & Baan, W. A. 1989, in The Center of the Galaxy, ed. M. Morris, 136, 383

Thomas, H. S., & Fuller, G. A. 2008, A&A, 479, 751

Turner, B. E. 1985, ApJ, 299, 312

Val'tts, I. E., Dzura, A. M., Kalenskii, S. V., et al. 1995, A&A, 294, 825

van der Tak, F. F. S., Black, J. H., Schöier, F. L., Jansen, D. J., & van Dishoeck, E. F. 2007, A&A, 468, 627

Voronkov, M. A., Caswell, J. L., Ellingsen, S. P., & Sobolev, A. M. 2010, MNRAS, 405, 2471

Voronkov, M. A., Caswell, J. L., Ellingsen, S. P., et al. 2012, in Humphreys, Cosmic Masers - from OH to H0, eds. R. S. Booth, W. H. T. Vlemmings, & E. M. L. Humphreys, 287, 433

Voronkov, M. A., Caswell, J. L., Ellingsen, S. P., Green, J. A., & Breen, S. L. 2014, MNRAS, 439, 2584

Walmsley, C. M., Batrla, W., Matthews, H. E., & Menten, K. M. 1988, A&A, 197, 271

Walsh, A. J., Bertoldi, F., Burton, M. G., & Nikola, T. 2001, MNRAS, 326, 36

Wang, J., Zhang, J., Gao, Y., et al. 2014, Nat. Comm., 5, 5449

Wilson, T. L. 2009, ArXiv e-prints [arXiv:`0903.0562`]

Yang, K., Chen, X., Shen, Z.-Q., et al. 2017, ApJ, 846, 160

Yang, K., Chen, X., Shen, Z.-Q., et al. 2019, ApJS, 241, 18

Yang, W., Xu, Y., Choi, Y. K., et al. 2020, ApJS, 248, 18

Yu, N.-P., Xu, J.-L., & Wang, J.-J. 2018, Res. Astron. Astrophys., 18, 015

Yusef-Zadeh, F., Cotton, W., Viti, S., Wardle, M., & Royster, M. 2013, ApJ, 764, L19

Zinchenko, I., Liu, S. Y., Su, Y. N., & Sobolev, A. M. 2017, A&A, 606, L6

---

[1] Max-Planck-Institut für Radioastronomie, Auf-dem-Hügel 69, 53121 Bonn, Germany
e-mail: `phumire@mpifr-bonn.mpg.de`

[2] Astron. Dept., Faculty of Science, King Abdulaziz University, PO Box 80203, Jeddah 21589, Saudi Arabia
[3] Xinjiang Astronomical Observatory, Chinese Academy of Sciences, 830011 Urumqi, PR China
[4] European Southern Observatory, Alonso de Córdova, 3107, Vitacura, Santiago 763-0355, Chile
[5] Joint ALMA Observatory, Alonso de Córdova, 3107, Vitacura, Santiago 763-0355, Chile
[6] National Radio Astronomy Observatory, 520 Edgemont Road, Charlottesville, VA 22903-2475, USA
[7] National Astronomical Observatory of Japan, 2-21-1 Osawa, Mitaka, Tokyo 181-8588, Japan
[8] Institute of Astronomy and Astrophysics, Academia Sinica, 11F of AS/NTU Astronomy-Mathematics Building, No.1, Sec. 4, Roosevelt Rd, Taipei 10617, Taiwan
[9] Department of Astronomy, School of Science, The Graduate University for Advanced Studies (SOKENDAI), 2-21-1 Osawa, Mitaka, Tokyo 181-1855, Japan
[10] Department of Space, Earth and Environment, Chalmers University of Technology, Onsala Space Observatory, 43992 Onsala, Sweden
[11] Department of Physics, Faculty of Science and Technology, Keio University, 3-14-1 Hiyoshi, Yokohama, Kanagawa 223-8522, Japan
[12] Institute of Astronomy, Graduate School of Science, The University of Tokyo, 2-21-1 Osawa, Mitaka, Tokyo 181-0015, Japan
[13] Argelander-Institut für Astronomie, Universität Bonn, Auf dem Hügel 71, 53121 Bonn, Germany
[14] Institute of Space Sciences (ICE, CSIC), Campus UAB, Carrer de Magrans, 08193 Barcelona, Spain
[15] New Mexico Institute of Mining and Technology, 801 Leroy Place, Socorro, NM 87801, USA
[16] National Radio Astronomy Observatory, PO Box O, 1003 Lopezville Road, Socorro, NM 87801, USA
[17] IRAP, Université de Toulouse, CNRS, UPS, CNES, Toulouse, France
[18] Leiden Observatory, Leiden University, PO Box 9513, 2300 RA Leiden, The Netherlands
[19] Department of Physics and Astronomy, University College London, Gower Street, London WC1E6BT, UK
[20] Centro de Astrobiología (CSIC-INTA), Ctra. de Torrejón a Ajalvir km 4, 28850 Torrejón de Ardoz, Madrid, Spain

Appendix A: Rotation diagrams

We make use of rotation diagrams as our first method to unveil the presence of methanol maser lines. This procedure assumes the Rayleigh-Jeans (RJ) approximation[8], valid when the following condition is fulfilled: $\nu[\mathrm{GHz}] \ll 20.84\,[\mathrm{GHz/K}]\,T_{\mathrm{ex}}[\mathrm{K}]$ (see, e.g., Wilson 2009). The rotation diagram method also assumes a negligible background continuum (see, e.g., Belloche et al. 2019, their Chapter 4.4), and relates the total column density N_{tot} of a given species with the excitation temperature T_{ex}[9] and the integrated intensity of the line profiles as

$$\frac{N_{\mathrm{tot}}}{N_{\mathrm{up}}} = \frac{Q_{\mathrm{rot}(T_{\mathrm{ex}})}}{g_{\mathrm{up}}} \exp\left(\frac{E_{\mathrm{up}}}{kT_{\mathrm{ex}}}\right), \tag{A.1}$$

where $Q_{\mathrm{rot}}(T)$ is the partition function of the species, which is the multiplication factor needed to go from a column density in a single state to the entire column density of a molecular species summed over all states (Mangum & Shirley 2015). g_{up} is the statistical weight of the upper level, E_{up}/k is the energy of the upper level above the ground state, and k is the Boltzmann constant. In the optically thin case, the beam-averaged N_{up} is given by

$$N_{\mathrm{up}} = \frac{8\pi k\nu^2}{hc^3 A_{\mathrm{ul}}} \int T_{\mathrm{mb}} dv, \tag{A.2}$$

where ν is the frequency, h is the Planck constant, c is the speed of light, A_{ul} is the Einstein coefficient for spontaneous emission, T_{mb} is the intensity in Kelvin units and v denotes the radial velocity over which the integral is calculated, covering the entire observed range of a specific line emission. Thus, the term $\int T_{\mathrm{mb}} dv$ corresponds to the integrated intensity of the line, assuming that the emitting region completely covers the beam. When plotting equation A.1 with N_{up} on a logarithmic scale, we obtain a straight line, with a slope proportional to the negative inverse value of T_{ex}.

Given the relatively broad frequency range covered by ALCHEMI, it can be expected that the RJ approximation will not be correct for all transitions and temperatures measured in the CMZ of NGC 253. It is impossible to know a priori whether the T_{ex} will be low enough to cause a significant distortion between the Planck function and the RJ approximation. Given the results summarized in our Table A.2, this approximation has an appreciable bias and we have decided to calculate a correction factor (CF) meant to be multiplied by the upper level column density of each methanol transition in the rotation diagrams. This CF is equal to the Planck function over the RJ approximation:

$$CF = \frac{h\nu}{kT_{\mathrm{ex}}} \frac{1}{\exp(\frac{h\nu}{kT_{\mathrm{ex}}}) - 1}. \tag{A.3}$$

Considering methanol transitions with frequencies of 200 and 300 GHz inside a region with a temperature of 10–20 K, we obtained correction factors in the range of 0.6–0.8 and 0.45–0.7, respectively. After applying this correction to our rotation diagrams (assuming RJ), the resulting T_{ex} obtained for each region vary mostly by less than 1 K. The total column densities, on the other hand, can decrease by ~50% in the coldest regions, such as regions 2 and 10 for E–CH$_3$OH (see Table A.2), and by ~20% in warmer environments. The lowest values obtained in this way are included in the uncertainties shown in Table A.2.

We could do an iterative process from the temperature obtained from RJ to the one obtained after applying the correction factor until reaching a certain T_{ex} asymptotically. However, since T_{ex} hardly varies, we decided to include the new N_{up} values inside the uncertainties after a single correction is applied. Indeed, the change of the T_{ex} assumed when applying CF will not have an important effect on the slope derived in the rotation diagrams. It might slightly increase the dispersion of the individual N_{up} values with respect to the LTE slope (solid black lines in Fig. 3).

This dispersion is inversely proportional to T_{ex}, and T_{ex} is higher for the A-CH$_3$OH species with respect to the E-CH$_3$OH species (see Table A.2). One might suspect that an increased dispersion may discard the $10_0 \rightarrow 9_1{-}A^+$ transition at 198.4 GHz as a maser candidate because of its departure from the LTE slope of a factor of 3.6 ± 1.2 in region 6, as indicated in Sect. 4.1.3, given our threshold of 3.3 (3σ; Sect. 4.1). However, this region has a T_{ex} of 24.3 K indicating that RJ is a good approximation for the Planck formula. All the other methanol maser candidates depart from LTE by a factor higher than four times the LTE expected value.

The results from our rotation diagrams fitting to the LTE lines are listed in Table A.2. The effect of having a strong continuum might affect our synthetic spectra, potentially leading to an overestimation of the emission (e.g., Belloche et al. 2019). However, comparing our data with the models, this can be ruled out. Indeed, we noticed that considering our deviation from the Planck function in the total column density uncertainties, the rotation diagram results are in better agreement with the modeling results (see Table 3). This is especially critical for the colder regions. It can also be appreciated that sometimes the lower limits are placed much below the ones derived by the radiative transfer models, as in the case of region 4, where the temperatures derived from the rotation diagram method seem to be underestimated by ~5 K with respect to the LTE models, generating an artificial scatter and lower total column densities. The latter support our predicament of including the newly derived upper-level column density values obtained after applying the CF inside an error bar instead of replacing the values obtained from RJ. Accounting for the excitation temperatures, they are always higher in the modeling as compared to the rotation diagrams for E-methanol the nuclear regions (3 to 6) in A-methanol, and the opposite is observed at the outskirts of the NGC 253's CMZ for the A-methanol case (regions 1 and 8 to 10).

---

[8] see, for instance, the derivation presented in Araya et al. (2005), between Equations A9 and A10.

[9] Under LTE, the underlying assumption for the use of the rotation diagram method, the excitation temperature of any transition is equal to the rotation temperature that describes the populations of the rotational levels

Table A.1. Selected methanol transitions.

Transition	ν [GHz]	A/E	R1	R2	R3	R4	R5	R6	R7	R8	R9	R10	potential blending lines
$5_{-1} \rightarrow 4_0$	84.521172	E	✓	✓	✓	✓	–	✓	✓	✓	✓	✓	–
$2_1 \rightarrow 1_1$	95.914310	A^+	✓	✓	✓	✓	–	✓	✓	✓	✓	✓	C_2H_5OH
$2_1 \rightarrow 1_1$	97.582798	A^-	✓	✓	✓	✓	–	✓	✓	✓	✓	–	CH_3COCH_3
$3_1 \rightarrow 4_0$	107.013831	A^+	–	–	✓	✓	–	✓	✓	–	–	–	CH_3COCH_3
$0_0 \rightarrow 1_{-1}$	108.893945	E	✓	✓	✓	✓	–	✓	✓	✓	✓	✓	–
$6_{-1} \rightarrow 5_0$	132.890759	E	✓	✓	✓	✓	–	✓	✓	✓	✓	✓	CH_3OCHO
$3_1 \rightarrow 2_1$	143.865795	A^+	*	✓	✓	✓	–	✓	✓	✓	✓	–	C_2H_5OH
$3_1 \rightarrow 2_1$	146.368328	A^-	*	✓	✓	✓	–	✓	✓	✓	✓	bN	cis–DCOOH, n–C_3H_7CN
$9_0 \rightarrow 8_1$	146.618697	A^+	✓	–	–	✓	–	–	*	✓	✓	–	SO_2
$8_0 \rightarrow 8_{-1}$	156.488902	E	–	–	–	✓	–	–	–	–	–	–	C_2H_3CN
$2_1 \rightarrow 3_0$	156.602395	A^+	–	N	✓	✓	–	✓	✓	–	✓	–	C_2H_5C–13–N
$7_0 \rightarrow 7_{-1}$	156.828517	E	–	–	–	✓	–	✓	✓	–	–	–	C_2H_5CN, NH_2CHO
$6_0 \rightarrow 6_{-1}$	157.048617	E	–	–	–	✓	–	✓	✓	–	–	–	HCOOH
$5_0 \rightarrow 5_{-1}$	157.178987	E	–	–	–	✓	–	✓	✓	–	–	–	CH_3COCH_3, ^{33}SO
$5_1 \rightarrow 5_0$	165.369341	E	✓	✓	✓	✓	–	✓	✓	✓	✓	*	C_2H_5CN
$4_1 \rightarrow 3_1$	191.810503	A^+	–	*	✓	✓	–	✓	✓	bN	✓	*	$HCOOC_2H_5$, n–C_3H_7CN
$4_1 \rightarrow 3_1$	195.146790	A^-	*	*	✓	✓	–	✓	✓	✓	✓	N	CH_3OCHO, CH_3OCH_3
$10_0 \rightarrow 9_1$	198.403067	A^+	*	*	✓	✓	–	✓	✓	N	bN	*	–
$1_1 \rightarrow 2_0$	205.791270	A^+	*	✓	✓	✓	–	✓	✓	✓	✓	bN	C_2H_5OH, CH_3OCHO
$1_1 \rightarrow 0_0$	213.427061	E	✓	✓	✓	✓	–	✓	✓	✓	✓	✓	c–C_3H
$5_1 \rightarrow 4_2$	216.945521	E	–	–	–	✓	–	✓	✓	–	–	–	–
$4_2 \rightarrow 3_1$	218.440063	E	*	✓	✓	✓	–	✓	*	✓	✓	✓	c–C_3H_2
$8_{-1} \rightarrow 7_0$	229.758756	E	✓	–	–	✓	–	✓	✓	✓	✓	–	CH_3CHO
$5_1 \rightarrow 4_1$	239.746219	A^-	✓	–	✓	✓	–	✓	✓	✓	✓	bN	HCOOD
$5_1 \rightarrow 4_1$	243.915788	A^+	*	–	✓	✓	–	✓	✓	*	✓	bN	$D_2\,^{34}S$, $^{34}SO_2$
$4_2 \rightarrow 5_1$	247.228587	A	–	–	bN	✓	–	–	✓	–	–	–	C_2H_5OH
$2_0 \rightarrow 1_{-1}$	254.015377	E	✓	✓	✓	✓	–	✓	✓	✓	✓	✓	c–C_3D_2, C_2H_5OH
$2_1 \rightarrow 1_0$	261.805675	E	✓	✓	✓	✓	–	✓	✓	✓	✓	✓	C_2H, c–C_3H_2
$6_1 \rightarrow 5_1$	287.670767	A^+	✓	–	✓	✓	–	✓	✓	✓	✓	–	CCS
$6_0 \rightarrow 5_0$	289.939377	E	–	–	✓	✓	–	✓	*	✓	✓	–	$S^{17}O$, $HNC^{18}O$
$6_1 \rightarrow 5_1$	292.672889	A^-	✓	–	✓	✓	–	✓	✓	*	✓	–	CH_3COCH_3, CH_3CHO
$3_0 \rightarrow 2_{-1}$	302.369753	E	✓	✓	✓	✓	–	✓	✓	✓	✓	✓	c–HCOOH, CH_3OCHO
$1_1 \rightarrow 1_0$	303.366921	A^{-+}	✓	✓	✓	✓	–	✓	✓	*	✓	✓	H_2CN
$2_1 \rightarrow 2_0$	304.208348	A^{-+}	✓	✓	✓	✓	–	✓	✓	✓	✓	✓	NH_2CHO, C_2H_5OH
$3_1 \rightarrow 3_0$	305.473491	A^{-+}	✓	✓	✓	✓	–	✓	✓	✓	✓	bN	C_2H_5CN, CH_3COCH_3
$4_1 \rightarrow 4_0$	307.165924	A^{-+}	✓	✓	✓	✓	–	✓	✓	✓	✓	✓	CH_3OCHO
$5_1 \rightarrow 5_0$	309.290360	A^{-+}	*	✓	✓	✓	–	✓	✓	✓	✓	bN	^{33}SO
$3_1 \rightarrow 2_0$	310.192994	E	✓	✓	✓	✓	–	✓	✓	✓	✓	✓	CH_3OCHO, CH_3COCH_3
$6_1 \rightarrow 6_0$	311.852612	A^{-+}	*	bN	✓	✓	–	✓	✓	✓	✓	✓	c–C_3H_2, CH_3COCH_3
$7_1 \rightarrow 7_0$	314.859528	A^{-+}	*	–	✓	✓	–	✓	✓	*	✓	–	C_2H_3CN
$6_2 \rightarrow 5_1$	315.266861	E	✓	–	✓	✓	–	✓	✓	*	*	–	C_2H_3CN
$8_1 \rightarrow 8_0$	318.318919	A^{-+}	–	–	✓	✓	–	✓	✓	bN	bN	–	c–C_3H_2, C_2H_5OH
$7_1 \rightarrow 6_1$	335.582017	A^+	✓	–	✓	✓	–	✓	✓	–	–	–	n–C_3H_7CN, l–C_3H_2
$7_0 \rightarrow 6_0$	338.124488	E	–	✓	✓	✓	–	✓	✓	✓	✓	–	CH_3OCHO
$7_1 \rightarrow 6_1$	341.415615	A^-	–	–	✓	✓	–	✓	✓	–	–	–	NH_2CHO, CH_3OCHO
$4_0 \rightarrow 3_{-1}$	350.687662	E	✓	✓	✓	✓	–	✓	✓	✓	✓	✓	NO
$1_1 \rightarrow 0_0$	350.905100	A^+	✓	✓	✓	✓	–	✓	✓	✓	✓	✓	CH_3COCH_3, $^{33}SO_2$
$4_1 \rightarrow 3_0$	358.605799	E	✓	*	✓	✓	–	✓	✓	✓	✓	–	CH_3OCHO, n–C_3H_7CN
$7_2 \rightarrow 6_1$	363.739868	E	–	–	✓	✓	–	✓	✓	–	–	–	–
TNoL			25(35)	23(29)	41(42)	49	–	46	45(48)	31(38)	35(39)	16(26)	
H_α			–	1147	58303	58579	17814	36998	36291	8150	7073	2603	

Notes. Selected methanol lines to perform our rotation diagrams. Possible contamination with other molecules is mentioned in the rightmost column. The symbol * indicates bad-shaped lines. The letter N indicates lines embedded in a noisy continuum but with intensities above the 3.5σ level. bN denotes lines tentatively detected (2–3σ). ✓ indicates well-distinguished/confidently-detected lines, and the dash (–) indicates a nondetection. The third last row provides the total number of lines (TNoL) detected toward each region, considering lines confidently observed (check-mark). The TNoL considering the ones not clearly detected (*, N, bN), are given in parenthesis. The last row presents the H_α mean intensity for each region considering an angular extent of $1\farcs6$ (the beam size), obtained from MUSE archival data (ID:0102.B-0078(A), PI:Laura Zschaechner) in units of 10^{-20} erg/s/cm^2/Å. For an alternative approach on line blending, see Tables C.1 and C.2.

Table A.2. Fit parameters from our rotation diagrams.

Region	N(Sp) [$\times 10^{13}$ cm^{-2}]	$T_{\rm ex}$ [K]	N(Sp) [$\times 10^{13}$ cm^{-2}]	T_{ex} [K]
	E–CH$_3$OH		A–CH$_3$OH	
R1	$67.3^{+10.1}_{-38.4}$	$9.7^{+1.0}_{-2.1}$	$9.9^{+1.5}_{-3.8}$	$25.0^{+3.1}_{-2.9}$
R2	$78.1^{+11.7}_{-30.6}$	$8.4^{+0.8}_{-1.9}$	$10.0^{+1.5}_{-5.0}$	$14.5^{+1.9}_{-2.0}$
R3	$263.0^{+39.4}_{-105.0}$	$19.0^{+1.6}_{-2.7}$	$84.2^{+12.6}_{-32.1}$	$23.1^{+3.1}_{-3.3}$
R4	$91.2^{+13.7}_{-28.8}$	$27.5^{+3.9}_{-4.0}$	$76.2^{+11.4}_{-26.5}$	$27.7^{+5.3}_{-5.5}$
R6	$253.7^{+38.1}_{-92.1}$	$20.3^{+2.9}_{-1.9}$	$115.4^{+17.3}_{-36.6}$	$24.3^{+3.1}_{-4.8}$
R7	$275.2^{+41.3}_{-134.3}$	12.3 ± 1.3	$58.4^{+8.8}_{-21.1}$	$25.7^{+4.6}_{-5.2}$
R8	$77.8^{+11.7}_{-44.4}$	$9.9^{+0.9}_{-1.9}$	$12.6^{+1.9}_{-4.1}$	$30.8^{+7.3}_{-7.1}$
R9	$103.3^{+11.7}_{-57.2}$	$10.4^{+1.0}_{-1.9}$	$17.9^{+2.7}_{-5.6}$	$29.3^{+7.7}_{-7.6}$
R10	$11.6^{+1.74}_{-6.8}$	$9.6^{+0.8}_{-2.7}$	$3.0^{+0.4}_{-1.1}$	$23.8^{+14.5}_{-13.5}$

Notes. Total column densities (N(Sp)) and excitation temperatures ($T_{\rm ex}$) for each methanol symmetric type derived from the best LTE fit to the rotation diagrams (see Fig. 3). Uncertainties correspond to the standard deviation (1σ).

Appendix B: Rotation diagram: Nonmasing outliers

Making use of the rotation diagram method (Sec. 4.1), we have found a variety of methanol lines that do not follow LTE conditions but that, at the same time, do not correspond to masers. These lines are placed beyond a 3σ scatter, surpassing by more than a factor of 3.3 the expected $N_{\rm up}$ value from LTE conditions. We list them in Table 2 and provide a description below, in frequency order.

We realized that the five A–CH$_3$OH lines, at 95.9 GHz, 97.6, 143.9, 146.4, and 156.6 GHz, that usually depart from the LTE conditions of A-type methanol, actually follow the LTE trend of the E–CH$_3$OH species. Since the conditions between A- and E-methanol types differ toward the edge of the CMZ, these five transitions are clearly apart from LTE conditions in regions 1, 2, and 7 to 9. Therefore we decided to not include them in the LTE fitting in any region.

With the exception of the line at 156.6 GHz, the other four can be considered as members of the same family, although varying between symmetric labels (A$^+$ and A$^-$), corresponding to the $(J+1)_1 \rightarrow J_1 - A$ series. In general, the mentioned five transitions have Einstein coefficients for spontaneous emission (A$_{ij}$) below 1.78×10^{-5} s^{-1}, unlike the other A–CH$_3$OH lines in LTE.

As can be seen in Fig 3, these five A–CH$_3$OH transitions with low A$_{ij}$ also have 60–600 times lower critical densities than transitions at similar $E_{\rm up}$/k and this is not significantly changed if $T_{\rm ex}$ is moderately (by less than a factor of five) lower than $T_{\rm kin}$. This means that those transitions require a particularly small critical density to emerge, pointing out that they are tracing conditions of cooler gas located in layers farther away from the GMC cores as compared to the rest of the A-methanol lines. The latter is also based on the overall higher temperatures in A-type methanol compared to E-type methanol in the nine analyzed regions (see fourth panel in Fig. 6).

The line at 261.8 GHz is located beyond LTE in region 6 only. This can be caused by line blending with C$_2$H and c–C$_3$H$_2$, molecules previously observed in the central regions of NGC 253 (Oike et al. 2004; Martín et al. 2006; Holdship et al. 2021).

In regions 1 and 8, the $6_2 \rightarrow 5_1 - E$ line at 315.3 GHz ($E_{\rm up}$/k=63.1 K) seems to act as a maser. However, this line is not clearly observed as an outlier in the other 7 regions. Additionally, if methanol is tracing two different temperatures, the line at 315.2 GHz is related to the temperature better described by A–CH$_3$OH and is therefore likely not a maser.

The line at 318.3 GHz ($E_{\rm up}$/k= 98.8 K) strongly departs from LTE in the inner regions (regions 3 to 6). Similar to the case of the line at 261.8 GHz, this departure is likely due to the contribution of c–C$_3$H$_2$.

The line at 338.1 GHz ($E_{\rm up}$/k= 78.8 K) falls beyond LTE in region 8. In regions 6 to 9 this transition is placed above the LTE trend described by E-type methanol, being closer to the conditions described by A-type methanol instead. In this case we can not argue for a higher critical density for this behavior, contrary to other E–CH$_3$OH transitions (see below).

The line at 350.7 GHz ($E_{\rm up}$/k= 36.3 K) appears to be out of LTE in region 6. Performing a simple LTE model for NO in region 6, we find that NO contributes to 70% to the measured blended feature. We also find that NO is stronger in region 6 than in any other studied region (by doing a moment 0 map of this line, not shown), explaining why we do not see the 350.7 GHz methanol line seemingly departing from LTE in any other region.

The E–CH$_3$OH transitions at 358.605 ($E_{\rm up}$/k= 36.4 K) and 363.739 GHz ($E_{\rm up}$/k= 79.4 K) are emerging at the highest densities, tracing conditions of A–CH$_3$OH. They clearly depart from LTE in region 7, and serve as a complementary case with respect to the five A–CH$_3$OH lines mentioned above.

B.1. Lines blended with maser candidates

The $5_{-1} \rightarrow 4_0 - E$ line at 84.52 GHz occupies a similar frequency window as the $12_{10} \rightarrow 12_{11} - E$ methanol line at 84.53 GHz in all selected regions except region 10, where the line profiles are narrow enough to be disentangled. Line blending, however, is unlikely since the potential companion line connects levels 1085 K above the ground state and has an Einstein coefficient ~2.6 times lower than the masing line (see Table 2). In addition to that, there is no observed emission from the line at 84.53 GHz in region 10 (only the maser line is observed). Furthermore, as mentioned in Sections 4.1 and 4.2, in general there is no methanol emission involving energy levels >150 K above the ground state.

The $7_{-1} \rightarrow 6_0 - E$ line at 181.295 GHz which, to our knowledge, was not yet reported as a (Galactic) maser line (e.g., Leurini et al. 2016), is dramatically contaminated by the J =2–1 HNC line at 181.324 GHz, impeding a proper line inspection. This methanol transition is also affected by its proximity to telluric contamination (H$_2$O at ~183 GHz) that decreases the quality of our data near this frequency.

The $9_{-1} \rightarrow 8_0 - E$ transition at 278.305 GHz is the highest excited line ($E_{\rm up}$/k~102 K) covered by our observations in the $J_{-1} \rightarrow (J-1)_0 - E$ series. It is strongly contaminated by the $2_{-2} \rightarrow 3_{-1} - E$ line at 278.342 GHz. Due to this blending, this methanol line is not considered in the rotation diagrams. However, as presented in Sect. 4.2, a maser line profile emerges in regions 8, 9 and 10.

The $9_0 \rightarrow 8_1 - A^+$ line at 146.618 GHz appears to be masing in region 4, with a departure from LTE of 3.3 ± 1.2 times. However, this line is considerably contaminated by SO$_2$ in region 5 (~80% of the total integrated intensity of the blended feature, Martín et al. in prep.) and therefore, due to the proximity to this region, we expect an important contamination in region 4 and also some contribution in region 7 (after performing a moment 0 map for SO$_2$, not shown). The above influences its departure from LTE in the mentioned regions, producing a larger displacement than for the lines at 84.5 GHz and 132.9 GHz, which are not contaminated. The $9_0 \rightarrow 8_1 - A^+$ line at 146.618 GHz is also blended with the $14_1 \rightarrow 13_2 - A^+$ methanol line at 146.617 GHz, which requires twice the $E_{\rm up}$/k (256 K, see Table 2) to emerge. However, the contribution of this companion line at 146.617 GHz to the maser line at 146.618 GHz is not higher than 2% (Martín et al. in prep.).

Appendix C: Detailed model analysis

In Sect. 4.2, we limited our LTE and non-LTE modeling to a single component for each methanol symmetric type and then we preferred to continue with the LTE model only. This is enough to characterize our selected regions for the scope of this study, resulting in synthetic spectra that adjust to most of the observed methanol emission lines, as can be seen in our Tables C.1 and C.2. The comparison between the observed and the resulting synthetic spectra clearly unveil lines with intensities far above the LTE trend.

In this Appendix, we present a couple of more sophisticated models, aiming to characterize in a more refined way both regions well characterized by LTE conditions and regions with strong maser emission. The former are being located toward the nucleus of NGC 253, while the latter occupy the outskirts of the CMZ of NGC 253, in a bi-symmetric configuration.

We performed a model (hereafter model (1)) to fit the spectrum of region 4 (see Table 1), which shows the best agreement between E- and A-type methanol in our rotation diagrams (see Table A.2), both in terms of excitation temperatures and column densities. In this model we used two physical components (both with slab geometry) for each methanol type.

In CASSIS it is possible to use the MCMC method to explore the space of parameters and fit the line profiles of both methanol types together by adjusting the ISO parameter, which corresponds to the column density ratio of E–CH_3OH over A–CH_3OH. Unfortunately, this two-component approach is constrained to a fixed single excitation temperature per component. Thus, our region with the lowest difference in $T_{\rm ex}$ (see Fig. 6) between methanol types, i.e. region 4, is the best candidate to perform such analysis (model (1)).

The other model (2), addressing region 8, presents the highest difference between A- and E-methanol excitation temperatures (Table A.2), in addition of having all maser lines but the one at 198.4 GHz observed through the rotation diagram method (see Table 2). For model (2) we found better results by fitting both methanol types together, as for our model (1), with two components each. This is not in contradiction with the rotation diagrams, as they only accounted for one gaseous component while here we are using two of them. It is then possible to have one component related to each slope in Fig. 3.

The resulting parameters of the two models are shown in Table C.3 after 600 iterations for each model. While model (1) describes the full LTE conditions, model (2) is mostly non-LTE: the component with the highest column density shows gas densities of $\sim 6 \times 10^5$ cm^{-3}, far below the critical densities of methanol lines used in Sect. 4.1. The LTE synthetic spectrum obtained for region 4 is shown in Fig. C.1 for selected lines covering the entire ALCHEMI frequency range. We did not find important overfits to the observed spectra in this two-component LTE modeling. Although some lines are still underpredicted at frequencies below ∼150 GHz, in general there is a better agreement in comparison to the previous model (single-component) results in terms of line shape (in blue in Fig. C.1).

Summing over column densities of each component in model (1) we obtain column densities of $1.86 \pm 0.024 \times 10^{15}$ and $8.29 \pm 0.17 \times 10^{14}$cm^{-2} for E–$CH_3OH$ and A–CH_3OH, respectively (model uncertainties only, the calibration uncertainty (15%, see Sect. 2) should be added). These values are slightly smaller than in our single-component approach (see Table 3). That is probably due to the avoidance of over-fitting in some line transitions when the spectrum becomes crowded due to nearby methanol lines, like our panels centered at 157.3, 241.8, 290.2 and 338.5 GHz presented in Fig. C.1.

Our non-LTE modeling allows us to obtain better results than the LTE model for region 8. This is remarkable in the case of the $J_K \rightarrow (J-1)_K$ transitions (for both methanol symmetric types). Namely, the $2_K \rightarrow 1_K$ line series (K=-1 ... 1) centered around 96.7 GHz, the $3_K \rightarrow 2_K$ series (K =-2 ... 2) at ∼145.1 GHz; the $4_K \rightarrow 3_K$ series (K =-3 ... 3) at ∼193.5 GHz, the $5_K \rightarrow 4_K$ series (K =-4 ... 4) at ∼241.8 GHz, and the $6_K \rightarrow 5_K$ series (K =-5 ... 5) at ∼290.1 GHz, as can be seen in Fig. C.2. Our only concern regarding this non-LTE approach is the overestimation of the $J_0 \rightarrow J_{-1} - E$ line series at about 157.3 GHz, with J from 1 to 3. From this model, it can also be observed that the line at 108 GHz is underpredicted by far, similar to the case of the maser candidates, although the optical depth for this transition is positive.

From model (2) we have obtained the optical depths (τ) for each methanol transition, and we use them to discriminate between maser line candidates and pure outliers in both our rotation diagrams and radiative transfer models (Tables 2 and 4, respectively). In this way, methanol maser candidates can be limited to transitions with negative τ only. The general departure from LTE observed in the outliers of the CMZ by the two methods outlined in Sects.4.1 and 4.2 can be explained by blending lines, non-LTE conditions, or an extra colder and more extended component, when they have positive τ.

Table C.1. E-type methanol lines used as input for our LTE model.

Transition	ν [GHz]	R1	R2	R3	R4	R5	R6	R7	R8	R9	R10	Blending lines
$6_{-2} \rightarrow 7_{-1}$	85.568131	NL	NL	F	F	N	N	~	NL	NL	NL	–
$5_{-2} \rightarrow 6_{-1}$	133.605439	~	NL	F	F	~	F	F	~	F	N	–
$8_0 \rightarrow 8_{-1}$	156.488902	~	N	F	F	F	F	F	N	~	NL	C_2H_5OH
$7_0 \rightarrow 7_{-1}$	156.828517	F	NL	F	F	F	F	F	N	~	NL	–
$6_0 \rightarrow 6_{-1}$	157.048617	~	NL	F	F	F	F	F	F	F	N	C_3H
$5_0 \rightarrow 5_{-1}$	157.178987	F	F	F	F	F	F	F	F	F	~	–
$4_0 \rightarrow 4_{-1}$	157.246062	F	F	F	~	F	F	F	F	F	F	–
$1_0 \rightarrow 1_{-1}$	157.270832	F	F	~	F	F	~	F	~	F	F	–
$3_0 \rightarrow 3_{-1}$	157.272338	F	F	~	F	F	~	F	F	F	F	–
$2_0 \rightarrow 2_{-1}$	157.276019	F	F	~	F	F	~	F	~	F	F	–
$5_1 \rightarrow 5_0$	165.369341	F	~	~	~	F	~	F	~	F	N	–
$5_1 \rightarrow 4_2$	216.945521	N	~	F	F	F	F	F	F	F	~	C_2H_3CN, CH_3OCHO
$8_0 \rightarrow 7_1$	220.078561	NL	NL	F	F	N	F	F	NL	F	NL	HC_3N
$3_{-2} \rightarrow 4_{-1}$	230.027047	F	F	~		F	N	F	F	F	F	CH_3NH_2
$5_0 \rightarrow 4_0$	241.700159	~	F	F	F	F	F	F	F	F	F	–
$5_2 \rightarrow 4_2$	241.904643	F	~	F	F	F	F	F	F	F	~	–
$6_1 \rightarrow 5_2$	265.289562	F	~	F	F	F	F	F	F	F	F	–
$5_2 \rightarrow 4_1$	266.838148	F	~	F	F	F	~	F	~	~	N	–
$6_0 \rightarrow 5_0$	289.939377	F	F	F	F	F	F	F	F	F	F	–
$6_2 \rightarrow 5_2$	290307.738	F	N	F	F	F	F	F	F	F	N	–
$3_0 \rightarrow 2_{-1}$	302.369773	F	F	F	~	F	~	F	F	F	F	–
$3_1 \rightarrow 2_0$	310.192994	~	F	F	F	F	F	F	F	F	F	–
$6_2 \rightarrow 5_1$	315.266861	F	N	F	F	F	F	F	~	~	N	C_2H_3CN
$7_0 \rightarrow 6_0$	338.124488	F	N	F	F	F	F	F	~	~	F	–
$7_1 \rightarrow 6_1$	338.614936	F	~	F	~	F	~	F	~	F	N	CH_3NH_2, HC_3N
$7_2 \rightarrow 6_2$	338.721693	F	~	F	F	F	F	F	~	F	N	–
$7_{-2} \rightarrow 6_{-2}$	338.722898	F	~	F	F	F	F	F	~	F	N	–
$4_0 \rightarrow 3_{-1}$	350.687662	F	F	F	N	N	N	F	F	F	F	NO
$7_2 \rightarrow 6_1$	363.739868	~	N	~	F	~	~	F	~	~	N	–

Notes. The upper energy level was limited to 150 K and the catalog used inside CASSIS was VASTEL (see Sect. 4.1). The frequency ranges approximately from 84 to 373 GHz. We indicate with letter N the lines that were not fitted (reproduced by less than 40% or over-predicted by more than 40% of its intensity). NL means that the corresponding transition was not observed and therefore not fitted. All the fitted transitions are labeled with the letter F. The symbol ~ is representing lines that were fitted at an important percentage, around 40–70%, and usually without confusion with other lines. Blending lines, in terms of integrated intensity contamination percentage, based on preliminary results from synthetic spectra in region 5 (Martín et al. in prep.) are shown in the last column when surpassing 5%.

Table C.2. A-type methanol lines used as input for our LTE model.

Transition	ν [GHz]	Type	R1	R2	R3	R4	R5	R6	R7	R8	R9	R10	Blending lines
$2_1 \rightarrow 1_1$	95.914310	A^+	N	N	N	F	F	~	N	N	N	~	C_2H_5OH
$2_1 \rightarrow 1_1$	97.582798	A^+	N	N	N	F	F	~	N	N	N	F	–
$4_1 \rightarrow 3_1$	191.810503	A^+	N	~	F	F	F	F	N	F	N	F	–
$4_1 \rightarrow 3_1$	195.146790	A^-	N	~	~	~	F	~	N	N	N	N	CH_3OCHO
$1_1 \rightarrow 2_0$	205.791270	A^+	~	F	F	F	~	F	F	F	F	~	C_2H_5OH
$4_2 \rightarrow 5_1$	234.683370	A^-	~	F	F	F	~	F	F	~	~	~	C_2H_5OH, H_2CS
$5_1 \rightarrow 4_1$	239.746219	A^+	F	F	F	F	F	F	N	~	~	~	–
$4_3 \rightarrow 4_2$	251.866524	A^{-+}	F	F	F	~	N	F	F	F	F	N	–
$5_3 \rightarrow 5_2$	251.890886	A^{+-}	F	F	F	~	N	F	F	F	F	F	–
$6_3 \rightarrow 6_2$	251.895728	A^{+-}	F	F	F	~	N	F	F	F	F	F	–
$4_3 \rightarrow 4_2$	251.900452	A^{+-}	F	F	F	~	N	F	F	F	F	F	–
$3_3 \rightarrow 3_2$	251.905729	A^{-+}	F	F	F	~	N	F	F	F	F	F	–
$3_3 \rightarrow 3_2$	251.917065	A^{+-}	F	F	F	~	N	F	F	F	F	F	–
$7_3 \rightarrow 7_2$	251.923701	A^{+-}	F	F	F	~	N	F	F	F	F	F	–
$8_3 \rightarrow 8_2$	251.984837	A^{+-}	F	F	F	~	N	F	F	F	F	F	
$6_1 \rightarrow 5_1$	287.670767	A^+	F	~	F	F	F	~	~	F	F	F	–
$1_1 \rightarrow 1_0$	303.366921	A^{-+}	F	~	~	~	–	F	F	~	~	~	H_2CN
$2_1 \rightarrow 2_0$	304.208348	A^{-+}	~	~	F	~	–	F	F	~	~	~	C_2H_5OH
$3_1 \rightarrow 3_0$	305.473491	A^{-+}	~	~	~	~	–	~	F	~	~	F	c–C_3H_2, CH_3SH
$4_1 \rightarrow 4_0$	307.165924	A^{-+}	F	~	~	N	–	~	F	~	F	F	CH_3OCHO
$5_1 \rightarrow 5_0$	309.290360	A^{-+}	F	~	~	~	–	~	F	F	F	F	–
$6_1 \rightarrow 6_0$	311.852612	A^{-+}	F	F	F	~	~	F	F	F	F	~	–
$7_1 \rightarrow 7_0$	314.859528	A^{-+}	~	F	F	~	~	F	~	~	N	~	–
$2_2 \rightarrow 3_1$	335.133570	A^-	N	~	F	F	F	F	F	F	F	~	CH_3COOH
$7_1 \rightarrow 6_1$	335.582017	A^+	~	~	~	~	F	~	F	F	~	~	–
$7_1 \rightarrow 6_1$	341.415615	A^-	F	N	~	F	F	F	F	F	F	~	–
$1_1 \rightarrow 0_0$	350.905100	A^+	F	F	F	F	F	F	~	F	F	F	–

Notes. Same as for Table C.1, but for A-type methanol. Lines denoted with the symbol – were not attempted to fit in Region 5 (see Section. 4.2.1).

Table C.3. Best E-type methanol fit parameters from our detailed two components modeling.

Region	Component	N(Sp) [cm^{-2}]	$T_{\rm kin}$ [K]	FWHM [km s^{-1}]	$V_{\rm LSR}$ [km s^{-1}]	ISO	$n_{\rm H_2}$ [cm^{-3}]
4	1	$7.67{\times}10^{14}{\pm}1.20{\times}10^{13}$	26.68 ± 0.21	84.78 ± 0.32	252	1.516 ± 0.025	–
	2	$4.19{\times}10^{14}{\pm}1.19{\times}10^{13}$	32.32 ± 0.39	30.66 ± 0.25	248	1.295 ± 0.061	–
8	1	$1.35{\times}10^{14}{\pm}1.29{\times}10^{13}$	24.76 ± 0.80	75.59 ± 0.37	205	1.984 ± 0.121	$2.777(\pm 0.101){\times}10^{8}$
	2	$1.34{\times}10^{15}{\pm}5.00{\times}10^{13}$	14.84 ± 0.32	62.42 ± 0.68	200	3.141 ± 0.578	$5.949(\pm 0.279){\times}10^{5}$

Notes. Uncertainties correspond to 3σ. Velocity uncertainties (not shown) correspond to less than 10% of the instrumental uncertainty (~8–9 km s^{-1}) . Column density (N(Sp)) values for A-type methanol can be obtained dividing them by the ISO number (column density ratio of E- over A-type methanol, see Appendix C), while the rest of the parameters are the same for both methanol symmetric types. The minus symbol (-) indicates that no $n_{\rm H_2}$ was derived as the model is in LTE.

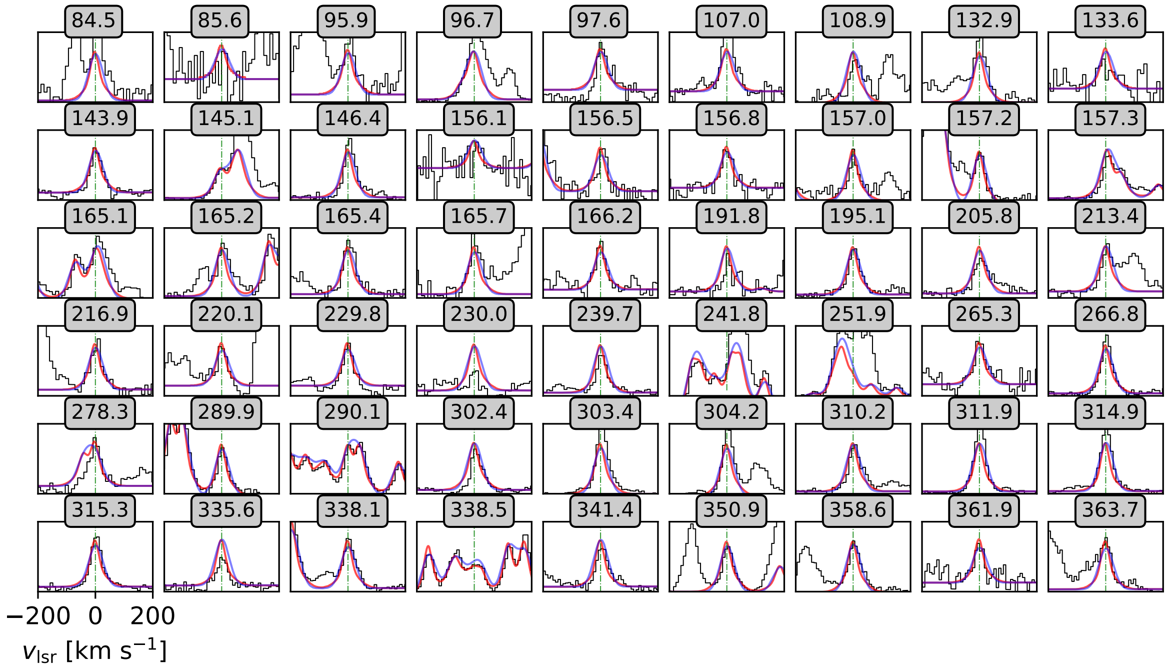

Fig. C.1. Two-component LTE model for region 4 (in red) over-plotted to the rest-frame spectra (in black). The common velocity range (in km s^{-1}, after applying the radio convention and subtracting the $v_{\rm LSR}$ velocity of the region, as in Fig. 2, namely 252 km s^{-1}, see Table 1) is depicted at the bottom left panel while line frequencies are indicated above each panel in GHz and by green dashed lines inside the panels. Previous single-component LTE modeling (see Fig. 7) is shown in blue for comparison.

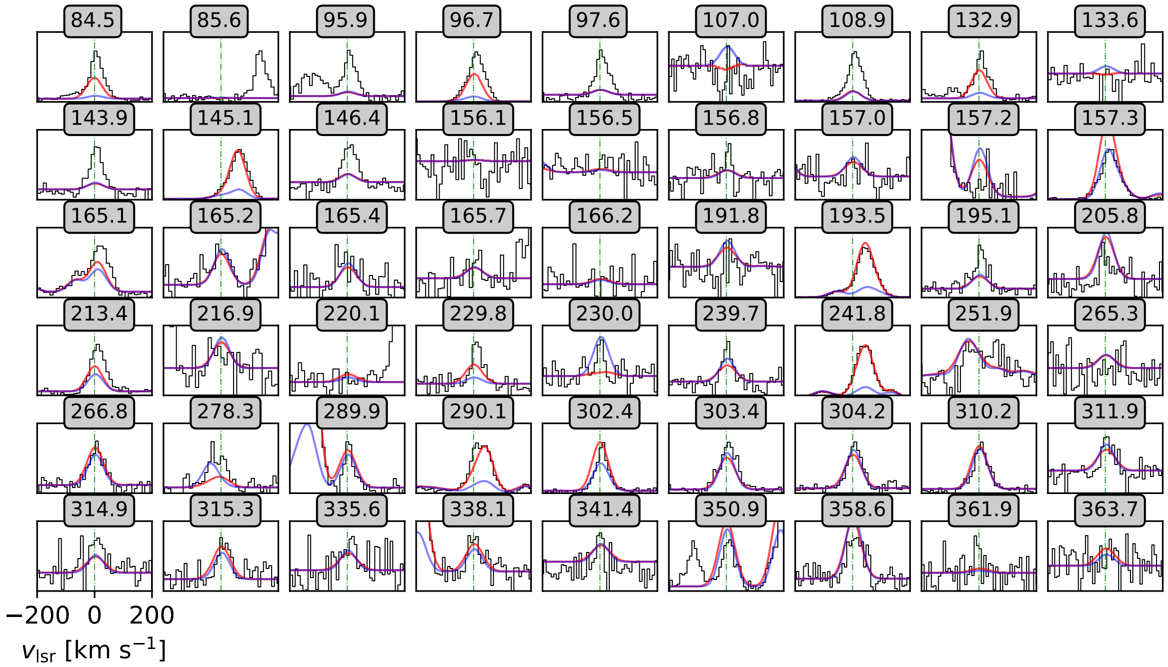

Fig. C.2. Two-component RADEX non-LTE model for region 8 (in red) over-plotted on the rest-frame spectra (in black). The common velocity range is depicted at the bottom left panel and was obtained in the same manner as in Fig. C.1 but this time subtracting a $v_{\rm LSR}$ velocity of 205 km s^{-1} (see Table 1). Line frequencies are indicated above each panel in GHz and by green dashed lines inside the panels. Previous single-component LTE modeling (see Fig. 7) is shown in blue for comparison.

Appendix D: Outliers identified through LTE modeling

As mentioned in Sect. 4.2.1, there are methanol transitions not reproduced by our synthetic spectra in LTE conditions. Without considering the two maser candidates at 95.2 and 278.3 GHz detected by our radiative transfer modeling, there are still a number of transitions not reproduced (see Table 4). Some intriguing cases will be described below, ordered by frequency.

The $\mathbf{3_1 \rightarrow 4_0 - A^+}$ transition line at 107.0 GHz ($E_{\rm up}$/k=28.3 K) has intensities surpassing the LTE models in regions 3, 4, 6, and 7. This line is not identified as a maser candidate through the rotation diagram method, presenting only a couple of values slightly above the LTE fit of the rotation diagrams by a factor ($N_{\rm up,107\,GHz}$ – $N_{\rm up,LTE}$) of 0.25 to 0.46 (in regions 6 and 4, respectively), while in other regions it falls below the fit, like in the case of region 7, where it appears below the expected value by a factor of 1.1. In the LTE modeling its intensity is not strongly underpredicted (see Fig. 8), in contrast to the case of the Class I methanol masers in the $J_{-1} \rightarrow (J{-}1)_0 - E$ and $J_0 \rightarrow (J-1)_1 - A^+$ line series (see Fig. 9).

Methanol transitions, frequently observed as masers in interstellar space have sometimes the property that they show, in case of absence of a proper stimulating environment, anti-inversion. A characteristic case is the 12.1 GHz $2_0 \rightarrow 3_{-1} - E$ transition, often seen as a Class II maser line in massive star forming regions (e.g., Breen et al. 2011). This line has been observed in absorption toward dark clouds, thus indicating a typical excitation temperature below 2.7 K in this class of objects (Walmsley et al. 1988). Furthermore, from Galactic data, Class I and Class II maser regions are not well correlated (Kang et al. 2015). The $3_1 \rightarrow 4_0 - A^+$ transition at 107.0 GHz may be a related case. The line shows weak absorption in regions 1 and 9, where class I emission is observed. This leads us to relate this line to a Class II maser. Another possibility is that this transition comes from colder gas, following an LTE behavior in the rotation diagrams but requiring an extra component to be fitted by synthetic spectra. The presence of an extra component is in line with recent observations performed by Holdship et al. (2021), based on C_2H observations from the same ALCHEMI dataset. They found an extended and relatively cold component seen predominantly at lower frequencies (mainly in the J=1–0 transition at 87 GHz), where C_2H has a gas density ($n_{\rm H2}$) in the range of (0.35–1.7)×10^4 cm^{-3}.

When this line is not in emission, it shows either absorption or a low signal. This happens in regions 1, 2, 5, 8, 9, and 10 (Fig. 8), the same regions where Class I masers are detected in emission in the rotation diagrams (see Sect. 4.1.1), with the only exception of region 7 and the previously avoided region 5. Masers related to both classes might arise in region 7 due to our limited angular resolution, that cannot disentangle individual maser spots. Coming back to the rotation diagram method, within all regions where the 107 GHz line is detected in emission, the only one where its intensity is lower than expected by the LTE behavior is region 7. This opens the possibility that this line is suffering absorption not detectable by the LTE models due to a colder gas component that may be contaminating our spectra below 156 GHz.

We cannot be confident about the nature of this line, but if it is maser emission, that will indicate a first detection of methanol Class II maser emission in NGC 253 and the farthest detection of such a maser (107 GHz) so far. We note that the strongest Class II line in our Galaxy is the $5_1 \rightarrow 6_0 - A^+$ line at 6.7 GHz (Leurini et al. 2016), first reported by Menten (1991), which belongs to the same family as the 107.0 GHz line detected in the present study. Absorption might then be expected for this methanol line in regions populated by Class I methanol masers. We highlight, however, that based on a non-LTE analysis of region 8, this line has positive optical depths (Appendix C).

The $\mathbf{0_0 \rightarrow 1_{-1} - E}$ transition at 108.9 GHz ($E_{\rm up}$/k= 5.2 K) was not reproduced by our models, although it follows LTE conditions according to the rotation diagrams, where it is placed slightly above the LTE fit in most regions (see Fig. 3). Its intensity cannot be reached by our non-LTE approximation either (see Appendix C) and, interestingly, its line shape is similar to that observed in our maser candidates at 84.5 and 132.9 GHz. We do not expect negative optical depths for this line (see Table 4) but also no clear blending lines, either from preliminary model results (Martín et al. in prep.), or from our current inspection (see Table A.1, last column). Masers in the $0_0 \rightarrow 1_{-1} - E$ transition are expected to be pumped by radiation of hot dust rather than by ultra-compact H II regions and to be thermalized faster than other Class II masers (Kalenskii et al. 2002).

Figure 7 shows that there are plenty of confirmed LTE lines spanning a frequency range between 86 and 364 GHz. As can be noted toward regions around the core of the CMZ (regions 3 to 6), the $J_1 \rightarrow J_0 - A^+$ series of lines at 304.2, 305.5, 307.2, and 309.3 GHz is slightly underestimated by our synthetic spectra and is weakly misaligned from the LTE behavior in the rotation diagrams. Those lines belong to the same family as the line at 318.3 GHz, previously observed to depart from the rotation diagrams (see Table 2). Since the difference between predicted and observed line strengths is mostly not remarkable, we do not account for them as new maser candidates. In addition, based on a non-LTE model performed for region 8 (Appendix C), only positive optical depths are calculated for these lines.

The $\mathbf{J_K \rightarrow (J-1)_K - X}$ line series, with X being either E, A^+, or A^-, are successfully reproduced in region 8 by a mixture between LTE and non-LTE models (see Appendix C), being placed out of LTE but with positive optical depth, indicating a quasi-thermal nature. We have therefore decided to discard them as maser candidates.

The $\mathbf{5_3 \rightarrow 5_2 - A^{-+}}$ line at 251.81 GHz is the only among 13 transitions in the $J_K \rightarrow J_K - A$ line series (251–252 GHz) which shows a clear departure from our LTE modeling. The intensities of this line are much higher than expected in the central regions of NGC 253. We performed an LTE model for SO (1000 iterations in region 6 only, not shown) that can account for ~64% of the emission at 251.83 GHz, and therefore we do not expect an important contribution for the methanol line, assuming that other species can be also contaminating. However, as this line is not fully reproduced, we add this as an outlier in our Table 4.

Appendix E: Maser line distribution at 146.6 GHz

As mentioned in Sect 4.1.3, the $9_0 \rightarrow 8_1 - A^+$ line at 146.6 GHz is observed to depart from LTE in regions 1, 7, 8, and 9, with intensities ≥8.4±1.2 stronger than predicted, indicating a maser behavior according to our threshold of 3.3 for this factor. Following its cousins at lower frequencies in the $J_0 \rightarrow (J-1)_1 - A^+$ series, at 44.1 (J = 7) and 95.2 GHz (J = 8), it belongs to the Class I maser category (e.g., Leurini et al. 2016; Yang et al. 2020, and references therein).

It can be noted in Fig. E.1 that, contrary to what is observed for methanol masers in the $J_{-1} \rightarrow (J-1)_{-1} - E$ family of lines (except the last covered transition at 278.3 GHz), the $9_1 \rightarrow 8_0 - A^+$ methanol line at 146.6 GHz peaks in region 6. That might be an indication that this line is a better tracer of the highest densities instead of cloud-cloud collisions, that dominate the outskirts of the CMZ of NGC 253.

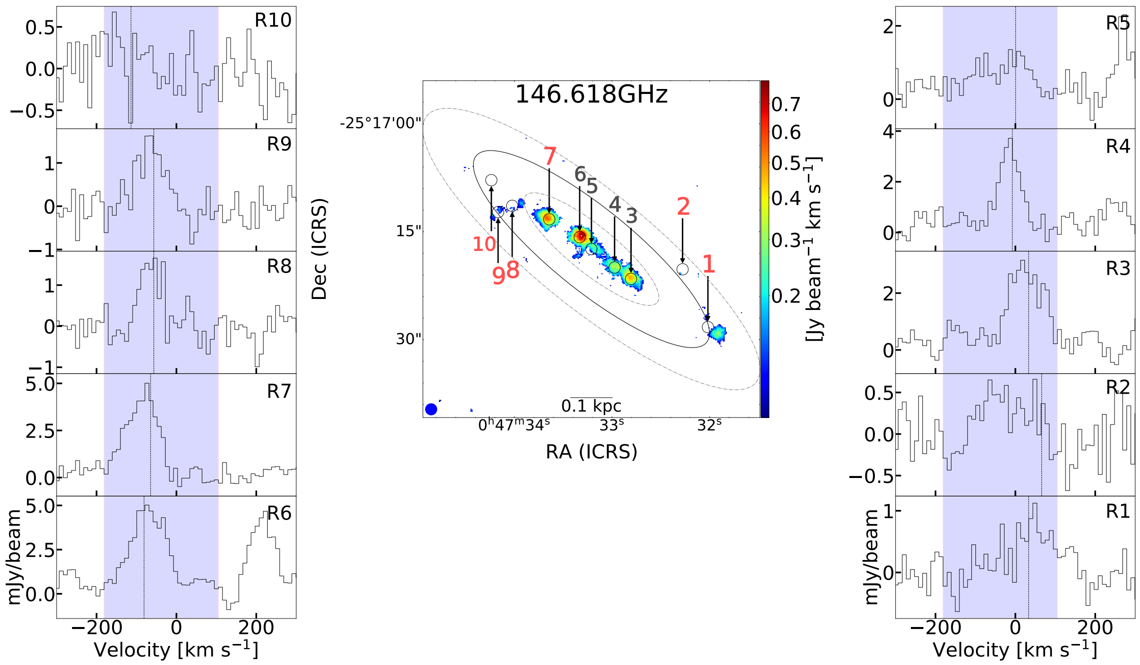

Fig. E.1. Same as for Figure 4, but for the $9_1 \rightarrow 8_0 - A^+$ methanol line at 146.6 GHz.

Appendix F: Equivalency between intensity and column density ratios

In Fig. 13 we present line intensity ratios between the $5_{-1} \rightarrow 4_0 - E$ methanol transition at 84.5 GHz and the average of a couple of E-type methanol lines that are always found to follow LTE conditions (according to our rotation diagrams; see Sect. 5.2). It is important to note a certain equivalency between LTE departure, in terms of $N_{\rm up,maser}/N_{\rm up,LTE}$ (as in Fig. 6) and line intensity ratios between the 84.5 GHz line and the proposed LTE average. They are not necessarily the same, especially considering optically thick transitions and negative optical depths and excitation temperatures present in masers. Therefore, we reproduce in Fig. F.1 the first panel of Fig. 6 with the values on the leftmost y-axis along with the intensity ratios averaged inside the beam size (1$''$.6 diameter) presented in Fig. 13. The results are in agreement in terms of distribution: regions where the $5_{-1} \rightarrow 4_0 - E$ line is observed in LTE through the rotation diagram method (regions 3, 4, and 6) present the lowest integrated intensity ratios. We note that region 5 was avoided when performing the rotation diagrams and that region 10 is not available for all the thermal lines used to obtain the LTE average. We found that a threshold of 3.3 in terms of upper level column density ratios is equivalent to a factor of 0.1244 in terms of integrated intensity ratios, at least within the studied regions.

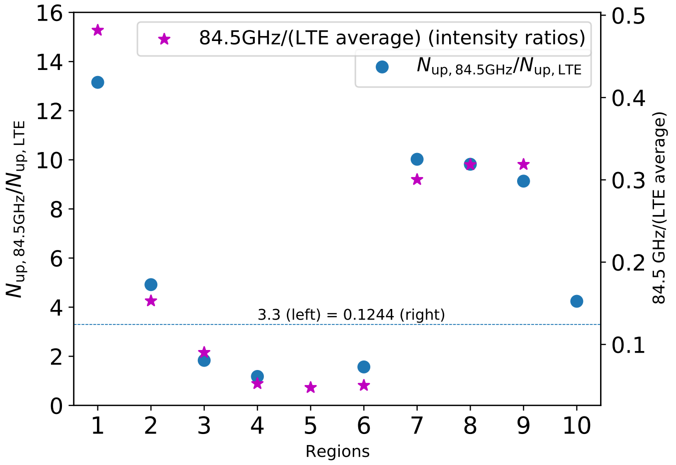

Fig. F.1. Magenta stars are scaled according to the left y-axis, and are equivalent to the magenta stars in the first panel of Fig. 6. Blue dots are scaled with respect to the right y-axis and correspond to integrated intensities of the $5_{-1} \rightarrow 4_0 - E$ methanol transition at 84.5 GHz over an LTE approximation (see Sect. 5.2) averaged inside a beam size aperture (1$''$.6 diameter) for each of the studied regions in this work (see Table 3).

APPENDIX D

Thesis Appendix

D.1 Column density calculation

In the optically thin approximation ($\tau \ll 1$), the column density can be calculated through the following equation (Mangum & Shirley, 2015):

$$N_{tot}^{thin} = \left(\frac{3h}{8\pi^3 S\mu^2 R_i}\right)\left(\frac{Q_{rot}}{g_J g_K g_I}\right)\frac{exp\left(\frac{E_u}{KT_{ex}}\right)}{exp\left(\frac{h\nu}{KT_{ex}}\right)-1}\times\frac{1}{(J_\nu(T_{ex})-J_\nu(T_{bg}))}\int\frac{T_R dv}{f} \tag{D.1}$$

whose components are:

- h = Planck constant
- S = line strength
- μ = permanent dipole moment
- R_i = normalized relative strength of all transitions
- Q_{rot} = rotational partition function
- g_{J} = rotational degeneracy (= $2J_{up}$+1) due to the projection of the angular momentum on the spatial axis z
- g_{K} = K degeneracy due to the projection of the angular momentum upon the molecular axis. It is 1 for linear molecules
- g_{I} = nuclear spin degeneracy. It is 1 for linear molecules
- E_u = upper energy above the ground level
- k = Boltzmann constant
- T_{ex} = excitation temperature
- ν = rest frequency of the transition
- J_ν = Rayleigh-Jeans equivalent temperature
- T_R = source radiation temperature
- f = filling factor.

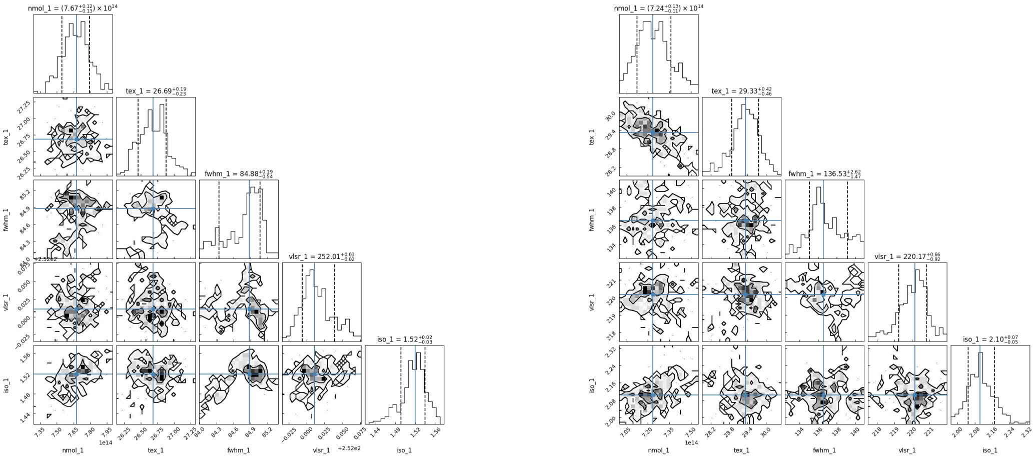

(a) Derived values for the main component in Region 4 assuming LTE conditions. For fits results see Fig. C.1 of Appendix C.

(b) Our best fits to Region 5 assuming LTE and fitting both methanol symmetric types together (see Appendix. C for details).

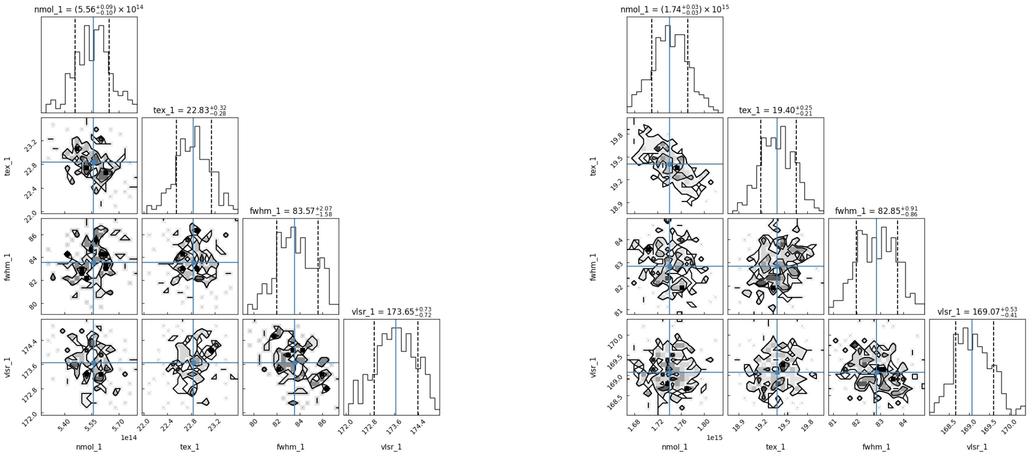

(c) Distribution of the free parameters used to fit A–CH_3OH in region 7.

(d) Distribution of the free parameters used to fit E–CH_3OH in region 7.

Figure D.1: Corner plots from our best model fits using CASSIS at different regions of NGC 253 (see Table 1 of Appendix C).

Applying the optical depth correction factor derived by Goldsmith & Langer (1999), Eq. D.1 can also apply to optically thick cases and when $h\nu \ll kT_{\rm ex}$ or $T_{\rm bg} \ll T_{\rm ex}$:

$$N_{tot} = N_{tot}^{thin} \frac{\tau}{1 - exp(-\tau)} \tag{D.2}$$

D.2 Software

D.2.1 CASSIS

The Centre d'Analyse Scientifique de Spectres Instrumentaux et Synthétiques (CASSIS) is a standalone user-friendly software developed since 2005 by the Institut de Recherche en Astrophysique et Planétologie (IRAP[1]), in Toulouse. Through the use of spectroscopic molecular databases such as CDMS (Müller et al., 2005), JPL (Pickett et al., 1998), or VASTEL[2], CASSIS interactively allows a line identification as well as spectral line modelling both in LTE and out of LTE (working as a wraper of RADEX (van der Tak et al., 2007)). Beam dilution effects are assumed in CASSIS by default and can be dismissed, when necessary, either applying a preliminary 'counter-beam dilution' to the input spectra or indicating a source size much larger than the beam (e.g. a source size of 500" for a 1.6" beam) in the Line Analysis module. This ensures a dilution factor of ∼1.

Besides the sophisticated radiative transfer modelling tool, CASSIS also allows the creation of rotation diagrams through its eponymous module. This is made from the creation of a .rotd file that is saved inside the "Deliver" directory and is created interactively by the user from continuum subtraction and single Gaussian fittings. When using the VASTEL catalog, it is possible to create a rotation diagram for A and E methanol separately. The rotation diagram module discriminates between lines blended with others of the same species and for this considers the total extension of the line fit in the spectral domain. It also allows the inclusion of transitions of interest to be adjusted in the rotational diagram (e.g. dismissing maser transitions), providing the total column densities, excitation temperature, and the reduced χ^2 uncertainties.

Future projects , which are under development (Emmanuel Caux, priv. comm.), include a Python-based version with the ability to model data-cubes instead of a single spectrum. More details about the usage of this software are available in its webpage (`http://cassis.irap.omp.eu/`).

Radiative transfer model for sulfur isotopologues

With CASSIS (Appendix. D.2.1) we have performed non-LTE models for the +50km s^{-1} Cloud. 200 iterations were applied using the Markov Chain Monte Carlo method (MCMC; Hastings, 1970). Due to a limited number of detected transitions, our non-LTE models are degenerated. They consist of two components, a hot/warm component emiting closer to the hot core (in dashed red lines in Fig. D.2) and a colder one (in dashed blue lines in Fig. D.2) obstructing the emission and producing self absorption near at the CS J =2–1 line center and slightly offset toward higher velocities in its J =3–2 transition (solid lines in magenta in Fig. D.2). More observations are required to determine if the latter correspond to infall motions (Evans, 2003).

---

[1] formerly the Centre d'Etude Spatiale des Rayonnements (CESR).

[2] which is based on JPL but explicitly distinguish between methanol symmetric types.

Table D.1: Model parameters used for the various CS isotopologue transitions detected in the 50 km s^{-1} Cloud. The models fitting are shown in Fig. D.2. These models were performed with CASSIS (see Sect. D.2.1) assuming a source size of 253" and a molecular abundance (N(H$_2$)) of 7.5E22 cm^{-2}, for both components.

Transition	Component	Column density [cm^{-2}]	T_{kin} [K]	FWHM [km s^{-1}]	velocity [km s^{-1}]
CS J =2–1,3–2	warm	3.6E15	21	18.2	48.4
	cold	3.6E13	11	15.0	48.4
^{13}CS J =2–1,6–5	warm	1.4E14	298	19.5	46.8
	cold	1.1E14	11	14.8	50.9
C^{34}S J =2–1,3–2,6–5	warm	2.0E14	299	19.6	46.4
	cold	1.2E14	18	14.5	48.9

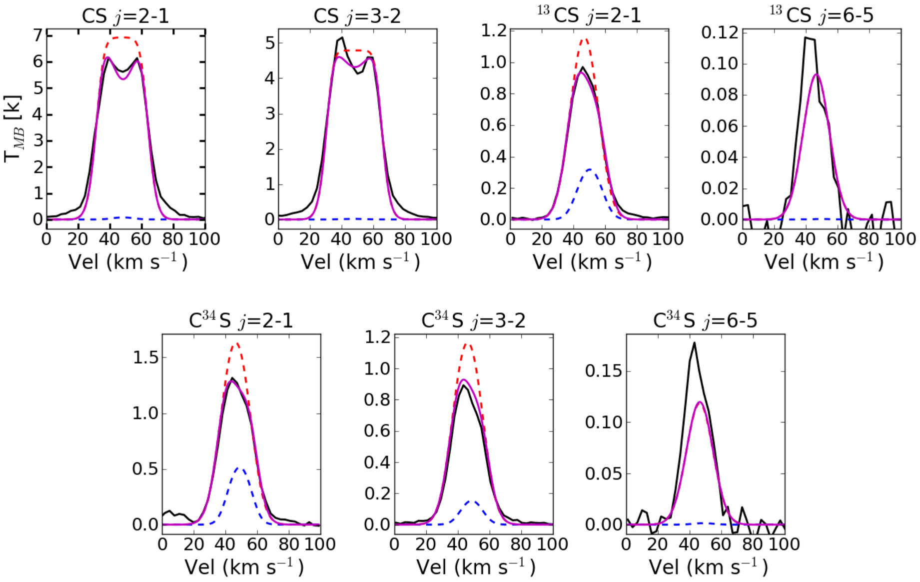

Figure D.2: CS isotopologues observed in the +50km s^{-1} Cloud. Observing information can be found in Table 1 of Appendix A. Model parameters are indicated TableD.1.

D.2.2 XCLASS

The eXtended CASA Line Analysis Software Suite (XCLASS; (Möller et al., 2017)) contains a number of subroutines allowing both interferometric and single-dish sub-mm spectra to be modelled through a variety of optimization algorithms, such as the Levenberg–Marquardt (LM; Moré 1978), simulated annealing, nested sampling, or MCMC. The optimization problem can also be solved by combining these different methods. A good example of the latter being the coupling between the Bees algorithm (Pham et al., 2006) with LM. The Bees algorithm is adequate when the minimum positions are randomly distributed and need to be searched in a large space of parameters without initial assumptions. Within XCLASS we only need to define the number of bees, number of processors, iterations, and limit of χ^2. The basic steps of the Bees algorithm can be summarized as follow (Nemmich et al., 2018):

1. Initialize population with random solution
2. Evaluate fitness of the population

```
3. While (stopping criterion not met)
4. //Forming new population.
5. Select sites for neighborhood search.
6. Recruit bees for selected sites (more bees for best sites) and evaluate fitnesses.
7. Select the fittest bee from each patch.
8. Assign remaining bees to search randmonly and evaluate their fitnesses.
9. End While
```

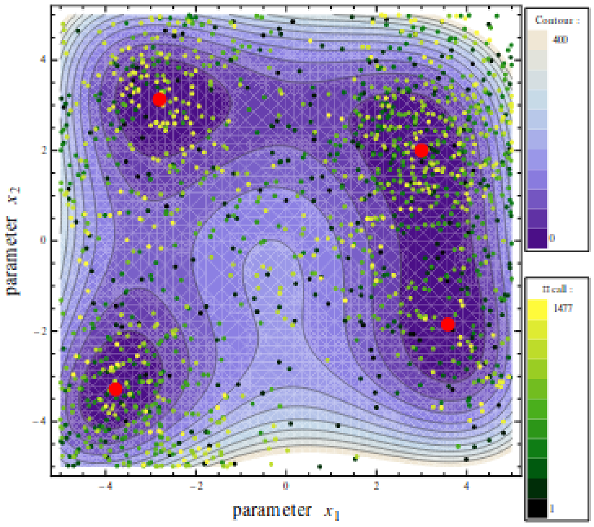

Figure D.3: Himmelblau function using the bees algorithm. Points indicate the distribution of the parameter values color-coded by the number of function calls. The red dots denote the four local minima of the Himmelblau function. Figure taken from the XCLASS Manual `https://xclass.astro.uni-koeln.de/sites/xclass/files/pdfs/XCLASS-Interface_Manual.pdf`

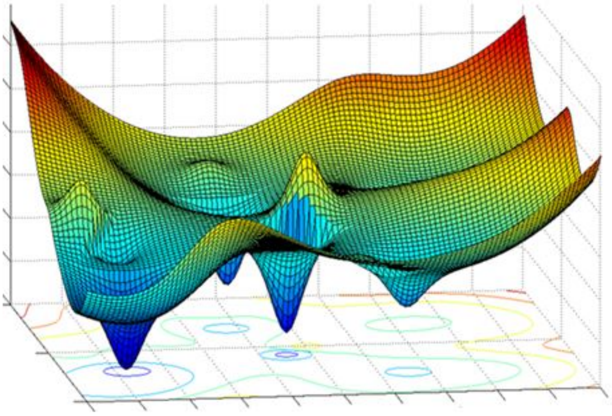

Figure D.4: We can imagine the Bees algorithm mapping the entire parameter space and then the LM algorithm elucidating the global minimum, which would be towards the observer in this 3D image. Figure from `https://www.fromthegenesis.com/gradient-descent-part-2/`.

The second method, LM, is prompt to stall at the first local minimum that it encounters, leaving an ample range of possible solutions without consideration, so it possesses the risk that the global minimum may never be found in a system with multiple minima. LM is more likely to find the global minimum if the initial guess is already close to the solution. To run this algorithm, we could set the same initical parameters as for Bees, except the number of best sites. The combination of these two methods allow the Bees algorithm to consider all the local minima and the LM to further elucidate which of them provides the best solution. Once the best solution is identified, LM is faster than Bees to approach the most accurate solution.

Although originally designed to work within CASA, XCLASS has now a stand-alone version, which is faster, lighter, and works with Python 3. The publicitly available version (only available for Python 2), which is the one we have utilized using CASA version 5.7, is restricted to LTE and continuum-subtracted spectra (can not reproduce absorption lines). Within the most user frienly packages available for non-LTE modelling, we refer the reader to SpectralRadex (van der Tak et al., 2007; Holdship et al., 2021).

We have used XCLASS during the development of Appendix C to confirm that the line ratios, chosen to trace shocks and the amount of cosmic rays, are a good approximation to column density distributions. For a large set of data, such as datacubes or subregions inside of them with more than $\sim 10\times 10$ pixels^2, it is necessary to modify the subroutine "task_myXCLASSMapFit.py", in order to avoid the creation of plots showing a zoom of the best LTE fit per each spatial pixel (spaxel). This will save a large amount of memory and prevents the crash of the code at the end of the process, something that can be very painful and harmful at the end of several hours of use. The lines to be commented in the subroutine are the ones related to the NumPlots variable (lines 3959 to 3983; Lin Y., priv. comm.). It is also important to provide the spectra in Kelvin because only a limited set of header keywords are otherwise recognized to perform a conversion to Kelvin ahead of the modelling.

Our results, which make use of the data presented in Appendix C but are not shown there, include the column densities and excitation temperatures of SiO, HNCO, $C^{17}O$, and CN, from the nuclear few hundred parsecs of NGC 253 (339×848 pc) utilizing the ALCHEMI survey (Sect. 1.3.6). The transitions utilized for each species are listed in Table D.2 and were chosen with the purpose of covering as much of the regions of interest as possible, i.e., our 10 selected positions indicated at the beginning of Appendix C and listed in Table 1 of Appendix C. Despite our efforts, region 10 could not be covered by SiO due to a lack of S/N.

The $N_{\rm tot}$(CN)/$N_{\rm tot}$($C^{17}O$) ratios are similar in distribution to its line intensity ratios, as can be seen in Fig. D.5. These lines also show separately column density distributions similar to their integrated intensity maps. No major issues were found while running XCLASS as they mostly have a single component line capable of being modelled by a single component Gaussian profile. The $N_{\rm tot}$(SiO) is also in good agreement with its integrated intensity map, with regions 3, 4, 6, and 7 showing the highest $N_{\rm tot}$ values.

Our only difficulty occurs with the multiplicity of lines found in HNCO, around our regions 3, 4, and 6. While SiO always shows one predominant line, without many or any additional components, HNCO presents up to four kinematic components (see Fig. 1.21). As a result we find that XCLASS attempts to fit with a single Gaussian the mostly three components of HNCO, yielding very high values of both column density and excitation temperatures (see Fig. D.5). This results in a very low $N_{\rm tot}$(SiO)/$N_{\rm tot}$(HNCO) ratios in these nuclear regions, preventing a direct comparison with the actual line ratios. In Fig. 1.21 it can be appreciated how the HNCO spectra are crowded with up to three kinematic components while SiO shows predominantly a single component. XCLASS allows us to provide as many Gaussian components as required. However, a rapid test in Region 6 delivers better fits but still high column densities, in high disagreement with the intensity distribution. Therefore, HNCO may either experience predominantly non-LTE conditions or XCLASS fails due to a different number of kinematic components per HNCO transition.

Table D.2: Transitions utilized as inputs in XCLASS (from the CDMS catalog). Only CN hyperfine components with the three highest CDMS/JPL intensities are indicated.

Frequency [GHz]	Transition	$log_{10}(A_{ij})$ [s^{-1}]	E_{up} [K]
SiO			
86.8470	J =2–1	-4.53	6.3
130.2686	J =3–2	-3.98	12.5
217.1050	J =5–4	-3.28	31.3
HNCO			
87.9252	4(0,4) – 3(0,3)	-5.06	10.6
109.9057	5(0,5) – 4(0,4)	-4.75	15.8
131.8857	6(0,6) – 5(0,5)	-4.51	22.2
$C^{17}O$			
112.359	J=1–0	-7.17	5.39
224.714	J=2–1	-6.19	16.2
337.061	J=3–2	-5.63	32.4
CN	N=1–0		
113.191	J=1/2–1/2, F=3/2–3/2	-5.18	5.43
113.488	J=3/2–1/2, F=3/2–1/2	-5.17	5.45
113.491	J=3/2–1/2, F=5/2–3/2	-4.92	5.45
	N=2–1		
226.6569	J=3/2–1/2, F=5/2–3/2	-4.02	16.3
226.8742	J=5/2–3/2, F=5/2–3/2	-4.02	16.3
226.8748	J=5/2–3/2, F=7/2–5/2	-3.94	16.3
	N=3–2		
340.0315	J=5/2–3/2, F=7/2–5/2	-3.42	32.6
340.2478	J=7/2–5/2, F=7/2–5/2	-3.38	32.7
340.2478	J=5/2–3/2, F=7/2–5/2	-3.42	32.7

D.3 Comparison between masing lines in NGC 253

In Figure D.6 we consider the maser-favoured $J_{-1} \rightarrow (J-1)_0 - E$ series, over-plotting their emission in each of the 10 studied regions for a given transition. The strongest masing lines at 84.5, 132.9, and 229.8 GHz, in terms of intensity, lie in region 7. This region (7) is centred at about the same location as region B in McCarthy et al. (2018b), the only location where they found the methanol maser line at 84.5 GHz. While our peak intensity is 1.5 times lower than the one observed by them, our beam is 4×3 times smaller. The second strongest line is detected in region 9 for the 84.5 GHz transition, in regions 3 and 6 for the 132.9 GHz transition, and in region 3 for the 229.8 GHz transition. In this last transition, the peak intensity in region 6 equals that in region 7. The 278.3 GHz transition is also plotted as its maser nature will be unveiled by the LTE modelling using CASSIS (see Sect. 4.2 of Appendix C). Maser emission in this last transition seems to show region 6 as the brightest spot, slightly surpassing region 7. A similar interchange in brightness depending on the transition was observed between lines at 36.1 GHz and 229.8 GHz by Fish et al. (2011) in the DR21 complex. We note, however, that in our case this interchange is likely an artifact due to line blending in the $9_{-1} \rightarrow 8_0 - E$ transition at 278.305 GHz with the $2_{-2} \rightarrow 3_{-1} - E$ transition at 278.342 GHz (see Subsect. 4.2.2 of Appendix C).

Another intriguing finding is that for the nuclear regions (3, 4, 5, and 6), the intensity of the

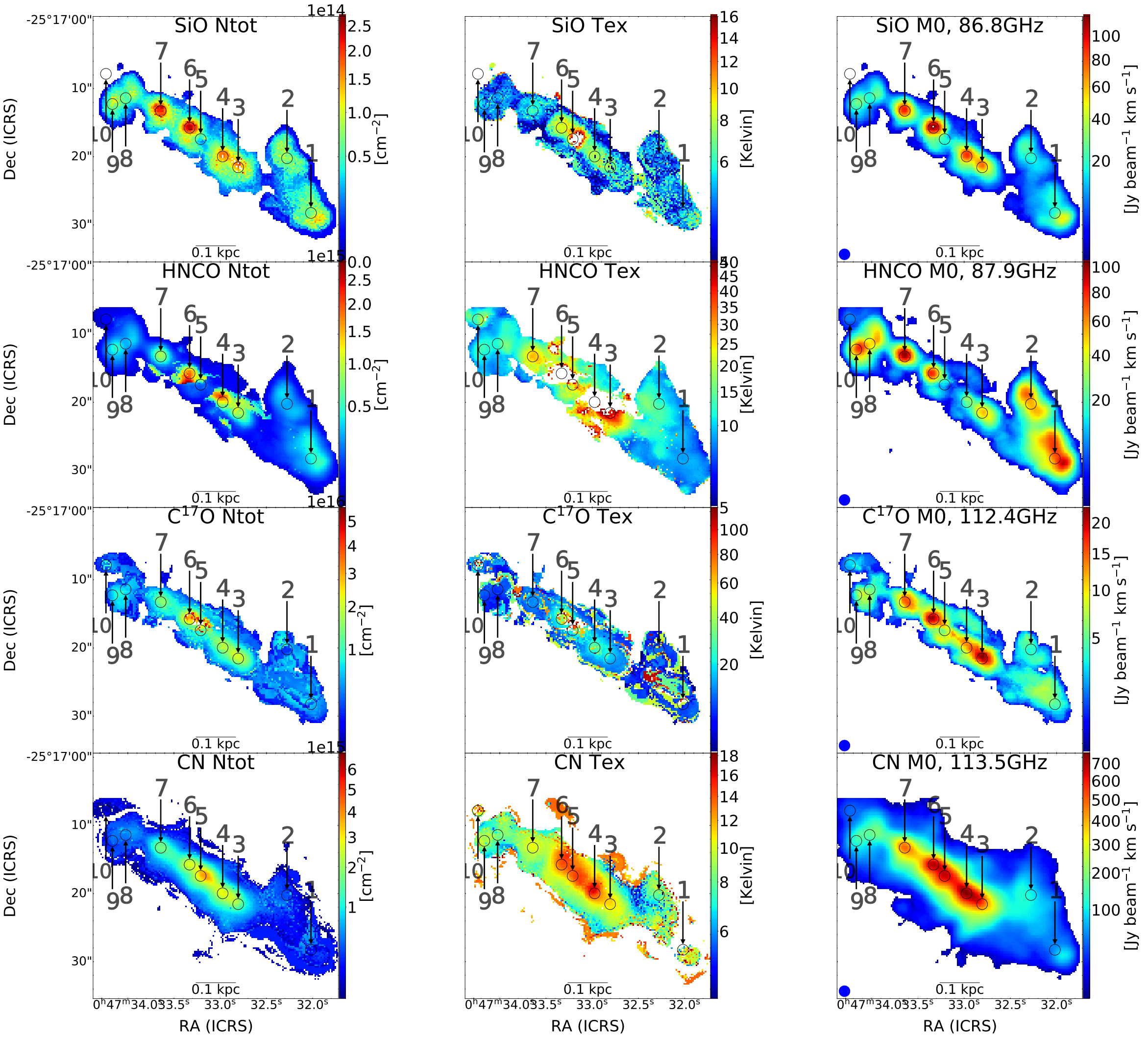

Figure D.5: Photodissociation regions traced by $N_{\rm tot}$(CN)/$N_{\rm tot}$(C^{17}O) column density ratios. A 5σ clipping was applied to the data before working with XCLASS. Higher ratios indicate a higher photodissociation level. A logarithmic stretch has been applied for an easy visualization. Value limits were set between 0.1 to 1.0 to avoid bad spaxels.

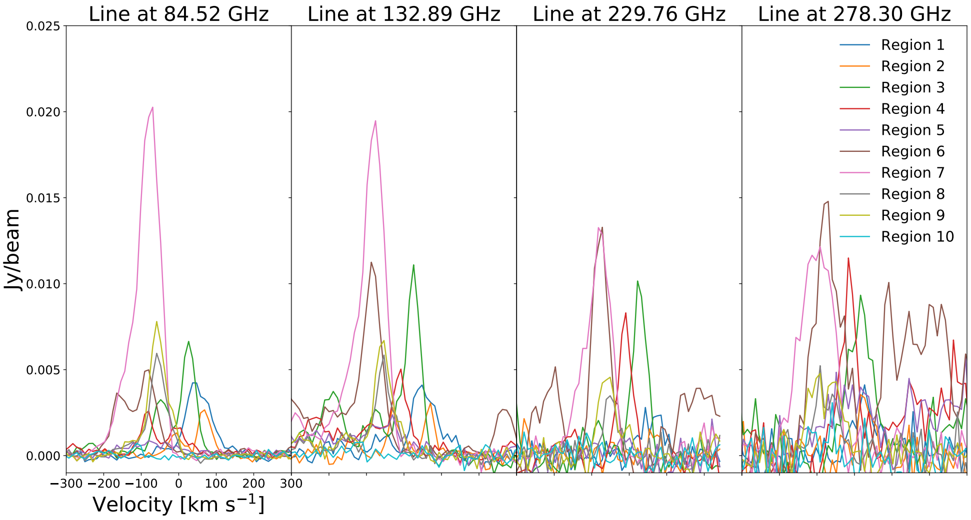

Figure D.6: Line strength comparison between methanol masers in the $J_{-1} \rightarrow (J-1)_0 - E$ series; frequencies are labelled at the top of each panel. The velocity was computed in the same manner as for Figure 2 of Appendix C. The velocity range and the intensity scale are common to all panels. We note the strongest intensities of the 84.52, 132.89 and 229.76 GHz lines in region 7, while the 278.30 GHz line provides the strongest peak in region 6.

132.9 GHz line doubles the one of the 84.5 GHz line. By comparison of each line profile, as noted in Figures 4 and 5 of Appendix C, the resulting increment in intensity is also correlated with a transition from a single line feature to two line components. This can be a result of two scenarios, (1) that a colder, more extended component is absorbing the line at lower frequency (84.5 GHz, ALMA Band 3) or (2) that the higher frequency line (132.9 GHz, ALMA Band 4) is less disturbed, showing a more homogeneous gas at similar velocities. As both lines belong to the same maser family, the first scenario may be the more likely one. However, in the first case we would expect self-absorption at the central frequency of the line, which is not observed. On the other hand, if case (2) is the one observed, then the presence of two velocity components will serve as another argument in favor of a disturbed environment prone to form masers in the $J_{-1} \rightarrow (J-1)_0 - E$ family, similar to the case of G+0.693–0.03, located in the Sagittarius B 2 star-forming region (Zeng et al., 2020). Finally, the lack of a second component in most of the regions detected in the 132.9 GHz line may be a result of its higher $A_{\rm ij}$, compared to lower-frequency transitions, impeding maser formation.

Regarding the $9_0 \rightarrow 8_1 - A^+$ transition at 146.6 GHz, which is also masing, the spatial distribution changes with respect to the two above mentioned $J_{-1} \rightarrow (J-1)_0 - E$ lines: its strongest emission is observed to be in region 6 instead of region 7 (see Fig. E.1 of Appendix C). This difference in distribution might be comparable to what is observed in the Galactic center object G+0.693–0.03 (Zeng et al., 2020), indicating that the $J_{-1} \rightarrow (J-1)_0 - E$ family of lines is preferentially enhanced in regions where cloud-cloud collisions take place, while the $J_0 \rightarrow (J-1)_1 - A^+$ series peaks at the sites of highest star formation. The fact that we do not observe an important emission at 146.6 GHz in region 4,

---

[2] `https://web-archives.iram.fr/IRAMFR/ARN/may95/node4.html`

may be due to a low column density there, while region 6 represents, even when also considering the central region 5, the region with the highest column density in our sample for A–CH_3OH, measured through both the rotation diagram method and the LTE modelling (Tables A.2 and 3 of Appendix C, respectively).

D.4 ALCHEMI spectral tuning

Table D.3 shows the ALCHEMI spectral tuning. This table provides the rest frequency coverage of each individual spectral setup in the lower (LSB) and upper (USB) receiver sidebands, in order of increasing frequency. Each sideband is covered by two slightly overlapping (1.875 GHz-wide) spectral windows. Observed frequencies were Doppler corrected to rest frequency assuming a receding velocity of 258.80 km s^{-1} (LSR, radio convention, see Meyer et al. (2004)). The ID of each setup corresponds to the ALMA band[3].

---

[3] `http://almascience.nrao.edu/aq/`

Table D.3: Imaged spectral tuning frequency coverage and amplitude scaling a_i: Amplitude scale factors considering compact and extended array dispositions. ^{c} This sideband was imaged in only one spectral window since the other suffered from poor atmospheric transmission

ID	Rest. Freq. Coverage (GHz)		a_i
	LSB	USB	Com./Ext.
B3a	84.172 – 87.614	96.190 – 99.335	0.976/1.108
B3b	87.423 – 90.980	99.174 – 102.731	1.003/0.789
B3c	90.777 – 94.334	102.531 – 106.088	0.990/1.107
B3d	94.131 – 97.688	105.885 – 109.441	0.997/1.128
B3e	97.488 – 101.045	109.242 – 112.798	1.009/0.948
B3f	100.848 – 103.993	112.617 – 116.005	1.001/0.922
B4a	125.193 – 128.804	137.281 – 140.977	0.996/0.998
B4b	128.771 – 132.457	140.934 – 144.625	1.003/1.026
B4c	132.424 – 136.110	144.587 – 148.273	1.015/1.001
B4d	136.077 – 139.763	148.240 – 151.931	0.980/0.989
B4e	139.731 – 143.421	151.894 – 155.584	0.992/0.968
B4f	143.384 – 147.069	155.547 – 159.237	1.021/1.014
B4g	147.037 – 150.723	159.200 – 162.891	0.992/1.002
B5a	163.215 – 166.761	175.306 – 178.834	1.016/1.147
B5b	166.566 – 170.112	178.657 – 182.203	0.998/1.050
B5c	169.917 – 173.469	183.684 – 185.560^c	1.013/0.974
B5d	173.274 – 176.820	185.365 – 188.911	0.993/0.928
B5e	185.380 – 188.890	197.441 – 200.988	0.992/0.856
B5f	188.713 – 192.241	200.798 – 204.338	0.955/0.428
B5g	192.058 – 195.598	204.149 – 207.695	1.033/0.927
B5h	195.409 – 198.955	207.506 – 211.046	1.001/0.974
B6a	211.286 – 214.733	226.279 – 229.766	0.948/0.995
B6b	214.545 – 218.096	229.578 – 233.121	1.000/1.005
B6c	217.908 – 221.459	232.941 – 236.492	1.004/1.034
B6d	221.271 – 224.822	236.304 – 239.847	1.001/1.010
B6e	224.634 – 228.185	239.667 – 243.218	0.995/0.990
B6f	243.202 – 246.753	258.235 – 261.786	0.867/0.991
B6g	246.565 – 250.116	261.598 – 265.157	1.015/1.003
B6h	249.936 – 253.479	264.969 – 268.512	0.924/0.992
B6i	253.299 – 256.842	268.332 – 271.875	0.959/1.006
B6j	256.662 – 260.141	271.703 – 275.126	1.027/1.008
B7a	275.348 – 278.726	287.333 – 290.761	1.020/0.975
B7b	278.490 – 281.978	290.536 – 294.014	1.013/1.008
B7c	281.753 – 285.231	293.789 – 297.267	0.988/1.003
B7d	284.996 – 288.484	297.041 – 300.509	1.257/1.040
B7g	295.015 – 298.663	307.050 – 310.528	0.990/0.984
B7h	298.257 – 301.876	310.293 – 313.781	0.833/0.998
B7e	300.519 – 303.997	312.555 – 316.023	0.993/1.014
B7f	303.772 – 307.240	315.808 – 319.266	0.996/0.994
B7i	328.313 – 331.811	340.579 – 344.097	1.023/0.956
B7j	331.636 – 335.184	343.922 – 347.460	0.989/0.984
B7k	334.999 – 338.527	347.275 – 350.803	0.972/1.017
B7l	338.372 – 341.870	350.658 – 354.136	1.028/0.967
B7o	348.851 – 352.469	360.887 – 364.425	0.922/1.007
B7p	352.204 – 355.822	364.239 – 367.767	1.025/1.034
B7m	354.156 – 357.694	366.441 – 368.298^c	1.034/1.044
B7n	357.509 – 361.047	369.814 – 373.202	1.008/0.991

APPENDIX E

Glossary

ALCHEMI	ALMA Comprehensive High-resolution Extragalactic Molecular Inventory
ALMA	Atacama Large millimetre/sub-millimetre Array
a.k.a.	also known as
AGN	Active Galactic Nucleus/Nuclei
APEX	Atacama Pathfinder EXperiment
CASSIS	Centre d’Analyse Scientifique de Spectres Instrumentaux et Synthétiques
CDMS	Cologne Database for Molecular Spectroscopy
CF	Correction Factor
CMZ	Central Molecular Zone
CNO burning	Carbon-Nitrogen-Oxygen burning
CNR	Circumnuclear Ring
COMs	Complex Organic Molecules
CR	Cosmic Ray
CRIR	Cosmic ray Ionization Rate
EMoCA	Exploring Molecular Complexity with ALMA
FWHM	Full Width Half Maximum
GC	Galactic Center
D_{GC}/R_{GC}	Galactocentric distance/radius
GMC	Giant Molecular Cloud

v_{HEL}	Heliocentric Velocity
IC	Index Catalogue
ICRS	International Celestial Reference System
ILR	Inner Lindblad Resonance
IMPRS	Internation Max Planck Research School
IPAC	Infrared Processing and Analysis Center
IRAM	Institut de Radioastronomie Millimétrique
IRAS	the Infrared Astronomical Satellite
ISM	Interstellar Medium
JPL	Jet Propulsion Laboratory
LMFIT	Non-Linear Least-Squares Minimization and Curve-Fitting for Python
l.o.s.	line of sight
LMC	Large Magellanic Cloud
LSR	Local Standard of Rest
LTE	Local Thermodynamic Equilibrium
MADCUBA	MAdrid Data CUBe Analysis
MASER	Microwave Amplification by Stimulated Emission of Radiation
MB	Main Beam
MCMC	Monter Carlo Markov Chain
Mpc	Megaparsec
MUSE	Multi Unit Spectroscopic ExplorerS
NASA	National Aeronautics and Space Administration
NGC	New General Catalogue
ngVLA	next generation Very Large Array
NRAO	National Radio Astronomy Observatory
PA	Position Angle
PDR	Photo-Dissociation Region

RJ	Rayleight-Jeans
Sgr. B2(N)	Sagittarius B2(North)
SFR	Star Formation Rate
S/N	Signal-to-Noise
SN(e)	Super Nova(e)
3C	Third Cambridge catalogue
TNoL	Total Number of Lines
UC	Ultra Compact
UV	Ultra Violet
VLA	Very Large Array
v_{sys}	Systemic Velocity
YSO	Young Stellar Object

List of Figures

List of Tables

Cover illustration: Claudia Isabel Álvarez Martínez-Conde